ornl

OAK RIDGE NATIONAL LABORATORY

UNION CARBIDE

NUREG/CR-2182
Volume 2
(ORNL/NUREG/TM-455/V2)

Station Blackout at Browns Ferry Unit One—Iodine and Noble Gas Distribution and Release

R. P. Wichner
C. F. Weber
R. A. Lorenz
W. Davis, Jr.
S. A. Hodge
A. D. Mitchell

Prepared for the U.S. Nuclear Regulatory Commission
Office of Nuclear Regulatory Research
Under Interagency Agreements DOE 40-551-75 and 40-552-75

OPERATED BY
UNION CARBIDE CORPORATION
FOR THE UNITED STATES
DEPARTMENT OF ENERGY

Printed in the United States of America. Available from
National Technical Information Service
U.S. Department of Commerce
5285 Port Royal Road, Springfield, Virginia 22161

Available from

GPO Sales Program
Division of Technical Information and Document Control
U.S. Nuclear Regulatory Commission
Washington, D.C. 20555

NUREG/CR-2182
Volume 2
ORNL/NUREG/TM-455/V2
Dist. Category RX, 1S

Contract No. W-7405-eng-26

Engineering Technology Division

Chemical Technology Division

STATION BLACKOUT AT BROWNS FERRY UNIT ONE — IODINE AND NOBLE GAS DISTRIBUTION AND RELEASE

R. P. Wichner
C. F. Weber
R. A. Lorenz
W. Davis, Jr.
S. A. Hodge
A. D. Mitchell

Manuscript Completed — July 22, 1982
Date Published — August 1982

Prepared for the
U.S. Nuclear Regulatory Commission
Office of Nuclear Regulatory Research
Under Interagency Agreements DOE 40-551-75 and 40-552-75

NRC FIN No. B0452

Prepared by the
Oak Ridge National Laboratory
Oak Ridge, Tennessee 37830
operated by
UNION CARBIDE CORPORATION
for the
DEPARTMENT OF ENERGY

CONTENTS

PREFACE

Notes Concerning Material Presented in Volume I

During the period since publication of the first volume* of this two-volume study of a postulated Station Blackout at the Browns Ferry Nuclear Plant, several matters concerning the material therein have required review and clarification. Volume I contains the accident sequence analysis pertinent to a prolonged Station Blackout, and because the fission product transport analysis, to be discussed in this second volume, directly follows and depends upon the events of the accident sequence, it is appropriate that a brief discussion of these matters precede the presentation of the volume II material.

First, as discussed in the Summary to Volume I, the TVA performed a battery capacity calculation as part of their review of the accident sequence analysis results obtained by ORNL. Whereas the ORNL study had involved an assumption of four hours to battery exhaustion, the TVA calculation showed that the batteries could be expected to last for six and one-half hours under Station Blackout conditions. The calculated events subsequent to battery failure are relatively insensitive to the time at which this failure occurs because of the slow variance of the decay heat four or more hours after shutdown; thus the degraded core analysis and the fission product transport analysis that is presented in this volume remain based on the results calculated under the nominal assumption of battery failure at the four hour point. Uncertainty regarding the battery lifetime is largely avoided in the material presented in this volume by measuring elapsed time from the point of battery failure.**

Nevertheless, there was question as to whether another failure mode such as depletion of the condensate storage tank water or overheating of the pressure suppression pool might lead to ECCS failure before battery exhaustion if the batteries were to last as long as the TVA study indicated. Appendix G of volume I, written as a result of the TVA calculations, shows that no other failure mode for ECCS injection would occur during the period from four to seven hours after the inception of Station Blackout; the extended analysis was taken to the seven-hour point to provide a reasonable overlap of the period of battery availability that TVA had predicted.

The difficulty arises from the implication in Volume I that the TVA study predicted a battery lifetime of seven hours whereas in fact the TVA calculations indicate that the batteries would be exhausted after six and one-half hours of duty under the conditions of a Station Blackout. This misrepresentation of the TVA study results was unintentional and is corrected here.

---

*D. H. Cook et al., 'Station Blackout at Browns Ferry Unit One — Accident Sequence Analysis,' NUREG/CR-2182, ORNL/NUREG/TM-455/V1, November 1981.

**A synopsis of the key events of the accident sequence is presented in terms of the elapsed time from battery failure in Table 1.1.

A second matter concerns the decay heat algorithm used for the MARCH code degraded core analyses presented in Section 9 of Volume I. This algorithm, given in Appendix B to Volume I, was used as a replacement to the decay heat subroutine of the original MARCH coding and was intended to provide a more realistic decay heat calculation by including consideration of actinide decay. However, as implemented, the revised algorithm predicts a decay heat power significantly higher than the ANSI 5.1 - 1979 standard with actinides. As shown in Fig. P.1, the decay heat algorithm used with the MARCH code to produce the results presented in Section 9 of Volume I closely matches the ANSI standard with actinides at 1000 seconds after shutdown but then diverges, exceeding the standard by approximately 45% at five hours (18,000 seconds) after shutdown.

Thus the decay heat model used for the MARCH calculations in the Station Blackout study is conservative (too high) with respect to the ANSI standard with actinides. Since this accident sequence extends over a period of hours, the time-integrated effect of the difference between the two models produces a significant change in the predicted timing of key events in the degraded core sequence. This is illustrated in Table P.1, which is a comparison of the Station Blackout key event timing as predicted by two MARCH runs which differ only in the decay heat algorithm employed. As shown, the lower decay heat power predicted by the ANSI 5.1 - 1979 Model with actinides results in a substantial slowing of the calculated accident sequences.

It should be noted that the events of the accident sequence before core uncovery presented in Section 7 of volume I were calculated with the BWR-LACP code which employed the ANSI 5.1 - 1979 standard decay heat model without actinides and therefore do not reflect the significant degree of conservatism inherent in the degraded core results calculated by the MARCH code. For future ORNL SASA studies both the MARCH code and the BWR-LACP code will employ the ANSI 5.1 - 1979 standard with actinide decay since this is believed to be the most realistic model currently available. Meanwhile, it is important that the reader recognize that the timing of events subsequent to core uncovery and the fission product transport analysis in this Station Blackout study are based upon a conservative decay heat model.

A third matter requiring discussion here is the reactor vessel steam relief valve capacity used for the Station Blackout study. As explained in Section 4 of Volume I, an actual capacity of 960,000 lb/h at 1115.0 psig was employed based on discussions with TVA engineers. However, in tests subsequent to the completion of the study, the measured capacity of a representative two-stage Target Rock relief valve identical to those installed at the Browns Ferry Nuclear Plant was found to be equivalent to 829,359 lb/h at 1115 psig.* Thus the relief valve capacity used for the Station Blackout calculations is too large. This has a negligible effect on the calculated results presented in Volume I except for the stuck-open relief valve results presented in Section 8.2, where the use of a larger-than-actual relief valve capacity is conservative. Therefore, the conclusion of Section 8.2, that reactor vessel level control can be maintained

---

*Private communication with J. A. Hunter, EG&G, Idaho. (The actual measured capacity was 838,900 lbs/h at 1128 psig.)

for at least five hours during a Station Blackout with one stuck-open relief valve would only be strengthened by the use of a smaller valve capacity.

Finally, for those readers unfamiliar with the application of the MARCH code to degraded core and containment analyses, it must be noted that this code has significant limitations. The general limitations with respect to LWR analysis with emphasis on PWR applications have been discussed elsewhere,* but the specific limitations with respect to BWR analysis are even more confining, because the code was originally written for PWR analysis and then modified to permit application to the BWR Mark I containment. For example, the core meltdown and slump into the reactor vessel bottom head as modeled in MARCH does not reflect the massive under-core structure of control rod guide tubes in a BWR and is therefore not realistic for such application, and the calculated temperatures in the small BWR drywell after vessel melt-through seem much too high.

For the reasons cited above, the degraded core and containment response analysis presented in Section 9 of Volume I must be considered to be no more than a reasonable approximation to the events and event timing that would occur in an actual prolonged Station Blackout. Since the fission product transport analysis to be presented in this volume is derived from the accident sequence analysis, this also can be no more than a reasonable approximation. Ongoing modifications and future improvements to the MARCH code will make more accurate approximations possible in the future.

---

*J. B. Rivard et al., 'Interim Technical Assessment of the MARCH code,' NUREG/CR-2285, SAND81-1672.R3, Nov. 1981.

Table P.1. Comparison of Station Blackout significant event timing as calculated by the MARCH code with two different decay heat algorithms

	Time after scram (min)		
	Decay heat model from Appendix B of volume I	Decay heat model from ANSI 5.1 - 1979 (with actinides)	Difference
Core uncovery	302	328	26
Begin melting	349	397	48
Core slump	378	443	65
Bottom head failure	413	484	71
Containment failure	513	640	127

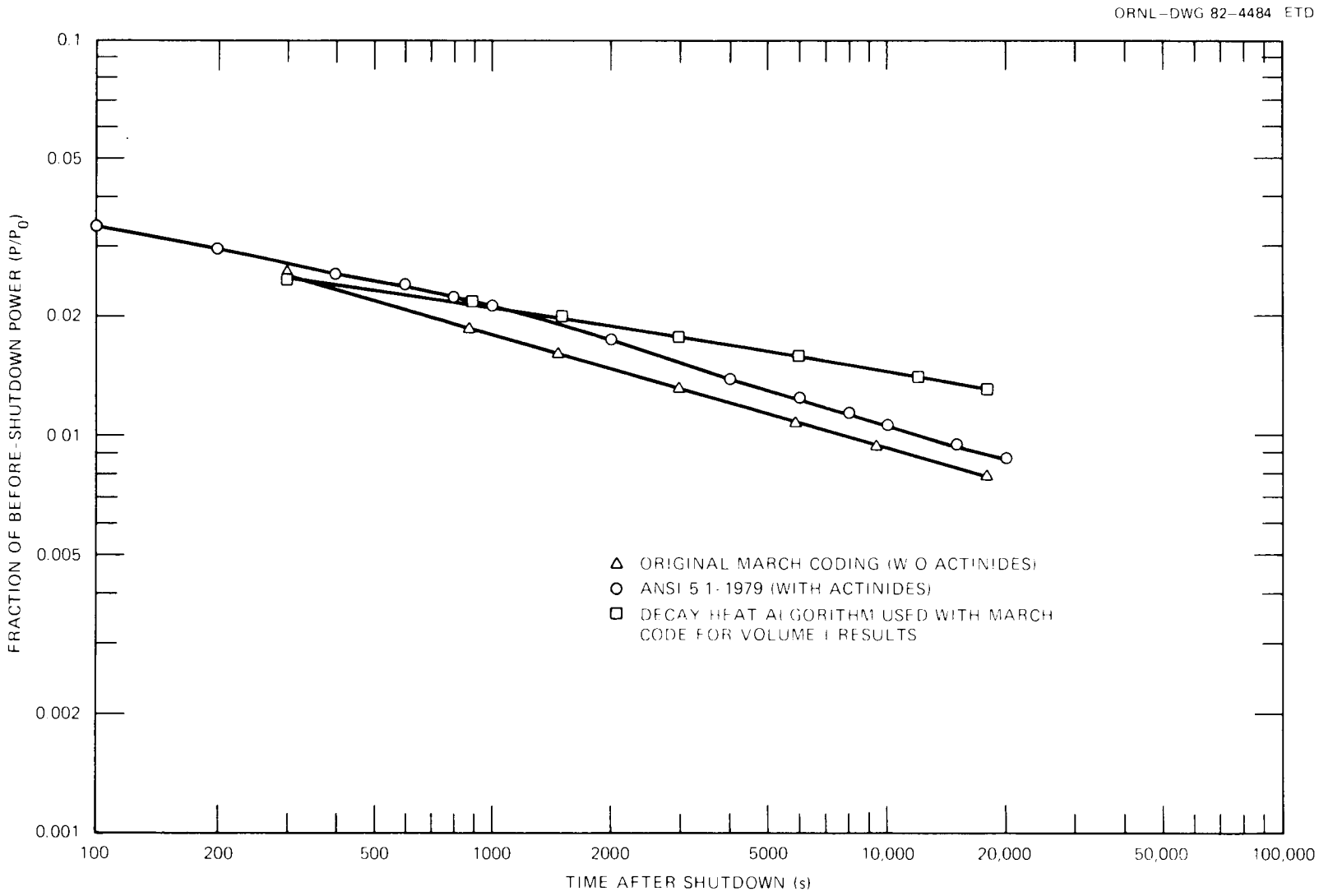

Fig. P.1. Comparison of results of decay heat algorithms.

STATION BLACKOUT AT BROWNS FERRY UNIT ONE – IODINE AND NOBLE GAS DISTRIBUTION AND RELEASE

R. P. Wichner
C. F. Weber
R. A. Lorenz
W. Davis, Jr.
S. A. Hodge
A. D. Mitchell

ABSTRACT

This is the second volume of a report describing the predicted response of Unit 1 at the Browns Ferry Nuclear Plant to a postulated Station Blackout, defined as a loss of offsite power combined with failure of all onsite emergency diesel-generators to start and load. The Station Blackout is assumed to persist beyond the point of battery exhaustion and the completely powerless state leads to core uncovery, meltdown, reactor vessel failure, and failure of the primary containment by overtemperature-induced degradation of the electrical penetration assembly seals. The sequence of events is described in Volume 1; the material in this volume deals with the analysis of fission product noble gas and iodine transport during the accident. Factors which affect the fission product movements through the series of containment design barriers are reviewed. For a reactive material such as iodine, proper assessment of the rate of movement requires determination of the chemical changes along the pathway which alter the physical properties such as vapor pressure and solubility and thereby affect the transport rate. A methodology for accomplishing this is demonstrated in this report.

---

1. INTRODUCTION

1.1 Scope and Objectives

The objectives of this report are to (1) define fission product pathways within the reactor vessel, the primary containment, and the reactor building for the postulated Station Blackout accident sequence at the typical BWR represented by Browns Ferry Unit 1, (2) list and examine the necessary assumptions required to estimate the rates of fission product movement from the core through the various containment barriers and the reactor building, and (3) estimate the fission product inventories and transport rates at each of a series of control volumes along the pathway as functions of time, with a final control volume representing the atmosphere external to the reactor building.

The sequence of events for the Station Blackout accident sequence is described and analyzed in Volume 1 of this report,[1.1] and is briefly summarized in Sect. 1.2 of this volume. Detailed thermal-hydraulic parameters for the event sequence after core uncovery such as primary system and containment temperatures, flows, and pressures were primarily determined from MARCH code results and are used as basic input data for the fission product transport calculations discussed in this volume.

The fission product transport analysis consists of the following steps:

1. Specification of the accident sequence and the behavior of the core, reactor vessel, wetwell, drywell, and the secondary containment-reactor building. The reactor vessel and containment structures are subdivided into control volumes that approximate the actual geometry.
2. Calculation of nuclide inventories. Initial inventories of all key noble gas and iodine nuclides and their significant precursors are estimated using the ORIGEN program with core loading and operating history data supplied by the Tennessee Valley Authority (TVA).
3. Fission product release rates from fuel are estimated using temperature-dependent release rate coefficients based on experimental values from the literature.
4. Calculational estimates are made of aerosol formation rates from overheated fuel and structures and from the interaction of molten core and concrete.
5. Complete mixing is assumed within each control volume, and the rate of convective transport between communicating control volumes is determined by the flows computed by the MARCH program.
6. The decontamination factors for the iodine species in the pressure suppression pool are determined by methods based on the published experimental results in the literature.
7. Calculational estimates are made of the deposition and revaporization rates of the iodine species on various surfaces within the containments and on the aerosols.
8. Iodine chemical species alterations are followed considering the effect of changing environmental conditions within the control volumes along the release pathway.

The fission product transport pathways are described in Sect. 2. Because the prolonged Station Blackout accident sequence is predicted to result in an ultimate gross failure of the drywell portion of the primary containment, this occurence dominates the transport pathway for this accident. Nevertheless, the pathways for leakage from the primary containments before gross failure are of interest and are discussed in Appendices A and B.

The methods used to estimate the release of fission products from the fuel and the generation of aerosols from both the overheated core and the core/concrete interaction are described in Sect. 3 and amplified in Appendix C.

The factors which determine the movement of noble gases and iodine within the containment structures are discussed in Sect. 4. A necessary prerequisite for iodine transport analyses is an evaluation of the chemical forms of iodine which might exist in the control volumes along the release pathway, and this is provided in Sect. 4.2. The effectiveness of

the pressure suppression pool in removing the various iodine species that are washed into it is central to the fission product transport analysis of any BWR and is discussed in Sect. 4.5.

The calculational methodology employed for the fission product transport analysis is described in Sect. 5. Much of this effort is original and will be used as a basis for future development of the technique as applied to other severe accident sequences to be analyzed under the Severe Accident Sequence Analysis (SASA) program.

The results of this analysis are limited to the transport of the fission product noble gases and iodines during the postulated Station Blackout sequence, and are discussed in Sect. 6. A summary of the results and the conclusions of the analysis are presented in Sect. 7.

1.2 Description of Assumed Accident Sequence – Browns Ferry Complete Station Blackout

A detailed description of the accident sequence assumed in this study is described in the companion document to this report.[1.1] Here we will summarize the most significant features of this postulated accident,* emphasizing aspects which bear most directly on fission product transport.

An overall summary of the major events in this sequence is provided in Table 1.1. In contrast to Ref. 1.1, events are given at times measured from battery exhaustion, which is estimated to occur 4 h following the initiating event, the loss of offsite power. A detailed listing of events in the initial 4-h time span before battery exhaustion is provided in Table 9.1 of Ref. 1.1. During this initial time period the HPCI system, which is powered by steam generated by decay heat, serves to keep the core covered with water drawn from the condensate storage tank; therefore neither fuel failure nor any events of significance to fission product transport occur.

Battery exhaustion results in loss of the HPCI and RCIC coolant injection systems, and a boiloff of coolant begins in which the reactor vessel level decreases as the decay-heat-generated steam is vented through the steam relief valves to the pressure suppression pool. The top of the core is uncovered one hour after the loss of battery power. The temperature of the exposed fuel increases as the water level drops, but the temperature of the fuel that remains below the water level stays at about 300°C. Steam is leaving the reactor vessel at about 1000 L/s (3600 lb/min) during this period.

At 95 min. after the loss of battery power, the first fuel rods reach 1000°C. The steam-zircaloy reaction is initiated but the reaction rate is

---

*Determination of the probability of occurrence of a Station Blackout at the Browns Ferry Nuclear Plant was not a part of this study. However, as noted in Sect. 2 of Vol. I, Station Blackout is an extremely unlikely event, and it is very improbable that a Station Blackout, if it did occur, would persist as long as the time required for battery exhaustion.

not significant. Steam is leaving the core region at about 440 L/s (1500 lb/min) and ultimately passing through the relief valves to the pressure suppression pool. Water covers only the lower 1.5 m (4.9 ft) of the fuel rods. The bulk water temperature in the pressure suppression pool is 103°C and the primary containment pressure is 2.2 bar* (32 psia). Gas is flowing from the wetwell to the drywell through the vacuum breakers at 21 L/s (45 ft^3/min).**

The fuel rods start to fail 103 min after battery exhaustion. The failure is caused by over-temperature (1300°C) and embrittlement from the steam oxidation of the Zircaloy cladding. The steam-zircaloy reaction is consuming about 5% of the steam flowing past the rods. Although the reaction occurs in every radial region, the outermost ring of fuel is not hot enough to drive the reaction very quickly. Steam is flowing out of the reactor vessel at about 440 L/s (1400 lb/min), and water covers only the lower 1.25 m (4.1 ft) of the fuel rods. The bulk water temperature in the wetwell has increased to 104°C and the primary containment pressure is 2.3 bar (33 psia). The temperature in the drywell is only slightly lower than the wetwell temperature. Gas is flowing from the wetwell to the drywell at 54 L/s (114 ft^3/min).

The steam-zircaloy reaction quickly heats the fuel rods in the central region of the core. Two hours after the start of the boiloff, portions of the core have reached the melting point of the fuel eutectic (~2280°C) and the steam-zircaloy reaction consumes about 70% of the steam. Gas is leaving the reactor vessel at 430 L/s (320 L/s steam, and 110 L/s hydrogen). Water covers the lower 0.9 m (3.0 ft) of the fuel. The water temperature in the pressure suppression pool has increased to 106°C. Gas is flowing from the wetwell to the drywell at 1070 L/s (2260 ft^3/min).

The temperature in the core continues to rise and more of the fuel reaches the melting point. The outer ring of fuel does not reach the melting point or the assumed fuel failure temperature (1300°C) due to the lower decay heat in these assemblies. The steam-zircaloy reaction does not occur to a significant degree in this fuel as a consequence of the lower temperatures. Thus, when the central core collapses into the lower head of the reactor vessel at 137 min after the start of the boiloff, this outer ring of fuel should remain in place.

The core collapses 137 min after the loss of battery power. The molten fuel is quenched in the pool of water which remains in the lower plenum of the vessel. Steam is evolved at a very fast rate, but since the reactor vessel is still intact, this steam is vented through the safety/relief valves (S/RVs) to the suppression pool. The steam rate leaving the core region achieves a maximum rate of about 20,000 L/s (93,000 lb/min). The steam leaving the reactor vessel achieves a maximum rate of about 30,000 L/s (74,000 lb/min), which requires the opening of five relief valves.

The high rate of addition of steam to the suppression pool causes an increase in temperature and an increase in the gas venting rate to the

---

*1 bar = 10^5 Pa = 1.01 atm.

**It should be noted that all flows and temperatures discussed in this section are those calculated by the MARCH code and the accuracy of these quantities is therefore subject to the limitations of this code.

drywell. The bulk water temperature in the wetwell rises to about 113°C, and the pressure in the primary containment rises to 3.7 bar (53 psia). Gases are flowing from the wetwell to the drywell at up to 3950 L/s (8380 ft³/min).

When the core collapses into the lower plenum of the vessel, the water quenches the molten pool. The water boils away and the molten fuel heats the lower head of the reactor vessel. The heat and pressure cause the head to fail 172 min after the start of the boiloff, and the contents of the reactor vessel are dropped into the drywell sump. The water in the drywell sump quenches the molten mass. The fast creation of steam in the drywell reverses the direction of gas flow between the wetwell and drywell. The vacuum breakers in the vent pipes close and steam is ejected through the downcomer pipes into the wetwell water. The flow rate is very fast for the first 2 min (~65,000 L/s), and subsequently decreases rapidly to ~4700 L/s.

The water covering the molten pool boils dry, and the fuel starts to interact with the concrete floor in the drywell. The core-concrete interaction starts about 232 min after the start of the boiloff. At this time, the temperature of the wetwell water is 154°C, and the temperature of the drywell atmosphere is 158°C. The pressure in the primary containment is 7.2 bar (103 psia). The reaction products of the core-concrete interaction are, to a large degree, noncondensable gases. The reaction products quickly heat the airspace of the drywell. At 249 min after the start of the boiloff, the temperature of the drywell atmosphere has increased to 264°C, and the pressure has increased to 8.9 bar (130 psia).

The high temperature in the drywell causes the electrical penetration assembly seals to fail at this time. The failure of the primary containment quickly lowers the pressure in the drywell to atmospheric conditions. The water in the wetwell flashes to steam and flows through the vacuum breakers, through the drywell, and out to the reactor building. Initially, the flow rate from the wetwell to the drywell is about 236,000 L/s (500,000 ft³/min), and the flow rate from the drywell to the reactor building is about 270,000 L/s (780,000 ft³/min). The flow rate slows during the next 15 min as the water in the wetwell cools to 100°C. At 266 min after the start of the boiloff, the flow rate from the wetwell to the drywell has decreased to 2900 L/s (6100 ft³/min), and the flow from the drywell to the reactor building has decreased to 25,000 L/s (73,000 ft³/min).

The gases which have passed through the electrical penetrations in the drywell wall flow through the reactor building and out to the atmosphere. The secondary containment (or reactor) building is divided into a number of interconnected compartments and levels. When the electrical penetration assemblies fail, the gases flow from the drywell, through the various levels of the reactor building, through the refueling floor, and out through pressure relief panels to the atmosphere.* The large panel

*The refueling floor is common to the three Browns Ferry reactor units, and it has been assumed that the Station Blackout accident sequence occurs simultaneously at each of the units. If the accident sequence occurred on just one unit, the pressure buildup on the refueling floor would be less, and the relief panels would probably not relieve to the atmosphere.

area should allow the gases to flow from the drywell to the atmosphere without significant resistance.

Five hours after the start of the boiloff, the flow rate from the suppression pool to the drywell is about 9600 L/s (20,300 ft^3/min). The flow rate from the drywell to the reactor building is about 46,000 L/s (97,000 ft^3/min). The temperature of the suppression pool water has dropped to 99°C, with essentially atmospheric pressure in the primary containment.

The remainder of the accident continues in this manner. The flow rates from the wetwell to the drywell, and from the drywell to the reactor building decrease erratically as the wetwell water cools and the core-concrete reaction slows. The temperature in the drywell increases during this period and rises to 700°C at 6 h after the start of the boiloff. The flow from the wetwell to the drywell stops at about 7 h after the start of the boiloff, but the core-concrete interaction continues.

A short synopsis of events is given in Table 1.2 which lists both times from battery failure (used in this report) and times from initiating event, as employed in volume 1.[1.1]

Figures 1.1 through 1.5 are adapted from the corresponding figures in Volume 1 to illustrate the variation of some key pressure vessel parameters during the accident sequence as predicted by MARCH.* Major sequence events, taken from Tables 1.1 and 1.2, are noted on these figures. The maximum core temperature is plotted in Fig. 1.1. Heatup follows core uncovery at 302 m reaching the maximum estimated eutectic temperature of ~2300°C (2573 K) at ~310 m. At 392 m inbuilt MARCH assumptions predict the core to slump, as indicated by the rapid drop in temperature as the core is quenched by water in the pressure vessel. Not shown in Fig. 1.1 is the subsequent rise in temperature for t > 392 m, which leads eventually to pressure vessel failure by melt-through.

It is important to note that MARCH presumes the entire core to slump to the reactor vessel bottom head at t = 392 m when 75% of the core is judged to be molten. This may not be a completely appropriate assumption since at t = 392 m the outer ring of fuel assemblies do not reach even 1300°C, the inception for cladding failure in this case. Therefore, for fission product transport analysis, we have assumed that only the central portion of the core (~90%) slumps to the bottom head, the balance remaining in place.

The rate of core melting, the fraction of cladding reacted with steam, and the mass of H_2 in the pressure vessel as predicted by MARCH are shown in Figs. 1.2 through 1.4. As noted above, Fig. 1.2 illustrates the MARCH assumption that core slumping occurs when 75% of the core reaches the eutectic melting temperature; this is represented by the vertical line at t = 392 m. As shown in Fig. 1.3, the fraction of clad reacted is predicted to be ~20% at the time of core slumping; the Zr/H_2O reaction thus continues for some period of time following core melting. In Fig. 1.4, the drop in H_2 in the reactor vessel at time of core slumping is due to the purging to the wetwell caused by the high steaming rates which occur at this time.

---

*It should be noted that the time axis on the abscissa of these figures represents the elapsed time from the inception of the Station Blackout.

Figure 1.5 shows that the average steam flow from the reactor vessel to the wetwell through the S/RV's generally runs about 10 kg/s from 240 to ~350 m. A sharp surge of flow is seen to occur momentarily at the time of core slumping.

Figures 1.6 through 1.8 illustrate some wetwell conditions during this sequence. The temperature of the wetwell atmosphere rises rapidly through the period of Zr/H_2O reaction and core melting as seen in Fig. 1.6. The temperature decrease at t = 500 m corresponds to the time of drywell failure, at which time the wetwell pressure falls (due to communication of these two zones via the vacuum breakers) and as the suppression pool boils. The predicted H_2 partial pressure in the wetwell atmosphere is shown in Fig. 1.8.

The composition of the wetwell atmosphere changes significantly during the course of the accident. Initially, the composition is roughly 95% N_2 with the balance primarily O_2; N_2 enrichment is employed to prevent H_2/O_2 deflagration. As time progresses, both the H_2O and H_2 partial pressures increase, the first because of the pool temperature rise and the latter resulting from the Zr/H_2O reaction. At the time of drywell failure (t = 503 m), the H_2O and H_2 partial pressures in the wetwell are predicted to be approximately equal (~2 bar) and together contribute about 50% of the total wetwell pressure. Following drywell failure, the large steam flow from the wetwell through the drywell purges the atmosphere of noncondensibles, and the pressure following this event is therefore primarily steam at atmospheric pressure.

Figures 1.9 through 1.11 illustrate the behavior of the drywell. Note that the drywell pressure (Fig. 1.9) begins to rise soon after the initiation of the Station Blackout because of steam flow through the S/RV's to the wetwell and, soon after, from the wetwell atmosphere back to the drywell via the vacuum reliefs. The pressure increase accelerates at core slumping (t = 392 m) and at the time of pressure vessel failure. Following pressure vessel failure, the drywell pressure continues to rise primarily due to the core/concrete reaction.

The venting rate from the failed drywell to the reactor building is shown in Fig. 1.10. The initial surge consists primarily of the H_2O, H_2, and N_2 contents of the drywell and wetwell. The more-or-less steady flow of ~30 m^3/s from t = ~510 m to ~880 m results from the core/concrete reaction and therefore consists mainly of H_2O and CO_2.

The drywell wall temperature history is shown in Fig. 1.11. Shown here is the temperature of the innermost nodal point which represents the inner surface temperature of the drywell liner. Note that some rather high drywell wall temperatures are predicted by MARCH at the end of the sequence. Therefore, we can expect that the paint on interior surfaces of the drywell would char (beginning at T = 300°C), and material sorbed on steel surfaces, such as the exterior and interior of the reactor vessel, would tend to desorb during this phase.

While Figs. 1.1 through 1.11 and Tables 1.1 and 1.2 serve to provide an overall view of the event sequence emphasizing features important to fission product transport, the interested reader should refer to Chapter 9 of Vol. $1^{1.1}$ for a full description of events. In particular, the set of figures 9.4, 9.6, 9.8, 9.10, 9.12–9.21, 9.23–9.27, 9.29–9.32, 9.37, and 9.39–9.42 in Ref. 1.1 provide a more complete description of pressure vessel, wetwell and drywell conditions.

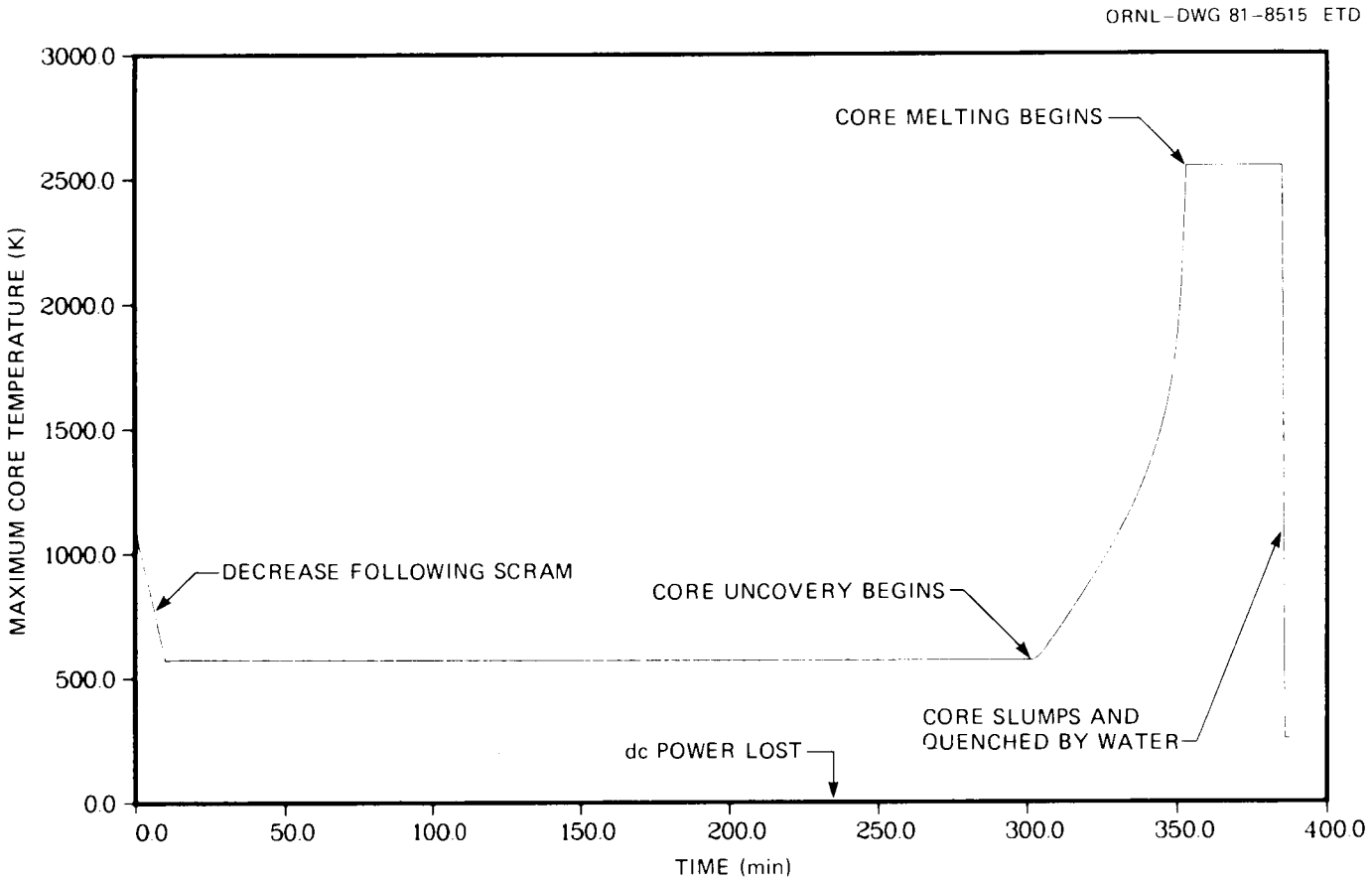

Fig. 1.1. Maximum core temperature.

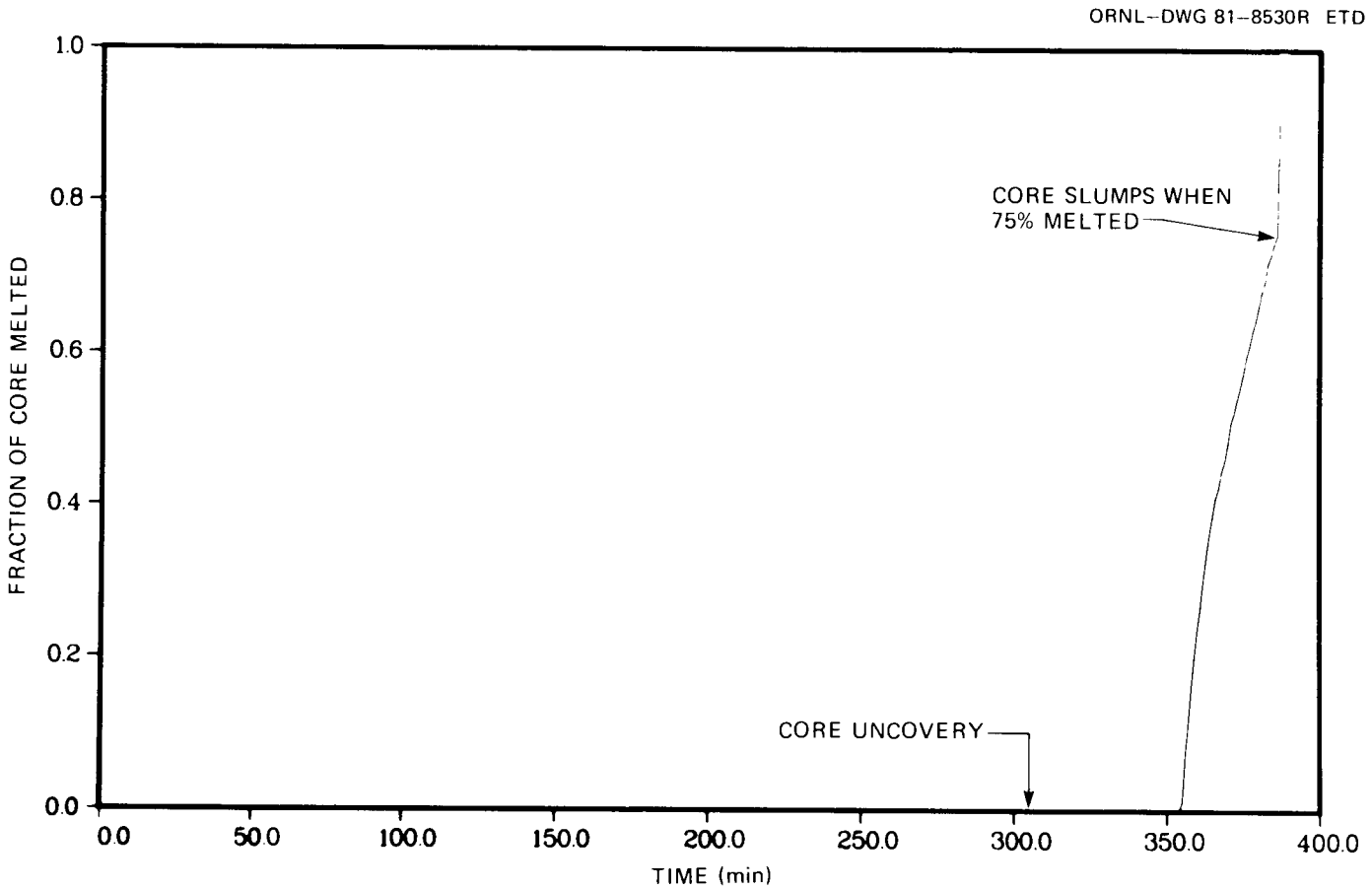

Fig. 1.2. Fraction of core melted.

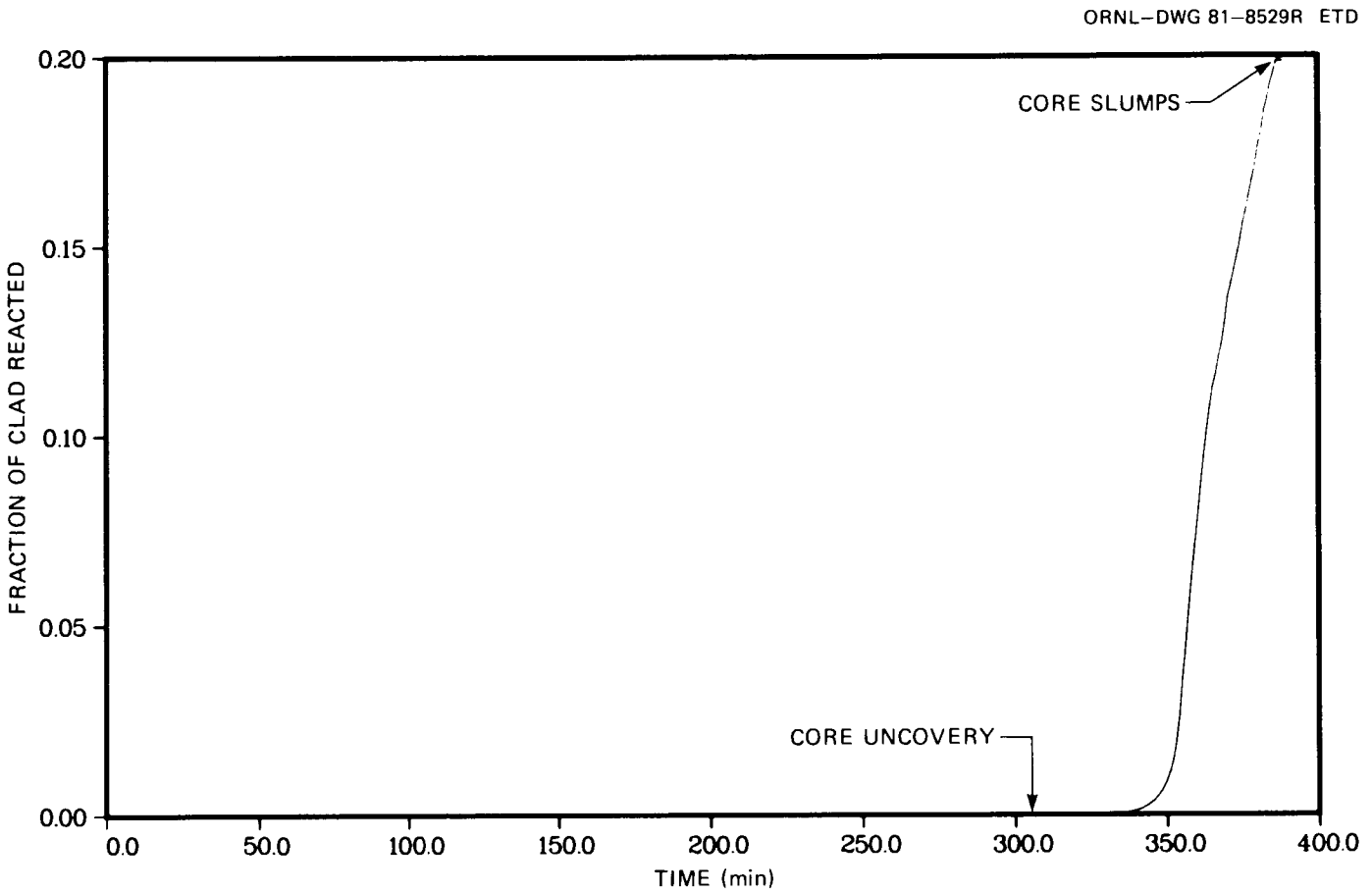

Fig. 1.3. Fraction of clad reacted.

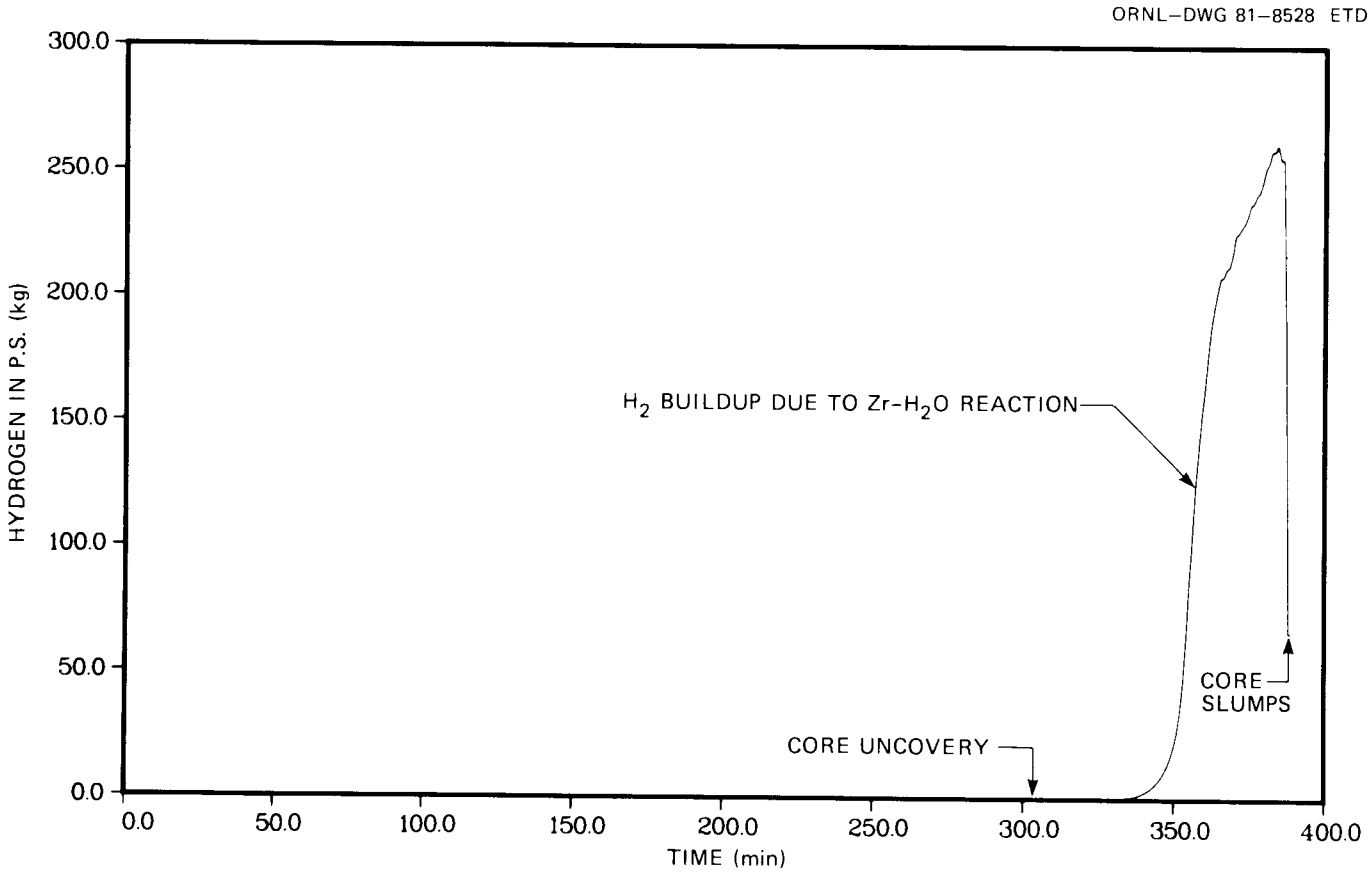

Fig. 1.4. Hydrogen mass in primary system.

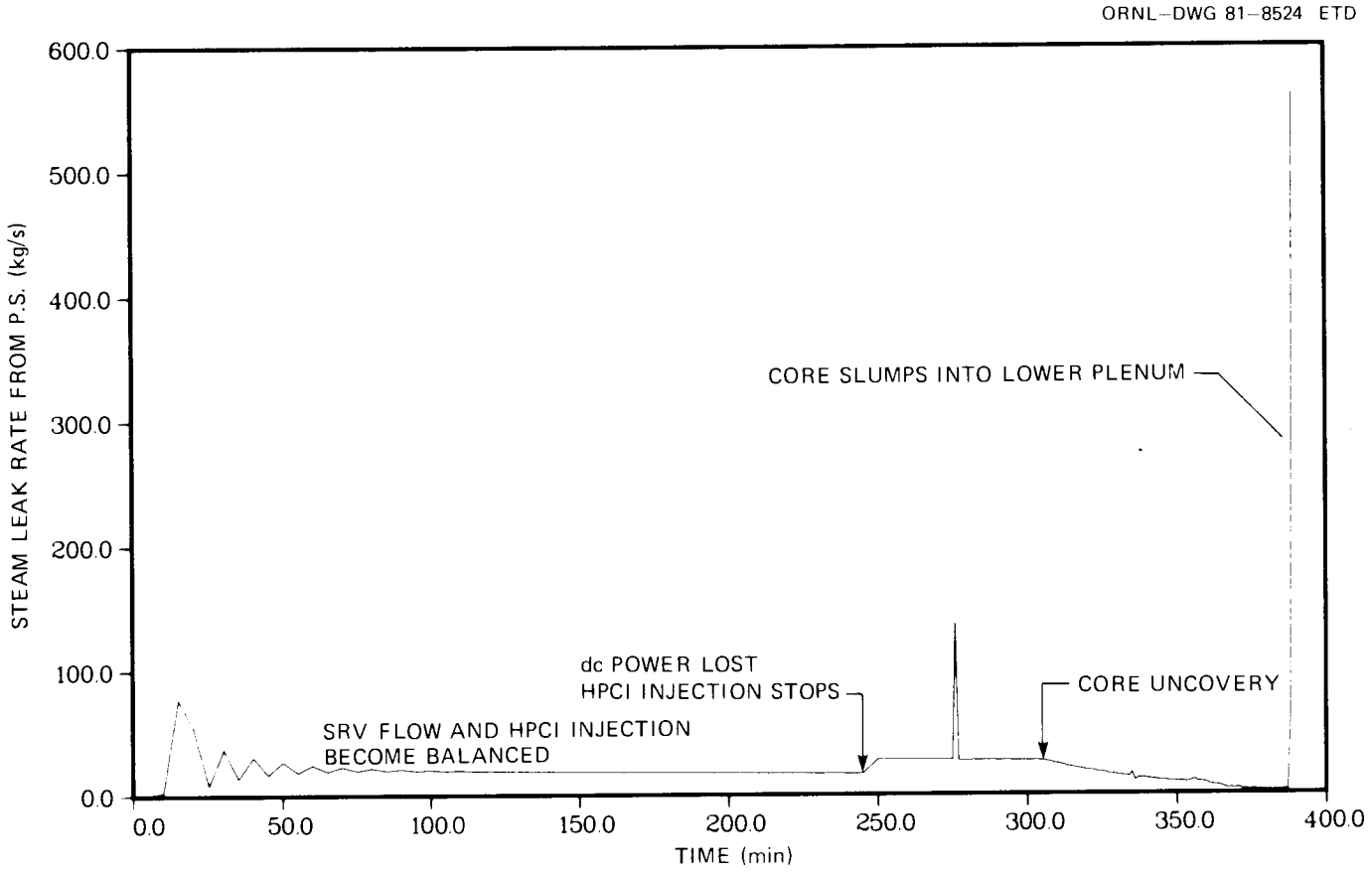

Fig. 1.5. Steam mass flow rate from primary system.

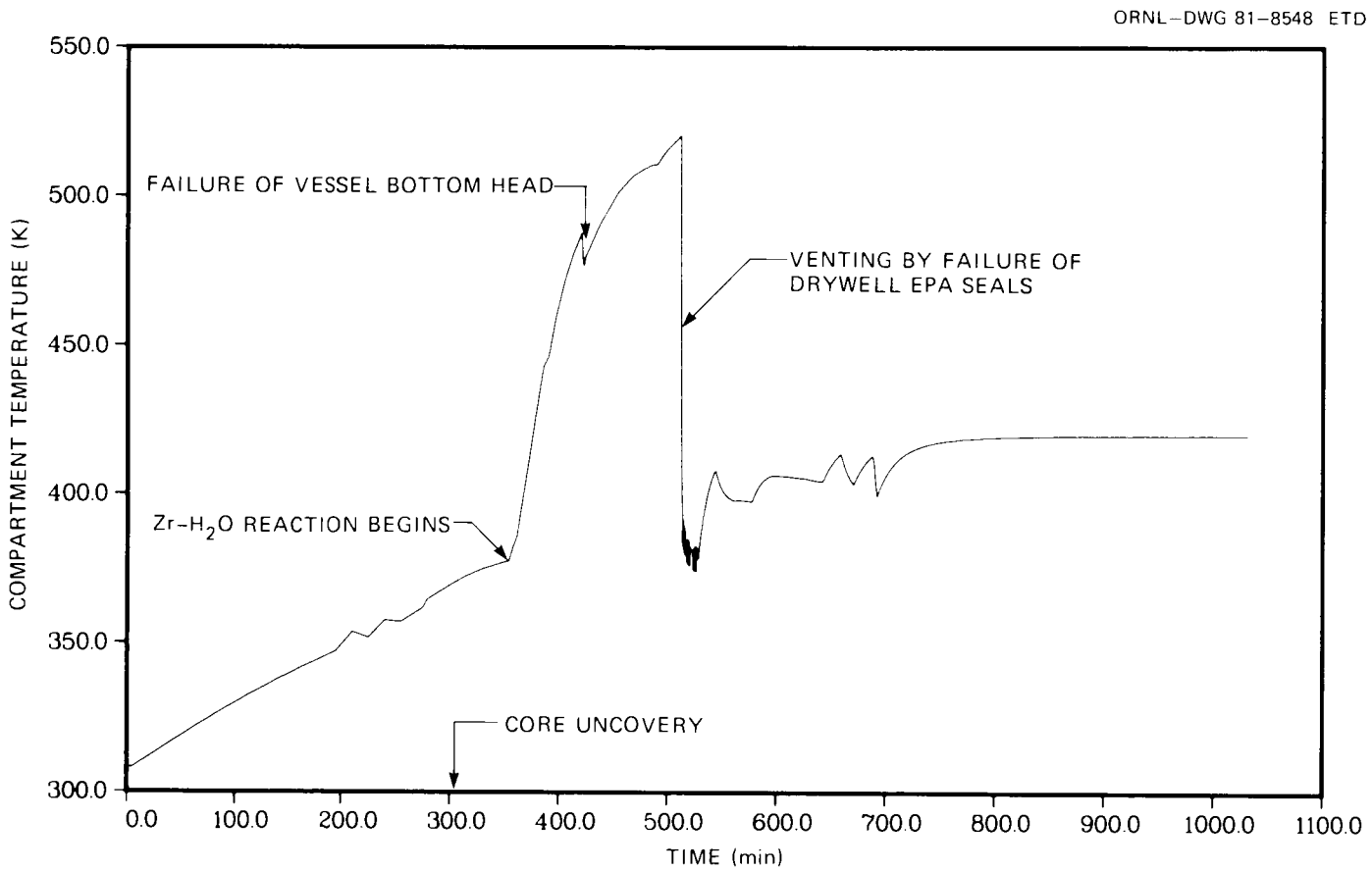

Fig. 1.6. Temperature history of wetwell atmosphere.

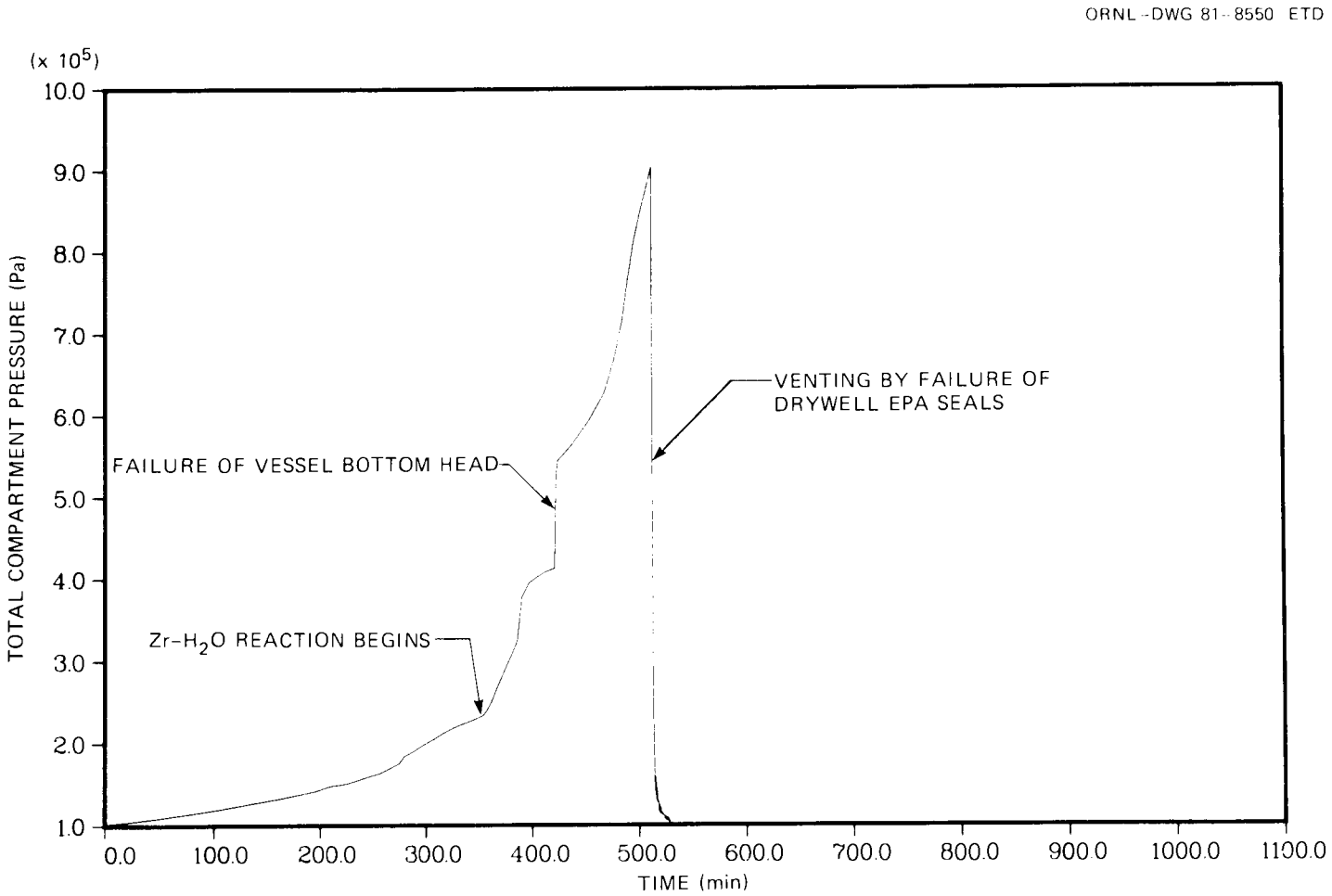

Fig. 1.7. Wetwell total pressure.

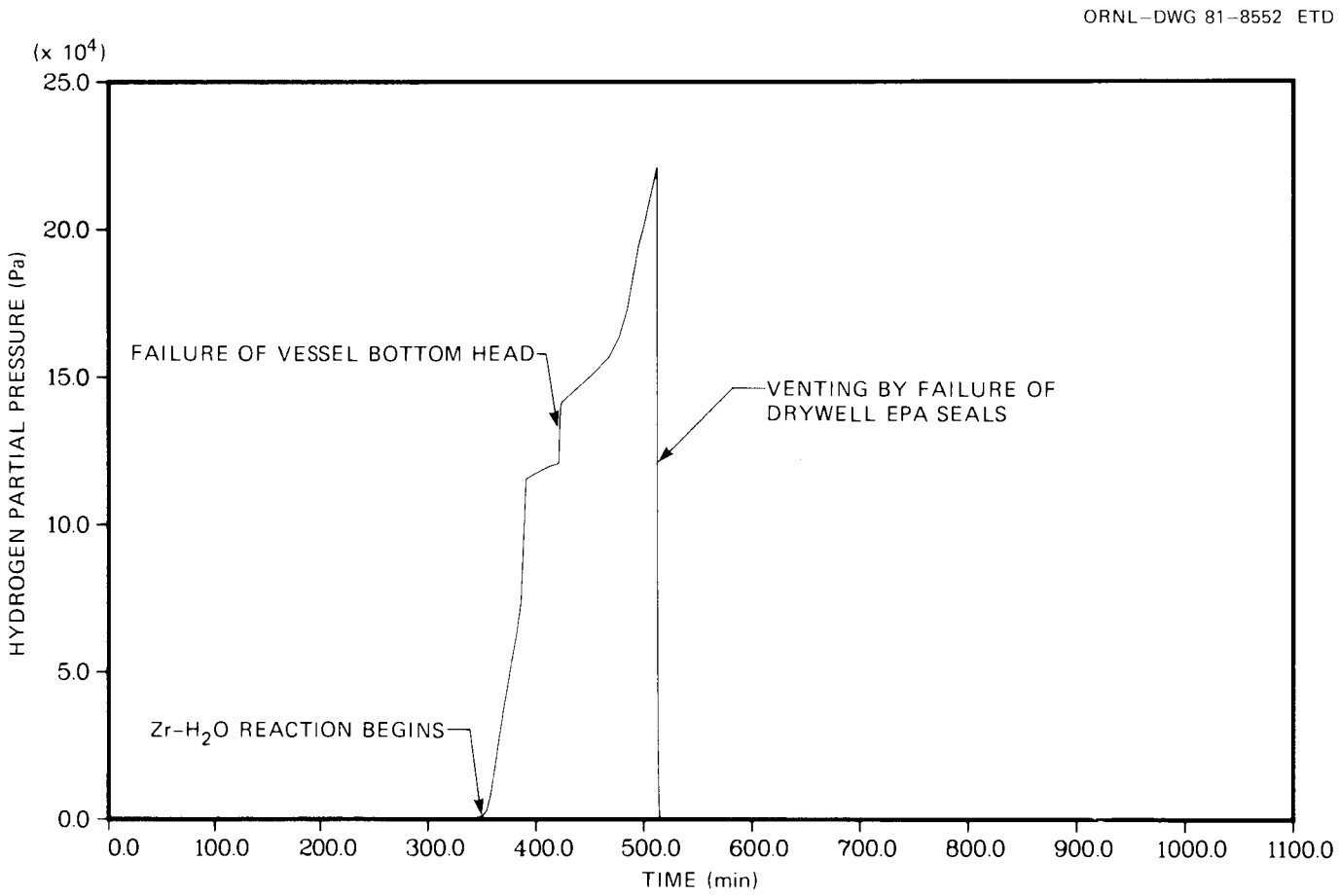

Fig. 1.8. Wetwell hydrogen partial pressure.

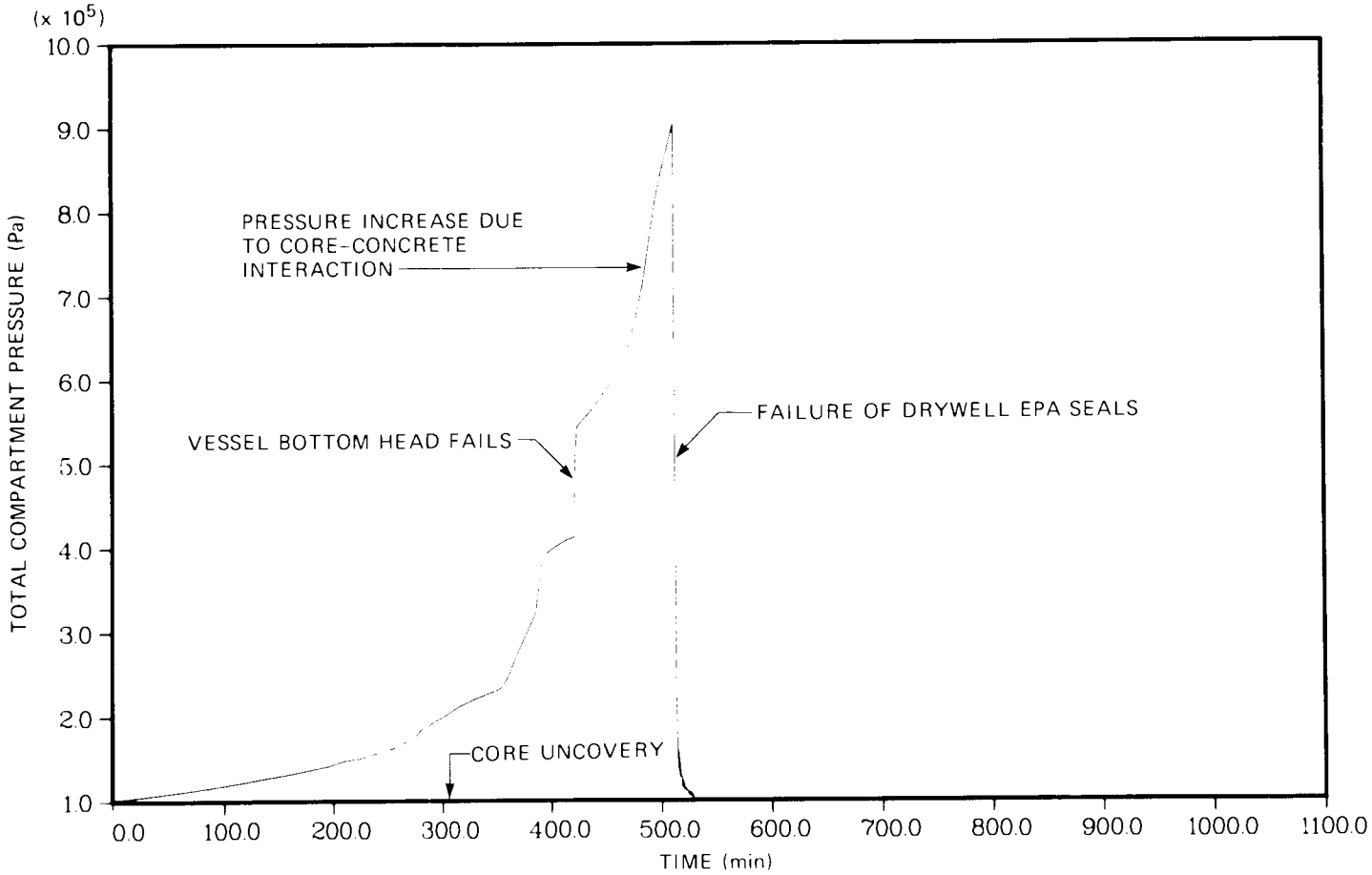

Fig. 1.9. Drywell total pressure.

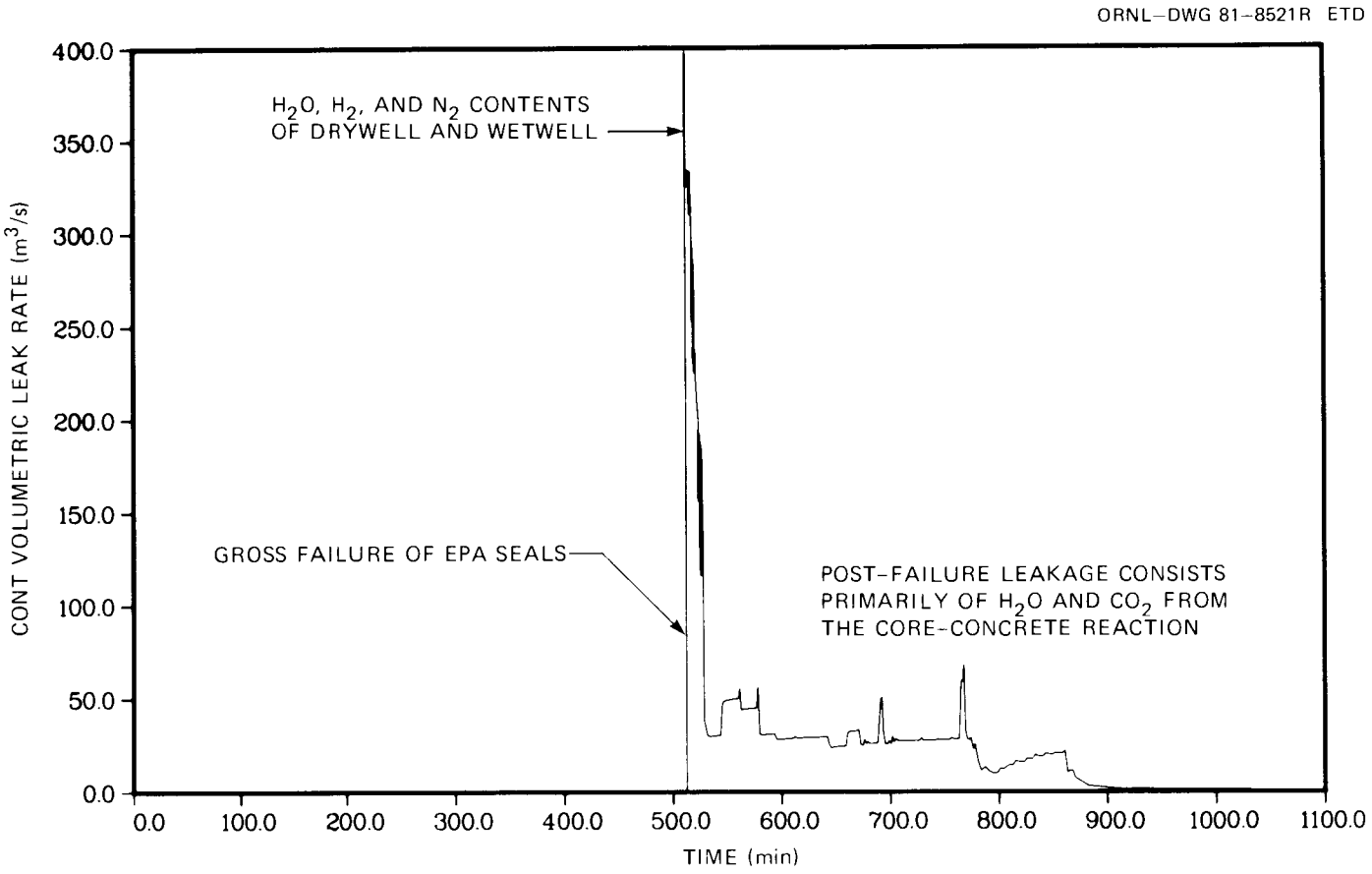

Fig. 1.10. Containment leak rate.

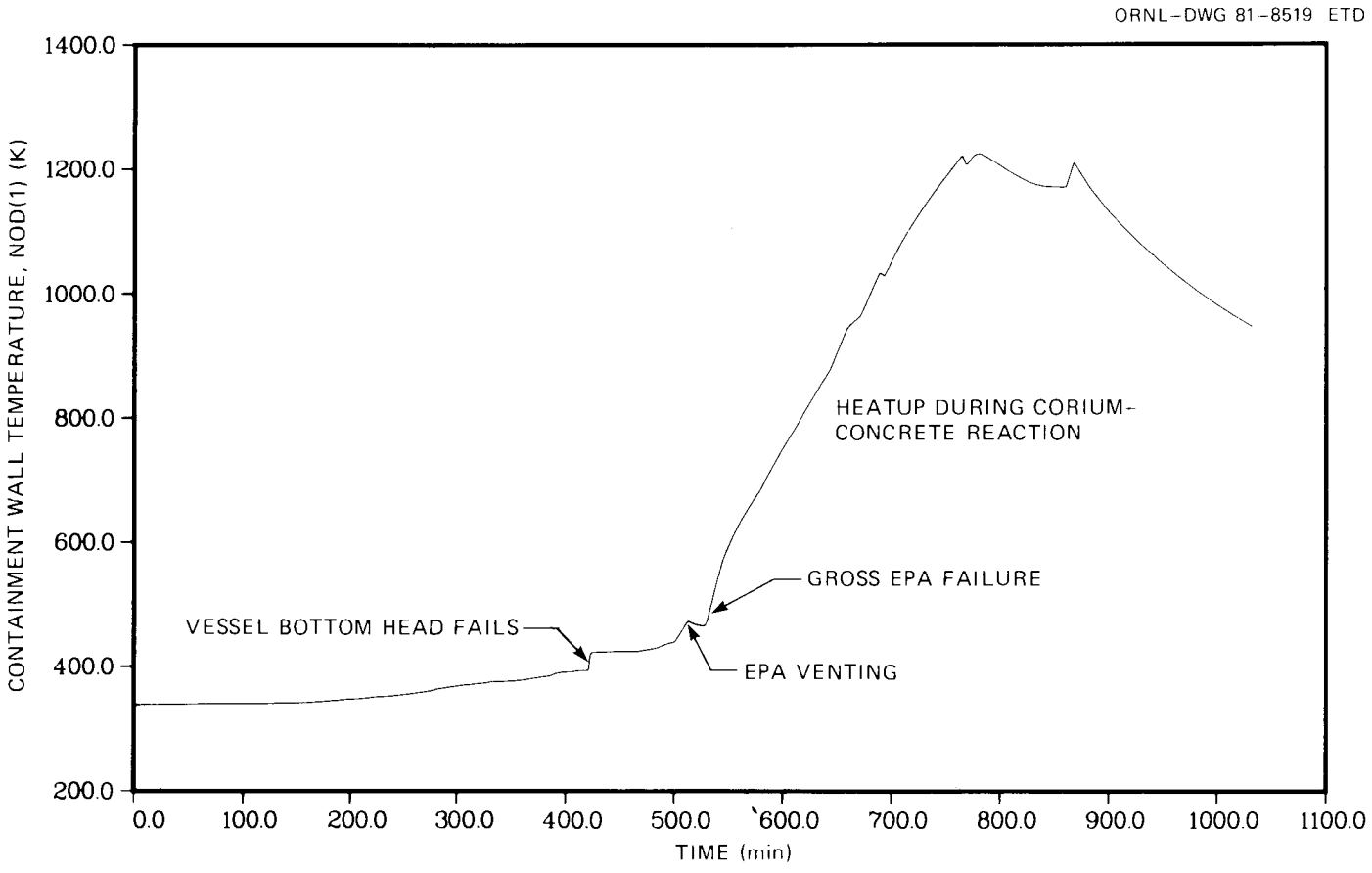

Fig. 1.11. Temperature of drywell liner.

Table 1.1. Summary of important events following loss of battery power

Time following battery exhaustion	Event	Average vessel relief valve flow [L/s (lb/h)]
1 h, 0 min	Top of core uncovered	1000 (216,000)
1 h, 35 min	Water covers lower 1.5 m (4.9 ft) of core First fuel rods reach 1000°C Steam–Zr reaction begins PSP bulk water temperature 103°C Containment pressure 2.20 bar[a] (32 psia) Gas flow wetwell→drywell 21 L/s (45 ft³/min)	440 (90,000)
1 h, 43 min	Water covers lower 1.25 m (4.1 ft) of core First fuel rods fail at 1300°C Steam–Zr reaction consumes 5% of steam PSP bulk water temperature 104°C Containment pressure 2.30 bar (33 psia) Gas flow wetwell→drywell 54 L/s (114 ft³/min)	440 (84,000)
2 h, 0 min	Water covers lower 0.91 m (3.0 ft) of core First fuel rods begin melting at 2280°C Steam–Zr reaction consumes 70% of steam PSP bulk water temperature 106°C Gas flow wetwell→drywell 1070 L/s (2260 ft³/min)	Steam 320 (50,000) H_2 100
2 h, 17 min	Central core collapses into lower plenum PSP bulk water temperature 113°C Containment pressure 3.70 bar (53 psia) Gas flow wetwell→drywell 3950 L/s (8380 ft³/min)	30,000 (4,470,000)

Table 1.1. (Cont.)

Time following battery exhaustion	Event	Average vessel relief valve flow [L/s (lb/h)]
2 h, 52 min	Reactor vessel lower head fails and core drops into drywell sump Initial gas flow drywell→wetwell 65,000 L/s (140,000 ft³/min) rapidly decreasing to ~4700 L/s (10,000 ft³/min)	
3 h, 52 min	Core-concrete interaction begins PSP bulk water temperature 154°C Drywell atmosphere temperature 158°C Containment pressure 7.20 bar (103 psia)	
4 h, 9 min	Drywell atmosphere temperature 264°C Containment pressure 8.60 bar (124 psia) Electrical penetration assemblies fail Drywell pressure lowers to atmospheric and PSP water flashes to steam Gas flow wetwell→drywell 236,000 L/s (500,000 ft³/min) Gas flow drywell→reactor building 370,000 L/s (780,000 ft³/min)	
5 h	Gas flow wetwell→drywell 9600 L/s (20,300 ft³/min) Gas flow drywell→reactor building 46,000 L/s (97,000 ft³/min)	
6 h	Drywell atmosphere temperature reaches 700°C	
7 h	Wetwell→drywell flow stops	

[a] 1 bar = 10^5 Pa = 1.01 atm.

Table 1.2. Synopsis of key events

	Time from battery loss[a] (m)	Time from initiating event[b] (m)
Battery exhaustion	0	240
Core uncovery begins	60	302
First cladding failure	103	343
Fuel melt initiation	120	355
Core slumps	137	392
Reactor vessel failure	172	426
Drywell vent initiation	238	503
Drywell seal failure	249	514

[a] Used in this report.

[b] Used in Vol. 1 and Figs. 1.1 through 1.11 taken from Vol. 1.

Note: times do not correspond exactly; taken from slightly differing MARCH runs.

References for Section 1

1.1 D. H. Cook et at., *Station Blackout at Browns Ferry Unit One — Accident Sequence Analysis*, NUREG/CR-2182, ORNL/TM-455/VI (November 1981).

2. FISSION PRODUCT PATHWAYS

A mechanistic determination of the degree of fission product leakage from the reactor building boundary requires knowledge of the transport pathway within the primary containment and reactor building as a basis for the estimate. In some accident sequences, the major fission product pathways are fairly self-evident. For example, in the present case the ultimate failure of the primary containment dominates the leakage pathway, and the loss of ac power (and dc power, 4 h later) precludes active involvement of electrically-driven reactor systems during the period of fission product releases. This principal pathway for the complete station blackout event at Browns Ferry is described in Sect. 2.1 and forms the basis for the transport calculation described in this report.

Accident sequences which do not lead to containment failure (and so are not dominated by a major leakage source) or those which include at least partial ac power availability require much more care in determining the flow pathways within the reactor systems. In such cases, a detailed description of the role of the systems in the sequence is required, including the behavior of primary, secondary, safety and auxiliary equipment which could affect transport.

We have undertaken an examination of reactor systems behavior during the complete Station Blackout accident sequence in order to ensure that no essential feature of the major leakage pathway was overlooked. This study did reveal some minor pathways, described in Sect. 2.2, which do not contribute significantly to the overall integrated leakage to the environment in this accident sequence, which is assumed to persist beyond the point of gross failure of the primary containment.* A detailed discussion of the various leakage pathways from the reactor vessel, drywell or wetwell into reactor systems outside the primary containment is provided in Appendix A.

2.1 Principal Leakage Pathways

The principal fission product path prior to reactor vessel failure is illustrated in Fig. 2.1. Convection by steam and hydrogen carries the fission products through the steam separators and dryers into the upper main steam lines and down through the intermittently open S/RV and tailpipe into the suppression pool via the T-quencher. (Details of the suppression pool behavior are provided in Sect. 9.5 and in Appendix D of volume 1.)[1.1] The steam is condensed, heating the pool and increasing the evaporation from its surface. Pressure in the wetwell becomes sufficient to open the vacuum relief check valves on the vent pipes well before any fuel failure occurs. The open vacuum reliefs allow flow from the airspace above the suppression pool back into the drywell causing the drywell pressure to increase. Projected leakage rates from the drywell and wetwell

*If the accident sequence were terminated by restoration of electrical power and core cooling before failure of the drywell, these alternate pathways would control the total release.

atmospheres to the reactor building in this initial phase are shown in Table 2.1 based on integrated leak rate tests performed on the Unit 1 containment during 1980 and discussed in Appendix B. The wetwell leaks into the lower reactor building through the reactor-building-to-wetwell vacuum breakers while the drywell leakage is into the upper levels of the reactor building. (These leakages are shown as open-headed arrows on Fig. 2.1.)

The altered pathway following reactor vessel failure is shown in Fig. 2.2. Here the S/RV's are closed, but the increased drywell pressure caused by the presence of the corium in the drywell drives vapor flow from the drywell into the suppression pool via the vent pipes and the downcomers. It should be noted that the concrete reactor pedestal and the biological shield surrounding the reactor vessel form only a minor flow obstruction since there are large openings in these structures. Further information regarding containment leakage prior to the predicted failure of the containment by overtemperature-induced degradation of the electrical penetration assembly seals is given in Appendices A and B.

As noted in Sect. 1, the electrical penetration assembly seals are projected to begin venting when the drywell temperature reaches 204°C and to fail completely at 260°C. Following this event, a large gas flow from the drywell to the reactor building occurs. Initially, this flow consists primarily of steam, hydrogen, nitrogen and some oxygen; later on the concrete degradation products contribute a major portion of the flow.

The situation in the reactor building after containment failure is illustrated in Fig. 2.3. As shown, the failure of the drywell electrical penetration assembly seals allows flow from the drywell atmosphere into the lower portion of the reactor building. There is also flow from the wetwell airspace through the vacuum breakers into the drywell and some of the suppression pool water flashes to steam at the time of depressurization. Leakage into the cavity surrounding the wetwell would be negligible in comparison to the drywell leakage following electrical seal failure. Since the reactor building floors contain large open areas, there is little to impede vertical flow in the reactor building and through the internal blowout panels which relieve at 36 lb/ft^2 into the refueling bay on the upper floor of the building. The refueling bay contains 18 blowout panels to the atmosphere which are actuated by 50 lb/ft^2 interior room pressure. With the assumption that the Station Blackout accident sequence is occurring simultaneously on all three Browns Ferry units, it is estimated that the reactor building pressure exceeds this value soon after drywell seal failure. Prior to activation of the refueling bay blowout panels, the reactor building is assumed to leak at a rate of 100%/d with 62 Pa (0.25 in. of H_2O) overpressure.*

2.2 Minor Leakage Pathways During Complete Station Blackout

Examination of the potential behavior of reactor, safety, and auxiliary systems during this accident sequence under the assumption that no

*Estimated from values cited in the Technical Specification.

independent failures occur revealed several flow pathways through which fission products can escape from the primary containment before gross containment failure occurs. These minor pathways are important to the early spread of radioactive contamination, but do not contribute significantly to the overall integrated leakage to the environment after primary containment failure.

Under blackout conditions, the main condenser system is isolated from the outside environment by several closed air-operated valves in the off-gas system and thereby serves as a fission products reservoir. However, there would be a leakage path from the main condenser system into the Turbine Building through the labyrinth seals of the low-pressure turbines since gland sealing would not be effective. The flows into the condenser system are leakage from the reactor vessel through the main steam isolation valves and through the steam trap drains in the HPCI and RCIC steam lines. These leakage rates, derived from the results of local leak rate testing, are discussed in Sect. A.3 of Appendix A.

A second leakage pathway exists through the bellows, resilient seals, and electrical penetration assembly seals of the drywell. These leakages are relatively small, but are significant with respect to environmental contamination because these leakages permit flow directly from the drywell into the reactor building atmosphere. Another pathway for a small flow directly into the building atmosphere is from the wetwell airspace through the shut but leaking reactor building-to-wetwell vacuum breakers.

The leakages briefly discussed above have been included in the fission product transport calculation and are discussed in much more detail in Appendix A. Other pathways for leakage into closed reactor systems outside containment are also discussed in this appendix, but have not been included in the transport calculation; with the assumption of no independent secondary failures, these systems are tight and the fission products would not proceed further into the environment.

Table 2.1. Projected primary containment leak rates

Pressure inside the containment (bar gauge)	Leak rate (% of vol/h)
1.70 (25 psig)	0.0560
3.40 (49 psig)	0.0620

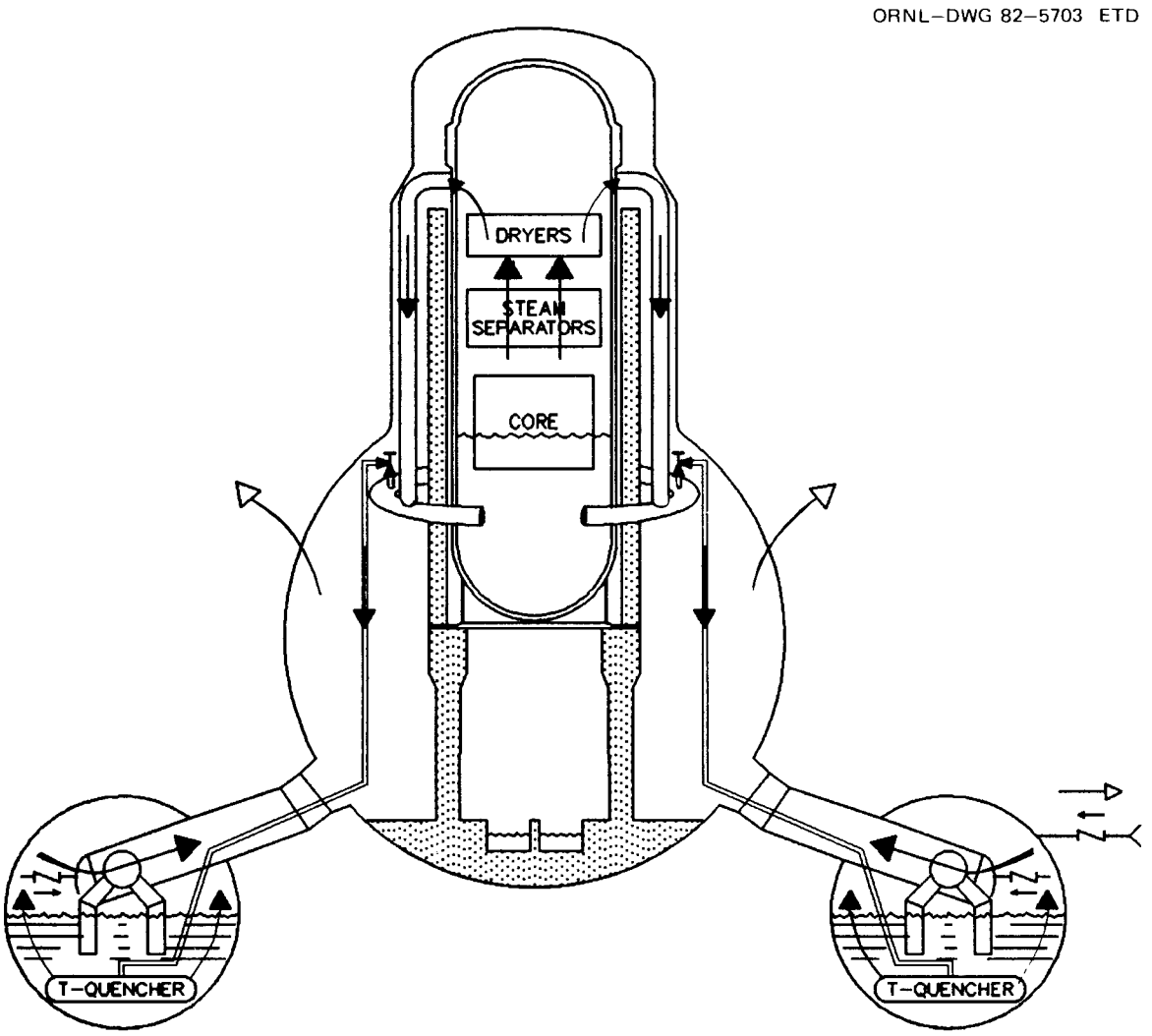

Fig. 2.1. Principal fission product pathway prior to reactor vessel failure.

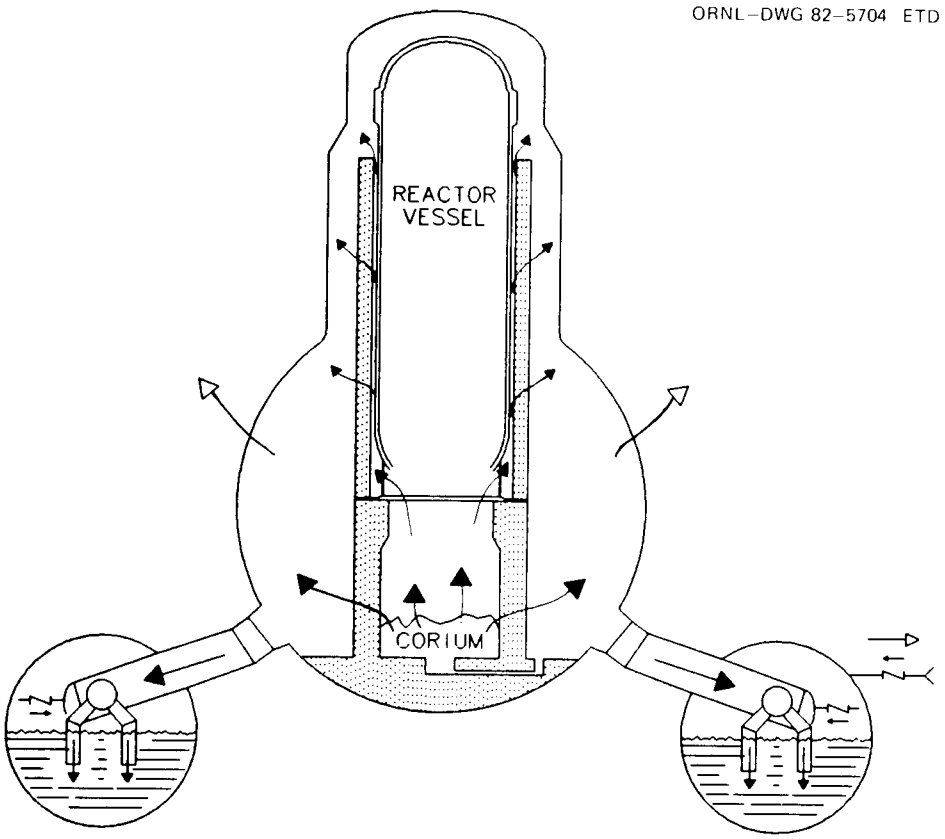

Fig. 2.2. Pathways following reactor vessel failure.

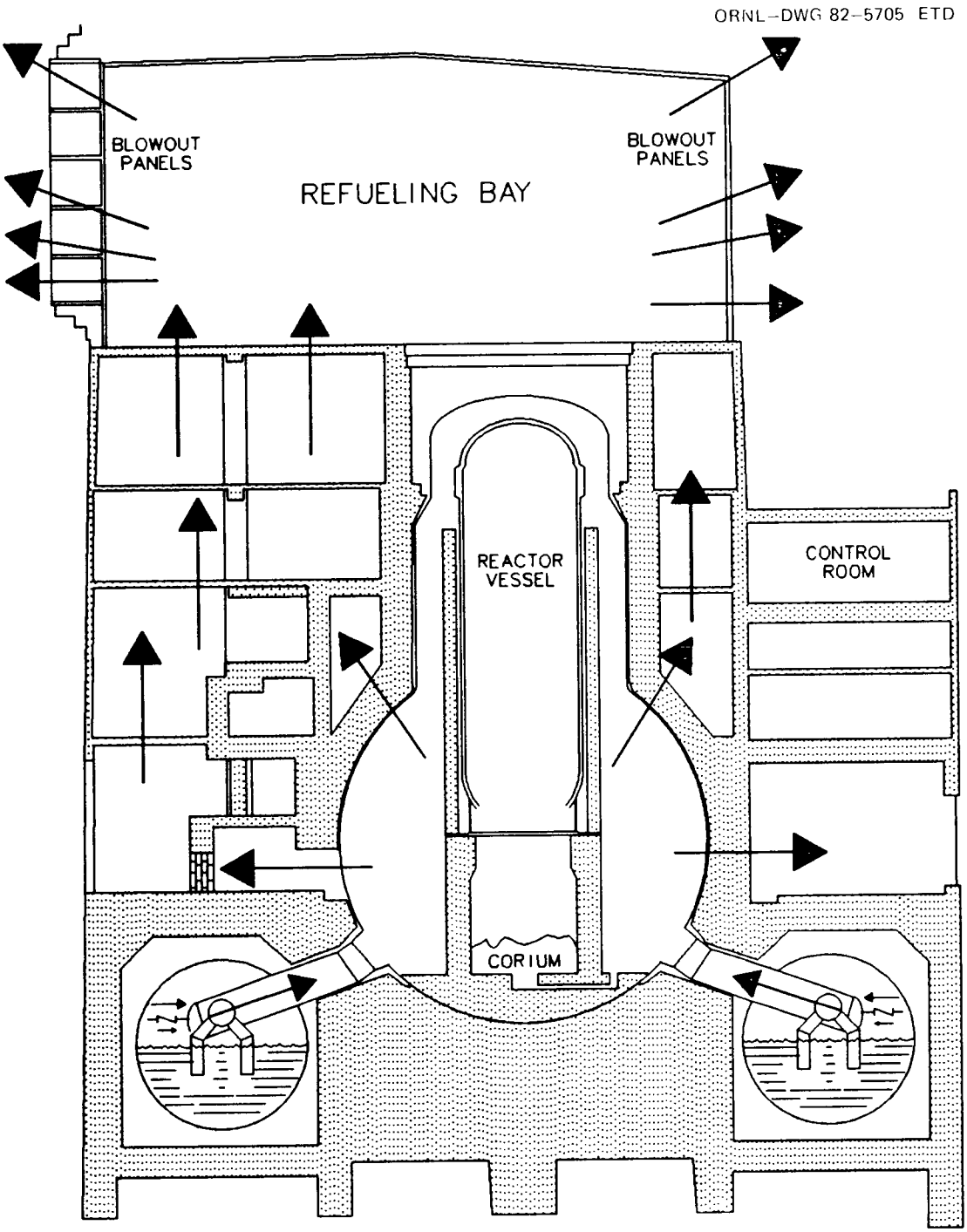

Fig. 2.3. Fission product transport through the containment structure.

3. FISSION PRODUCT RELEASE FROM FUEL AND AEROSOL FORMATION RATES

3.1. Fission Product Release from Fuel

In this section expressions are developed to predict the release rate of noble gases, iodine, cesium, and tellurium from overheated fuel.* The conditions for cladding burst, which initiates release, are presented in Sect. 3.1.1. In Sect. 3.1.2 an existing model is summarized for low temperature release ($T < 1300°C$).

A release rate model for temperatures above 1300°C is presented in Sect. 3.1.3. The model is based on an extensive review of the literature performed for a recent NRC review.[3.1a] Release rates from fuel are given in terms of an empirical rate coefficient, k_i, defined as the fractional release per minute for fission product – i at a given temperature. Thus, for an approximately isothermal time segment, δt (min), the fraction of the initial fission product inventory present at the beginning of the time period that is released in time δt is

$$f = 1 - e^{-k\delta t} . \qquad (3.1)$$

3.1.1 Prediction of rupture temperature

At temperatures <1300°C fuel rod cladding failures would occur in a ductile manner by expansion (ballooning) provided sufficient excess internal pressure is available. The internal pressure would be generated by the initial helium fill gas (3 bar at room temperature for an 8 x 8 P fuel rod) plus the fission gas released to the plenum and void spaces during the previous normal reactor operation. A correlation of rupture temperature, pressure difference, and heatup rate has been devised by Chapman.[3.1b] By accounting for the thicker wall of the 8 x 8 P cladding and adding 20°C for the uniform temperature effect,[3.1b] we obtain:

$$T = 3980 - \frac{0.0209\ P}{1 + 0.0357\ R} - \frac{8697\ P}{100 + 3.57\ R + 2.853\ P} , \qquad (3.2)$$

where

T = temperature at rupture, °C,

P = pressure differential at rupture, kPa,

R = heatup rate, °C/s.

---

*Other fission products will be included in future work for other accident sequences.

The internal pressure can be calculated with sufficient accuracy by assuming a void volume increase of 15 cm^3 resulting from ballooning and using an effective gas temperature equal to the average of the plenum and the peak cladding temperatures.

At primary system pressures above ~2500 kPa (350 psia), the fuel rod internal pressure in Browns Ferry-1 fuel rods will not be sufficient to fail the cladding by ductile expansion and rupture. At temperatures $\geq$1300°C, oxidation (or perhaps hydriding at certain locations) will severely embrittle the cladding so that failure can occur by cracking or fragmentation. Therefore, 1300°C will be treated as the failure temperature for fuel rods that escape failure by the previously described ductile mechanism.

3.1.2 Fission product release at T $\leq$ 1300°C

Correlations for the release of noble gases, cesium, and iodine from ruptured rods at temperatures below 1300°C have been developed[3.2-3.10] in recent studies. Even though this temperature range is too low to be of major interest in this study - indeed rupture in the Station Blackout sequence is not estimated to occur until the temperature has reached ~1300°C - some aspects of the low temperature release model are instructive for the purpose of extrapolation to higher temperatures. In other accident sequences where reactor vessel depressurization occurs (consequently rupturing the cladding at temperatures below 1300°C) and where the fuel temperature increase is arrested at ~1300°C, the method discussed in the following paragraphs can be used to estimate noble gas, cesium, iodine, and tellurium releases.

For the purpose of calculating fission product release, the simplifying assumptions are made that the fractional release rates during the accident are not affected by the operating conditions preceding the accident. The initial fission product inventory and the release during the accident are calculated independently for each of the radial and axial zones defined within the reactor core.

Only limited amounts of data for release of tellurium <1300°C are available.[3.5,3.10-3.12] Based on these limited test data, it can be assumed that the release of tellurium to the pellet-to-cladding gap space preceding the accident (the gap inventory) is the same fractionally as fission gas, iodine, and cesium, but that the release rate for tellurium from the gap space is only 6% of that of iodine.

3.1.2.1 Fission products in the plenum and void spaces from normal operation preceding the accident. The model rod selected for estimating the typical fractional release rates has the physical dimensions of those in an 8 x 8 P bundle [a bundle containing 62 fuel rods prepressurized to 3 atm (303 kPa) with helium,* which has an average burnup of 15,000 MWd/te, and an average fission gas release to the plenum of 4.0%]. Other details are presented in Table 3.1. The cesium, iodine, and tellurium gap inventories shown in Table 3.1 are equivalent to the percentage of fission gas

*The bundle also contains two water rods.

release to the voids and plenum during normal reactor operation. For fission gas release, the selection of 4.0% of the stable fission gas released to the plenum and voids during normal operation was based on information from several sources,[3.5,3.10-3.12] taking into consideration the mix of fuel types currently in Browns Ferry-1 (7 x 7, 8 x 8, 8 x 8 R, and 8 x 8 P.) The peak-to-average burnup ratio of 1.25 is based on two sources.[3.10,3] Because of radioactive decay during movement from the UO_2 matrix to the open voids and decay while residing in the voids and plenum, the plenum gas will be somewhat depleted of radioactive isotopes; although this depletion will be greater for the shorter half-life isotopes.[3.5,3.7,3.12,3] The breakdown can be simplified by the assumption that the plenum content of any gaseous isotopes with a half-life less than 30 days is 0.5% of the total. These amounts of the fission gases (4.0% of the stable and long half-life isotopes, and 0.5% of the shorter lived isotopes) can be assumed to be released from the fuel rods at the instant of cladding rupture due to high internal pressure.

3.1.2.2 Additional release of fission gas to the plenum for 600°C $\leq$ T $\leq$1300°C. An additional amount of stable fission gas, equal to 0.7 to 1.7% of the total rod inventory was released from test fuel rod segments when heated from 500 to 1200°C.[3.3,3.10] The lower amount was slowly released at 500°C; the larger amounts were released within a few minutes at the higher temperatures. The rate of release of this stable secondary gas to the open pores in the fuel rod can be expressed as

$$k_r = 3.617 \times 10^{-6}\ e^{5.22 \times 10^{-3}\ T}\ , \qquad (3.3)$$

where

k_r = fraction of stable gas released per min from the pellet,

T = fuel temperature, °C, for 600°C $\leq$ T $\leq$ 1300°C.

This rate relationship is illustrated in Fig. 3.1. The released gas will accumulate in the plenum until the cladding fails. If the cladding ruptures before reaching 1300°C, fission gas will continue to be released from the fuel in accordance with Eq. (3.3). A maximum value must be placed on the release of this secondary gas as follows:

$$F(max) = 0.000014\ T\ , \qquad (3.4)$$

where F(max) is the maximum fraction of the original fuel rod inventory with 600°C < T $\leq$ 1300°C. This relationship is shown in Fig. 3.2.

The amount of short half-life gas species in this secondary gas is not known, but is probably slightly depleted. It is therefore recommended that both the release rate and the maximum amount be reduced a factor of 4 for short half-life gaseous isotopes released by Eqs. (3.3) and (3.4).

3.1.2.3 Cesium, iodine, and tellurium release at $T \leq 1300°C$. The LOCA source term model,[3.4,3.6] extrapolated to 1300°C, can be used to calculate the release of cesium and iodine from the ruptured fuel rods. The model accounts separately for the burst release (that amount carried out by the plenum gas at the moment of rupture as it flows along the pellet-to-cladding gas space and out the rupture opening) and diffusional release from the gap space (the slower release following plenum blowdown). The release of tellurium was not measured in these tests, but a reasonable assumption is that it is 6% of that of iodine.

In the temperature range of 700 to 900°C (extrapolated to 1300°C for this study), burst release can be expressed as

$$M_B = \alpha V_B \, (M_o/A)^a \, e^{-(C/T)} , \qquad (3.5)$$

where

M_B = mass (g) of cesium, iodine, or tellurium (total of all isotopes) released in the burst,

V_B = volume of plenum gas (cm^3) vented at 0°C and primary system pressure

M_o = inventory (g) of cesium, iodine, or tellurium (total of all isotopes) in the pellet-cladding gap,

A = internal area (cm^2) of the cladding associated with M_o,

T = temperature (K) at the rupture location.

The parameters α, a, and C are adjustable constants that are derived from the experimental data. The pertinent values are listed in Table 3.2. (Note that M_o should not be confused with the total mass of cesium, iodine, or tellurium in the fuel.) Although the burst release correlation was tested at 960°C[3.10] extrapolation above this temperature is subject to a possibly larger error. The cesium, iodine, and tellurium released in the burst will come from the gap space and will be depleted in short half-life isotopes as with the fission gas.

This model calculates an initial rate of release from the gap space following plenum blowdown for temperatures in the range of 500 to 1200°C as follows:

$$R_o = \delta(W/P)(M_o/A)^a \, e^{-(\gamma/T)} , \qquad (3.6)$$

where

R_o = initial rate (g/h) of release of cesium or iodine by diffusion,

W = width (μm) of radial gap,

P = system pressure (MPa),

M_o = total calculated mass (g) of cesium or iodine initially in the gap,

T = temperature (K) at rupture location.

Values of the adjustable constants δ and γ are presented in Table 3.2.

The source term model[3.4-3.6] includes a depletion equation that effectively reduces R_o as the gap space is emptied. For most LOCA time-temperature scenarios, the change in R_o is small. Therefore, for this study we will maintain the initial rate for diffusional release of the gap contents, but modify the equation to calculate directly a fractional release rate as follows:

$$k_2 = R_o/60\ M_T\ , \tag{3.7}$$

where

k_2 = fraction of initial total fuel rod inventory of cesium or iodine released per minute,

R_o = initial release rate calculated from Eq. (3.6) (g/h),

M_T = total initial mass of cesium or iodine in the fuel rod (g).

The factor of 60 in this equation changes the hourly release rate R_o to the desired release per minute. Note that R_o and k_2 will be different for cesium, iodine, and tellurium and that Eqs. (3.6) and (3.7) calculate the release of the gap inventory that is depleted in short half-life isotopes.

3.1.3 Fission gas release at temperatures > 1300°C

Above 1300°C the release of fission gas occurs by many mechanisms: grain growth, grain boundary separation, bubble coalescence and tunnel formation at grain boundary surfaces and edges, and bubble and atom diffusion within the grains. For simplification, we will use the fractional release rate model previously described, with rate coefficients based on experimental data. The gas release rate given by Eq. (3.3) and Fig. 3.1 serves also as a good approximation for fission gas release above 1300°C. It is clear that these fractional release rates are not constant with time.[3.14,3.16] Using Eq. (3.3) rates for cases of very slow heatup would result in excessive, unrealistic releases. Since the true effect of heatup rate and time at temperature is not known, we have chosen to limit the release in the following empirical manner:

$$F_{max} = 0.0182 + 9 \times 10^{-5}\ (T-1300)^{1.4}\ , \tag{3.8}$$

where F_{max} is the fraction of the original total inventory in the fuel rod. This limit is shown in Fig. 3.2. It should be assumed that all remaining gaseous isotopes are released in equal fractional amounts. Note that Eqs.(3.4) and (3.8) are designed to limit the maximum release during the heatup cycle only. They should not be interpreted as prohibiting additional release when the fuel and temperature decrease.

As mentioned previously, if the fuel rod does not rupture by ductile failure below 1300°C, we will assume that it does fail, without cladding expansion, at 1300°C. In such a case the high primary system pressure will prevent a sudden burst release from occurring, but for calculational purposes we will assume that the fission products are released in one time-step after the temperature of 1300°C is reached.

3.1.4 Cesium, iodine, and tellurium release between 1300 and 1500°C.

In this temperature range the release of cesium and iodine accelerates, apparently because of release from the grain boundaries. Rapid releases much greater than the gap inventory have been observed.[3.8,3.15] In this range the release rate of both cesium and iodine can be expressed as follows:

$$k_3 = 7.66 \times 10^{-14}\, e^{0.017\,T}, \qquad (3.9)$$

where

k_3 = fraction of cesium or iodine remaining in fuel rod released per min,

T = temperature, °C, for $1300°C \leq T \leq 1500°C$.

These rates are also plotted in Fig. 3.1. For tellurium, we assume similar behavior at a reduced rate:

$$k_4 = 4.60 \times 10^{-15}\, e^{0.017\,T}, \qquad (3.10)$$

where

k_4 = fraction of tellurium remaining in fuel rod released per min,

T = temperature, °C, for $1300°C \leq T \leq 1500°C$.

If rupture does not occur below 1300°C, the cladding failure should occur at 1300°C and the burst release should be assumed to be zero. All isotopes of cesium, iodine, and tellurium will be released equally, and the maxima given by Eq. (3.8) should apply.

3.1.5 Cesium, iodine, and tellurium release above 1500°C

In this high temperature range the releases of cesium and iodine can be considered to be identical to those of the fission gases. The release rates and maxima shown in Figs. 3.1 and 3.2 [Eqs. (3.3) and (3.8)] apply. For tellurium the release rates are given by

$$k_s = 2.17 \times 10^{-7}\, e^{5.22 \times 10^{-3}\, T} \qquad (3.11)$$

where

k_s = release rate coefficient for Te, min^{-1}

T = fuel temperature, C, for T > 1500.

The maximum release rate given by Eq. (3.8) and Fig. 3.2 should apply.

3.1.6 Fission product release from the corium debris bed in the pressure vessel prior to melt-through

In accordance with MARCH input, the core is predicted to collapse onto the lower head when a selected fraction of the core (here assumed to be 0.75) attains the melting point of the fuel/cladding mixture, approximately 2300°C. Although the volatile fission products are driven off quite rapidly at 2300°C (at ~100% of current inventory/min according to Eq. 3.1), the 25% of the core which has not melted is substantially cooler and therefore still contains a significant fraction of the initial inventory of volatiles at the time of core collapse. Thus, the rate of release from the debris bed prior to pressure vessel failure assumes some degree of importance because the fission product pathway for material evolved in the reactor vessel differs significantly from the pathway to the atmosphere from the drywell floor, which is where the debris bed is situated after melt-through of the reactor vessel lower head.

Thus, the temperature of the corium debris is a potentially important parameter which is not well analyzed in the MARCH subroutine INTER. With the existing models, the core experiences an initial quench to the mixed-mean temperature of the core plus steel structure in the lower head, and there is an additional heat loss because of rapid steam evolution from the remaining water in the lower head. After this rapid quench, the debris temperature increases at a rate dependent upon the heat source from fission product decay and the Zircaloy/water reaction, if selected by the user. For the Station Blackout analysis we have excluded the Zircaloy/water heat release from contributing to the debris bed temperature increase, which causes calculated debris bed temperatures to be several hundred degrees lower than those which would be predicted for cases in which complete Zircaloy/water reaction in the bottom head was assumed.

This fission product release rate from the debris bed should be less than that of an intact portion of the core at the same temperature because of the significantly lower surface-to-volume ratio in the debris bed. In

the absence of experimental data for the debris bed release or the existance of a formulated model, a reasonable or intuitive reduction of the release rate from the debris bed relative to the release rate from an intact core has been assumed. Accordingly, releases from the debris bed have been estimated using the release rate coefficient developed for the intact core multiplied by the surface area ratio of the core (intact cladding surface) relative to the exposed upper surface of the debris bed. Since the core heat transfer surface area is approximately 250 times that of the debris bed, we have assumed a reduction factor of 250.

3.1.7 Fission product release during molten core-concrete interaction.

A large amount of gas is generated as concrete decomposes during this phase of the accident. The gas passes up through molten core material or passes around or through core debris if the core material is below its melting point. The preferred method for calculating fission product release for the core-concrete interaction period would be to estimate mass transfer to the decomposition gases. However, since the gas flow rates predicted by the MARCH subroutine INTER are not reliable, we used the simple assumption that fission product release occurred only from the molten (or rubbled) core on the concrete according to Eq. (3.3) using an area ratio correction factor, as for the fuel rubble in the reactor vessel. The area ratio of the intact core surface to the surface of the rubble bed in the drywell, which is assumed to cover the entire drywell floor, is approximately 25. Therefore, fission gas, iodine, and cesium release rate coefficients for "sparging" release on the drywell floor have been calculated using Eq. (3.3) with a factor of 25 reduction. Similarly, tellurium release for this case has been estimated using Eq. 3.11, applying the same factor of 25 area ratio reduction.

3.2 Aerosol Formation Rates

3.2.1 Vaporization of structural materials

The aerosol particles formed during core melting are composed primarily of vaporized structural materials such as cladding, stainless steel, inconel, control rod alloys, and fuel. During the heat-up cycle, volatile fission products such as cesium can also significantly contribute to the aerosol content. Vaporization can occur from two distinctly different geometries: the essentially intact core with steam flowing upward through the core, and the molten pool configuration with either natural convection steam flow above the pool or the gaseous decomposition products of concrete bubbling up through the molten core material.

In order to calculate the vaporization rate of these materials for the Browns Ferry Station Blackout, we have made use of experimental data, primarily that generated in the SASCHA facility, Karlsruhe, Germany.[3.17,3.18] A semi-empirical model was derived for the release of structural materials from molten fuel mixtures in pool configuration. The details of this mass transfer model are given in Appendix C.

The model assumes that a mass transport coefficient exists that is identical for all species in the melt:

$$q = k_G p^* \quad , \tag{3.12}$$

where

q = mass transport flux, mol/s·cm²,

k_G = mass transport coefficient, mols/cm²·s·atm,

p^* = vapor pressure of each component above the melt surface, atm.

As shown in Appendix C, a value of k_G x 6 x 10^{-6} mol/s·cm²·atm was determined for the release of structural materials from large molten pools such as that predicted to collect in the bottom of the reactor vessel. The mass transfer coefficient can be assumed constant for the range of temperatures expected to exist for melted fuel.

Table 3.3 lists the partial pressures of structural materials components to be used in Eq. (3.11) at 2400°C. These partial pressures will change with temperature, but very little experimental information is available. For the temperature dependence of the vapor pressures, we have assumed that all components follow the vapor pressures of Fe, Ni, and Cr, which are similar. Therefore, the composition of the aerosol must remain constant as given in Table 3.3. Mathematically, the total vapor pressure is as follows:

$$p = 1.8 \times 10^6 \, e^{-\frac{43500}{T}} \quad , \tag{3.13}$$

where

p = total partial pressure of all structural materials, atm,

T = absolute temperature, K.

Equation (3.13) has been assumed to be valid below the melting points of the materials involved. The SASCHA data, taken mainly in the fully molten temperature range of 2350°C to 2750°C, indicate steeper temperature dependence.[3.17]

For the intact but overheated core, there will usually exist a flow of steam upward through the core. For the Browns Ferry Station Blackout, we have assumed that the steam flowing through the overheated intact core becomes saturated with structural material vapors according to Eq. (3.13). Vaporization from each of the ten radial zones has been treated separately since their temperatures would differ significantly.

3.2.2 Aerosol formation from molten fuel-concrete interaction

The heat from molten fuel causes concrete to decompose, forming large quantities of gas, primarily CO_2 and H_2O. Along with the gas, an aerosol is formed which is composed principally of oxides of Si, Al, Ca, Fe, Cr, and Sn.[3.19] The concentration of the aerosol has been related to the temperature and the superficial velocity of the gas produced from the concrete decomposition.[3.19] This relation can be expressed as

$$C = 10^3 \, (240 \, V_s + 33) \, e^{-\frac{19000}{T}} \qquad (3.14)$$

where

C = concentration of solids in the aerosol, g/m³,

V_s = superficial velocity of escaping gas, m/s, and

T = melt temperature (K) at the reactor interface.

The gas volume and velocity must be calculated for the reaction interface temperature. The total aerosol mass release rate is equal to the concentration C multiplied by the decomposition gas flow rate at the reaction temperature.

A particle size distribution for this type of aerosol has been published.[3.19] MARCH contains a subroutine (INTER) that calculates the gas production rate, thereby enabling determination of the superficial velocity and aerosol concentration according to Eq. (3.14). In the case of the Browns Ferry Station Blackout, this aerosol will mix with gas and other aerosols in the drywell where the aerosol behavior code HAARM-3 has been applied.

3.2.3 Method of applying the aerosol source term to the Browns Ferry Station Blackout

In this section we describe briefly the methods, assumptions, and approximations used in calculating aerosol production and transport for the Browns Ferry Station Blackout accident sequence.

Intact core. For the intact core, including the partially molten condition before core collapse, aerosol production is calculated by assuming that the steam flowing up through the core (dumped to the pressure suppression pool by means of pressure relief valves) is saturated with structural material vapor according to Eq. (3.13). The aerosol has the composition given in Table 3.3. The mass of aerosol is calculated from Eq. (3.12) using the volume flow rate of steam and the ideal gas law assuming that the molecular weight of the structural materials vapor is 57.1 and oxidizes to a molecular weight of 89.1. In all of the Browns Ferry aerosol calculations, fission products are allowed to plateout on aerosol particles, but they are assumed to be weightless. According to this procedure, the concentration of structural materials in steam leaving a core region at 2400°C is 40 g/m³ (62 g/m³ oxidized). At 2400°C this material

is in the vapor form; condensation to form solid particles will occur as the steam flows upward past the point of maximum fuel rod temperature and cools.

Core collapsed into pool geometry in the bottom of the primary vessel. In this geometry we calculate the formation of aerosol using Eqs. (3.12 and 3.13) and a natural convection mass transfer coefficient of 6×10^{-6} mol/s·cm²·atm. While in this configuration, there is very little flow of steam out of the primary vessel. The surface area of the pool is 2×10^{5} cm². At 2400°C the mass transport flux is 9.24×10^{-7} mol/s·cm² and the mass transport rate is 0.185 mol/s (10.6 g/s). The concentration of structural material vapor at the pool surface is 40 g/m³ (62 g/m³ oxidized). As steam circulates by natural convection within the reactor vessel, the steam and vapor cool to form particles which agglomerate, settle, and plate out by other mechanisms.

Aerosol generated by the core-concrete interaction. The amount of aerosol created by core-concrete interaction is obtained by multiplying the aerosol concentration from Eq. (3.14) by the volumetric flow rate of concrete decomposition gas produced. The surface area for core melt-concrete interaction is 3×10^{5} cm². The initial particle size for HAARM input is obtained from Ref. 3.19. While the containment is intact, much of the aerosol will be scrubbed out of the air by passage through the wetwell water.

3.3 Aerosol Transport in the Drywell

3.3.1 Introduction

The presence of large amounts of aerosol particles in the drywell atmosphere (resulting primarily from core-concrete interaction) creates a significant transport mechanism for iodine and other reactive fission products. Because large amounts of certain fission products tend to deposit on aerosols, which may plate or settle onto interior surfaces or be discharged to the containment or biosphere as the drywell leaks, a transport calculation must consider the details of particulate movement in and from the drywell. In the current study, this is done by using the computer code HAARM-3,[3.23] which is noted for extremely fast solutions of problems involving a single control volume.

The HAARM-3 program evaluates the change of aerosol concentration with time caused by factors such as time variation of aerosol generation rate and leakage, the settling of particles onto horizontal surfaces and the deposition onto all surfaces by diffusion and thermophoresis.* However, the effect of steam condensation is neglected. Aerosol production in the drywell begins when core debris melts through the bottom head of the reactor vessel and then drops to the concrete floor.

---

*Mass transfer driven by a temperature gradient (toward the lower temperature at the drywell wall).

3.3.2 HAARM-3 input data*

The input data required by HAARM-3 are divided into the four categories of Table 3.4-3.8, as follows: (1) parameters specified by a description of the accident (Table 3.4); (2) relatively standard parameters whose values are suggested by Gieseke et al.[3.23] (Table 3.5); (3) parameters, or tables of parameter versus time, obtained from MARCH output; (4) parameters from other sources, including dimensional properties of the Browns Ferry-1 drywell (Tables 3.7 and 3.8). Table 3.8 shows the derivation of the two area/volume ratios AFOV and AWOV listed in Table 3.7.

Table 3.6 lists the time-dependent variables RLEK, TGRAD, TEMPT, and P that are derived from MARCH output. Although MARCH also calculates rates of reaction of concrete with core debris, values of SOURS are based on the SANDIA experimental studies described in ref. 3.27. Drywell pressure (P) and temperatures of drywell atmosphere and the concrete floor from MARCH are plotted in Figs. 3.3 and 3.4; leak rates (due to EPA seal failure) and rates of reaction of concrete with core debris (after the core melts through the bottom head) are shown in Figs. 3.5 and 3.6, respectively.

The five time-dependent variables P, TEMPT, RLEK, TGRAD, and SOURS are terms in the integro-differential equations upon which the HAARM-3 program is based. Because of limitations of subroutines used to perform numerical integration (the Adams-Moulton and Runge-Kutta methods shown in Table 3.5), values of P, TEMPT, RLEK, TGRAD, and SOURS used in HAARM-3 calculations were obtained from the smoothed curves of Figs. 3.3-3.6. By such smoothing the discontinuities of pressure (Fig. 3.3), temperature (Fig. 3.4), leak rate (Fig. 3.5), and concrete reaction rate (Fig. 3.6) were replaced by continuous (although rapid) changes. The smoothed values of these variables are listed in Table 3.9.

3.3.3 Aerosol generation

As stated above, the aerosol generation rate, SOURS (particles cm^{-3} s^{-1}), is calculated from the SANDIA correlation[3.27]

$$C = 10^3 \, (240 \, V_s + 33) \, e^{-19000/T} \qquad (3.14)$$

where

C = aerosol concentration above the melt, g/m^3,

V_s = superficial gas velocity, m/s,

T = reaction temperature at the concrete/core-debris interface temperature, K.

---

*This is believed to be the first practical application of HAARM-3 to BWR primary and secondary containment volumes. Accordingly, the material presented in the remainder of this section is presented in considerable detail.

Equation (3.14) requires two input parameters from the MARCH code, namely, V_s and T. There are at least two sets of data printed by the MARCH program that can be used to calculate superficial velocities. The two that follow were used to check the calculations, although the first was used in the evaluation of aerosol concentrations from Eq. (3.14).

(1) Drywell leak-rate data

Leak-rate data from Table 3.9 (shown in Fig. 3.5) can be used to calculate the superficial gas velocity above the concrete-corium mass from the relation

$$V_s = R_1(P_o/P_{dw})/A \qquad (3.15)$$

where

R_1 = drywell leak rate, m^3/s,

P_o = pressure of containment building into which the drywell gas is leaking,

P_{dw} = drywell pressure,

A = area of concrete-corium reaction surface, estimated to be 30 m^2.

Superficial velocities calculated from Eq. (3.15) are presented in column 3 of Table 3.10. Aerosol concentrations based on these velocities are presented in column 4 of this table in terms of g/cm^3; the generation rate is shown in column 6 of Table 3.10. The specific mass generation rate (g/s) was calculated by multiplying the mass concentration above the melt by the factor V_sA. Finally, the aerosol-particle generation rate (SOURS) is given by

$$S(t) = CV_sA/(V_{dw}\ \rho\ V_p)\ , \qquad (3.16)$$

where

S(t) = primary-particle generation rate (SOURS), particles $cm^{-3}\ s^{-1}$,

V_{dw} = drywell volume, 4.5×10^9 cm^3,

ρ = primary-particle density, g/cm^3,

V_p = effective primary-particle volume, cm^3/particle.

The HAARM-3 program requires, as input data, three variables of the particle-size distribution, namely: (1) the mass-mean particle radius, r_{s0}, shown in Table 3.4 as RSOR for particles being generated and as RAIR for any particles already in the drywell at the start of calculations; (2)

the geometric standard deviation, σ_g, shown in Table 3.4 as SIGSOR for particles being generated and as SIGAIR for particles already in the drywell at the start of calculations; and (3) a source-rate term, SOURS of Table 3.6, that is based on the effective mass particle radius, r_p. These variables are related by the equations[3.28].

$$\ln r_p = \ln r_g + 1.5 \ln^2 \sigma_g \tag{3.17}$$

$$\ln r_{s0} = \ln r_g + 3.0 \ln^2 \sigma_g \tag{3.18}$$

where

r_g = geometric number mean radius,

σ_g = geometric standard deviation.

Two particle size distributions were analyzed, a reference case based on experimental and theoretical studies[3.26,3.29] and a case involving larger particles for the purpose of examining the significance of this variable. Experimental data from SANDIA[3.26] are presented in Fig. 3.7. They show considerable scatter that suggest some deviation from a log normal distribution. However, when treated as log normal, the parameters are as follows:

$$r_g = 0.1136 \ \mu m, \ \sigma_g = 2.289 \ .$$

The earlier work of Lindauer and Castleman[3.29] presented studies of σ_g in the range 1.15 to 3.0. Based on these and the above listed $r_g = 0.1136$ μm, the reference case was specified as

$$r_g = 0.1 \ \mu m \text{ and } \sigma_g = 1.8.$$

The alternative case was defined by the values

$$r_g = 0.89 \ \mu m \text{ and } \sigma_g = 2.29,$$

corresponding to $r_{s0} \simeq 7. \ \mu m$. The effective volume of a primary particle at generation time was based on r_p, calculated according to Eq. (3.17), and the assumption of particle sphericity, namely,

$$V_p = (4/3)\pi r_p^3 \ . \tag{3.19}$$

Values of particle concentrations and particle generation rates based on $r_g = 0.1$ μm and $\sigma_g = 1.8$ are given in columns 5 and 7, respectively, of Table 3.10. The particle density, ρ, has been taken as 3.0 g/cm³, corresponding to the concrete oxides CaO, SiO, and Al_2O_3.

(2) The concrete reaction-rate data

The rate of reaction of concrete with corium at successive times after battery failure are presented in Table 3.9 and Fig. 3.6. From the assumed composition of the concrete (44.1 w/o $CaCO_3$, 10.8 w/o $Ca(OH)_2$, 35.7 w/o SiO_2, and 6.7 w/o Al_2O_3), there are generated 0.027 g H_2O/g concrete reacted plus 0.194 g CO_2/g concrete reacted. From these values and the concrete reaction rate, a second estimate of the superficial gas velocity above the concrete-corium mass is given by

$$V_s = R_c\ (0.027/18.0 + 0.194/44.0)\ 82.05\ (T/P_{dw})\ (10^{-6}/A) \qquad (3.20)$$

where

R_c = concrete reaction rate (from MARCH), g/s,

18.0 = g-molecular weight of water,

44.0 = g-molecular weight of CO_2,

82.05 = gas constant, cm^3 atm/(g-mole K),

10^{-6} = m^3/cm^3.

Values of the superficial velocity calculated from Eq. (3.20) are presented in column 2 of Table 3.10. These values differ to a small extent from those listed in column 3, which were calculated from leak-rate data by use of Eq. (3.15). However, the two sets agree well enough to provide confidence in the consistency of the leak-rate data and concrete reaction-rate data provided by the MARCH code.

The superficial velocity is a critical variable in its effect on the aerosol generation rate and on the aerosol source strength, Eq. (3.16). In fact, since the term 240 V_s dominates the term 33 in Eq. (3.14) during the time period of this analysis, the aerosol source strength rate is approximately proportional to V_s^2. Thus, the choice of its value is critical. The 30-m^2 area used above to calculate the superficial velocity is simply the area of the intersection of the interior of the biological shield with the horizontal concrete base of the drywell. Gases formed during reaction of concrete with core debris rapidly flow into the drywell space exterior to the biological shield. During this transition, the cross-sectional area for flow increases by a factor of 2 to 3, or more, thereby effecting a decrease in the value of V_s^2 of 4 to 10 and a corresponding increase in particle setting rates. In effect, the estimates of aerosol generation rate given in Table 3.10 may be too high by a factor between 4 and 10.

A basic assumption of HAARM-3 is that the aerosol particle sizes fit a log-normal probability distribution. That is, if r is a random variable representing particle radius, then ln r is a normally distributed random variable. In many cases this assumption is valid;[3.23,3.24] however, there are situations where this is not exactly true.[3.25,3.26] Thus, use of a calculation based on spherical particles introduces an uncertainty in HAARM-3 output; i.e., there is an unknown parameter, the

"dynamic shape factor," which would take into account the effects of nonspherical particle shape on particle mobility. While such quantities are essential for a complete model, and may play a significant role in computations, their values are not easily determined, and, in many cases, represent little more than guesses.

An estimate of the fraction of reacted concrete which becomes aerosols can be obtained by a comparison of Fig. 3.8 with Fig. 3.6. To a first approximation, about 1% of the mass equivalent of reacted concrete becomes gas borne as aerosol.

Various tables of information produced by the HAARM-3 program are used in subsequent analyses of this report, as follows.

1. The concentration and particle-size distribution, as functions of time, of suspended aerosol leaking from the drywell into the containment. Such information is used to calculate how much of an element, such as iodine and cesium, is transported to the containment.

2. The quantities of aerosol settled or plated out, and their particle size distributions, as functions of time, in the drywell. These data are used to calculate surface areas on which an element can be sorbed and, therefore, not released to the containment or to the biosphere.

Specific HAARM-3 output needed for fission product transport calculations are the total suspended aerosol surface areas, amounts of settled or plated particles, and the amount of aerosol that has leaked into the containment building, all at each time step. Surface areas, used in subsequent calculations of quantities of iodine species, for example, adsorbed on aerosols, are evaluted from mass, density, and effective primary particle radii. Thus, agglomerates of primary particles are assumed to provide the same free surface area for fission product deposition as the total of their substituent particles would provide. The justification for this assumption lies in the fact that molecular species are much smaller than the particulates, and therefore migrate easily between agglomerated particles. Furthermore, the agglomeration utilizes only a small portion of the primary particle surfaces, especially since most agglomerates tend to be linear rather than spherical.

3.3.4 Thermophoresis

When the gas temperature exceeds the wall temperature, enhanced particle deposition will occur by the process of thermophoresis. The HAARM-3 program can estimate the contribution of this mechanism; to do so, the input data must include one or more values of the gas-phase temperature gradient at the wall. Such input may be as a table of gradients versus temperature or as a single, constant gradient. Values of this variable used in the present study are shown in the last column of Table 3.10. These smoothed numbers were estimated from the rate of temperature increase of the drywell steel liner, shown in Fig. 1.11, by use of the equation

$$\frac{dT}{dx} = 100\,\frac{mC(dT/dt)}{kA} = 100\,\frac{z\rho C(dT/dt)}{k}\ ,$$

where

dT/dx = gas phase temperature gradient at the drywell wall, K/cm;

dT/dt = rate of temperature rise of drywell wall (from Fig. 1.11), K/s;

A = area of drywell liner, m^2;

C = heat capacity of stainless steel, 476 J/(kg·K) [0.1137 Btu/(lb_m·°F)];

k = thermal conductivity of the gas, assumed constant at 0.064 W/(m·K) [0.037 Btu/(h·ft·°F)];

z = thickness of drywell liner, 0.635 cm (0.25 in.);
ρ = density of stainless steel, 7.80E-3 kg/cm^3 (486.9 lb_m/ft^3).

The factor 100 in Eq. (3.21) is used to convert 1 meter to 100 cm. With the above parameters, Eq. (3.21) reduces to

$$dT/dx = 3680\ dT/dt.$$

3.3.5 HAARM-3 results

HAARM-3 results for the reference case (0.10-μm geometric mean radius and 1.80 standard deviation, with thermophoresis) are shown in Figs. 3.9 through 3.12 which contain, respectively: (1) a plot of suspended-aerosol concentration, in μg/cm^3, versus time after failure of batteries: (2) plated mass versus time; (3) settled mass versus time; and (4) leaked mass versus time. These plots vividly show the fluctuations and magnitudes of these variables as time passes. A much briefer, but perhaps more informative, summary of the HAARM-3 results is given in Table 3.11 which presents masses of suspended material, plated, settled, and leaked materials at 300 and 800 minutes after battery failure for the best-estimate initial particle size with and without thermophoresis.

Table 3.12 shows results for a pair of cases with a much larger initial particle size. Both tables are based on the smoothed data of Table 3.9; hence, at both time values (as well as at all time increments in HAARM-3 output) the total masses are the same. For example, at 800 minutes 6.61E+6 g of aerosol have been generated and either transported to walls, floors, and reactor building or are still suspended in the drywell. We note that total quantities of aerosol generated in HAARM-3 calculations may be compared with the source rates given in the penultimate column of Table 3.10. Data in this column were obtained by simple trapezoidal intergration of aerosol weight generation rate versus time. Thus there is an independent check on the mass balancing within the HAARM-3 program and the total quantity of aerosol generated may be read from the last column of Table 3.10 or from Fig. 3.12.

For the reference case, Table 3.11 shows that most of the aerosol leaks from the drywell into the reactor building. The magnitude of this leakage is large, namely 97 and 94% at 300 and 800 minutes after battery failure, respectively.

We may note that an assumption of constancy of r_{s_0} would not be greatly in error since this variable fluctuates only between its input value of 0.2819 μm and a maximum value of 0.555 μm, as shown in Fig. 3.13. As expected, settled masses increase as particle size increases while plated weights decrease as particle size increases.

The effect of thermophoresis is significant in terms of the quantity of aerosol plated. Thus, this variable increase by a factor of about 5 (Table 3.11) for the smaller particle size distribution and by a factor of 20 (Table 3.12) for the larger particle size distribution. However, the overall effect on leakage is small.

As discussed in Sect. 3.3.4, the value of the temperature gradient in the gas phase at the drywell liner is in doubt because it is based on the MARCH output for the temperature increase of the drywell liner. There is the possibility that MARCH calculates this incorrectly, thereby leading to incorrect values of the temperature gradient. (We attempted to use the procedures discussed on pages 3-49 and 3-50 of the MARCH User's Manual[3.30] to calculate temperature gradients and obtained results totally inconsistent with the reported drywell wall temperatures.)

It appears that the errors are in the direction of overestimating the thermophoretic effect; i.e., MARCH evidently overestimates the rate of temperature increase of the drywell liner which leads to overestimates of the temperature gradient in the gas adjacent to the liner. In this case, the error would not greatly effect the calculated amount of aerosols which leak from the drywell, since in this case the thermophoretic effect does not dominate. However, the plated masses (see Table 3.11), estimated to be 1.1 and 4.8% of the total at 300 and 800 min respectively, are probably overestimated.

3.4 Aerosol Transport in the Reactor Building

3.4.1 Introduction

As described in Sect. 3.3 and summarized in Table 3.11, most of the approximately 6.6 Mg of aerosol generated in the drywell during the period up to 800 min. after battery failure flows into the reactor building after failure of the electrical penetration seals. The gas carrying the aerosol particles is hot; its temperature is shown as a function of time in Fig. 3.4. As the gas flows through the building on its way to the biosphere, it will probably cool somewhat due to transfer of heat to surfaces (walls, floors, stairwells, etc) and as a result of mixing with the building air. However, no thermal-hydraulic analysis of the reactor building is available for the Station Blackout accident sequence. Because of this, it is not possible to analyze aerosol transport in the building in the same detail as for the drywell.

The drywell gas composition changes rapidly as soon as core debris starts to react with the concrete floor, as shown by the mole fractions in Table 3.13. Other important thermodynamic properties, such as viscosity, density, and average molecular weight, also undergo large changes. Rates of leakage of gas from the drywell into the reactor building change with time, as do the parameters that define the particle size distribution.

The leak rate and mass-mean radius are shown in Figs. 3.5 and 3.13, respectively, while these and other important properties defining the leak are presented in Table 3.14. One important property is the total quantity of gas that has leaked into the building. This variable, obtained by integrating the MARCH output concerning leak rate versus time, is listed in the penultimate column of Table 3.14 and shown graphically in Fig. 3.14. It is apparent that the reactor building provides only a small holdup time before radioactive aerosol will reach the biosphere. This statement is based on the assumption that the gas does not cool significantly on its passage through the building, and therefore, that there is little or no condensation of water, which is a major component of the gas (Table 3.13).

Recognizing the considerable uncertainties mentioned above, the HAARM-3 program was executed for conditions definable in the absence of a thermal hydraulic analysis. The purpose of this analysis is to ascertain whether there is any significant retention of aerosol in the builidng under the very conservative assumptions presently available.

3.4.2 HAARM-3 input data

Again we divide input required by HAARM-3 into four categories, as shown in Tables 3.15-3.18. many of these values are the same as those of Tables 3.4-3.7; however, there are significant differences. Particularly noteworthy is the time variation of particle size distribution (Tables 3.14 and 3.17). In this analysis we assume that there is no thermophoretic effect; that is, the variable TGRADW in Table 3.16 is set equal to 0.0. Other parameters of Table 3.18 differ from those of Table 3.7 because of differences in surface areas and volumes between drywell and reactor building.

The HAARM-3 program can be programmed to utilize input consisting of particles whose size and standard deviation vary with time.[3.23] This option has been used in calculations 3, 4, and 8 of Table 3.14. As may be seen in the third and fourth columns of this table, the parameters specifying size do not change much.

3.4.3 HAARM-3 results

Some of the results from the HAARM-3 calculations are summarized in Table 3.19 while others are presented in Figs. 3.15-3.19. The table lists the suspended mass, plated mass, settled mass, leaked mass, and total mass at 300 and 800 min after battery failure.

It is apparent from Table 3.19 that the reactor building does not retain a major portion of the aerosol according to the model used in these calculations. As described previously, this model contains no thermal-hydraulic analysis. Thus, those processes that could contribute to plating and settling of aerosol, namely heat transfer to various surfaces and condensation of steam, have been neglected of necessity. The estimates of about 78 and 90% of the aerosol having been discharged from the building at 300 and 800 min, respectively, are conservative. At present, there is no way to determine the degree of conservatism.

Total quantities of material within or discharged from the reactor building at 300 and 800 min after battery failure are 2.73 and 6.48 Mg,

respectively, as shown in Table 3.19. These should be compared with corresponding values 2.56 and 6.24 Mg, respectively, in Table 3.11. These latter values were calculated as the quantities of aerosol that leaked from the drywell into the building. The total quantities of aerosol entering or leaving the building, based on the variable particle size data (Table 3.19), thus exceed the quantities discharged from the drywell. The discrepancy in the material balance is not large; at 300 min after battery failure it corresponds to about 11%, while it corresponds to less than 4% at 800 min after battery failure. These discrepancies are actually so small as to lend additional credibility to the calculations for the reactor building model used in this section.

3.5 Aerosol Deposition in the Reactor Vessel

The degree of aerosol deposition in the reactor vessel has been estimated using the results of a series of calculations previously performed at Battelle Columbus Laboratories with the TRAP-MELT code.

These calculations indicate that between 60 and 99% of the aerosols generated within a BWR reactor vessel by the overheating of core and structural material would be retained on the internal surfaces of the vessel. The most effective aerosol trap would be the extensive surface area of the steam dryer assembly. The predominant deposition mechanism would be thermophoresis.

These computations involve some uncertainty and their interpretation requires the use of reasonable judgement, particularly with respect to the assumed initial aerosol particle size, to which the thermophoretic deposition mechanism is extremely sensitive. After consultation[3.31], it has been assumed that 80% of the aerosols generated within the reactor vessel* would be retained therein, while the reactor vessel is intact.

---

*It should be recalled that the BWR reactor vessel has extensive internal surface area (upper plenum, standpipes, steam separators, steam dryers) above the core.

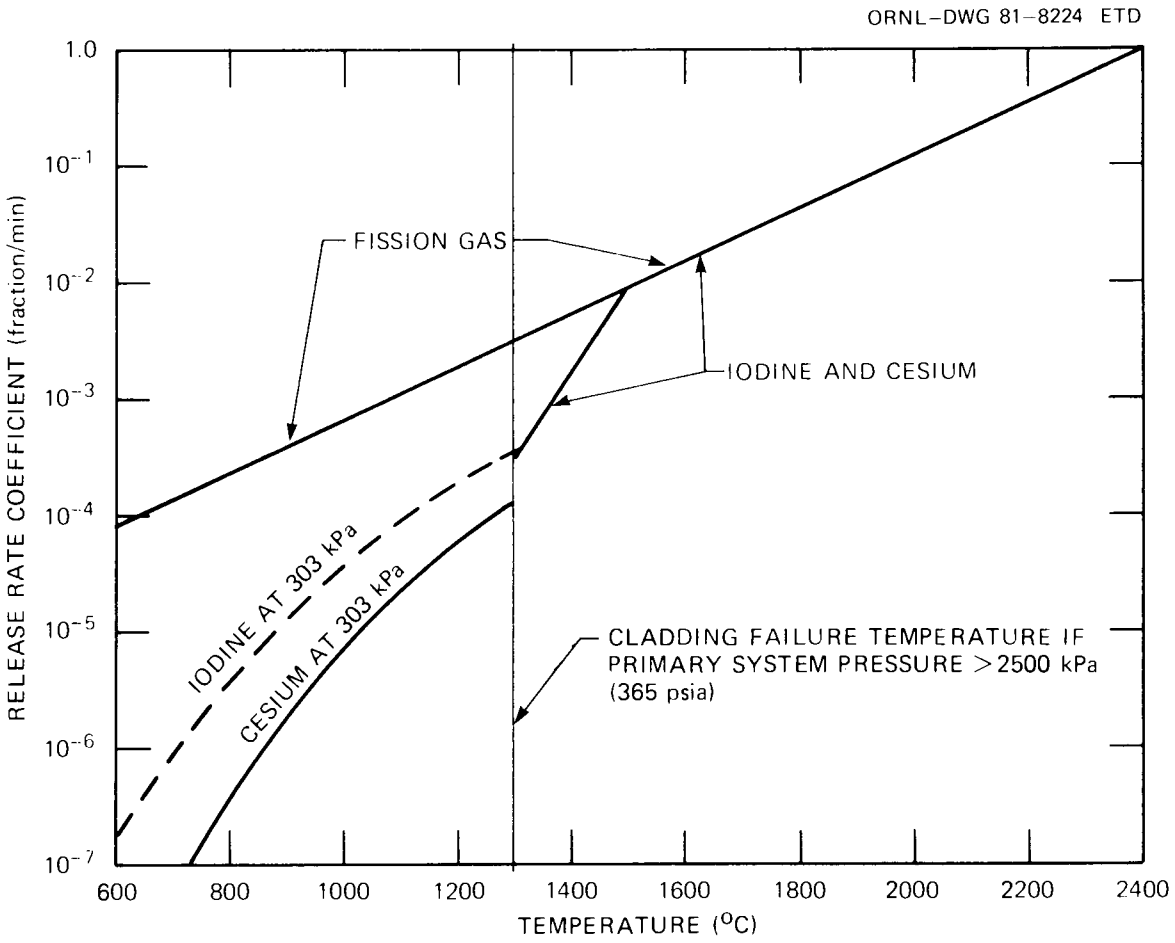

Fig. 3.1. Release rate coefficients for fission gas, iodine, and cesium.

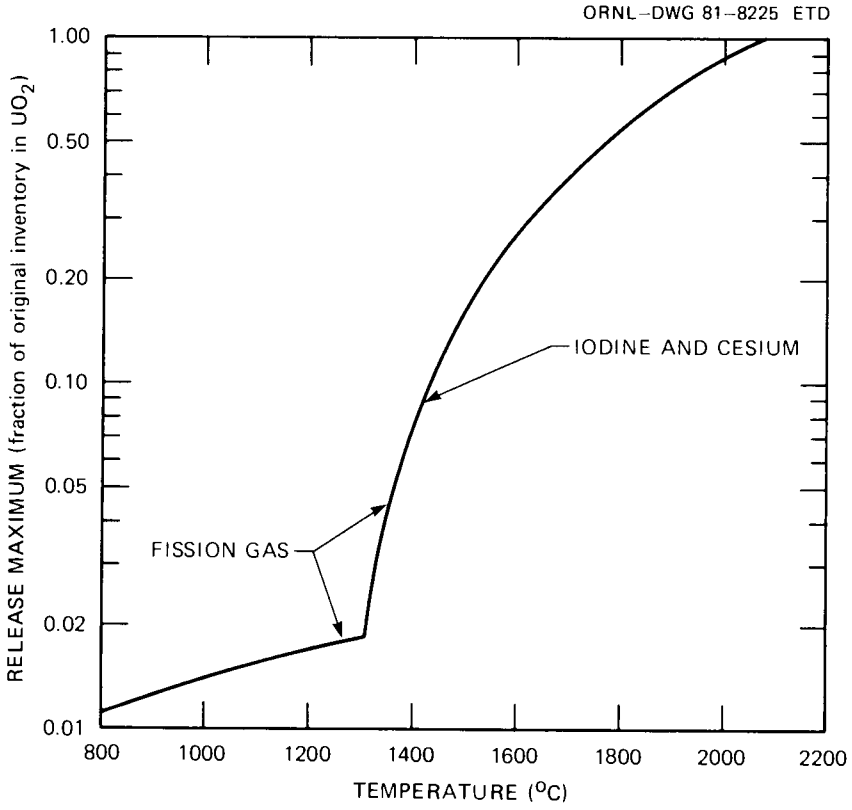

Fig. 3.2. Maximum release of fission gas, iodine, and cesium.

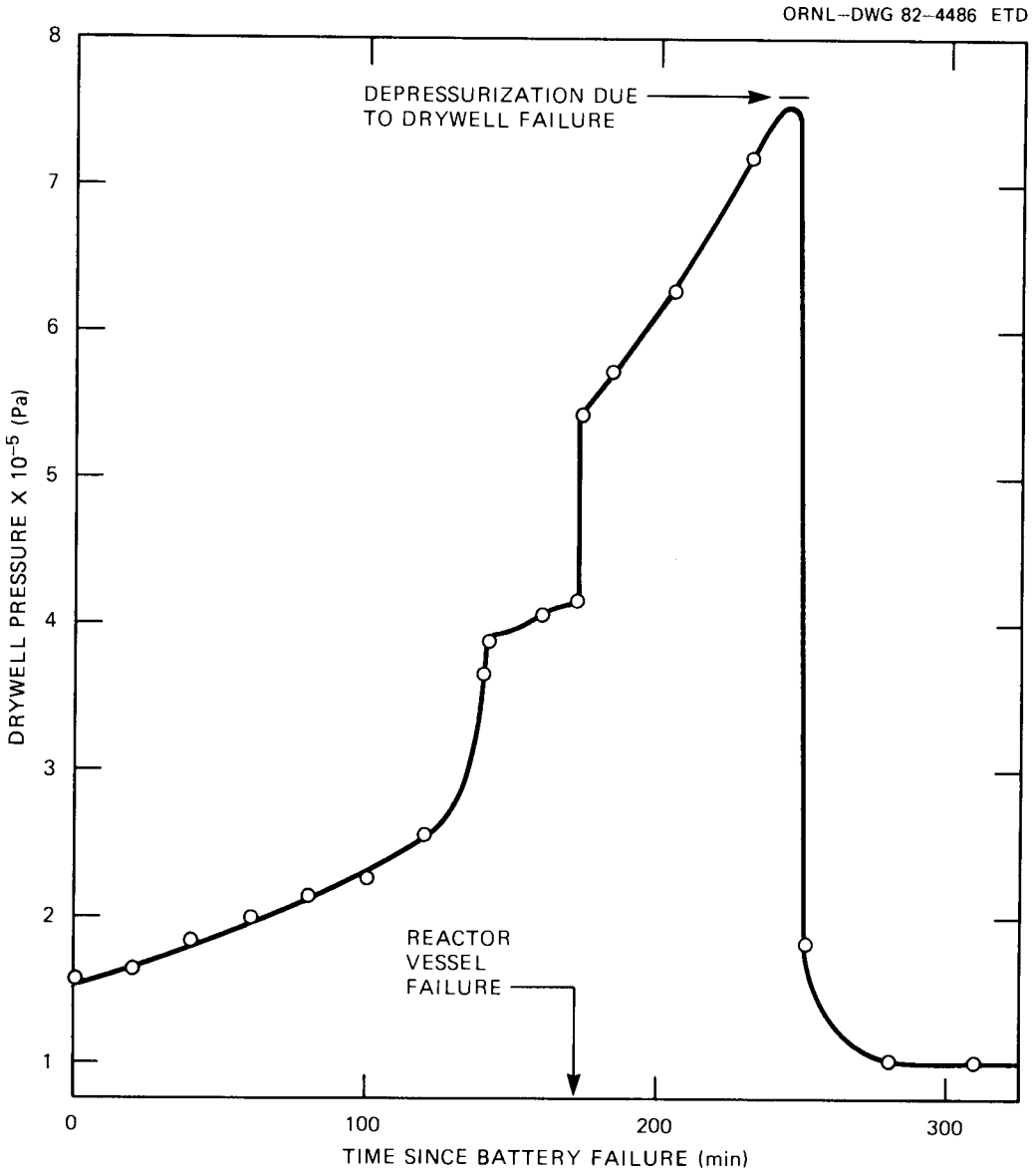

Fig. 3.3. MARCH output (o) used to derive smoothed pressure-time data for HAARM-3 input.

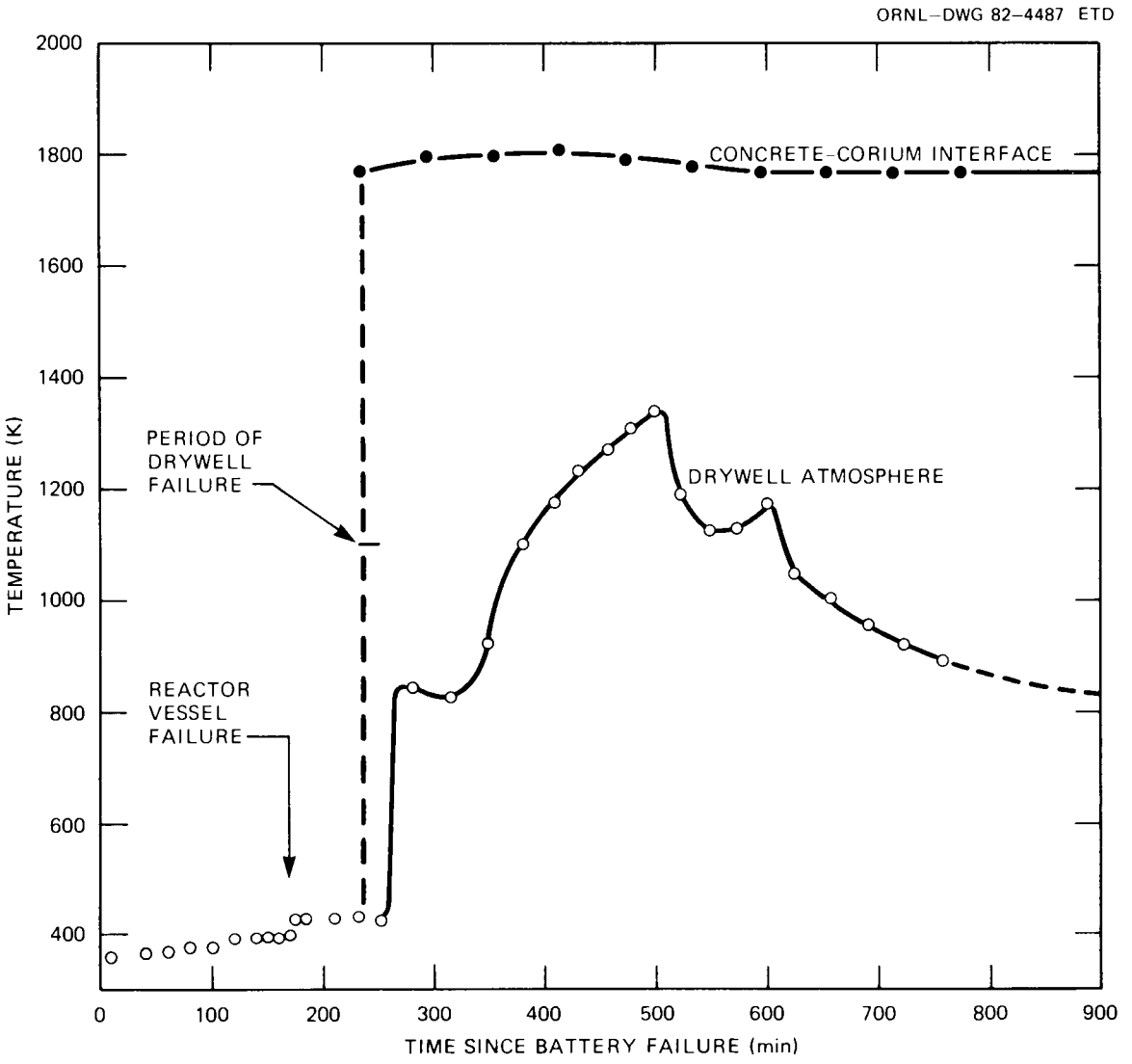

Fig. 3.4. MARCH output (• and o) used to derive smoothed temperature-time data for HAARM-3 input.

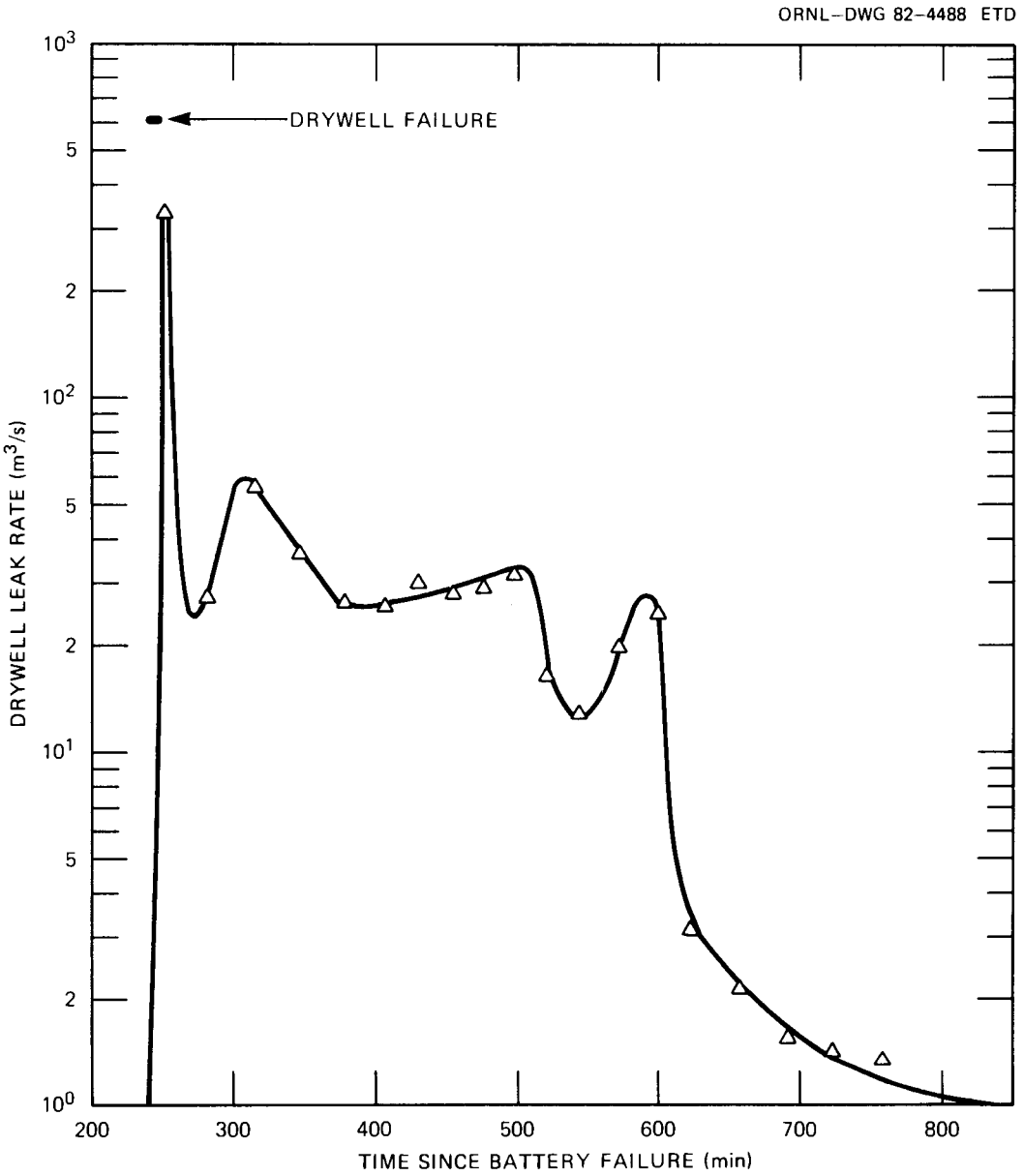

Fig. 3.5. MARCH output (Δ) used to derive smoothed leak rate-time data for HAARM-3 input.

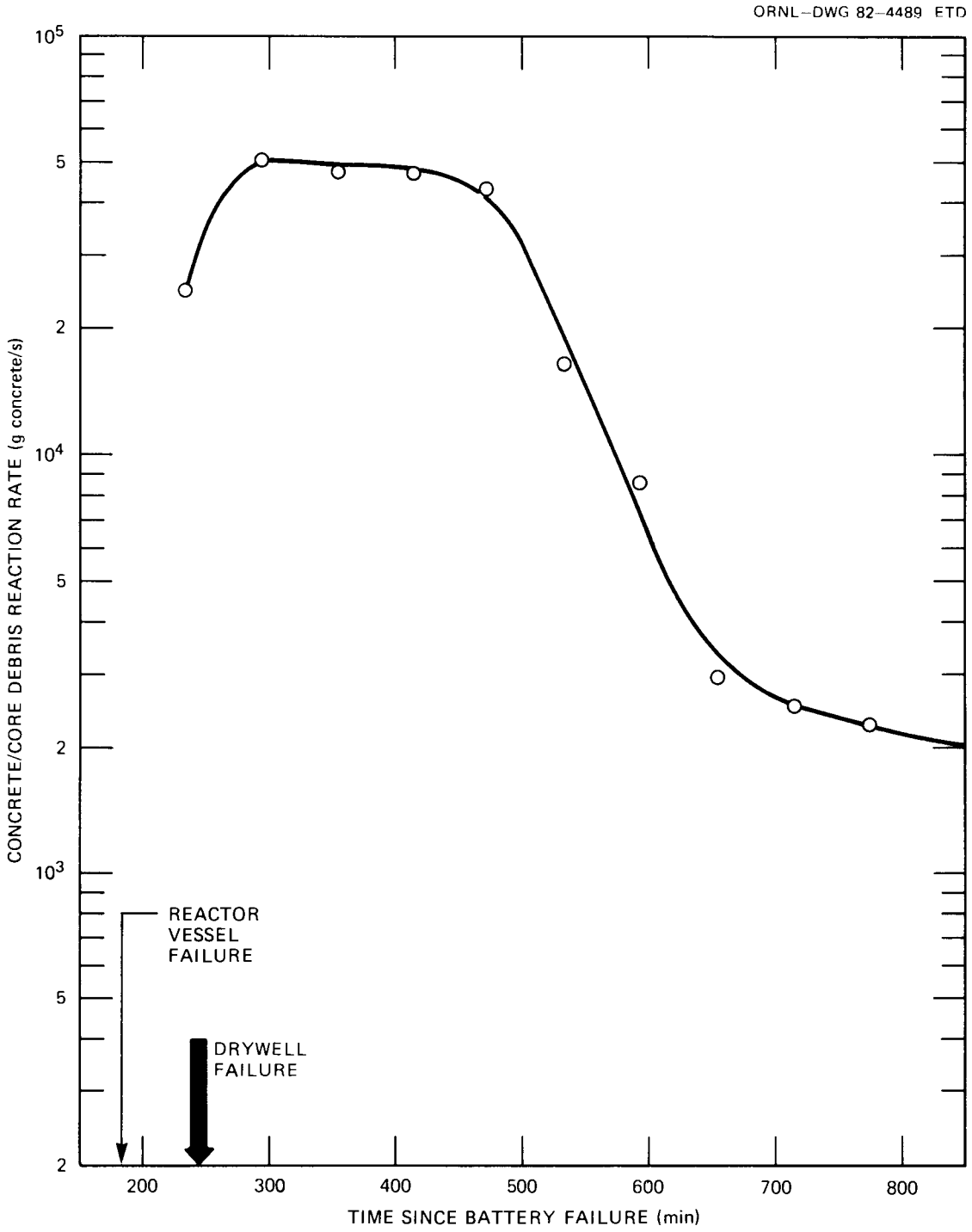

Fig. 3.6. MARCH output (o) used to derive concrete reaction rate-time data for comparison with the SANDIA correlation.

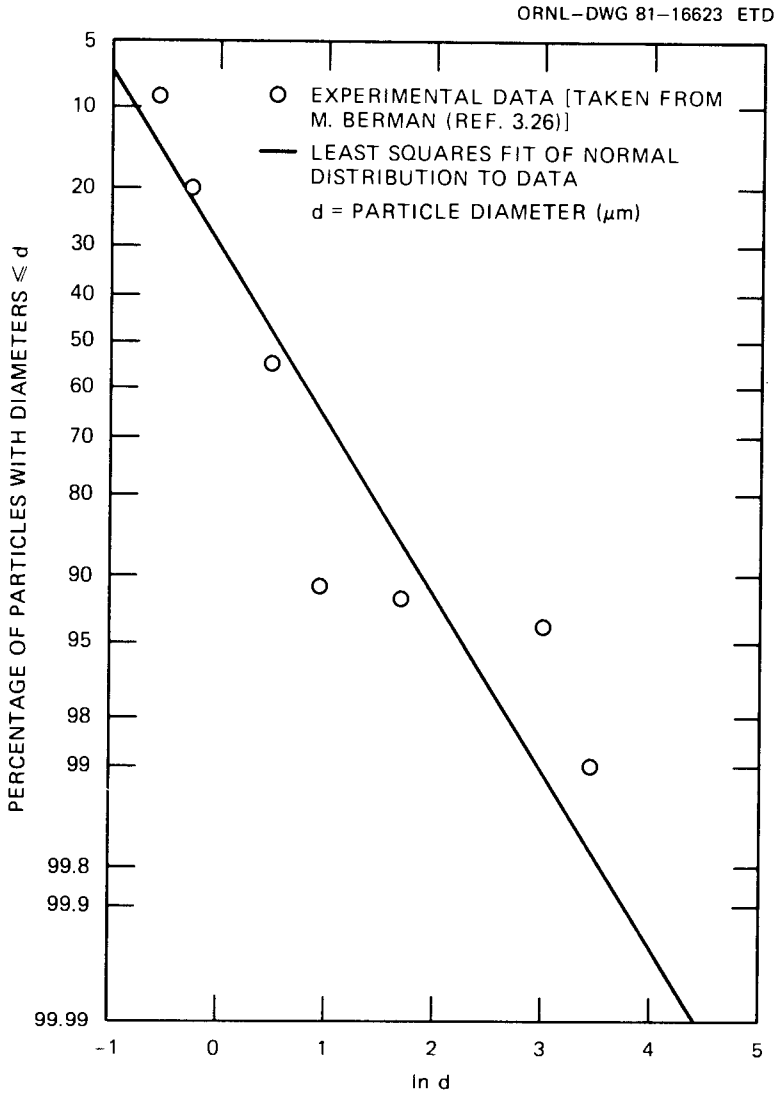

Fig. 3.7. Drywell aerosol source particle size distribution.

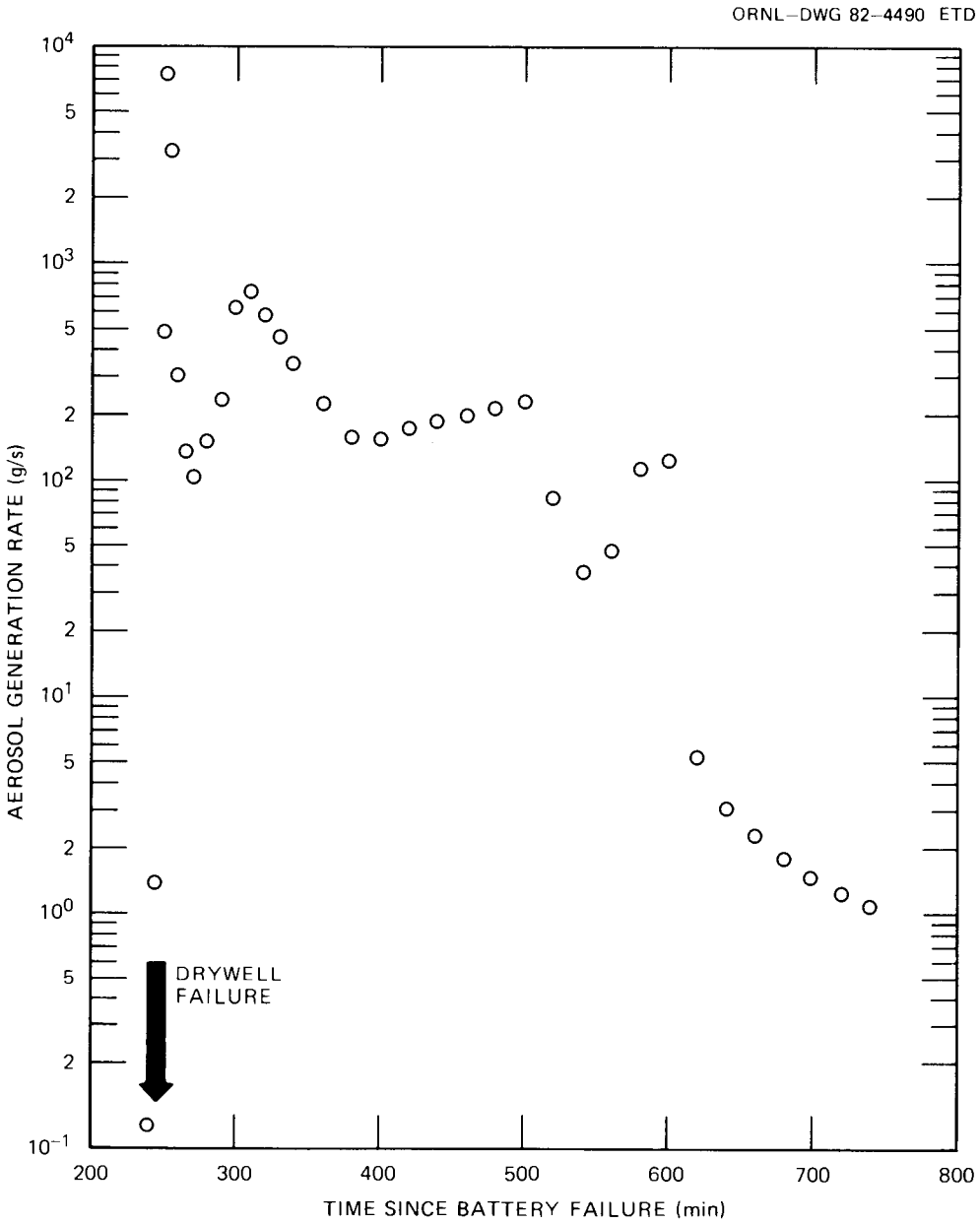

Fig. 3.8. Aerosol generation rate in the drywell.

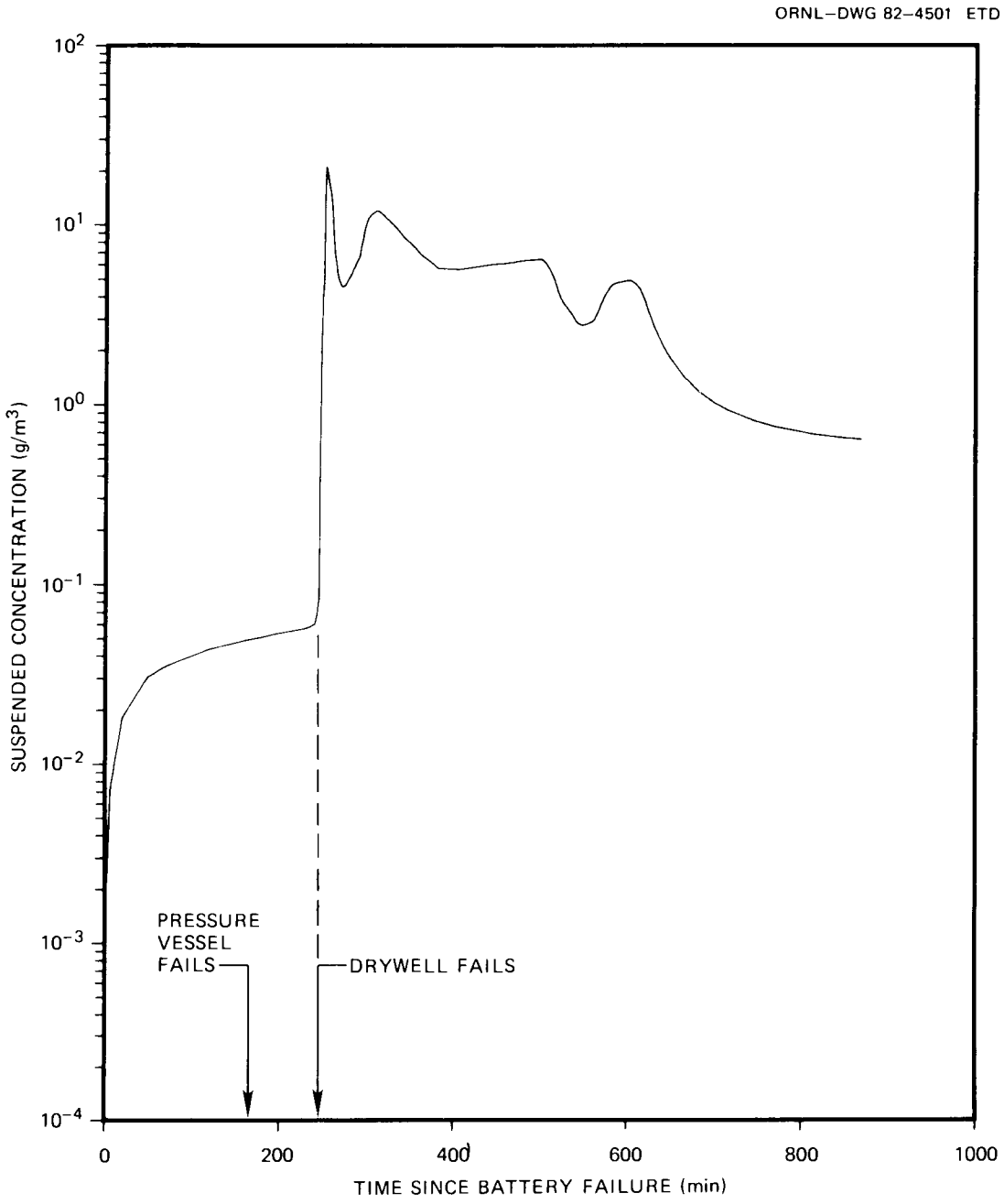

Fig. 3.9. Aerosol concentration in the drywell during the first 800 min after battery failure [reference case with initial mass-mean particle radius (r_{s0}) of 0.2819 μm and σ_s = 1.8].

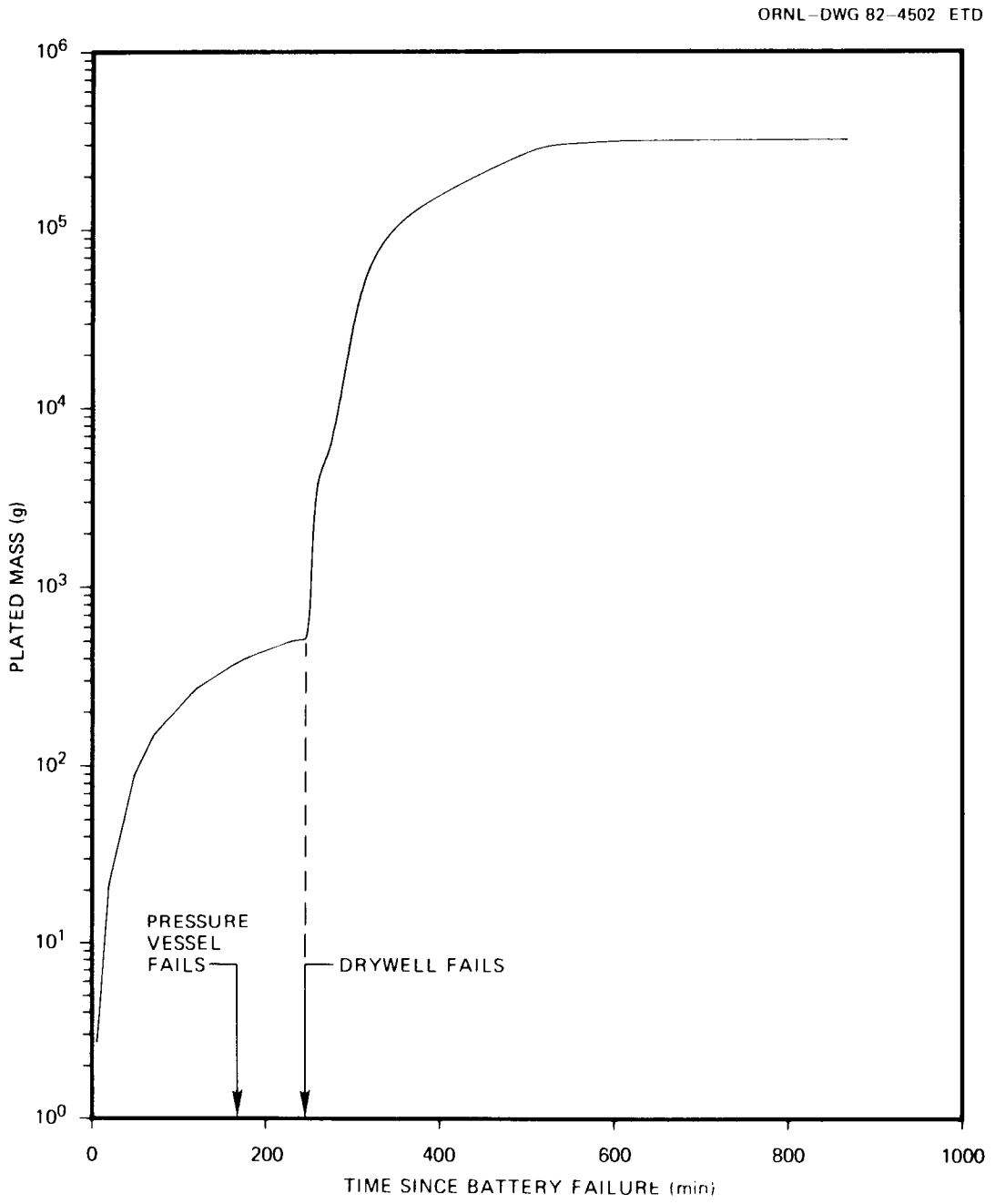

Fig. 3.10. Plated mass of aerosol in the drywell during the first 800 min after battery failure [reference case with initial mass-mean particle radius (r_{s0}) of 0.2819 μm and σ_g = 1.8].

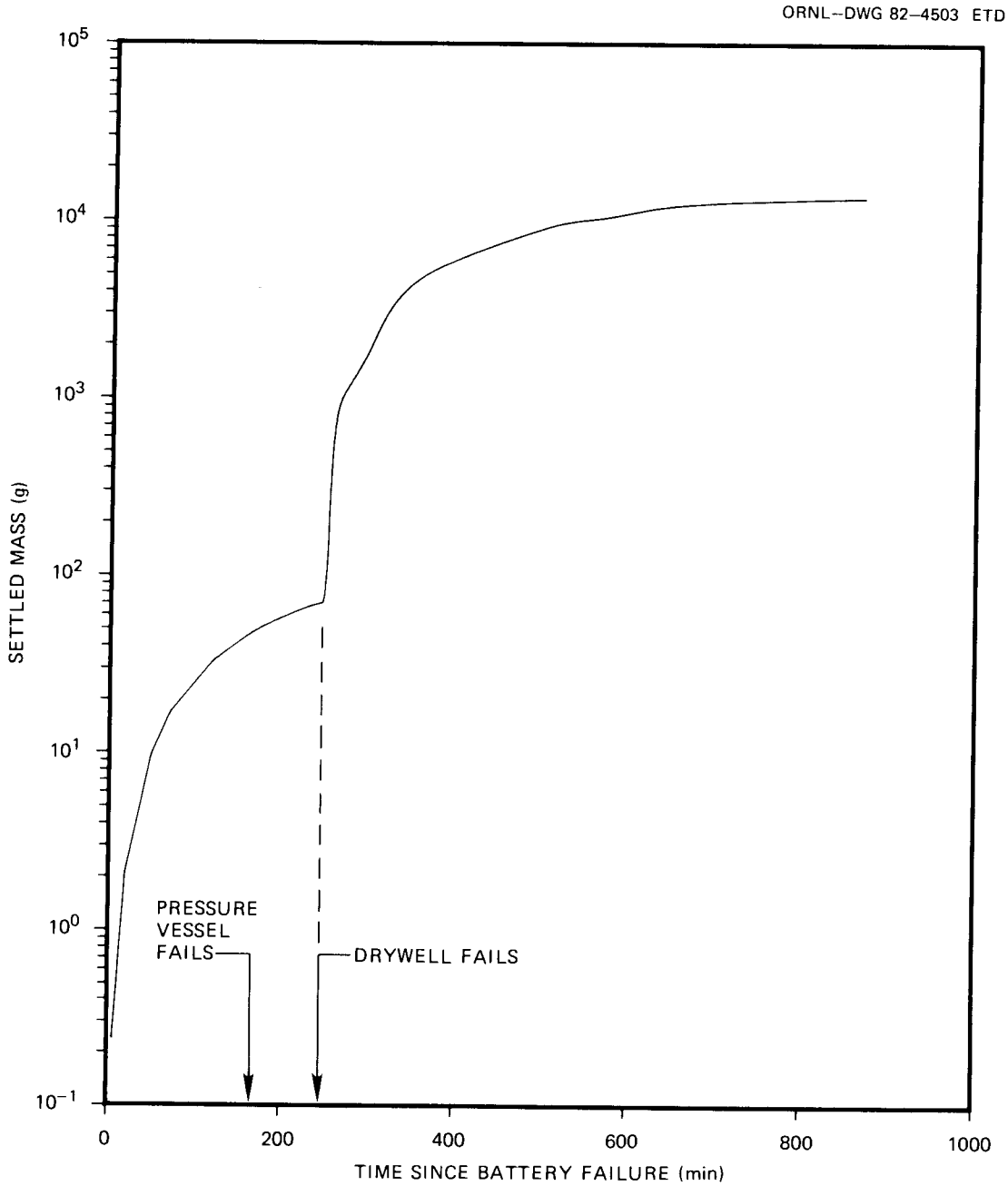

Fig. 3.11. Settled mass of aerosol in the drywell during the first 800 min after battery failure [reference case with initial mass-mean particle radius (r_{g0}) of 0.2819 μm and σ_g = 1.8].

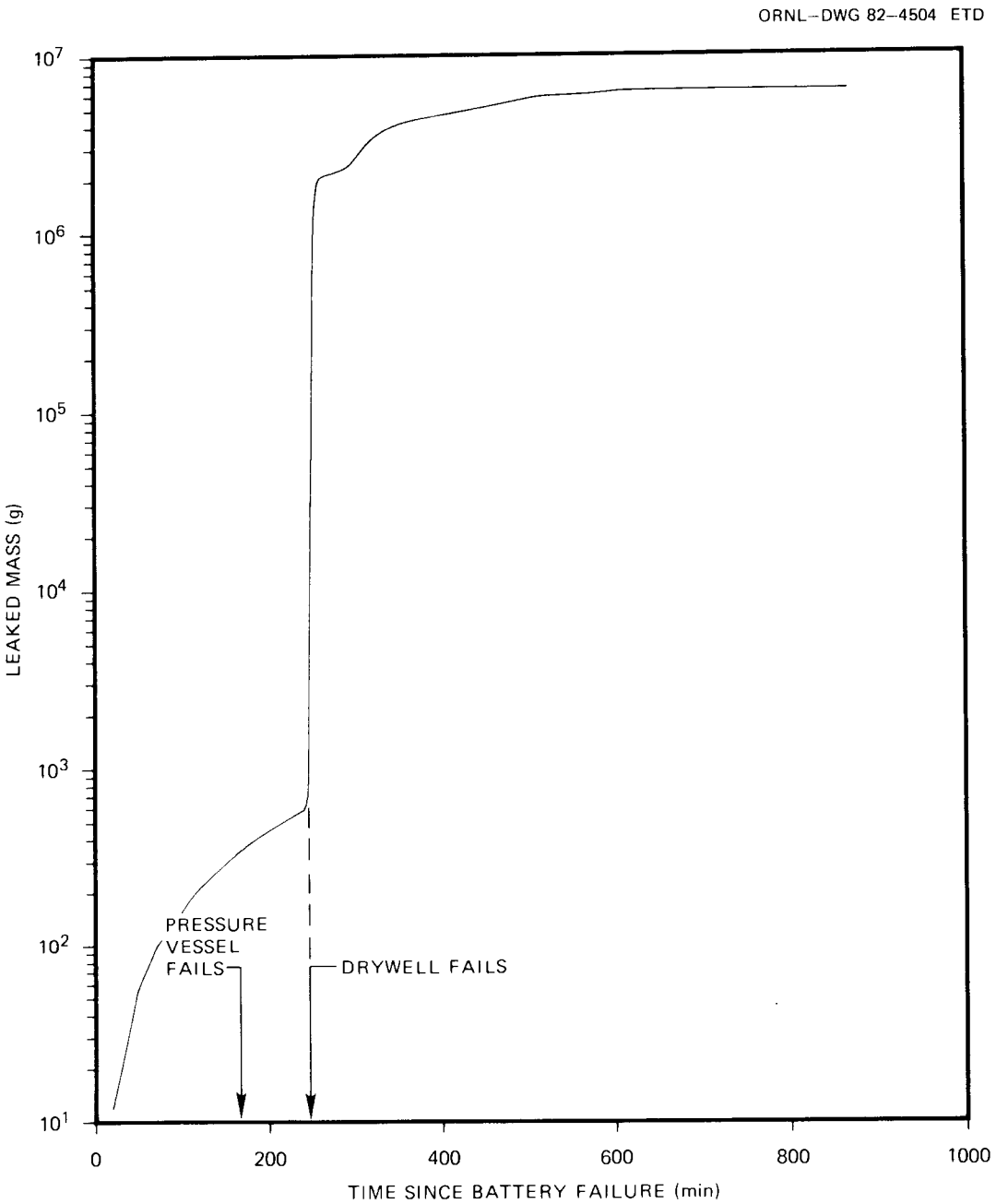

Fig. 3.12. Mass of aerosol leaked from drywell into reactor building and biosphere during first 800 min after battery failure [reference case with initial mass-mean particle radius (r_{s0}) of 0.2819 μm and σ_g = 1.8].

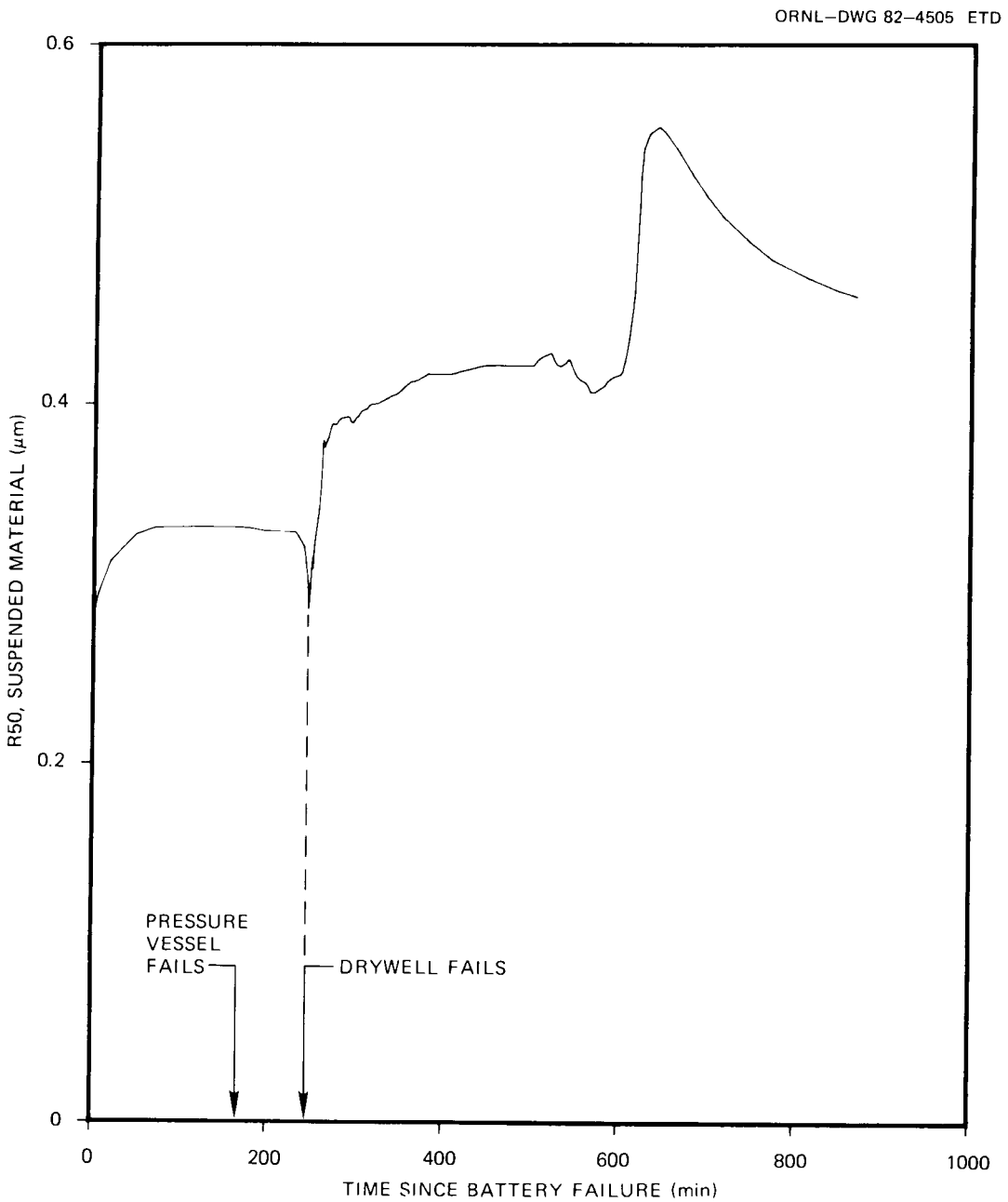

Fig. 3.13. Mass-mean radius of suspended aerosol during the first 800 min after battery failure [reference case with initial mass-mean particle radius (r_{s0}) of 0.2819 μm and σ_g = 1.8].

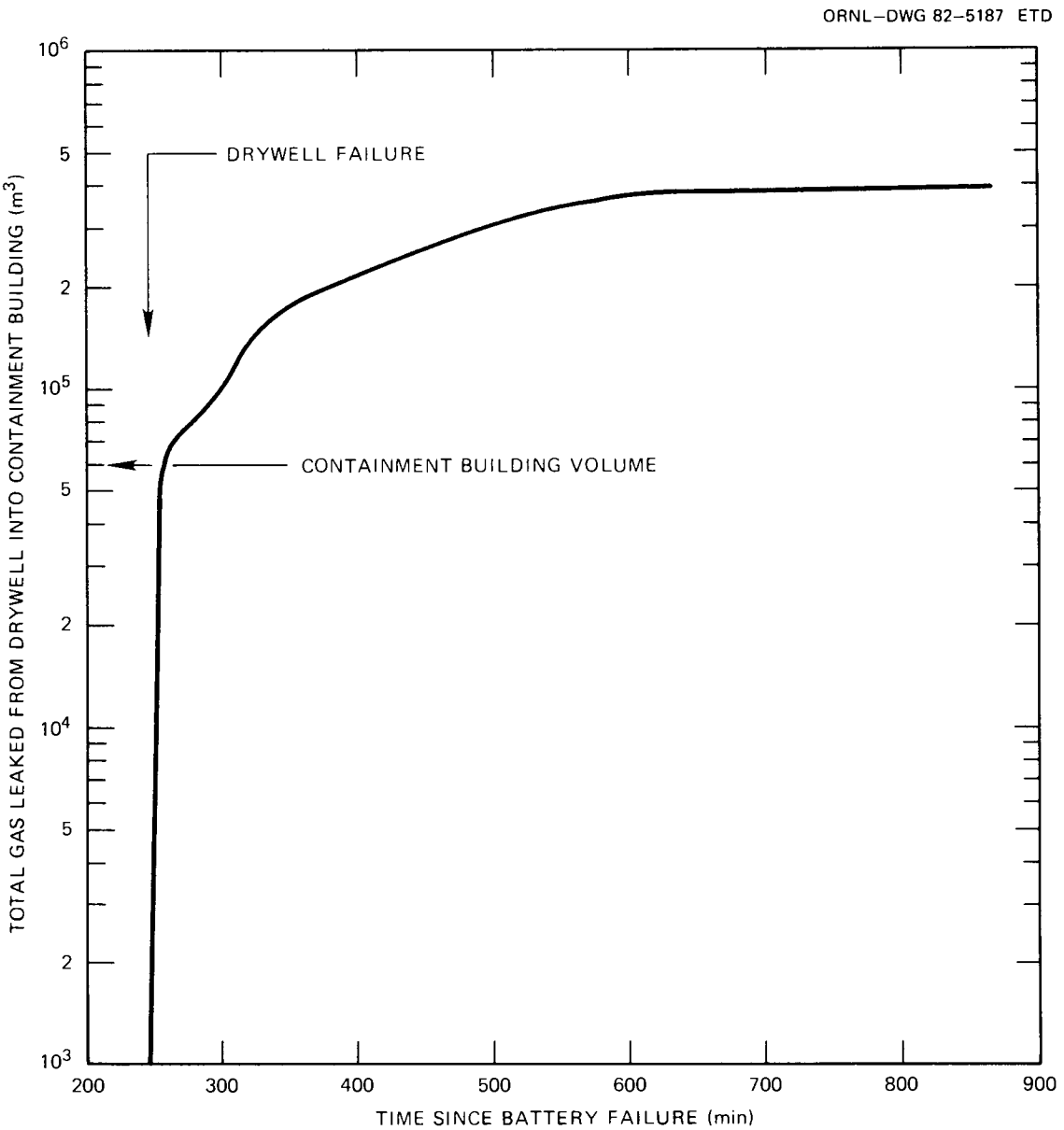

Fig. 3.14. Total gas leaked from drywell into containment building. Volume is based on gas temperature of drywell and no steam condensation.

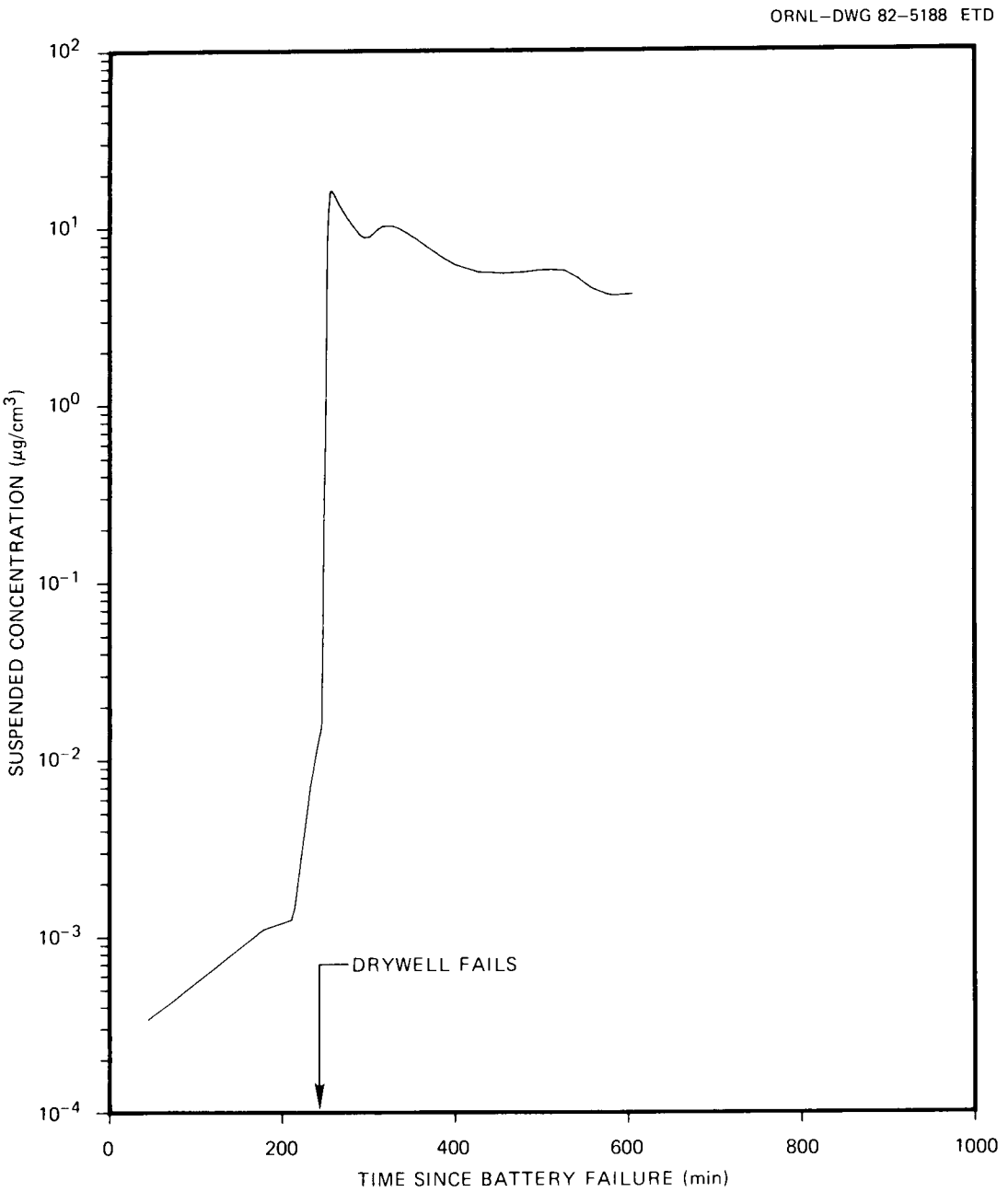

Fig. 3.15. Aerosol concentration in the reactor building during the first 800 min after battery failure.

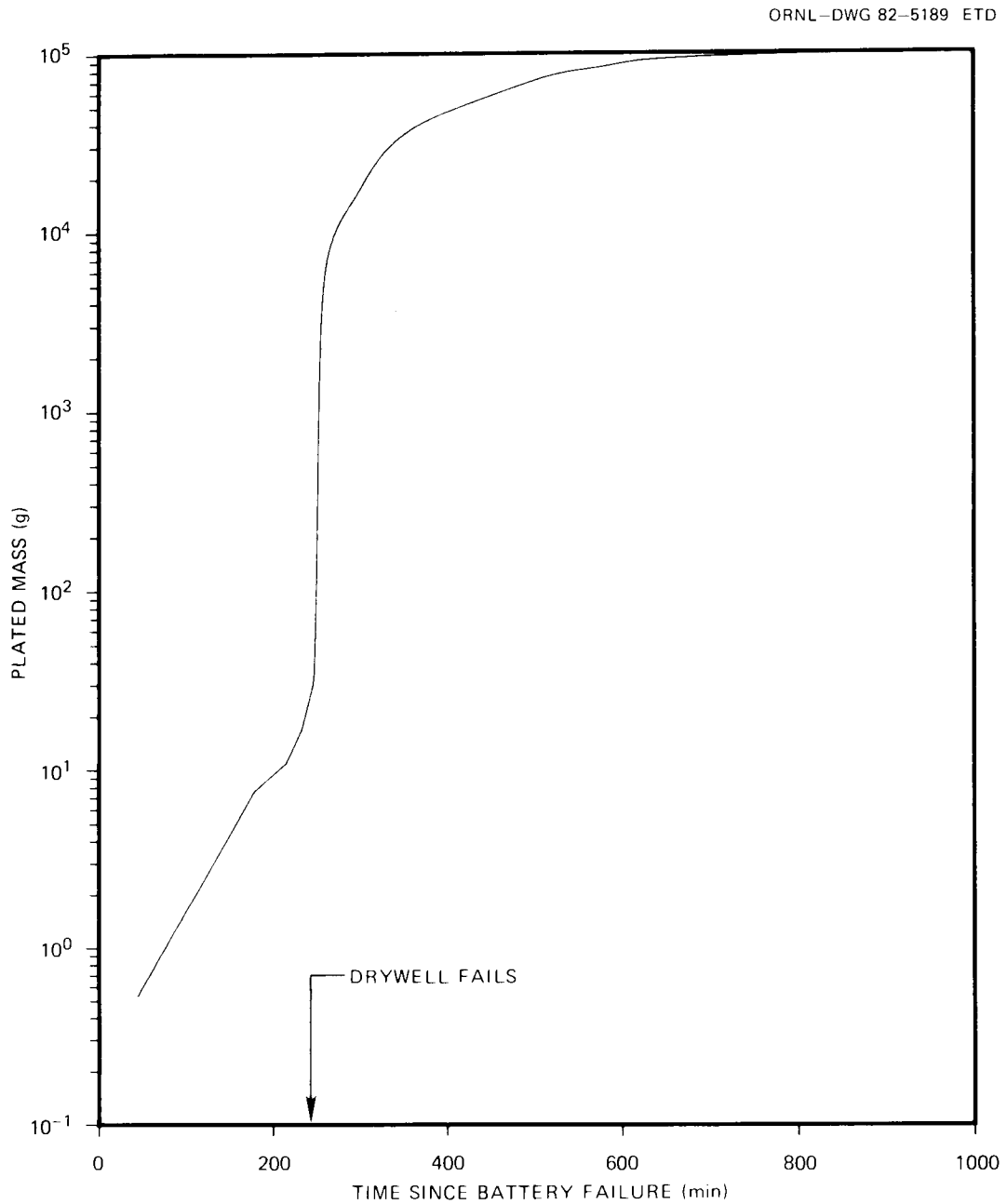

Fig. 3.16. Plated mass of aerosol in the reactor building during the first 800 min after battery failure.

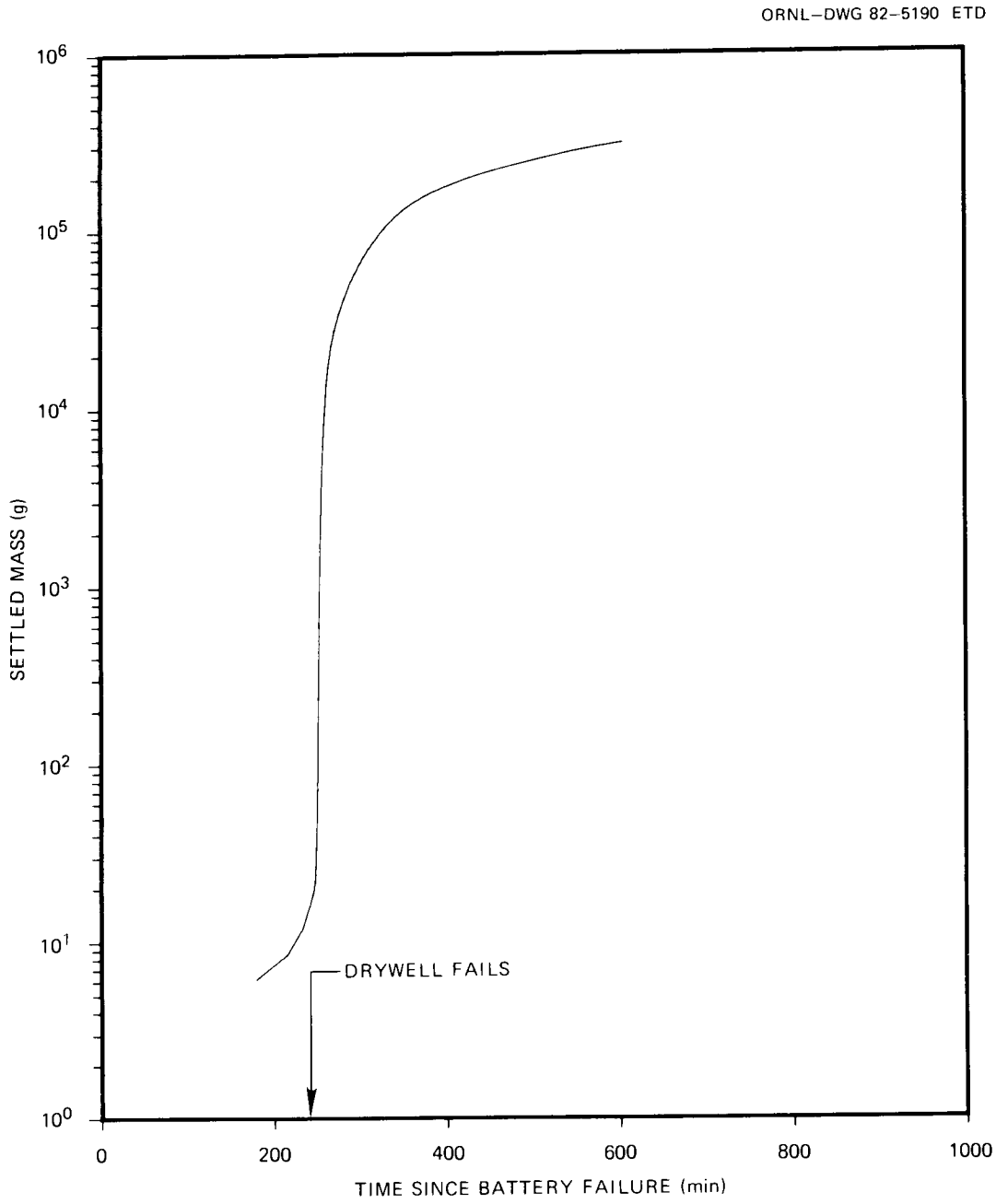

Fig. 3.17. Settled mass of aerosol in the reactor building during the first 800 min after battery failure.

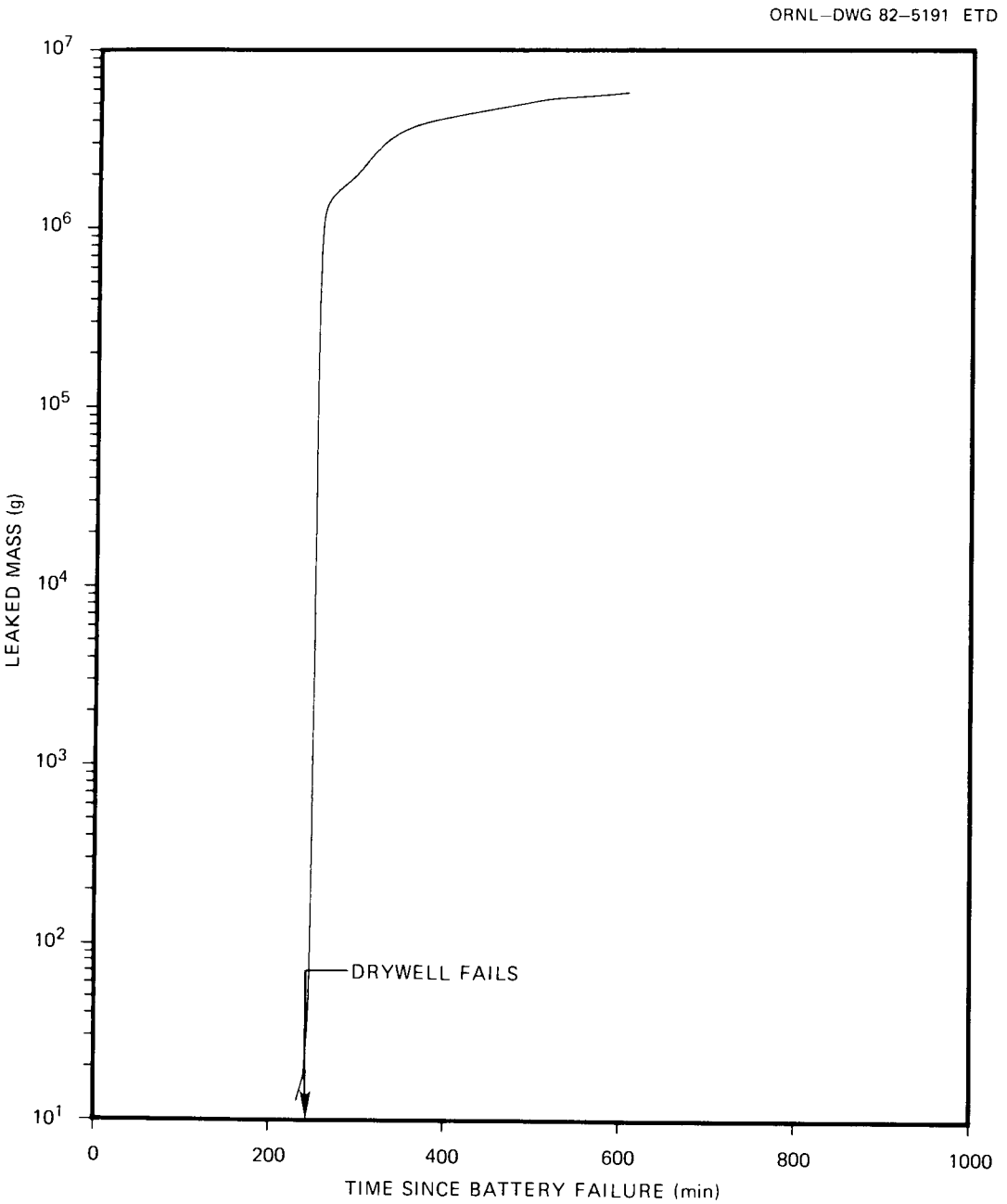

Fig. 3.18. Mass of aerosol leaked from the reactor building into the biosphere during the first 800 min after battery failure.

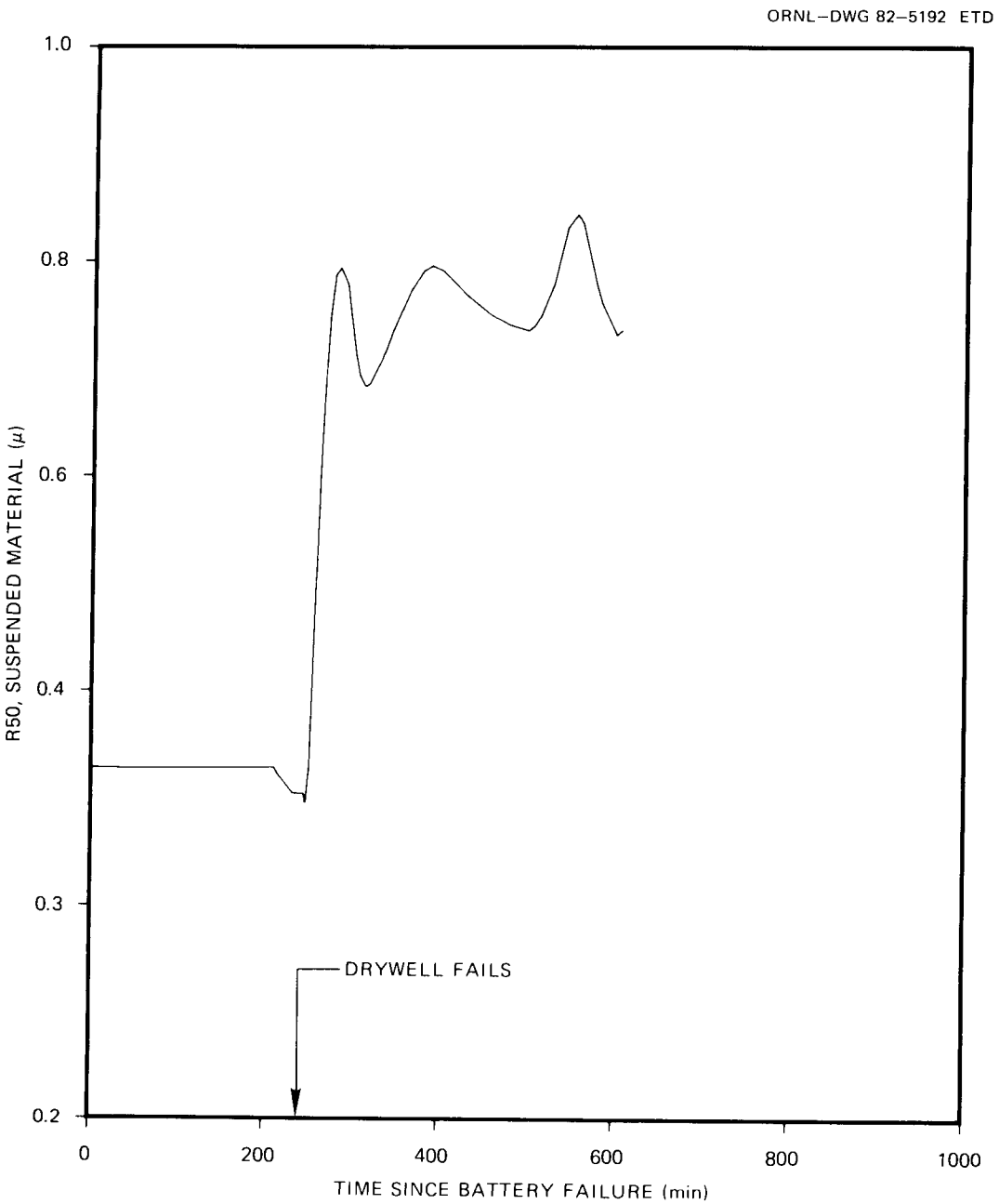

Fig. 3.19. Mass-mean radius of suspended aerosol in the reactor building and biosphere during the first 800 min after battery failure.

Table 3.1. Characteristics of model fuel rod[a]

Characteristic	Fuel rod average	Fuel rod peak
Burnup (MWd/te)	15,000	18,750
Total Cs content (g/cm)	0.01118	0.01398
(g/rod)	4.260	
Total I content (g/cm)	0.001118	0.001398
(g/rod)	0.426	
Total Te content (g/cm)	0.002236	0.002796
(g/rod)	0.852	
Initial stable fission gas, Cs, I, and Te gap inventory (%)	4.0	8.0
Volume of initial fission gas gap inventory (cm^3 STP)[b]	47.3	
Cs gap inventory (g/cm^2 cladding)	1.388×10^{-4}	3.345×10^{-4}
I gap inventory (g/cm^2 cladding)	1.338×10^{-5}	3.345×10^{-5}
Te gap inventory (g/cm^2 cladding)	2.676×10^{-5}	6.690×10^{-5}

[a]10.41-mm cladding ID, 0.813-m cladding wall thickness, 10.41-mm pellet diam, 3.81-m fuel column length, 0.25-m plenum length, 37-cm^3 (plenum plus void volume); volume of prepressurizing helium, 102.7-cm^3 (STP).

[b]STP refers to a standard temperature and pressure at 0°C and 0.101 MPa (1 atm).

Table 3.2. Values of parameters for cesium and iodine release

Parameter	Cesium	Iodine	Tellurium[a]
α, $(g/cm^3).(g/cm^2)^{-a}$	3.49	0.163	9.78×10^{-3}
a	0.8	0.8	0.8
C, K^{-1}	7.42×10^3	3.77×10^3	3.77×10^3
δ, $(g.MPa/m.h).(g/cm^2)^{-a}$	1.90×10^3	1.22×10^2	7.32
γ, K^{-1}	1.98×10^4	1.48×10^4	1.48×10^4

[a]Based on iodine release with parameters α and δ reduced a factor of 16.7.

Table 3.3. Effective vapor pressures and aerosol composition at 2400°C

Material	Effective vapor pressure (atm)	Aerosol compositon (mass %)
Fe	0.0569	36.80
Mn	0.0576	36.80
Cr	0.0279	16.43
Sn	0.0039	5.48
Ni	0.0036	2.41
UO_2	4.0×10^{-4}	1.53
Zr	4.0×10^{-4}	0.42
Co	3.8×10^{-4}	0.14
Total	0.151	100.0

Table 3.4. HAARM-3 input from accident specifications: aerosol transport in the drywell for station blackout at Browns Ferry-1

Variable definition	Variable		Note
	Name	Value	
Settling terms (1 = yes/0 = no)	ISETL	1	
Plating terms (1 = yes/0 = no)	IPLAT	1	
Leakage terms (1 = yes/0 = no)	ILEAK	1	
Agglomeration, Brownian (1 = yes/0 = no)	IAGGB	1	
Agglomeration, gravity (1 = yes/0 = no)	IAGGG	1	
Agglomeration, turbulent (1 = yes/0 = no)	IAGGT	0	
Source terms (1 = yes/0 = no)	ISORS	1	
Number of discrete volumes for distribution calculations	IVOL	0	*a*
Source rate conversion factor	SO	1.0	*b*
Source geometric standard deviation,	SIGSOR	1.8 (2.29)	*c*
Source mass median radius, μm	RSOR	0.2819 (6.979)	*d*
Initial concentration of aerosol, particles cm^{-3}	XIN(1)	0.0	
Aerosol sigma (size of initial particles)	SIGAIR	1.8 (2.29)	*e*
Aerosol 50% (mass median) radius, μm	RAIR	0.2819 (6.979)	*e*
Initial time, s	TO	0.0	
Source cutoff time, s	TAUIN	5.20D+4	
Maximum time, s	TMAXIN	5.20D+4	
Leakage rate, s^{-1}	RVL	0.0	*f*

[a] A log-normal distribution is assumed.

[b] This factor is required to convert source-rate values to units of particles/($cm^3 \cdot s$). The MARCH program provides values of the rates of reaction of corium with concrete in units of (g concrete/s) at a series of times, as noted in Table 3.4. However, the SANDIA equation provides values of aerosol concentrations in units of g/m^3. For convenience, values of the required HAARM-3 input were calculated separately, thereby making SO = 1.0 dimensionless.

[c] See Lindauer and Castelman[3.29] for studies of initial size distribution of aerosols. The reference value $\sigma_g = 1.8$ was chosen from the work of these authors. The value 2.29 geometric mean standard deviation, in parenthesis, was used in additional calculations as part of a brief parametric study.

[d] The value 6.979 μm, in parentheses, was used in additional calculations.

[e] Not used.

[f] RVL is set to 0.0 since a table of leak rate versus time has been calculated from MARCH output.

Table 3.5. HAARM-3 input suggested in Users Manual: adapted for transport in the drywell for station blackout at Browns Ferry-1

Variable definition	Variable	
	Name	Value
Method of integration (2 = Adams - Moulton with fixed incrementing) (1 = Runge - Kutta with fixed incrementing) (0 = Adams - Moulton with variable incrementing)	INDIN	0
Maximum number of time steps ($\leq$1000)	KMAX	1000
Increment for time index for output	ISEQ	10
Time step, initial, s	HIN	1.00D-6
Convergence criterion	TOLIN	1.00D-3
Diffusion boundary layer thickness, cm	DELTA	1.00D-4
Shutoff value for ratio agglomeration rate/ settling rate	EPSN	0.0
Shutoff value for ratio airborne mass concentration/initial airborne mass concentration	EPSM	0.0
Shutoff value for ratio particulate volume/ maximum particulate volume	EPSL	1.00D-6
Diffusion boundary layer thickness in plating equation, cm	DELTA1	1.00D-4
Density modification factor	ALPHA	1.0
Klyachko terminal settling velocity calculation (1 = yes/0 = no)	KLYACH	0
Collision efficiency for gravitational agglomeration	EFF	1.0
Dynamic shape factor	CHI	1.0
Time-varying alpha (1 = yes/0 = no)	IALVAR	1
Collision shape factor	GAMMA	1.0
Attenuation (1 = yes/0 = no)	LAMSIG	1
Variable alpha (1 = yes/0 = no)	IEFF	1
Temperature gradient at wall (no thermal plating if 0)	TGRADW[a]	200.0 (0.0)
Thermal conductivity ratio (gas/aerosol)	TCR	1.0 D-3
Mixture effects (1 = yes/0 = no)	IMIX	0

[a]Calculations were performed both with and without thermophoresis, as described in the text. The value 200.0 simply signals input of a table of TGRAD versus time rather than the single value 200.0 K/cm. The value 0.0 in parenthesis was used to indicate the absence of thermophoresis in other calculations.

Table 3.6. HAARM-3 input from MARCH calculations: for the drywell for station blackout at Browns Ferry-1

Variable definition	Variable		Note
	Name	Value	
Number of values in table of leak rate versus time	NLEEK	40	
Leak rate, s^{-1}	RLEK(I)		*a*
Time, s	TLEK(I)		*a*
Number of values in table of source rate versus time	NSOUR	40	
Source rate (of generation of aerosol due to concrete/corium reaction), particles cm^{-3} s^{-1}	SOURS(I)		*b*
Time, s	TSOUR(I)		*b*
Number of values in table of drywell temperature and pressure versus time	NTP	50	
Temperature of drywell atmosphere and, after bottom meltthrough, of concrete/corium interface, K	TEMPT(I)		*c*
Pressure in drywell, dyne cm^{-2}	P(I)		*c*
Time, s	TPT(I)		*c*
Number of values in table of temperature gradient in gas at the drywell wall	NTG	40 (0)	*d*
Temperature gradient in gas at drywell wall, K/cm	TGRAD(I)		*d*
Time, s	TG(I)		*d*

[a]The values of leak rate versus time are listed in Table 3.9.

[b]The MARCH program prints values of the rate of reaction of concrete, in g/s, with core debris versus time. When used, such rates must be multiplied by $0.508\ f/[(4/3)\pi r^3 \rho \times 4.5 \times 10^9]$, where 0.508 is the weight fraction of $CaO + SiO_2 + Al_2O_3$ in concrete, r is the assumed effective radius of the concrete/corium aerosol, ρ is particle density, 4.5×10^9 cm^3 is the volume of the drywell, and f is the (unknown and probably time dependent) fraction of concrete that is converted to aerosol. See Table 3.4 for SO. (Instead of using the MARCH output to calculate tabular values of SOURS(I), the results of the SANDIA experimental program on aerosol generation were used. The values of source rate versus time are shown in Table 3.9.

[c]The values of temperature and pressure versus time are shown in Table 3.9.

[d]Calculations were performed both with 40 values of temperature gradient versus time and with no temperature gradient. Values of this variable, when used, are listed in Table 3.9.

Table 3.7. HAARM-3 input from other sources: for the drywell

Variable definition	Variable		Note
	Name	Value	
Area of drywell floor/drywell volume, cm^{-1}	AFOV	2.48D-3	*a*
Density of aerosol material	RHO	3.0 D+0	*b*
Viscosity of air, poise (dyne s cm^{-2})	VISC	1.75D-4	*b*
Area of drywell vertical surface/drywell volume, cm^{-1}	AWOV	7.84D-3	*c*
Reference temperature, K	TEMP	3.91D+2	
Volume of drywell, cm^3	VOL	4.50D+9	*a*
Density of drywell gas, g cm^{-3}	RHOAIR	6.68D-4	*b*
Molecular weight of drywell atmosphere, g/mol	GASMW	2.13D+1	

[a] See Table 3.8

[b] From MARCH temperature plus standard thermodynamic calculations.

[c] This variable is the sum of vertical and horizontal down-facing areas divided by the drywell volume; that is, the sum of 2.68E-3 and 5.16E-3 from Table 3.8.

Table 3.8. Drywell areas and free volume: Browns Ferry-1

Surface	Units	Horizontal area		Vertical area	Total area
		Facing up	Facing down		
Internal surface of drywell liner, including concrete floor	m^2	631	711	430	1772
	ft^2	6791	7650	4634	19075
Reactor pedestal	m^2	5.4		552	558
	ft^2	58		5945	6003
Reactor vessel	m^2	37	76	448	561
	ft^2	400	818	4824	6042
CRD housings	m^2			302	302
	ft^2			3255	3255
Steam, feedwater, and recirculation pipes	m^2	159	159	405	723
	ft^2	1710	1710	4358	7778
Known totals	m^2	832	946	2138	3916
	ft^2	8959	10178	23016	42153
Allowances for unknown values for other piping, instrument lines, wiring, etc.	m^2	283	262	184	729
	ft^2	3041	2822	1984	7847
Total areas	m^2	1115	1208	2323	4645
	ft^2	12000	13000	25000	50000
Area/volume	cm^{-1}	2.48E-3	2.68E-3	5.16E-3	

The drywell free volume is 4500 m^3 (159,000 ft^3).

Table 3.9. Smoothed data obtained from MARCH output

Time since battery discharge (min)	Drywell temperature (K)	Reaction pressure (Pa)	Leak rate (m^3/s)	Concrete	
				Temperature (K)	Reaction rate (g concrete/s)
0.0	356.0	1.53E+05		356.0	
60.0	369.0	1.93E+05		369.0	
140.0	387.0	3.65E+05		387.0	
150.0	390.0	3.95E+05		390.0	
160.0	392.0	4.05E+05		392.0	
170.0	400.0	4.15E+05		400.0	
180.0	420.0	5.62E+05		420.0	
200.0	420.0	6.17E+05		420.0	
220.0	420.0	6.80E+05		420.0	
230.0	430.0	7.15E+05		430.0	
240.0	420.0	7.50E+05	1.0 E+00	1770.0	2.9 E+04
245.0	420.0	7.0 E+05	1.0 E+01	1770.0	3.3 E+04
250.0	420.0	2.0 E+05	1.0 E+02	1775.0	3.6 E+04
252.0	425.0	1.75E+05	3.5 E+02	1775.0	3.7 E+04
255.0	430.0	1.5 E+05	2.0 E+02	1775.0	3.9 E+04
260.0	450.0	1.31E+05	5.0 E+01	1780.0	4.1 E+04
265.0	600.0	1.20E+05	3.0 E+01	1780.0	4.3 E+04
270.0	800.0	1.12E+05	2.4 E+01	1785.0	4.5 E+04
280.0	845.0	1.02E+05	2.6 E+01	1790.0	4.8 E+04
290.0	840.0	1.01E+05	3.3 E+01	1790.0	4.9 E+04
300.0	835.0	1.01E+05	5.5 E+01	1790.0	5.0 E+04
310.0	830.0	1.01E+05	5.8 E+01	1795.0	4.95E+04
320.0	830.0	1.01E+05	5.2 E+01	1795.0	4.95E+04
330.0	840.0	1.01E+05	4.5 E+01	1800.0	4.9 E+04
340.0	870.0	1.01E+05	3.9 E+01	1800.0	4.9 E+04
360.0	1000.0	1.01E+05	3.1 E+01	1800.0	4.9 E+04
380.0	1100.0	1.01E+05	2.6 E+01	1800.0	4.9 E+04
400.0	1150.0	1.01E+05	2.6 E+01	1800.0	4.9 E+04
420.0	1200.0	1.01E+05	2.7 E+01	1800.0	4.8 E+04
440.0	1245.0	1.01E+05	2.8 E+01	1800.0	4.6 E+04
460.0	1280.0	1.01E+05	2.95E+01	1795.0	4.3 E+04
480.0	1310.0	1.01E+05	3.15E+01	1790.0	3.9 E+04
500.0	1340.0	1.01E+05	3.3 E+01	1785.0	3.2 E+04
520.0	1190.0	1.01E+05	1.9 E+01	1780.0	2.4 E+04
540.0	1130.0	1.01E+05	1.25E+01	1775.0	1.7 E+04
560.0	1125.0	1.01E+05	1.45E+01	1770.0	1.22E+04
580.0	1140.0	1.01E+05	2.4 E+01	1770.0	8.9 E+03
600.0	1170.0	1.01E+05	2.5 E+01	1770.0	6.5 E+03
620.0	1050.0	1.01E+05	3.8 E+00	1770.0	4.8 E+03
640.0	1020.0	1.01E+05	2.65E+00	1765.0	3.8 E+03
660.0	1000.0	1.01E+05	2.15E+00	1765.0	3.2 E+03
680.0	970.0	1.01E+05	1.8 E+00	1765.0	2.85E+03
700.0	940.0	1.01E+05	1.55E+00	1765.0	2.65E+03
720.0	920.0	1.01E+05	1.4 E+00	1765.0	2.5 E+03
740.0	900.0	1.01E+05	1.25E+00	1765.0	2.40E+03
760.0	880.0	1.01E+05	1.18E+00	1765.0	2.32E+03
810.0	848.0	1.01E+05	1.03E+00	1765.0	2.14E+03
850.0	842.0	1.01E+05	1.01E+00	1765.0	2.02E+03
860.0	840.0	1.01E+05	1.00E+00	1765.0	1.98E+03
900.0	810.0	1.01E+05	9.8 E-01	1765.0	1.86E+03

Table 3.10. Superficial velocities, aerosol concentrations, and aerosol generation rates immediately above corium within the 30 m² area of the biological shield

[Calculated from the data in Table 3.9 using Eqs. (3.14-3.20)]

Time (min)	Superficial velocity (m/s) from		Aerosol concentration		Aerosol generation rate		Total aerosol generated (grams)	Gas temperature gradient at wall (K/cm)
	Concrete reaction	Leak rate	grams/m³	Particles/cm³[a]	grams/s	Particles/cm³/s[a]		
240.0	2.66E-02	4.49E-03	7.42E-01	1.25E+07	1.00E-01	3.73E+02	0.00E+00	
245.0	3.24E-02	4.81E-02	9.70E-01	1.63E+07	1.40E+00	5.23E+03	2.25E+02	2.00E+01
250.0	1.24E-01	1.68E+00	9.81E+00	1.65E+08	4.95E+02	1.85E+06	7.48E+04	2.00E+01
252.0	1.47E-01	6.73E+00	3.70E+01	6.22E+08	7.48E+03	2.79E+07	5.53E+05	2.00E+01
255.0	1.83E-01	4.49E+00	2.49E+01	4.19E+08	3.36E+03	1.25E+07	1.53E+06	2.00E+01
260.0	2.30E-01	1.28E+00	7.90E+00	1.33E+08	3.04E+02	1.14E+06	2.08E+06	2.00E+01
265.0	3.52E-01	8.42E-01	5.44E+00	9.14E+07	1.37E+02	5.13E+05	2.14E+06	2.00E+01
270.0	5.26E-01	7.21E-01	4.91E+00	8.26E+07	1.06E+02	3.97E+05	2.18E+06	2.00E+01
280.0	6.51E-01	8.58E-01	5.87E+00	9.86E+07	1.51E+02	5.64E+05	2.26E+06	1.10E+02
290.0	6.67E-01	1.10E-00	7.29E+00	1.23E+08	2.41E+02	8.99E+05	2.38E+06	2.00E+02
300.0	6.76E-01	1.83E+00	1.16E+01	1.95E+08	6.39E+02	2.39E+06	2.64E+06	2.00E+02
310.0	6.66E-01	1.93E+00	1.26E+01	2.11E+08	7.29E+02	2.72E+06	3.05E+06	2.00E+02
320.0	6.66E-01	1.73E+00	1.14E+01	1.91E+08	5.91E+02	2.21E+06	3.45E+06	2.00E+02
330.0	6.67E-01	1.50E+00	1.02E+01	1.72E+08	4.61E+02	1.72E+06	3.76E+06	2.00E+02
340.0	6.91E-01	1.30E+00	8.99E+00	1.51E+08	3.50E+02	1.31E+06	4.00E+06	2.00E+02
360.0	7.94E-01	1.03E+00	7.32E+00	1.23E+08	2.27E+02	8.48E+05	4.35E+06	2.00E+02
380.0	8.73E-01	8.67E-01	6.28E+00	1.06E+08	1.63E+02	6.10E+05	4.58E+06	2.00E+02
400.0	9.13E-01	8.67E-01	6.28E+00	1.06E+08	1.63E+02	6.10E+05	4.78E+06	2.00E+02
420.0	9.33E-01	9.00E-01	6.49E+00	1.09E+08	1.75E+02	6.54E+05	4.98E+06	2.00E+02
440.0	9.28E-01	9.33E-01	6.69E+00	1.13E+08	1.87E+02	7.00E+05	5.20E+06	2.00E+02
460.0	8.92E-01	9.83E-01	6.80E+00	1.14E+08	2.01E+02	7.50E+05	5.43E+06	2.00E+02
480.0	8.28E-01	1.05E+00	7.00E+00	1.18E+08	2.20E+02	8.24E+05	5.69E+06	2.00E+02
500.0	6.95E-01	1.10E+00	7.08E+00	1.19E+08	2.34E+02	8.73E+05	5.96E+06	2.00E+02
520.0	4.63E-01	6.33E-01	4.28E+00	7.19E+07	8.13E+01	3.04E+05	6.15E+06	2.00E+02
540.0	3.11E-01	4.17E-01	2.99E+00	5.02E+07	3.73E+01	1.39E+05	6.22E+06	1.00E+02
560.0	2.22E-01	4.83E-01	3.25E+00	5.46E+07	4.71E+01	1.76E+05	6.27E+06	5.00E+01
580.0	1.64E-01	8.00E-01	4.90E+00	8.24E+07	1.18E+02	4.39E+05	6.37E+06	2.00E+01
600.0	1.23E-01	8.33E-01	5.08E+00	8.53E+07	1.27E+02	4.74E+05	6.52E+06	5.00E+00
620.0	8.16E-02	1.27E-02	1.38E+00	2.32E+07	5.25E+00	1.96E+04	6.59E+06	0.00E+00
640.0	6.28E-02	8.83E-02	1.15E+00	1.93E+07	3.03E+00	1.13E+04	6.60E+06	0.00E+00
660.0	5.18E-02	7.17E-02	1.06E+00	1.78E+07	2.28E+00	8.52E+03	6.60E+06	0.00E+00
680.0	4.48E-02	6.00E-02	1.00E+00	1.68E+07	1.80E+00	6.73E+03	6.61E+06	0.00E+00
700.0	4.04E-02	5.17E-02	9.59E-01	1.61E+07	1.49E+00	5.55E+03	6.61E+06	0.00E+00
720.0	3.73E-02	4.67E-02	9.34E-01	1.57E+07	1.31E+00	4.88E+03	6.61E+06	0.00E+00
740.0	3.50E-02	4.17E-02	9.09E-01	1.53E+07	1.14E+00	4.24E+03	6.61E+06	0.00E+00
760.0	3.31E-02	3.93E-02	8.97E-01	1.51E+07	1.06E+00	3.95E+03	6.61E+06	0.00E+00
810.0	2.94E-02	3.43E-02	8.71E-01	1.46E+07	8.97E-01	3.35E+03	6.61E+06	0.00E+00
850.0	2.76E-02	3.37E-02	8.68E-01	1.46E+07	8.77E-01	3.27E+03	6.62E+06	0.00E+00
860.0	2.69E-02	3.33E-02	8.66E-01	1.46E+07	8.66E-01	3.24E+03	6.62E+06	0.00E+00
900.0	2.44E-02	3.27E-02	8.63E-01	1.45E+07	8.46E-01	3.16E+03	6.62E+06	0.00E+00

[a] The geometric number mean radius = 1.000E-01 microns.
The geometric standard deviation = 1.800E+00.
The effective mass radius = 1.679E-01 microns.
The 50% mass radius, r50, = 2.819E-01 microns.

Table 3.11. A summary of HAARM3 results for the drywell reference case and reference case without thermophoresis

Source Particles					
Geometric mean radius, r_g (μm)		0.1			
Geometric standard deviation, σ_g		1.8			
Initial mass mean radius, r_{50} (μm)		0.2819			
Initial effective mass radius, r_p (μm)		0.1679			
300 minutes after battery failure					
		Reference case		Reference case without thermophoresis	
			Percent of total		Percent of total
Suspended aerosol concentration	(g/m^3)	1.07E+1		1.11E+1	
Suspended mass	(g)	4.80E+4	1.82	5.00E+4	1.89
Plated mass	(g)	2.84E+4	1.06	8.23E+3	0.311
Settled mass	(g)	2.03E+3	0.077	2.06E+3	0.078
Leaked mass	(g)	2.56E+6	97.05	2.58E+6	97.72
Total mass	(g)	2.64E+6	100.00	2.64E+6	100.00
800 minutes after battery failure					
Suspended aerosol concentration	(g/m^3)	7.05E-1		7.04E-1	
Suspended mass	(g)	3.17E+3	0.048	3.17E+3	0.048
Plated mass	(g)	3.19E+5	4.83	6.72E+4	1.02
Settled mass	(g)	1.33E+4	0.20	1.44E+4	0.216
Leaked mass	(g)	6.28E+6	94.92	6.53E+6	98.72
Total mass	(g)	6.61E+6	100.00	6.61E+6	100.00

Table 3.12. A summary of the effect of increased initial particle size for the drywell: with and without thermophoresis

Source Particles					
Geometric mean radius, r_g (μm)			0.89		
Geometric standard deviation, σ_g			2.29		
Initial mass mean radius, r_{50} (μm)			6.979		
Initial effective mass radius, r_p (μm)			2.492		
300 minutes after battery failure					
		With thermophoresis		Without thermophoresis	
			Percent of total		Percent of total
Suspended aerosol concentration	(g/m^3)	8.76E+0		8.80E+0	
Suspended mass	(g)	3.94E+4	1.49	3.96E+4	1.50
Plated mass	(g)	3.05E+4	0.115	3.01E+2	0.011
Settled mass	(g)	3.94E+5	14.94	3.95E+5	14.96
Leaked mass	(g)	2.20E+6	83.45	2.20E+6	83.52
Total mass	(g)	2.64E+6	100.00	2.64E+6	100.00
800 minutes after battery failure					
Suspended aerosol concentration	(g/m^3)	1.32E-1		1.32E-1	
Suspended mass	(g)	5.94E+2	0.009	5.94E+2	0.009
Plated mass	(g)	3.90E+4	0.590	2.25E+3	0.034
Settled mass	(g)	1.46E+6	22.06	1.47E+6	22.17
Leaked mass	(g)	5.12E+6	77.34	5.15E+6	77.79
Total mass	(g)	6.61E+6	100.00	6.61E+6	100.00

Table 3.13. Some properties of drywell gas from MARCH output and thermodynamic calculations

Time (min)	Temperature (K)	Pressure [Pa (atm)]	Component mole fractions						Viscosity (poise)	Density (g/cm^3)	Molecular weight (g/mole)
			N_2	O_2	H_2	CO	CO_2	H_2O			
0	356	1.57D+05 (1.55)	0.540	0.143	0.000	0.000	0.000	0.317	1.79D-04	1.35D-03	25.42
20	357	1.65D+05 (1.63)	0.516	0.137	0.000	0.000	0.000	0.347	1.77D-04	1.39D-03	25.10
40	364	1.84D+05 (1.82)	0.470	0.125	0.000	0.000	0.000	0.405	1.75D-04	1.49D-03	24.47
60	369	1.99D+05 (1.97)	0.440	0.117	0.000	0.000	0.000	0.443	1.73D-04	1.57D-03	24.06
80	373	2.14D+05 (2.11)	0.414	0.110	0.000	0.000	0.000	0.475	1.72D-04	1.64D-03	23.70
100	376	2.27D+05 (2.23)	0.396	0.105	0.000	0.000	0.000	0.498	1.71D-04	1.70D-03	23.46
120	379	2.55D+05 (2.52)	0.391	0.104	0.006	0.000	0.000	0.499	1.72D-04	1.90D-03	23.30
140	390	3.67D+05 (3.62)	0.360	0.096	0.072	0.000	0.000	0.472	1.76D-04	2.48D-03	21.81
142	390	3.90D+05 (3.85)	0.351	0.093	0.087	0.000	0.000	0.470	1.75D-04	2.59D-03	21.44
144	390	3.94D+05 (3.89)	0.349	0.093	0.089	0.000	0.000	0.469	1.75D-04	2.61D-03	21.38
146	390	3.94D+05 (3.89)	0.349	0.093	0.090	0.000	0.000	0.468	1.75D-04	2.61D-03	21.37
148	390	3.95D+05 (3.90)	0.350	0.093	0.091	0.000	0.000	0.466	1.75D-04	2.62D-03	21.35
150	391	3.97D+05 (3.92)	0.349	0.093	0.092	0.000	0.000	0.467	1.75D-04	2.63D-03	21.32
152	391	3.99D+05 (3.94)	0.348	0.093	0.094	0.000	0.000	0.465	1.75D-04	2.64D-03	21.30
154	391	4.01D+05 (3.96)	0.347	0.092	0.095	0.000	0.000	0.466	1.75D-04	2.65D-03	21.27
156	391	4.04D+05 (3.98)	0.346	0.092	0.095	0.000	0.000	0.466	1.75D-04	2.66D-03	21.24
158	391	4.05D+05 (4.00)	0.346	0.092	0.096	0.000	0.000	0.466	1.75D-04	2.66D-03	21.22
160	391	4.07D+05 (4.01)	0.346	0.092	0.097	0.000	0.000	0.465	1.75D-04	2.67D-03	21.20
162	391	4.08D+05 (4.03)	0.345	0.092	0.098	0.000	0.000	0.465	1.75D-04	2.68D-03	21.18
164	395	4.11D+05 (4.06)	0.346	0.092	0.098	0.000	0.000	0.464	1.77D-04	2.67D-03	21.19
166	391	4.11D+05 (4.06)	0.344	0.091	0.100	0.000	0.000	0.465	1.76D-04	2.69D-03	21.14
168	392	4.12D+05 (4.07)	0.344	0.091	0.100	0.000	0.000	0.465	1.76D-04	2.69D-03	21.13
170	394	4.14D+05 (4.08)	0.344	0.092	0.101	0.000	0.000	0.463	1.77D-04	2.69D-03	21.13
172	394	4.15D+05 (4.10)	0.344	0.091	0.101	0.000	0.000	0.464	1.77D-04	2.69D-03	21.12
174	424	5.44D+05 (5.37)	0.051	0.014	0.019	0.000	0.000	0.916	1.51D-04	2.91D-03	18.42
174	425	5.52D+05 (5.46)	0.054	0.014	0.022	0.000	0.000	0.909	1.52D-04	2.94D-03	18.41
183	425	5.73D+05 (5.66)	0.044	0.012	0.020	0.000	0.039	0.885	1.54D-04	3.21D-03	19.31
209	426	6.29D+05 (6.20)	0.026	0.007	0.026	0.020	0.097	0.824	1.60D-04	3.76D-03	20.67
231	430	7.17D+05 (7.08)	0.011	0.003	0.044	0.058	0.072	0.812	1.61D-04	4.10D-03	19.92
251	420	1.81D+05 (1.79)	0.044	0.012	0.053	0.021	0.022	0.849	1.53D-04	9.68D-04	18.54
281	842	1.01D+05 (1.00)	0.000	0.000	0.273	0.408	0.098	0.221	3.41D-04	2.93D-04	20.27
314	827	1.01D+05 (1.00)	0.000	0.000	0.146	0.219	0.038	0.596	3.17D-04	2.78D-04	18.86
348	921	1.01D+05 (1.00)	0.000	0.000	0.268	0.401	0.053	0.278	3.61D-04	2.53D-04	19.13
379	1099	1.01D+05 (1.00)	0.000	0.000	0.357	0.535	0.055	0.052	4.17D-04	2.12D-04	19.09
408	1176	1.01D+05 (1.00)	0.000	0.000	0.364	0.545	0.043	0.048	4.35D-04	1.95D-04	18.77
430	1231	1.01D+05 (1.00)	0.000	0.000	0.370	0.555	0.034	0.041	4.48D-04	1.83D-04	18.52
456	1270	1.01D+05 (1.00)	0.000	0.000	0.377	0.565	0.024	0.034	4.58D-04	1.75D-04	18.26
478	1307	1.01D+05 (1.00)	0.000	0.000	0.379	0.567	0.020	0.035	4.66D-04	1.69D-04	18.14
499	1340	1.01D+05 (1.00)	0.000	0.000	0.377	0.565	0.023	0.035	4.74D-04	1.66D-04	18.22
521	1190	1.01D+05 (1.00)	0.000	0.000	0.386	0.579	0.003	0.032	4.37D-04	1.81D-04	17.70
546	1125	1.01D+05 (1.00)	0.000	0.000	0.281	0.421	0.000	0.298	4.18D-04	1.92D-04	17.73
572	1130	1.01D+05 (1.00)	0.000	0.000	0.129	0.193	0.000	0.678	4.13D-04	1.93D-04	17.88
600	1170	1.01D+05 (1.00)	0.000	0.000	0.097	0.145	0.000	0.758	4.26D-04	1.87D-04	17.92
623	1048	1.01D+05 (1.00)	0.200	0.046	0.067	0.100	0.197	0.390	4.05D-04	2.99D-04	25.71
657	1002	1.01D+05 (1.00)	0.083	0.019	0.028	0.042	0.402	0.425	3.90D-04	3.59D-04	29.55
690	956	1.01D+05 (1.00)	0.039	0.009	0.013	0.019	0.477	0.443	3.74D-04	3.94D-04	30.92
724	920	1.01D+05 (1.00)	0.020	0.005	0.007	0.010	0.506	0.454	3.62D-04	4.16D-04	31.42
757	890	1.01D+05 (1.00)	0.010	0.002	0.003	0.005	0.518	0.461	3.52D-04	4.33D-04	31.61

Table 3.14. Particle size parameters and volumes of gas leaking from the drywell into the reactor building

Time since battery discharge (min)	Aerosol concentration (g/m^3)	Mass mean radius, r_{so} (μm)	Geometric standard deviation (σg)	Effective radius, rp (μm)	Integrated discharge from drywell to reactor building		Rate of aerosol entry to building [particles/(cm^3.s)]
					Aerosol (g)	Gas (m^3)	
245.013	8.28E-02	0.2999	1.7488	0.1877	7.06E+02	9.90E+02	1.69E+02
245.690	3.78E-01	0.2859	1.7882	0.1723	8.41E+02	1.26E+03	1.37E+03
247.088	2.12E+00	0.2949	1.7609	0.1824	4.61E+03	2.36E+03	1.23E+04
250.050	4.75E+00	0.3148	1.7139	0.2037	5.57E+04	7.75E+03	8.10E+04
250.339	6.61E+00	0.3085	1.7299	0.1966	6.76E+04	9.04E+03	1.74E+05
251.038	1.46E+01	0.3182	1.7057	0.2075	1.53E+05	1.42E+04	5.38E+05
252.034	2.07E+01	0.3229	1.7003	0.2116	4.75E+05	2.47E+04	1.03E+06
252.314	2.10E+01	0.3246	1.6968	0.2134	5.95E+05	2.77E+04	1.04E+06
253.013	2.06E+01	0.3276	1.6925	0.2162	8.72E+05	3.49E+04	9.47E+05
254.131	1.91E+01	0.3318	1.6862	0.2204	1.23E+06	4.43E+04	6.71E+05
256.752	1.59E+01	0.3418	1.6736	0.2296	1.75E+06	5.72E+04	2.34E+05
260.143	1.03E+01	0.3775	1.6317	0.2635	2.03E+06	6.43E+04	3.63E+04
262.275	6.98E+00	0.3759	1.6556	0.2567	2.08E+06	6.65E+04	1.76E+04
269.825	4.59E+00	0.3881	1.6419	0.2684	2.15E+06	7.26E+04	7.66E+03
270.943	4.52E+00	0.3892	1.6435	0.2688	2.16E+06	7.34E+04	7.36E+03
274.299	4.64E+00	0.3883	1.6473	0.2672	2.18E+06	7.57E+04	7.57E+03
288.140	6.29E+00	0.3929	1.6459	0.2707	2.31E+06	8.72E+04	1.31E+04
296.179	9.21E+00	0.3913	1.6449	0.2699	2.44E+06	9.69E+04	2.96E+04
301.282	1.10E+01	0.3944	1.6450	0.2720	2.61E+06	1.05E+05	4.12E+04
309.391	1.19E+01	0.3974	1.6464	0.2737	2.92E+06	1.19E+05	4.52E+04
310.579	1.20E+01	0.3979	1.6459	0.2742	2.97E+06	1.21E+05	4.50E+04
312.607	1.19E+01	0.3993	1.6460	0.2751	3.06E+06	1.25E+05	4.36E+04
316.521	1.14E+01	0.4001	1.6466	0.2755	3.21E+06	1.31E+05	4.01E+04
327.427	1.02E+01	0.4018	1.6464	0.2768	3.56E+06	1.48E+05	3.02E+04
343.085	8.36E+00	0.4056	1.6462	0.2794	3.93E+06	1.67E+05	1.93E+04

Table 3.14. (Continued)

Time since battery discharge (min)	Aerosol concentration (g/m^3)	Mass mean radius, r_{s0} (μm)	Geometric standard deviation (σg)	Effective radius, rp (μm)	Integrated discharge from drywell to reactor building		Rate of aerosol entry to building [particles/(cm^3.s)]
					Aerosol (g)	Gas (m^3)	
361.121	6.83E+00	0.4126	1.6459	0.2843	4.21E+06	1.85E+05	1.22E+04
376.640	5.98E+00	0.4161	1.6452	0.2869	4.38E+06	1.98E+05	9.02E+03
404.602	5.64E+00	0.4168	1.6450	0.2874	4.63E+06	2.20E+05	8.35E+03
413.550	5.73E+00	0.4179	1.6449	0.2882	4.71E+06	2.27E+05	8.55E+03
435.080	5.94E+00	0.4206	1.6450	0.2901	4.92E+06	2.45E+05	9.06E+03
459.128	6.11E+00	0.4217	1.6452	0.2908	5.17E+06	2.65E+05	9.82E+03
486.530	6.36E+00	0.4215	1.6448	0.2908	5.48E+06	2.91E+05	1.14E+04
500.372	6.42E+00	0.4216	1.6443	0.2909	5.66E+06	3.05E+05	1.15E+04
501.909	6.37E+00	0.4228	1.6435	0.2920	5.67E+06	3.06E+05	1.10E+04
504.845	6.17E+00	0.4246	1.6443	0.2930	5.71E+06	3.09E+05	9.93E+03
515.331	5.01E+00	0.4275	1.6464	0.2945	5.80E+06	3.17E+05	5.92E+03
525.957	3.68E+00	0.4221	1.6497	0.2899	5.85E+06	3.22E+05	3.30E+03
540.218	2.92E+00	0.4253	1.6442	0.2935	5.90E+06	3.28E+05	1.94E+03
547.627	2.76E+00	0.4169	1.6509	0.2860	5.91E+06	3.31E+05	1.95E+03
558.812	2.90E+00	0.4122	1.6455	0.2841	5.94E+06	3.35E+05	2.40E+03
565.104	3.23E+00	0.4068	1.6471	0.2800	5.95E+06	3.39E+05	3.3EE+03
578.525	4.43E+00	0.4097	1.6433	0.2830	6.02E+06	3.47E+05	6.14E+03
591.258	4.83E+00	0.4156	1.6442	0.2868	6.11E+06	3.57E+05	7.28E+03
601.035	4.92E+00	0.4181	1.6432	0.2888	6.18E+06	3.64E+05	6.61E+03
608.864	4.72E+00	0.4370	1.6394	0.3029	6.22E+06	3.69E+05	3.61E+03
620.888	3.68E+00	0.5259	1.5838	0.3830	6.25E+06	3.71E+05	3.05E+02
630.535	2.72E+00	0.5506	1.6289	0.3852	6.26E+06	3.72E+05	1.23E+02
664.089	1.44E+00	0.5403	1.6911	0.3571	6.27E+06	3.74E+05	8.75E+01
745.738	8.12E-01	0.4901	1.6767	0.3283	6.27E+06	3.77E+05	3.77E+01
868.771	6.41E-01	0.4600	1.6565	0.3139	6.28E+06	3.81E+05	2.76E+01

Table 3.15. HAARM-3 input from accident specifications and output from drywell calculations: aerosol transport in the reactor building for station blackout at Browns Ferry-1

Variable definition	Variable		Note
	Name	Value	
Settling terms (1 = yes/0 = no)	ISETL	1	
Plating terms (1 = yes/0 = no)	IPLAT	1	
Leakage terms (1 = yes/0 = no)	ILEAK	1	
Agglomeration, Brownian (1 = yes/0 = no)	IAGGB	1	
Agglomeration, gravity (1 = yes/0 = no)	IAGGG	1	
Agglomeration, turbulent (1 = yes/0 = no)	IAGGT	0	
Source terms (1 = yes/0 = no)	ISORS	1	
Number of discrete volumes for distribution calculations	IVOL	0	
Source rate conversion factor	SO	1.0	*a*
Source geometric standard deviation, μm	SIGSOR	1.65	*b*
Source mass median radius, μm	RSOR	0.40	*b*
Initial concentration of aerosol, particles cm^{-3}	XIN(1)	0.0	
Aerosol sigma (size of initial particles), μm	SIGAIR	1.65	*c*
Aerosol 50% (mass median) radius, μm	RAIR	0.40	*c*
Initial time, s	TO	0.0	
Source cutoff time, s	TAUIN	5.20D+4	
Maximum time, s	TMAXIN	7.20E+4	
Leakage rate, s^{-1}	RVL	0.0	

[a] This factor is required to convert source-rate values to units of particles/(cm^3 s). The HAARM-3 run of the reference case of Sect. 3.3 provides values of the rate of leakage of aerosol, from the drywell into the reactor building and the aerosol concentration as a function of time, as shown in Table 3.14.

[b] These approximate averages from calculations concerning the drywell are actually not used. Instead, we use the HAARM-3 option of time-dependent particle size parameters. See Tables 3.14 and 3.17.

[c] Not used.

Table 3.16. HAARM-3 input suggested in Users Manual: adapted for transport in the reactor building for station blackout at Browns Ferry-1

Variable definition	Variable	
	Name	Value
Method of integration (2 = Adams - Moulton with fixed incrementing) (1 = Runge - Kutta with fixed incrementing) (0 = Adams - Moulton with variable incrementing)	INDIN	0
Maximum number of times steps (<1000)	KMAX	1000
Increment for time index for output	ISEQ	10
Time step, initial, s	HIN	1.00D-6
Convergence criterion	TOLIN	1.00D-3
Diffusion boundary layer thickness, cm	DELTA	1.00D-4
Shutoff value for ratio agglomeration rate/ settling rate	EPSN	0.0
Shutoff value for ratio airborne mass concentration/ initial airborne mass concentration	EPSM	0.0
Shutoff value for ratio particulate volume/maximum particulate volume	EPSL	1.00D-6
Diffusion boundary layer thickness in plating equation, cm	DELTA1	1.00D-4
Density modification factor	ALPHA	1.0
Klyachko terminal settling velocity calculation (1 = yes/0 = no)	KLYACH	0
Collision efficiency for gravitational agglomeration	EFF	1.0
Dynamic shape factor	CHI	1.0
Time-varying alpha (1 = yes/0 = no)	IALVAR	1
Collision shape factor	GAMMA	1.0
Attenuation (1 = yes/0 = no)	LAMSIG	1
Variable alpha (1 = yes/0 = no)	IEFF	1
Temperature gradient at wall (no thermal plating if 0)	TGRADW	0.0
Thermal conductivity ratio (gas/aerosol)	TCR	1.0 D-3
Mixture effects (1 = yes/0 = no)	IMIX	0

NOTE: Calculations were performed only without thermophoresis, as described in the text.

Table 3.17. HAARM-3 input data from HAARM-3 calculations: for the reactor building from drywell calculations of Sect. 3.3 for station blackout at Browns Ferry-1

Variable definition	Variable		Note
	Name	Value	
Number of values in table of leak rate versus time	NLEEK	40	
Leak rate, s^{-1}	RLEK(I)		*a*
Time, s	TLEK(I)		*a*
Number of values in table of source rate versus time	NSOUR	777	*b*
Number of values in table of source rate versus time	M1	50	*c*
Time, s	TSN(I)	50	*c*
Source rate, particles cm^{-3} s^{-1}	SN(I)	50	*c*
Source geometric standard deviation	SSIG(I)	50	*c*
Source mass median radius, μm	SRG(I)	50	*c*
Number of values in table of leakage-gas temperature and pressure versus time	NTP	50	
Temperature of leakage gas, K	TEMPT(I)		*d*
Pressure in reactor building, dyne cm^{-2}	P(I)		*d*
Time, s	TPT(I)		*d*

[a] The values of leak rate versus time are listed in Table 3.9.

[b] The value NSOUR = 777 is an indicator to the HAARM-3 program that input will include a table of source rate, particle size standard deviation, and mass mean radius [SN(I), SSIG(I), and SRG(I)] versus time [TSN(I)]. The actual number of entries in this table is given by N1.

[c] Values of SN(I), SSIG(I), and SRG(I) versus time are obtained from HAARM-3 output for the drywell, Sect. 3.3.

[d] Values of temperature versus time are shown in Table 3.9. Building pressures were set to 1.01E+6 dynes/cm^2 for all times.

Table 3.18. HAARM-3 input from other sources: for the reactor building

Variable definition	Variable Name	Variable Value	Note
Area of building floor/building volume, cm^{-1}	AFOV	2.32D-3	*a*
Density of aerosol material	RHO	3.0 D+0	*b*
Viscosity of air, poise (dyne s cm^{-2})	VISC	1.75D-4	*c*
Area of building vertical surface/building volume, cm^{-1}	AWOV	2.66D-3	*b*
Volume of building, cm^3	VOL	5.93D+10	*a*
Density of building gas, g cm^{-3}	RHOAIR	6.68E-4	*c*
Molecular weight of building atmosphere, g/mole	GASMW	21.30	*c*

[a] From Table 5.18 of this report, the total building area, A, is 29,480 m^2 and the total volume, V, is 59,283 m^3. These are equivalent to a square room of 117.17 m length and width and 4.318 m height.

[b] This is an assumed value.

[c] This is an assumed value, taken from the 152-min data of Table 3.13. However, not the variations of gas properties in this table.

Table 3.19. A summary of HAARM-3 calculations for the reactor building

		Percent of total
Approximate size parameter of particles entering from drywell[a]		
Geometric mean radius, r_g (μm)	0.19	
Geometric standard deviation, σ_g	1.65	
Initial mass mean radius, r_{s0} (μm)	0.40	
Initial effective mass radius, r_p (μm)	0.27	
300 minutes after battery failure		
Suspended aerosol concentration, (g/m^3)	8.86	
Suspended mass, (g)	5.25E+5	19.21
Plated mass, (g)	1.73E+4	0.63
Settled mass, (g)	6.51E+4	2.38
Leaked mass, (g)	2.13E+6	77.78
Total mass, (g)	2.73E+6	100.00
800 minutes after battery failure		
Suspended aerosol concentration, (g/m^3)	2.20	
Suspended mass, (g)	1.31E+5	2.02
Plated mass (g)	9.79E+4	1.55
Settled mass, (g)	3.92E+5	6.05
Leaked mass, (g)	5.86E+6	90.42
Total mass, (g)	6.48E+6	100.00

[a] As noted previously, the calculations were based on a table of time-dependent radii and standard deviation.

References for Section 3

3.1a. "Fission Product Release from Fuel," pp. 4.1-4.32 in *Technical Bases for Estimating Fission Product Behavior During LWR Accidents*, Chapter 4, NUREG-0772 (June 1981).

3.1b. R. H. Chapman, *Multirod Burst Test Program Progress Report for April-June 1979*, NUREG/CR -1023 (ORNL/NUREG/TM-351) (November 1979).

3.2. R. A. Lorenz, J. L. Collins, and S. R. Manning, *Fission Product Release from Simulated LWR Fuel*, NUREG/CR-0274 (ORNL/NUREG/TM-154) (October 1978).

3.3. R. A. Lorenz, J. L. Collins, A. P. Malinauskas, O. L. Kirkland, and R. L. Towns, *Fission Product Release from Highly Irradiated Fuel*, NUREG/CR-0722 (ORNL/NUREG/TM-287R2) (February 1980).

3.4. A. P. Malinauskas, R. A. Lorenz, and J. L. Collins, "Fission Product Release During LWR Loss-of-Coolant Accidents," *Trans. Am. Nucl. Soc.* 32: 651 (June 1979).

3.5. R. A. Lorenz, J. L. Collins, and A. P. Malinauskas, *Fission Product Source Terms for the LWR Loss-of-Coolant Accident*, NUREG/CR-1288 (ORNL/NUREG/TM-321) (July 1980).

3.6. R. A. Lorenz, J. L. Collins, and A. P. Malinauskas, "Fission Product Source Terms for the Light Water Reactor Loss-of-Coolant Accident," *Nucl. Technol.* 46(3): 404-10 (December 1979).

3.7. R. A. Lorenz, "ANS-5.4 Fission Gas Release Model, III. Low Temperature Release," pp. 336-45 in *Proceedings of the ANS Topical Meeting on Light Water Reactor Fuel Performance*, CONF-790441-8, 1979.

3.8. R. A. Lorenz, J. L. Collins, M. F. Osborne, and A. P. Malinauskas, "Fission Product Release from LWR Fuel Defected in Steam in the Temperature Range 500 to 1600°C," pp. 167-70 in *Proceedings of the Specialists' Meeting on the Behaviour of Defected Zirconium Alloy Clad Ceramic Fuel in Water Cooled Reactors*, CONF-790935-3, 1979.

3.9. R. A. Lorenz, J. L. Collins, M. F. Osborne, and A. P. Malinauskas, "Fission Product Release from High Gap-Inventory LWR Fuel Under LOCA Conditions," *Trans. Am. Nucl. Soc.* 34: 462-63 (1980).

3.10. R. A. Lorenz, J. L. Collins, M. F. Osborne, R. L. Towns, and A. P. Malinauskas, *Fission Product Release from BWR Fuel Under LOCA Conditions*, NUREG/CR-1773 (ORNL/NUREG/TM-388) (July 1981).

3.10a. R. A. Lorenz, D. O. Hobson, and G. W. Parker. "Fuel Rod Failure Under Loss-of Coolant Conditions in TREAT," *Nucl. Technol.* 11: 502-20 (August 1971).

3.11. D. L. Acey and J. C. Volglewede, *A Comparative Analysis of LWR Fuel Designs*, NUREG-0559 (July 1980).

3.12. R. A. Lorenz and G. W. Parker, "Calculation of Amount of Radioactivity in Fuel Rod Void Spaces," in *Nuclear Safety Program Annual Progress Report for Period Ending December 31, 1967*, ORNL-4228 (April 1968).

3.13. L. D. Noble, "ANS-5.4 Fission Gas Release Model, I. Noble Gases at High Temperature," pp. 321-27 in *Proceedings of the ANS Topical Meeting on Light Water Reactor Fuel Performance*, CONF 790441-8, 1979.

3.14. Technical Bases for Estimating Fission Product Behavior During LWR Accidents, NUREG-0772 (June 1981).

3.15. R. A. Lorenz, J. L. Collins, A. P. Malinauskas, M. F. Osborne, and R. L. Towns, *Fission Product Release from Highly Irradiated Fuel Heated to 1300-1600°C in Steam*, NUREG/CR-1286 (ORNL/NUREG/TM-346) (in preparation).

3.16. G. W. Parker et al., *Out-of-Pile Studies of Fission Product Release from Overheated Reactor Fuels at ORNL, 1955-1965*, ORNL-3981 (August 1967).

3.17. H. Albrecht, V. Matschoss, and H. Wild, "Experimental Investigation of Fission and Activation Product Release from LWR Fuel Rods at Temperatures Ranging from 1500-2800°C," *Proceedings of the Specialists' Meeting on the Behavior of Defected Zirconium Alloy Clad Ceramic Fuel in Water Cooled Reactors*, CONF-790935-3 (September 1979).

3.18. H. Albrecht and H. Wild, "Investigation of Fission Product Release by Annealing and Melting of LWR Fuel Pins in Air and Steam," *Proceedings of the topical Meeting on Reactor Safety Aspects of Fuel Behavior*, Aug. 2-6, 1981, Sun Valley, Idaho (to be published).

3.19. D. A. Powers, "Molten Core/Concrete Interaction Experimental Program," in *Light Water Reactor Safety Research Program Quarterly Report, July-September 1979*, vol. 13, NUREG/CR-1177 (SAND79-2290) (September 1980).

3.20. E. Sowa and J. Pavlik, "The Interaction of High Temperature Core Debris with Concrete and Refractory Material," *Nucl. Technol.* 54: 234 (August 1981).

3.21. A. G. Croff, *ORIGEN2 - A Revised and Updated Version of the Oak Ridge Isotope Generation and Depletion Code*, ORNL-5621 (July 1980).

3.22. J. H. Goode, R. G. Stacy, and V. C. A. Vaughen, *Comparison Studies of Head-end Reprocessing Using Three LWR Fuels*, ORNL/TM-7103 (June 1980).

3.23. J. A. Gieseke, K. W. Lee and L. D. Reed, *"HAARM-3 Users Manual,"* Battelle Columbus Laboratories, Columbus, OH, BMI-NUREG-1991, 1978.

3.24. G. Herdan, *Small Particle Statistics*, Elsevier.

3.25. G. Creek, Personal Communication, August 1981.

3.26. M. Berman, *"Light Water Reactor Safety Research Program Quarterly Report, July-September 1979*, Vol. 13," NUREG/CR-1177 (SAND79-2290), Sandia National Laboratories, 1979.

3.27. D. A. Powers, *Containment Safety Studies*, Appendix 5A, Empirical Description of the Rate of Aerosol Generation During Melt/Concrete Interactions, in Report of the Zion/Indian Point Study: Vol. 1, prepared by W. B. Murfin, Sandia Laboratories, NUREG/CR-1410 (SAND80-0617/1), August 1980.

3.28. C. Orr, Jr., and E. Y. H. King, "Sampling and Particle-Size Measurements," Chapter 5, pp. 93-114 in *Handbook on Aerosols*, R. Dennis, editor. Technical Information Center, U.S. Department of Energy, 1976 (TID-26608).

3.29. G. C. Lindauer and A. W. Castelman, Jr., "Initial Size Distribution of Aerosols," *Nucl. Sci. Eng.* 43, 212 (1971).

3.30. R. O. Wooton and H. I. Avci, *MARCH Code Description and User's Manual*, Battelle Columbus Laboratories, USNRC Report NUREG/CR-1711 (October 1980).

3.31. J. A. Gieseke, Battelle Columbus Laboratories, Personal Communication (April 1982).

4. TRANSPORT RATE ASSUMPTIONS

4.1 Noble Gas Solubility

Noble gases are set apart from the other elements by their relative inability to react chemically. However, the noble gases do interact with their environment and can be trapped in solutions and on surfaces. This transport calculation considers noble gases to be soluble in the wetwell water. The halogen precursors, which contribute to the noble gas radioactivity, are treated in a superficial manner for this calculation.

Noble gases dissolve in water to some extent. Experiments have been performed to measure this solubility for krypton and xenon.[4.1-4.3] The experimentally determined solubility can be expressed by

$$\log_{10} (S_{kr}) = -60.434 + 3410/T + 20.5 \log_{10} (T) \quad (4.1)$$

and

$$\log_{10} (S_{Xe}) = -60.836 + 3605/T + 20.5 \log_{10} (T) \quad (4.2)$$

where

S_{Kr} = krypton solubility (mL gas/1000 g H_2O)

S_{Xe} = xenon solubility (mL gas/1000 g H_2O)

T = temperature (°K)

Equations (4.1) and (4.2) are based upon data in the temperature range from 10 to 75°C, and therefore must be extrapolated for use with suppression pool temperaures which range up to 116°C. In addition, these equations presume 1 atmosphere partial pressure of gas in equilibrium with the liquid. Thus, assuming a Henry's Law relationship,[4.4] the concentrations of Kr and Xe in the suppression pool are obtained from the values determined in Eqs. (4.1) and (4.2) multiplied by the partial pressure of Kr or Xe in the gas phase. The following liquid to gas phase concentration ratios are thereby obtained for Kr and Xe:

Water Temperature (°C)	Ratio liquid qas concentration from Eqs. (4.1) and (4.2)	
	Kr	Xe
100	0.0352	0.0465
116	0.0365	0.0459

The total quantity of Kr and Xe in the wetwell must be taken into account when one apportions these noble gases between the water and the airspace in accordance with Eqs. (4.1) and (4.2). The following sources are summed to determine the total wetwell inventory: (1) inventories in water and airspace from the previous timestep, (2) decay from iodine in the suppression pool and airspace during the timestep, and (3) Kr and Xe entering the wetwell with either downcomer or T-quencher flows.

4.2 Molecular Forms of Iodine

Iodine can exist in a variety of chemical forms, depending on the temperature, pressure, chemical environment, and total concentration, each of which has a different tendency for chemisorption, condensation, and dissolution in water. Ideally, therefore, the mixture of iodine chemical species should be determined along the leakage pathway from the fuel to the outside air or water in order to properly evaluate deposition rates at each control volume along the pathway.

In some cases, the iodine species mixture can be so determined, provided the ambient conditions are known. For example, in the gas phase above about 700°C, equilibrium thermodynamics can provide this information with some confidence. However, the results depend on proper specification of ambient conditions, most importantly, the amount of gaseous cesium available locally for chemical combination. If these conditions are known, the reaction kinetics are sufficiently rapid so that equilibrium thermodynamics results can be expected to yield a realistic estimate of the iodine species mixture in the gas phase above about 700°C.

Realistic determination of the iodine species mixture for other conditions are more difficult. Below 700°C in the gas phase, reaction kinetics becomes a progressively more significant factor, and hence equilibrium results are progressively less meaningful. Since kinetic data for this case is limited, we will assume the species mixture to be 'frozen' at the 700°C equilibrium condition as the gaseous flow proceeds along the pathway to lower temperatures.

There are similar difficulties in the liquid phase caused by inadequate kinetic data. Here the equilibrium mixtures are fairly well known and there are some kinetic data. However, the rates of oxidation and reduction are only poorly known for iodine species in water. For the present, the following assumptions seem most appropriate for determining iodine species in water:

1. We will assume the first step of the hydrolysis reaction to be rapid; i.e., the conversion of dissolved I_2 to I^- and HOI(d).
2. The second phase of this reaction, the disproportionation of HOI to I^- and IO_3^- appears to be slow relative to the time scale of events (seconds) and hence will be neglected initially.
3. Redox reactions also appear to be slow. (These, for example, could involve the oxidation of I^- to I_2 and subsequently IO_3^- by oxygen in the suppression pool.) Thus, redox reactions in water will be neglected in this study.

The dominant molecular form of iodine on release from overheated fuel has been the subject of some recent discussion, and is presently an issue which remains uncertain. However, in the approach taken here, we circumvent this uncertainty by assuming that the gaseous discharge from the fuel

quickly comes to a gas phase chemical equilibrium in the immediate vicinity of the fuel. Thus, the particular species mixture on evolution and the chemical forms within the pellet are not relevant to this approach.

Nevertheless, a short discussion of iodine release from fuel is provided for general interest. The species mixture on evolving from fuel probably varies with temperature. Iodine evolved below ~1400°C, which amounts to about 5% of the total inventory for BWRs (apparently less than this for PWRs), appears to be predominantly CsI. This quantity of iodine is believed to evolve from the UO_2 grains perhaps during reactor operation and deposit in open pores and the cladding surface as CsI. Hence, on cladding rupture and overheating, it vaporizes as CsI. At higher temperatures (>1400°C), the survival of the CsI molecule becomes progressively less likely and the dominant chemical form most likely becomes atomic I. This is not only due to temperature-induced loss of stability of CsI, but also to the more agressive phenomena involved in the release mechanism at these elevated temperatures. Above ~1400°C, instead of simply vaporizing a surface deposit, iodine is released from the fuel via diffusion through UO_2 grains and as a result of grain boundary motion. These more aggressive conditions make it probable that as maximal temperatures of unmelted fuel are approached (at ~2200°C), the released iodine form is predominately atomic I.

4.2.1 Iodine species distribution in the gas phase

Above ~700°C chemical equilibration of all gaseous components occurs rapidly and chemical thermodynamics can be used as a reliable tool for predicting compositions, provided, of course, that the ambient conditions are known. Such rather exhaustive chemical thermodynamic analyses have been performed by R. Sallach and R. Elrick[4,6], the results of which will be used here.

Sallach and Elrich computed equilibrium compositions of 23 chemical species, including four iodine species - CsI, I, I_2, and HI - from 700°C to 2400°C, for two total pressures (1 and 150 bars), for a range of iodine and hydrogen concentrations. For all cases, it was assumed that Cs was available in great excess for formation of CsI. Equilibrium compositions were computed by FLUQUE, which is a chemcial potential minimization code, for a range of conditions involving the following 23 chemical compounds of Cs, I, Te, H, and O:

Elements	Vapor species
Cesium (Cs)	CsI, CsOH, $(CsOH)_2$, Cs_2O, CsO, Cs, Cs_2
Iodine (I)	CsI, I, I_2, HI
Tellurium (Te)	Te_2, Te, TeO, TeO_2, Te_2O_2, H_2Te
Hydrogen (H)	CsOH, $(CsOH)_2$, HI, HO, H, H_2O_2, HO_2, H_2, H_2Te
Oxygen (O)	CsOH, $(CsOH)_2$, CsO_2, CsO, HO, O, H_2O_2, HO_2, H_2O, O_2, TeO, TeO_2, Te_2O_2

Some typical results are illustrated in Fig. 4.1 for an I/H_2O molar ratio of 2×10^{-5} and a large Cs excess (Cs/I = 10). We note here that

CsI is the dominant iodine species at lower temperatures. However, the degree of CsI stability with increasing temperature is sensitive to the I/H_2O ratio (increasing with increasing I/H_2O), and the total pressure (increasing with increasing pressure) as well as the H/O ratio and the degree of excess Cs. Fortunately, the dependence on H/O ratio is not great when hydrogen exists in excess; i.e., $H/O > 2$. Therefore, we will simplify the present estimates by recognizing that the atmosphere will be reducing where these equilibrium estimates will be applied; i.e., in the pressure vessel for zones of $T > 700°C$, for which cases there is virtually no dependence on H/O ratio.

Sallach and Elrich also observed that CsI stability is reduced at lower Cs concentrations; however, this does not seem to be a very sensitive relationship. Since we do not now know the cesium concentrations, we have no choice but to make the reasonable assumption that it will exist in excess and that the degree of the excess does not change results significantly.

We also note that for the temperature regime where these equilibrium calculations will be applied ($T > 700°C$), levels of I_2 are negligible relative to CsI, I, and HI forms. Therefore, we simplify data storage requirements for the transport calculation by lumping the I and HI species, which seems reasonable since these are both highly reactive forms and hence should chemisorb at similar rates.

In summary, in the gas phase for temperatures above 700°C assuming excess H and Cs, we will compute the fraction of iodine existing as CsI from the chemical equilibrium results of Sallach and Elrich. For this case,

$$\text{(fraction I as CsI)} = f\ (\text{temperature},\ I/H_2O,\ \text{total pressure}).$$

The remaining fraction, the sum of I + HI is simply 1 - fraction CsI.

As the pathway progresses to zones of $T < 700°C$, equilibrium calculations became unrealistic due to kinetic effects. For these lower temperature zones, we will assume that the I fractions in the form of CsI and HI remain frozen at the values which existed at the last control volume in which $T \geq 700°C$. Atomic I would not exist at these progressively lower temperatures, hence we will assume that atomic I continues to I_2 when the temperature falls below 700°C.

4.2.2 Iodine species in water

Iodine, when dissolved in water, undergoes chemical change to a variety of forms, some of which are volatile and hence contribute to an effective iodine vapor pressure, while some are highly involatile and essentially fixed in water. Our conclusion at this time is that while these chemical changes are known to a large degree, important pieces of information are missing; this prevents calculation of effective volatility and other transport parameters solely from basic chemical principals. The missing data lie in the realm of reaction kinetics, principally rates of oxidation and reduction and the effect of radiation on reaction rates and equilibria. Equilibrium estimates under simple laboratory conditions seem to be fairly well determined, at least at low temperatures ($\approx$25°C).

A summary of iodine behavior in water has been given by Bell and Toth.[4.7] With no oxygen or hydrogen present, the following situation exists:

Molecular iodine in water reacts in two steps:

$$I_2(d) + H_2O = I^- + HOI(d) + H^+ , \quad (4.3)$$

followed by disproportionation of HOI,

$$3HOI = 2I^- + IO_3^- + 3\ H^+ . \quad (4.4)$$

The rates of Eqs. (4.3) and (4.4) are temperature, pH, and concentration dependent, but generally Eq. (4.3) is fast (seconds) while Eq. (4.4) is much slower (many minutes at 25°C). Therefore, a reasonable approximation for transient calculations of less than several minutes duration is to assume Eq. (4.3) goes to equilibration while neglecting Eq. (4.4).

The significance of these assumptions is that only the species I_2 and HOI contribute to iodine volatility; the other forms are essentially nonvolatile and hence fixed in water. Therefore, as noted in Ref. 4.7, the degree of completion of these hydrolysis reactions profoundly affects the iodine volatility. At long times when iodate formation is complete, the volatility would be approximately a factor of 10^5 lower than would exist at short times following I_2 addition. What is meant by 'short times' and "long times" depends on the reaction rate of Eq. (4.4), which in turn depends on the temperature, the pH, and the iodine concentration. (Oxidation and reduction reactions and radiation also affect the population of the volatile species I_2 and HOI. See the discussion in Sect. 4.5.3). Volatilities of the important iodine species and values for the equilibrium constants for the hydrolysis reactions are given in Table 4.1.

All volatility estimates for HOI are highly conjectural since it has never been measured, while volatilities of I_2 and CH_3I are well known. For the equilibrium constants, only the values for 25°C are based on measurements; the values given for 100 and 300°C were obtained by extrapolation. The values at 300°C are therefore especially uncertain.

This situation is complicated by the presence of H_2 or O_2, and in some cases, by the presence of both O_2 and H_2 in nonequilibrium. Hydrogen can reduce IO_3^- to I_2,

$$2H^+ + 2IO_3^- + 5H_2(d) = I_2(d) + 6H_2O , \quad (4.5)$$

and further reduce I_2

$$I_2(d) + H_2(d) = 2H^+ + 2I^- . \quad (4.6)$$

Thus, in the presence of H_2, Eqs. (4.5) and (4.6) must be accounted for, as well as the hydrolysis reactions, Eqs. (4.3) and (4.4).

In the presence of excess oxygen, it is more convenient to write the oxidation reactions,

$$2I^- + 2H^+ + 1/2O_2 = I_2(d) + H_2O \ , \qquad (4.7)$$

$$2I_2 + 2H_2O + 5O_2 = 4IO_3^- + 4H^+ \ . \qquad (4.8)$$

Actually, the oxidation reactions [Eqs. (4.7) and (4.8)] are related to the reduction reactions [Eqs. (4.5) and (4.6)], the link being the formation of water, via

$$H_2 + 1/2O_2 = H_2O \ . \qquad (4.9)$$

If Eq. (4.9) represents a true equilibrium condition, Eqs. (4.7) and 4.8) may be derived directly from the given reduction reactions. This, however, is quite unlikely under suppression pool conditions, where either a net reduction or oxidation may occur, depending on the relative kinetics of the reactions involved.

The incoming gas released below the surface of the suppression pool contains large amounts of H_2 resulting from the steam/Zr reaction, while the wetwell atmosphere, though inerted with N_2 to preclude H_2/O_2 deflagration, still contains ~5% oxygen. Hence a corresponding level of dissolved oxygen will exist in the suppression pool water. Furthermore, at suppression pool temperatures ($\leq$116°C), equilibration of H_2 and O_2 is not likely. Hence both reduction and oxidation reactions can occur, the degree of which can be assessed only from reaction kinetics test data for these conditions. Furthermore, the presence of radiation is known to affect redox reaction rates.

How does this view of iodine chemical species in water compare with test data?

Devell et al.[4,8] injected superheated steam (175 to 320°C) containing iodine into 0.5 to 3 m^3 volume of water held at 100°C. The injected iodine species was not specified – it was presumably I_2, but if it were HI, interpretation of the results may differ. Devell found a decontamination factor (DF) of ~300 when the iodine concentration was ~5 x 10^{-7} M in neutral water. The DF dropped to 3 at the higher concentration of ~10^{-5} M. In these tests, the amount of iodine trapped in water corresponded to the amount hydrolyzed via Eqs. (4.3) and (4.4). Furthermore, the amount dissolved in water was not removed by continued steam purge or boiling leading Devell et al. to conclude that the hydrolysis of I_2 is not easily reversible. They concede that this is not in accord with the presently accepted chemical theory.

Witherspoon and Postma[4,9] determined the retention of iodine in water boiled to dryness. About 500 μg of I (presumably I_2) was dissolved in 200 mL of distilled water (pH = 7, presumably air saturated?) which was boiled to dryness. It was found that only ~4% of the dissolved iodine was released to air, 96% retained in the solid residue remaining in the flask. Interpretation of this result in terms of basic chemistry has not been made. Evidently volatile I_2 is evolved on boiling, but not as rapidly as the water. Therefore, the remaining water becomes concentrated in iodine until the solubility of some species, perhaps H_2IO_5, is reached, causing it to precipitate.

However, this is conjecture. The behavior of iodine removal from boiling sparged water solutions is not well known in terms of basic iodine chemistry.

4.2.3 Organic iodide production

Despite several reviews of this subject within the last 10 years, the sources and rates of organic iodide production are poorly known. The state of knowledge is particularly poor with respect to estimation of formation rate within the time span of a core heatup event (~ hours). Most of the studies and reviews deal instead with equilibrium levels attained in containment atmospheres and by-in-large ignore formation rate, which is the essential information required for assessment of a transient situation.

A prime difficulty in the interpretation of organic iodide production levels is that the principal mechanisms of formation are not known. Bennett et al.[4,9a] clearly show that when I_2 vapor contacts paints of various types, methyl and ethyl iodide are produced. However, a major review paper (WASH-1233)[4,10] discounts surface reactions as the major source. A formation mechanism which appears to be most frequently cited is based on reaction of I_2 with either atmospheric methane or with low molecular weight organic vapors created by heat and radiation acting on organic contaminants (oil, carbon). The presence of moisture and radiation seems conducive to organic iodide production while oxygen inhibits formation.

It is important to include organic iodide as a vapor species of iodine and carry it along the transport pathway despite the large uncertainty which exists in the ability to predict formation rates. The reason is that in cases where projected iodine leakages are quite small on a fractional basis, as is anticipated for even serious postulated BWR accidents, the contribution of organic iodide to the total amount leaked may be significant.

Based on our review of recent reports dealing with organic iodide production, we have adopted the following means for estimating the formation rate. According to Postma and Zavodski[4,10] (WASH-1233), the steady-state level of organic iodide produced in about 70 containment tests may be predicted from

$$\text{percent formation} = 0.19 \times C^{-0.26} , \tag{4.10}$$

where C is the iodine concentration as I_2 in the vapor in terms of mg/M^3. Equation (4.10) represents a mean through data which scatter about a factor of 10 above and below the mean.

We employ a conversion rate assuming that these equilibrium levels were attained in about 4 h, as reported for one of the test runs on which Eq. (2.7) was based. This yields,

$$\text{conversion rate of I vapor to organic iodide, \%/h} = 0.05 \times C^{-0.26} . \tag{4.11}$$

For the frequently assumed nominal containment concentration of 100 mg/M^3, Eq. (4.11) predicts a conversion rate of 0.014 %/h to organic iodide.

There appears to be general agreement that organic iodide production occurs at low, containment level, temperatures and does not occur for T > ~300°C. Therefore, Eq. (4.11) will be applied only in the gaseous containment volume.

This is admittedly a less than satisfactory procedure for estimation of the organic iodide rate of formation. However, it does provide a means for consideration of organic iodine, and will have to serve until better calculational methods are available.

Although methyl iodide, probably the principal constituent of organic iodide, decomposes completely in water to methyl alcohol and I^-, the rate of decomposition appears to be sufficiently slow to be neglected for a transient condition lasting hours at suppression pool conditions. For example, Lemire et al.[4,10] report that for pH = 10, T = 80°C, 43% of the initial CH_3I in water remains after 1 h for an initial concentration level of 10^{-6} mol/L. The rate of decomposition is increased by (1) higher temperature, (2) higher concentration, (3) addition of hydrazine, and (4) high pH.

For the suppression pool, the conditions of pH = ~9 and very low concentration should tend to offset the higher temperature of ~116°C. Therefore, we will neglect the rate of decomposition of organic iodide, although the temperature effect is larger in the suppression pool water.

4.2.4 Summary, iodine molecular forms

Because of data storage considerations, the number of molecular forms of iodine carried along in each control volume is limited to two. This requires lumping of species with reasonably similar behavior, as shown below.*

	[1]	[2]
PV,[a] T > 700°C, gaseous	CsI	I + HI
PV, T < 700°C, gaseous	CsI	I_2 + HI + I
	or (I_2	HI + I)
PV, water	I	I^- + IO_3^-
WW, water	I_2 + HOI + CH_3I	I^- + IO_3^-
WW, gaseous	Org-I	I_2
DW, gaseous[b]	Org-I	I_2

[a] After PV failure, gas composition in DW is identical with PV: assumed species are org-I and I_2.

[b] Organic iodide converts to I_2 when T > 300°C.

*PV = pressure vessel, DW = drywell, WW = wetwell.

In the pressure vessel prior to failure where temperatures exceed 700°C, the three major gaseous species are CsI, I, and HI. The latter two may be placed together since their deposition characteristics are expected to be similar, i.e., chemisorption with similar deposition velocity, whereas CsI will deposit by condensation.

For the pressure vessel water, we assume that the hydrolysis reactions are not kinetics limited and go essentially to completion, i.e., all iodine exists essentially as I^- and IO_3^- with minute amounts of $I_2(d)$. All of this iodine becomes vaporized following core melting which boils the water to dryness and subsequently vaporizes the residue.

In the wet-well water we lump the volatile (I_2 + HOI + org-I) in one category and the nonvolatile species (I^- + IO_3^-) in the other. We rely on test measurements of suppression pool DFs to assess the distribution between these two iodine categories.

In both of the gaseous containment volumes, we will assume the two major iodine species to be organic iodine and I_2. This holds true also for the pressure vessel gas volume following bottom head failure when comingling equalizes the compositions in the pressure vessel and the drywell.

In the latter stage of the Station Blackout accident sequence, drywell temperatures reach 700°C according to the thermal-hydraulics estimate calculated by the MARCH code. Since organic iodides are destroyed by high temperature, we will assume that all organic iodide in the drywell is converted to I_2 when temperatures exceed 300°C.

4.3 Iodine Deposition Rates

4.3.1 General considerations

Several processes could be involved in iodine deposition depending on the iodine species present, the nature of the surface, the temperature, and other factors.

The first step in the adsorption process is mass transport to the solid surface, the rate of which is given by

$$w \quad \frac{\text{mass}}{\text{cm}^2 \cdot \text{s}} = k_g (C - C^*) , \tag{4.12}$$

where k_g (cm/s) is the mass transfer coefficient and the driving force is the concentration difference between the bulk gas (C) and that existing adjacent to the surface (C*). In turbulent flow, k_g depends principally on the gas velocity and secondarily on fluid properties and geometrical factors. In most deposition experiments, k_g ranges between about 0.1 and 1 cm/s.

Most frequently, deposition rates are presented in terms of a deposition velocity, V_g, defined by

$$w \quad \frac{\text{mass}}{\text{cm}^2 \cdot \text{s}} = V_g C . \tag{4.13}$$

Some test conditions were such that $C^* << C$, in which case $V_g = k_g$, i.e., the deposition velocity equals the mass transfer coefficient. Tests in which this appear to be the case are reported by Morris and Nichols[4,11] for adsorption on silver and copper. However, C^* is not, in general, negligible with respect to the bulk concentration, and hence V_g and k_g are unequal. Nevertheless, the value of k_g, which can be approximated from the flow conditions, places an upper bound on V_g.

If the partial pressure exceeds the vapor pressure of the condensed phase at the given temperature, deposition proceeds by condensation,

$$XI(g) \longrightarrow XI(L) \ , \tag{4.14}$$

where XI(g) represents the iodine species contained in the gas phase and XI(L) the condensed phase. In post-accident conditions, deposition occurs via condensation for low vapor pressure iodine species such as CsI or other metal iodides. Deposition by condensation should be mass transfer controlled with C^* equal to the concentration in equilibrium with the condensed phase.

If the species partial pressure is not quite high enough for condensation, deposition could still occur via the related process of physical adsorption.

$$XI(g) \longrightarrow XI(p.a.) \ , \tag{4.15}$$

where XI(p.a.) represents the physically adsorbed state. Physical adsorption of CsI is probably unimportant since it deposits largely by condensation. Conversely, the species HI is so volatile that it likely will not physically adsorb to any significant degree. Physical adsorption of I_2, however, could be a factor in the lower temperature zones, i.e., temperatures below about 150°C. Physical adsorption is characterized by a weak temperature dependence and the capability for multiple adsorbed layers, and does not strongly depend on the nature of the surface material. It may have been the principal deposition mechanism for experiments using I_2 below about 150°C.

Since iodine as HI, I, or I_2 is reactive with many metals, for example with iron,

$$I_2 + Fe \longrightarrow FeI_2 \ , \tag{4.16}$$

chemical reaction with the surface could occur. Writing symbolically, surface chemical reaction may be represented as

$$XI(a) \longrightarrow ZI(s), \tag{4.17}$$

where XI(a) is the adsorbed iodine species and ZI(s) is the result of reaction with the adsorbing surface. In general, high iodine concentrations in the gas phase favor formation of metal iodides; e.g., at 400°C, FeI_2

will form at iodine partial pressures above about 10^{-5} bar. Low temperatures thermodynamically favor metal iodide formation, however, at progressively lower reaction rates.

Morris and Nichols[4.11] and others report that oxidation of steel in steam is somehow enhanced by the presence of iodine, that is, the reactions

$$\left\{\begin{array}{l} 2Fe + 3H_2O \rightarrow Fe_2O_3 + 3H_2 \\ Fe + I_2 \rightarrow FeI_2 \end{array}\right\} \qquad (4.18)$$

mutually enhance each other even for Fe in the form of 304 stainless steel. Thus, in some cases, the presence of steam enhances adsorption by accelerating metal iodide formation. Resenberg et al.[4.12] report reduced desorption rates in steam relative to air, probably due to the same effect. However, the mechanism of enhanced adsorption on steel and reduced desorption due to the presence of steam are only poorly understood.

Materials which have a chemical affinity for iodine will tend to chemisorb iodine at partial pressures below that required for stable compound formation. Chemisorption is highly material specific and temperature sensitive and is limited to one monolayer. On steel, maximum chemisorption coverage is about 5 $\mu g/cm^2$ with surface oxidation reducing this value by about a factor of 100.[4.13] Chemisorption also differs from physical adsorption in that the end result is an I-atom situated at an active site.

This discussion illustrates the complex nature of iodine deposition on solid surfaces. In general, the deposition velocity defined by Eq. (4.13) has no physical significance and therefore should be used only for conditions very similar to those of the experiment.

4.3.2 Deposition of CsI

Deposition on walls. There appear to be no experimental studies on CsI deposition. However, the predominant deposition mode will undoubtedly be condensation and therefore should not differ from other condensation processes.

Deposition by condensation is limited by the mass transfer coefficient and, contrary to chemisorption, does not depend on the surface concentration. Hence, CsI deposition is given by

$$w_1 = k_g (C_1 - C_1^*) , \qquad (4.19)$$

where

w_1 = CsI deposition rate, g-mol/$cm^2 \cdot s$,

k_g = mass transfer coefficient, cm/s,

C_1 = bulk concentration, g-mol/cm^3,

C_1^* = equilibrium concentration above condensed CsI, g-mol/cm^3.

The value of C_i^* is obtained from the vapor pressure of CsI, and by assuming ideal gas behavior, i.e.,

$$\log P_i^* = 17.47 - 9678/T - 3.52 \log T \ , \tag{4.20}$$

$$C = P^*/RT \ , \tag{4.21}$$

where

T = surface temperature, K

P_i^* = vapor pressure of CsI, bar.

The value of k_g depends primarily on flow conditions in cases when the relative velocity between solid and fluid is significant. For this case, the Reynolds Analogy may be used to approximate k_g:

$$\frac{k_g}{U} = f \ , \tag{4.22}$$

where U is the fluid velocity in the core due to steam production and loss through the S/RV's and f is the flow friction factor. In our case, U appears to average ~300 cm/s (~10 ft/s) for the period up to pressure vessel failure at t = 380 m. Since the value of f is generally between 0.004 and 0.008 in the low Reynolds number (~10^4) range, we assume for the period up to pressure vessel failure,

$$k_g = 1.8 \text{ cm/s} \ . \tag{4.22a}$$

No flows are presently computed emanating from the reactor vessel following failure of the bottom head. Actually there will be some natural convection flow, but these are difficult to estimate. Since these flows will be small, we will assume them to be zero for this study. Until estimates of the natural convective communication between the failed pressure vessel and the drywell can be estimated, we assume all the fission products in the pressure vessel at time of failure remain there for the duration of the accident.

Deposition on aerosols. For CsI deposition onto aerosol particles, we will use existing correlations for mass transfer to spherical particles. For small particles with low relative velocity with respect to the gas, the mass transfer rate may be estimated using [4.14]

$$k_g \frac{dp}{D} = 2 \ , \tag{4.23}$$

where

dp = particle diameter, cm,

D = diffusion coefficient of CsI in gas, cm^2/s.

The value of D for CsI in steam at 70 bar and ~1200°C is about 0.04 cm^2/s. For a 10 μm particle, Eq. (4.23) thus predicts k_g = ~80 (cm/s), which is a fairly rapid rate. We therefore expect rapid CsI deposition by condensation on aerosol particles in the pressure vessel.

4.3.3 Deposition of HI and I

Deposition on steel. Genco et al.[4,15] measured the rate of HI deposition on 304 SS and Zircaloy in the range 115 to 750°C and 0.1 to 3400 mg/m^3 gas concentration. A variety of gas compositions were used. The carrier gas velocity was generally ~7 cm/s. It is expected that deposition rates of I would closely approximate those measured for HI.

Genco et al.[4,15] preferred the following square root relationship for correlating the deposition rate of HI on solid surfaces,

$$w \left(\frac{m_g}{cm^2 \cdot s}\right) = \frac{k}{2}\sqrt{\frac{C_g}{t}} \quad . \tag{4.24}$$

However, in view of the numerous uncertainties regarding interpretation of these data, it is probably better to use the simple deposition velocity expression, i.e.,

$$w = V\, C_g \quad , \tag{4.24}$$

where for HI on steel in a steam environment, the deposition velocity, V (cm/s), is given by

$$\log V = 1.3 \times \frac{10^3}{T} - 4.3 \quad , \tag{4.26}$$

where

T = surface temperature, K.

Deposition on aerosols. The appropriate expression for HI and I sorption on aerosol particles is problematical since there exist no data in this area. Since the chemical affinity of iodine for aerosol particles is low, it is reasonable to assume that in regions where CsI and HI exist, i.e., in the pressure vessel at T > 300°C, deposition of CsI by condensation dominates over chemisorption of HI or I. Therefore, we will neglect chemisorption of HI, I (and I_2) on aerosol particles in the pressure vessel.

Physical adsorption of iodine onto aerosols in the containment could be significant for times when containment temperatures are fairly low (approximately <200°C). However, the principle species here will be I_2 as discussed in Sect. 4.3.4.

4.3.4 Deposition of I_2

The form I_2 is the dominant species of iodine in the containment, hence deposition of I_2 on containment surfaces is emphasized. The chemical forms HI, I, and CsI dominate under pressure vessel conditions.

The surfaces in the primary containment are generally painted to protect the underlying metal surfaces. The drywell walls are painted with Amercoat 66 (an epoxy paint). The reactor vessel and associated piping is covered with mirror insulation which provides a large metal surface for deposition. The wetwell is painted with Placite (an epoxy-phenolic paint) which is a common coating for demineralized water tanks. Less is known about the large variety of surfaces in the secondary containment building, so an assumption was made that the deposition would occur at a rate given for Amercoat 1756 (an acrylic-latex paint).

Deposition on steel. Genco et al.[4,15] measured the adsorption of I_2 on 304 SS in the temperature range 150 to 550°C. With large deviations, the data are correlated in terms of the deposition velocity

$$w \quad \frac{\text{mol}}{\text{cm}^2\ \text{s}} = V\, C_g \ ,$$

with the deposition velocity V given by

$$\log V = 2.14 \times \frac{10^3}{T} - 7.8 \ . \tag{4.27}$$

These deposition velocities are about a factor of 100 lower than those given above for HI and I indicative of lower chemical reaction of I_2 relative to the more reactive HI.

Sorption on paint. Resenberg et al.[4,12] measured the sorption of I_2 on a variety of painted surfaces in steam/air atmospheres up to 170°C. Generally, different paints showed different deposition velocities and sorptive capacities with each group of similar paints in general behaving characteristically different from other groups.

The behavior of Amercoat 66, an epoxy paint used for drywell surfaces did not significantly vary with temperature up to 170°C. For this paint

$$\left\{ \begin{array}{l} V = 0.4 \text{ cm/s} \ , \\ (\text{sorptive capacity at } 170^\circ\text{C}) \tilde{=} 0.5 \text{ mg/cm}^2 \end{array} \right\} . \tag{4.28}$$

The deposition velocity was actually observed to diminish from the initial value of ~0.4 cm/s to 0 when fully loaded. We will assume a constant V until the 0.5 mg/cm² loading is reached.

No tests have been conducted on Placite, the epoxy-phenolic paint used in the wetwell. Phenolic paints as a group adsorbed I_2 more slowly than epoxy paints and showed more temperature dependence. Since wetwell temperatures do not vary greatly, we will use the measured average deposition velocities for Amercoat-66 and a phenolic paint at ~115°C, and similarly average sorptive capacities at this temperature

$$\left\{\begin{array}{l} V = 0.3 \text{ cm/s}, \\ (\text{sorptive capacity at } 115^\circ\text{C}) = 0.8 \text{ mg/cm}^2 \end{array}\right\}. \qquad (4.29)$$

It should be pointed out that drywell temperatures in excess of 170°C are predicted for the Station Blackout accident sequence. Epoxy paints begin to degrade at ~300°C and to char at higher temperatures. There exist no data regarding the sorptive capacity of painted surfaces at these elevated temperatures.

Deposition on aerosols. Deposition of I_2 on drywell aerosols could play a significant role in the determination of iodine leakage rates. In the absence of hard information in this area, we will make the following reasonable assumptions:

As noted above, mass transfer rates to small aerosol particles tend to be rapid. Hence adsorption of I_2 on the oxidic aerosols produced in the drywell should not be mass-transfer limited.

For the lower drywell temperatures (approximately <200°C), the physical adsorption process is expected to be the main sorptive mechanism involved. If one assumes ~10 monolayers of I_2, and a surface roughness factor of ~50, a sorptive capacity of ~50 $\mu g/cm^2$ results for I_2 on aerosols at these lower temperatures.

4.3.5 Deposition of organic-I

Deposition on steel. Rosenberg et al.[4,12] noted that the deposition rate of CH_3I on 304 SS was about 4 to 5 orders of magnitude lower than for I_2 under similar conditions. A maximum sorptive capacity of 0.12 $\mu g/cm^2$ was observed at 115°C and 210 mg/m^3 gas phase concentration.

Deposition on paint. Tests on Amercoat 66 at 115°C showed the following behavior:

$$\left\{\begin{array}{l} V = 0.018 \text{ cm/s}, \\ (\text{sorptive capacity}) = 25 \ \mu g/cm^2 \end{array}\right\}. \qquad (4.30)$$

No tests were conducted specifically on Placite, but averaging test results at 115°C for an epoxy and phenolic paint yields the following approximate behavior:

$$\left\{\begin{array}{l} V = 0.011 \text{ cm/s}, \\ (\text{sorptive capacity}) = 17 \ \mu g/cm^2 \end{array}\right\}. \qquad (4.31)$$

Deposition on aerosols. There appears to be no data on the deposition of organic-I on aerosol particles characteristic of the core-concrete interaction.

4.3.6 Summary of deposition assumptions

The assumptions in Sect. 4.3 are summarized in Table 4.2.

4.4 Iodine Desorption Rates

4.4.1 General considerations

Iodine tends to desorb from solid surfaces as the temperature rises and/or the iodine partial pressure falls. In general, the rate and the degree of desorption depend on the nature of the deposit (i.e., condensation, chemisorption, etc.), the type of solid material, temperature, and the chemical environment.

Iodine desorption is an important factor in the pathway analysis for the Station Blackout sequence which includes periods of primary vessel ($t > 390$ m) and drywell temperature rise, beginning at about $t = 500$ m at which time drywell structures begin to exceed 200°C.

4.4.2 Evaporation of condensed iodine

The evaporation of condensed iodine species, here exclusively CsI, follows the same rate expressions as deposition by condensation; i.e., Eqs. (4.19) through (4.23) apply except that C^* exceeds C resulting in a negative deposition rate (evaporation).

4.4.3 Desorption of physically adsorbed species

This applies mainly to I_2 and organic-I adsorbed on aerosol particles in the drywell. In the absence of specific information in this area, we will use the following reasonable assumptions based on the general character of physical adsorption. As noted earlier, physical adsorption is a process somewhat similar to condensation; hence the desorption process should be similar to evaporation. As with evaporation, we would expect a mass transfer limited process. Since the mass of physically adsorbed material is small (assumed to be 10 monolayers) and the mass transfer coefficient from aerosol particles is generally large, it is assumed that the physically adsorbed I_2 and organic-I desorb completely when the temperature exceeds 200°C, (17°C above the normal boiling point of I_2). That is, for I_2 and organic-I on aerosol particles in the drywell, we assume

$$\begin{cases} C_s = 50\ (\mu g/cm^2) & , T < 200°C \\ C_s = 0 & , T > 200°C \end{cases} , \qquad (4.32)$$

where C_s is the surface concentration equivalent to about 10 monolayers assuming a surface roughness factor of 50.

4.4.4 Desorption of I_2 and HI from stainless steel

Data on I_2 and HI sorption on steel are generally presented in terms of a deposition velocity, an empirical constant which tends to conceal the fact that several different mechanisms could be involved in the sorption process. At low iodine partial pressures ($P < \sim 10^{-6}$ bar at 400°C, or $C < 2$ mg/m³) chemisorption predominates and coverages should not exceed ~5 μg/cm² on bare steel. Coverages increase at higher iodine pressures due probably to the formation of FeI_2. Complicating the situation is the observation that iron oxidation is enhanced by the presence of steam with iodine. It has been observed[4.12,4.14] that such adsorption with simultaneous rusting tends to inhibit subsequent iodine desorption.

Osborne has observed[4.13] that in the chemisorption regime, desorption affected by dropping the iodine partial pressure to zero is a rather slow and incomplete process. It, however, was observed in these tests that desorption affected by elevation of temperature was complete (i.e., the surface loadings dropped to the lower equilibrium) and occurred in about 1 day.

As noted earlier, iodine deposits on steel in excess of ~5 μg/cm² probably involve chemical reaction with iron to form FeI_2. Desorption for this case therefore involves either vaporization or decomposition of FeI_2. Furthermore, the presence of steam plus iodine enhances iron oxidation forming a rust layer that appears to protect the iodine deposit. For example, Rosenberg et al,[4.12] report only 3% desorption in a steam/air environment compared with ~65% desorption in pure air in 20 and 60 h respectively. However, the experience of Osborne at al.[4.13] shows that the desorption rate in steam/air would have been accelerated if the steel temperature were increased during the test as well as merely reducing the iodine partial pressure.

Desorption rates from steel therefore depend on the temperature (or rate of temperature increase), the magnitude of the surface deposit, and the gaseous environment, particularly the iodine concentration in the gas phase. All of these vary during the course of the accident; moreover all appear to significantly effect the desorption rate. There is not a sufficient data base for predicting iodine desorption rates in these circumstances. Furthermore, the sorption mechanism for the high loading deposits in the presence of steam are uncertain so that theoretical modeling for this case would be highly speculative. We have therefore adopted the following reasonable desorption rate until such time that a more soundly based estimate is provided:

$$\left\{\begin{array}{l}\text{(Desorption rate from steel)} = 0.07\%/\text{m} \\ \text{Occurs when } C < 1 \text{ mg/m}^3 \ (P < 10^{-6} \text{ bar at } 400^\circ\text{C})\end{array}\right\} . \qquad (4.33)$$

The 0.07%/min rate corresponds to ~100%/d, which has frequently been observed.

4.4.5 Desorption from painted surfaces

Rosenberg et al.[4.12] report that from 50 to 75% of the iodine sorbed on epoxy or phenolic base paints is retained when the iodine partial pressure is reduced to near zero. These data were acquired with an iodine concentration initially at ~170 mg/m³ test and subsequently dropped to zero. Test temperatures ranged up to 170°C. In general, desorptions were complete in ~24 h.

Since the desorption rate from paint depends primarily on the iodine concentration in the gas and the temperature, the test data are not of sufficient scope for development of a well-based desorption rate expression. Further, surface temperatures in the drywell of up to ~700°C may occur, far above the chemical stability of any organic material and far above the maximum test temperature of 170°C. It is therefore necessary to adopt some reasonable assumptions for this case. The following are proposed:

$$\left\{\begin{array}{l} T < 300^{\circ}C \\ (\text{desorption rate from paint}) = 0.035\%/m \end{array}\right\} , \qquad (4.34)$$

when $C < 1$ mg/m³

and

$$\left\{\begin{array}{l} T > 300^{\circ}C \\ (\text{desorption rate from paint}) = 0.07\%/m \end{array}\right\} . \qquad (4.35)$$

for all values of C

Equation (4.34) corresponds to ~50% loss in 24 h as observed by Rosenberg et al. for 170°C and below. All paints should carbonize above ~300°C resulting in a more rapid iodine desorption.

4.5 Suppression Pool Decontamination

4.5.1 Flows through the suppression pool

A cross-sectional view of the Mark I containment pressure suppression pool is illustrated in Fig. 4.2. As shown, each of the 13 safety relief valve (SRV) tailpipes is connected to a 'T-quencher' device (rotated 90° in Fig. 4.2 for the purpose of illustration) situated ~4.7 m (14 ft) below the water surface. The T-quencher design provides good contact between the SRV gaseous discharge flow and the suppression pool water.

Communication between the drywell and wetwell is provided by eight large diameter [2.08 m (6 ft, 10 in.)] main vents which connect with a vent header in the wetwell above the suppression pool, as depicted. Flows

from the drywell to the wetwell enter below the water surface through 96 downcomers connected to the vent header. Although the downcomer exits are 1.22 m (4.0 ft) below the normal water level, gas/liquid contact is far less efficient compared with relief valve discharges through the T-quencher.

Flow from the wetwell airspace to the drywell will occur whenever the wetwell pressure is more than 0.5 psi greater than the drywell pressure. In such case, 12 'vacuum reliefs' (actually check valves) located on the main vent lines open, allowing flow from the wetwell airspace through the main vents to the drywell.

The temperature and pressure of the suppression pool during the Station Blackout accident sequence is shown in Fig. 4.3 as predicted by the MARCH program. The pool temperature rises from 103.7°C at the time of first cladding failure (103 min) to a maximum of 116°C at the time of drywell failure (238 min.) During this time span, the static pressure in the wetwell is seen to rise from 2.5 bar to a peak of 9 bar following reactor vessel failure, just before failure of the drywell. After drywell failure (238 min), the pressure reduces rapidly to 1 bar. From the saturation temperature curve shown in Fig. 4.3, it is seen that the pool is subcooled until drywell failure, after which there is a period of 44 min (from 247 min to 291 min) when the pool temperature exceeds its boiling point. The pool either boils during this time or quiescently evaporates water from its surface.

The flow rate into the pool via the T-quencher (from the reactor vessel) is shown in Fig. 4.4 in terms of m^3/s at pool mid-depth conditions. This SRV flow increases from 7.2 m^3/s at the time of cladding failure and peaks at 8.7 m^3/s at 110 min. The flow subsequently decreases as the core uncovery continues, until core slump (137 min), when a short duration burst of flow to the pool occurs which reaches a maximum rate of 300 m^3/s. This burst is due to the quenching of the collapsed core in the water within the bottom head of the reactor vessel.

Following dryout of the reactor vessel lower head at 141 min, some small SRV flow would continue to the suppression pool due to thermal expansion of gases in the reactor vessel. During this time span (141 min to 172 min), the average vessel temperature increases about 200°C which would result in a flow of ~0.140 m^3/s, (140 L/S) as indicated in Fig. 4.4.

It should be pointed out that the flow from the reactor vessel to the pool during the time indicted on Fig. 4.4 (100 min to 172 min) utilizes only one (of the 13) relief valve and consequently only one T-quencher.* Therefore, localized concentration variations in the pool could occur, with higher fission product levels and temperatures in the vicinity of the active T-quencher.

The fraction of noncondensibles in the T-quencher flow, estimated from the MARCH program results, is also shown in Fig. 4.4. In general, an

---

*Except during the period immediately following core slump, when the combined capacity of five relief valves is required to handle the short-duration burst of steam from the quenched core.

increase in the fraction of noncondensibles tends to reduce the decontamination factor of the pool for soluble gas species. There is some indication, however, that this is not true for particulates. The noncondensibles in this case consist of H_2 generated by the steam/Zircaloy reaction in the core. The noncondensible fraction peaks at 0.4 at t = 130 min.

Figure 4.5 illustrates the flow communication between the wetwell and the drywell from the time of cladding failure (102 min) to the end of the sequence. The flow is from the drywell through the main vents and downcomers into the wetwell from the time of reactor vessel failure to the time of drywell failure. A peak flow rate of ~4000 L/s enters the suppression pool via the 96 downcomers during this time interval.

At other times, the flow direction is from the wetwell airspace to the drywell through the vacuum breakers. This flow peaks at ~316 m^3/s as the suppression pool flashes due to the depressurization following failure of the drywell (238 min), and diminishes thereafter, reflecting the steadily slower rate of steam generation from the heated suppression pool.

4.5.2 Suppression pool chemical considerations

The suppression pool consists of 3830 m^3 of neutral water (pH = ~7) contained within a partially deoxygenated wetwell atmosphere (oxygen concentration <4.0%). If all the iodine in the core (235 g-atom) were dissolved in the suppression pool, the final concentration would be 6.1×10^{-5} g-atom/L.

The portion of the iodine entering the pool as molecular iodine (I_2) undergoes the following hydrolysis reaction:

$$I_2 + H_2O = I^- + HOI + H^+ \qquad (4.36)$$

followed by disproportionation of the HOI via

$$3HOI = 2I^- + 3H^+ + IO_3^- \ . \qquad (4.37)$$

Equilibrium estimates indicate[4,16] that under suppression pool conditions (100°C, pH = 7, 6×10^{-5} mol/L concentration) reactions (4.36) and (4.37) proceed almost to completion - only about the fraction 10^{-5} of the original iodine entering the pool remains as I_2, the balance becoming I^- and IO_3^-. Since I^- and IO_3^- possess essentially no volatility, there is a strong tendency for I_2 dissolved under these conditions to remain in the water.

However, under conditions where there is a relatively short contact time between I_2 in a vapor bubble and the surrounding pool water, the kinetics of these reactions would have to be taken into account. Under suppression pool conditions, reaction (4.36) appears to proceed quickly (<1 s) but the second step, reaction (4.37), requires several minutes to complete. Since HOI possesses significant volatility, the effectiveness of the suppression pool in retaining iodine by dissolution of I_2 under transient conditions cannot be predicted from purely chemical considerations until the kinetics of I_2 hydrolysis have been worked out and the volatility of HOI determined.

Based on discussions in Sect. 4.2, it appears that the dominating form of iodine entering the suppression pool with the vapor from the reactor vessel is not I_2, but probably CsI or some other iodide. This dissolves simply as

$$CsI = Cs^+ + I^- . \tag{4.38}$$

To attain any significant volatility from dissolution in this fashion, oxidation of the iodide ion would be required. (Effects of oxidation, reduction, and radiation are discussed in Sect. 4.5.3.)

Brief mention should be made regarding the effect of pH and the expected changes in the pH of the pool as the accident sequence progresses. The dominating effect of fission products on the pool pH appears to be an increased alkalinity due to dissolution of alkali metals. The reduced form of the alkali metals (Cs and Rb), i.e., the metal, would be expected from the reactor vessel and would react with water as follows:

$$Cs^\circ + H_2O = Cs^+ + OH^- + 1/2H_2(g) . \tag{4.39}$$

If all the Cs and Rb in the core (2960 mol) reacted with suppression pool water as above, an OH^- concentration of 7.7×10^{-4} mol/L would result, which is equivalent of a final pH of 9.15 at 100°C. This increase in pH from 7 to 9.15 tends to enhance equilibrium I_2 solubility and also to accelerate the hydrolysis reactions.

Note also that reaction (4.39) produces 1/2 mol of H_2 per mole Cs or Rb. Mixed uniformly in the wetwell gas space, this quantity of H_2 would achieve a volume concentration of 0.92%.

4.5.3 Redox and radiation effects

The actual conditions in the suppression pool could be significantly different from those described in the previous section which were based mainly on experiences under simple, clean, laboratory conditions. There are a number of potential factors which could significantly alter iodine chemistry in the pool, the most prominent probably being the presence of hydrogen, oxygen, and radiation. Unfortunately, knowledge in these areas is insufficient for quantitative prediction; qualitatively, the following effects from these factors may occur in varying degree.

Iodine, present as iodate, could be reduced to the more volatile forms HOI or I_2 by the presence of hydrogen, for example, as follows:

$$IO_3^- + 5/2H_2 + H^+ = 1/2I_2^\circ + 3H_2O . \tag{4.40}$$

If the principal chemical form of iodine in the pool is the reduced form I^-, as seems likely, then oxidation effects would probably play a more significant role. Oxidation of I^- to I_2 may be induced by the oxygen present due to the suppression pool atmosphere (which is partially deoxygenated air), or due to the radiolysis of water, which produces a complex

mixture of ions, molecules, and free radicals. For example, 100 eV of absorbed radiation energy dissociates 4.9 molecules of water to yield[4.16]

$$4.9\ H_2O = 2.7\ e^- + 2.7\ OH\cdot + 3.4\ H^+ + 0.70\ H^- + 0.45\ H_2 + 0.75\ H_2O_2 + 0.6\ H\cdot \qquad (4.41)$$

Thus H_2 is a primary product of radiolysis as well as a secondary product formed in a number of ways, e.g.,

$$2\ H\cdot = H_2\ . \qquad (4.42)$$

Oxygen, as a secondary product, might also be formed in a number of ways, e.g., the decomposition of the peroxide,

$$H_2O_2 = H_2O + 1/2\ O_2\ . \qquad (4.43)$$

However, the principal oxidizing species formed by the radiolysis of H_2O appears to be the free radial, OH·, which oxidizes I^- to I_2 according to the reaction

$$2I^- + 2OH\cdot = I_2(d) + 2OH^-\ . \qquad (4.44)$$

Possibly, the radiolysis product H· could directly oxidize I^- as follows:

$$I^- + H\cdot = 1/2H_2 + 1/2I_2\ . \qquad (4.45)$$

The extent to which these reactions occur in the suppression pool is not known. However, there appear to be some possible mechanisms for altering the effective volatility of iodine from the predicted under idealized, laboratory conditions.

4.5.4 Experimental values for suppression pool decontamination factors (DFs)*

A recent review by Rastler[4.17] has provided a comprehensive summary of suppression pool decontamination experimentation. Before presenting this summary or other data, it is well to point out that the theory regarding iodine scrubbing by the suppression pool is not developed.** Therefore, it is quite difficult to resolve evident or apparent discrepancies from one experiment to another performed under somewhat different conditions. In addition, it is not possible to rationally extrapolate to

---

*The decontamination factor (DF) is the ratio of the fission product mass transported into the suppression pool to the mass which is released from the pool surface.

**An ongoing task by SAI sponsored by EPRI may soon help in filling this void.

realistic conditions, which in many cases are significantly different from those employed in usually smaller scale experimentation.

It is well to emphasize the factors which affect the DF to varying and unknown degrees:

Pool geometry, i.e., the pool depth and type of inlet nozzle, which affect the contact time, and the pool volume which affects the final pool pH and concentration.

Inlet vapor flowrate affects bubble formation and hence contact time.

Fraction of noncondensibles in the inlet flow affects the rate of change of bubble size, the bubble final size, and the rate of diffusive contact between iodine in the bubble with water surfaces.

Concentration of dissolved iodine exerts a 'backpressure' which inhibits iodine dissolution.

Pool temperature affects the iodine chemistry, water transport properties, and bubble dynamics; particularly important appears to be the degree of subcooling (or superheating).

Pool pH affects iodine equilibria and kinetics.

The type of iodine species in the inlet flow. Forms of lower solubility (e.g., CH_3I) exhibit a lower DF.

Some of the above factors are of paramount importance in determining the DF. In the absence of some theoretical development, it is therefore quite difficult to assess the values presented in experiments conducted under different conditions. Sorting out this situation is beyond the scope of this task, and we will therefore lean heavily on the summary and conclusions presented by Rastler.[4,17] In our judgment, they are the best values attainable at this time, and further improvement in this area would require significant experimental and theoretical effort. However, Rastler's conclusions refer to the Mark-III containment whereas the Mark-I containment is used at Browns Ferry. The major difference between these containment types as they affect DFs appears to be in the geometry of the downcomers, which require some alteration of Rastler's recommended DFs.

Rastler's 'minimum supportable' DFs are presented in Table 4.3. First, it should be noted that flow into the wetwell in the Station Blackout accident sequence occurs only under subcooled pool conditions (see Figs. 4.3 and 4.5). Therefore, we need not be concerned with Rastler's DF values for a saturated pool. Secondly, we should note that in Table 4.3 the DF values for flow from T-quenchers and from the 'vents' are presented as equal. (The 'vent' in the Mark III containment is schematically equivalent to the 'downcomer' used in the Mark I containment.) This equality would not be appropriate at Browns Ferry.

Pending future correction or modification by further study, it is assumed here that DFs associated with downcomer flow (from the drywell) are a factor of 10 lower than T-quencher flow (from the reactor vessel) because of the lesser submergence of the downcomer exits. Based on the above discussion and the data summary of Rastler, the suppression pool DFs assumed in this study are presented in Table 4.4.

4.5.5 Evolution of iodine during suppression pool vaporization or boiling

As noted in Fig. 4.3, there exists a period of about 44 min (from 247 to 291 min from time of battery failure) in which the mean pool temperature exceeds the saturation temperature. Initially, the temperature excess is estimated to be 16°C, which would cause volume boiling of the pool.

Since net flows from the wetwell airspace to the drywell are fairly large during this time interval (as shown in Fig. 4.4) and the pathway to the Reactor Building has been opened by the previous failure of the electrical penetration assembly (EPA) seals, the effective iodine volatility under these circumstances would have a significant impact on the degree of release.

As noted in Sect. 4.5.3, the effective iodine volatility under realistic suppression pool conditions is uncertain becuase of the presence of factors not yet incorporated into calculational models or included in the experiments conducted to date. These factors include:

(1) The presence of radiation - principally from the decay of cesium and rubidium, which forms water radiolysis products that might either reduce or oxidize iodine species. Very roughly, the integrated gamma dose in the suppression pool after core degradation would be 10^6 Rad, which would cause significant radiolytic effects.

(2) The presence of hydrogen and oxygen - hydrogen (from the reactor vessel) and oxygen (from the initial wetwell airspace) might cause either a net oxidation or reduction of iodine species.

(3) Iodide - iodine would probably be introduced into the suppression pool in a reduced form (as the iodide) rather than as molecular iodine (I_2), which has been assumed in volatility calculations in the literature, as well as apparently assumed in the reported experiments.

The selection of an appropriate iodine volatility is difficult, as illustrated by the range of theoretical and measured values listed in Table 4.5. The first value, reported in NUREG 0772,[4.7] is calculated on the basis of an assumed addition of I_2 to pure water, complete equilibration with the iodate and iodide hydrolysis products, and a HOI volatility one-half that of molecular iodine I_2.* This leads to an extremely low volatility, equivalent to a partition coefficient** of 5×10^7 for the temperature, iodide concentration, and pH conditions of the suppression pool during the postulated Station Blackout accident.

The use of such a low volatility value leads to a correspondingly low estimate of the iodine vaporized from the suppression pool during the

---

*HOI volatility, when determined, will probably prove to be less than this assumed value.

**The partition coefficient (PC) is defined as the ratio of the equilibrium concentration in the liquid to the concentration in the gas.

period of rampant pool boiling as shown in the following example:

partition coefficient (example case)	5×10^{7}
fraction of pool vaporized	~4%
volume of steam vaporized	2.6×10^{8} L
iodine concentration in liquid	4.0×10^{-5} mol/L
iodine concentration in gas	0.8×10^{-12} mol/L
moles I vaporized	2.1×10^{-4}
fraction I vaporized.	1.3×10^{-6}

For the above example, it was assumed that all of the initial core iodine inventory of 154 mol was dissolved in the suppression pool. As shown, only the fraction 1.3×10^{-6} of this dissolved iodine may be expected to evolve while the pool boils (or partially vaporizes) following drywell venting. In terms of absolute values, this represents ~193 Ci of iodine - ~1.3×10^{-6} of a total inventory of 1.45×10^{8} Ci.

As noted in Table 4.5, other volatility estimates for iodine are much higher. If one were to assume no iodate formation, as would be appropriate for short intervals following the introduction of I_2 to water, the estimate of the volatility of iodine would increase by a factor of 10^{5}. In this regard, the measured volatilities of Kelley,[4.18] Pelletier,[4.19] and Lin[4.20] are invariably higher than the estimated values which are based on complete iodate formation.

It should be emphasized that none of the available theoretical or measured volatilities is appropriate for application to the conditions in the suppression pool during the rapid depressurization period immediately following the assumed gross failure of the drywell electrical penetration assembly seals. The depressurization would cause about 4% of the pool volume to flash to steam during this period. Our best judgement is that a partition coefficient of 10^{5}, representing an iodine volatility 500 times higher than that of the previous example, is a reasonable estimate. Based on this higher volatility, about 0.067% of the iodine inventory in the pressure suppression pool would be vaporized during the pool boiling phase. Since only about 15% of the core inventory of iodine is transported to and dissolved in the pressure suppression pool at the time of drywell failure,* this represents 0.067 x 0.15, or about 0.01% of the initial core inventory.

It should be pointed out that the potential for iodine removal from the suppression pool to the drywell during the time interval of pool boiling is perhaps greater by direct liquid ejection than by iodine vaporization, as postulated above. As shown in Fig. 4.2, the main vent terminus, where the vacuum breaker inlets are located is only about 1.5 m (5 ft) above the pool water level. Therefore, any liquid level rise of this magnitude due to volume boiling could incorporate water with the steam flow through the vacuum breakers and vent headers into the drywell. Using the above-cited concentrations and assuming a partition coefficient of 10^{5}, about 2500 L of water contains as much iodine as is estimated to be

---

*The remainder of the iodine released from the fuel is primarily condensed as CsI on aerosol particles and deposited on the inner surfaces of the reactor vessel. See Sects. 5 and 6.

vaporized. Therefore, the potential for direct carryover of iodine in water from the wetwell to the drywell appears to be high. (It should be further noted that this possibility appears to be absent for the Mark II and Mark III containments where the wetwell/drywell vacuum breakers are situated much higher above the pool surface.)

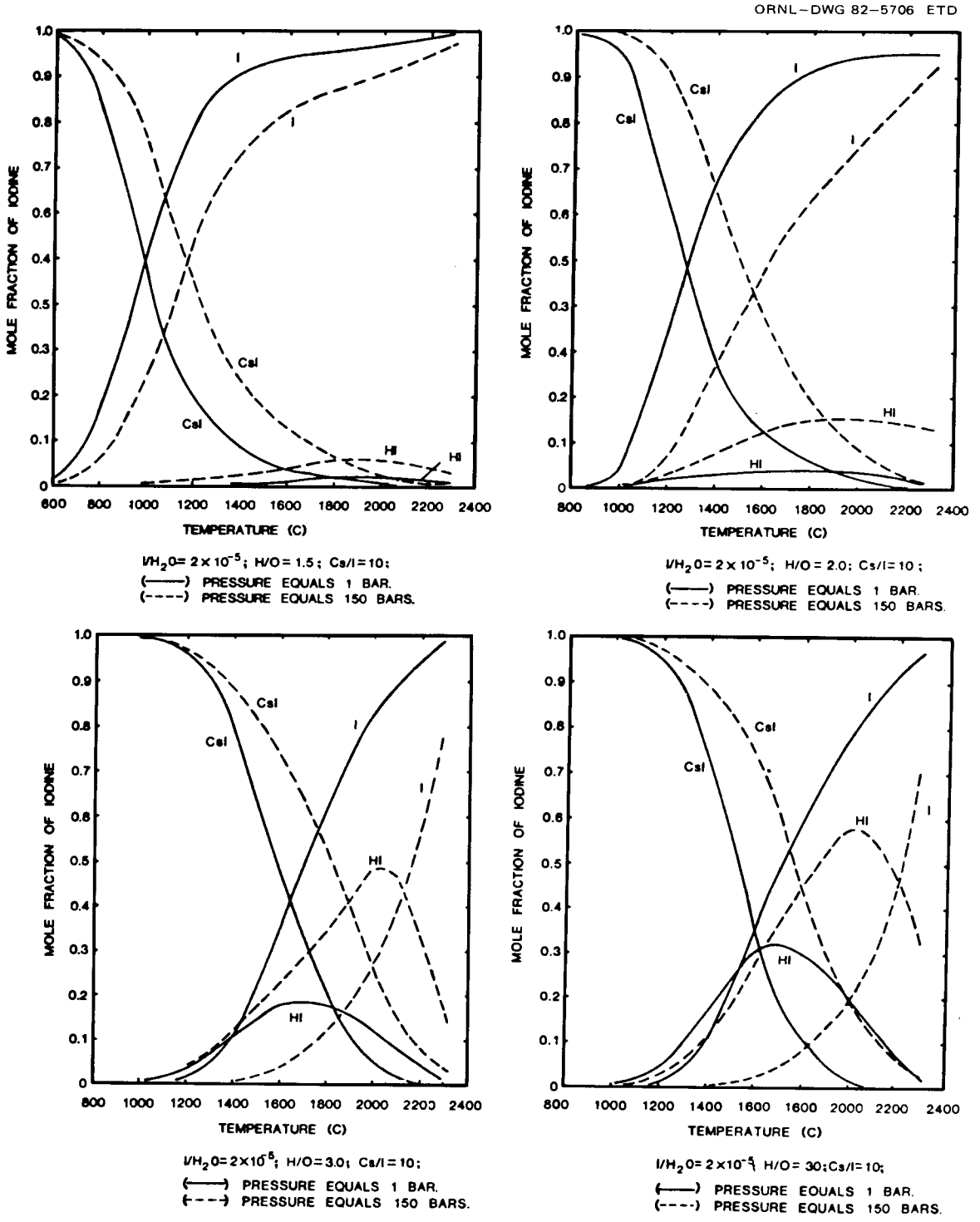

Fig. 4.1. Relative abundance of iodine species in the cesium-iodine-hydrogen-oxygen system for the conditions given (from ref. 4.21).

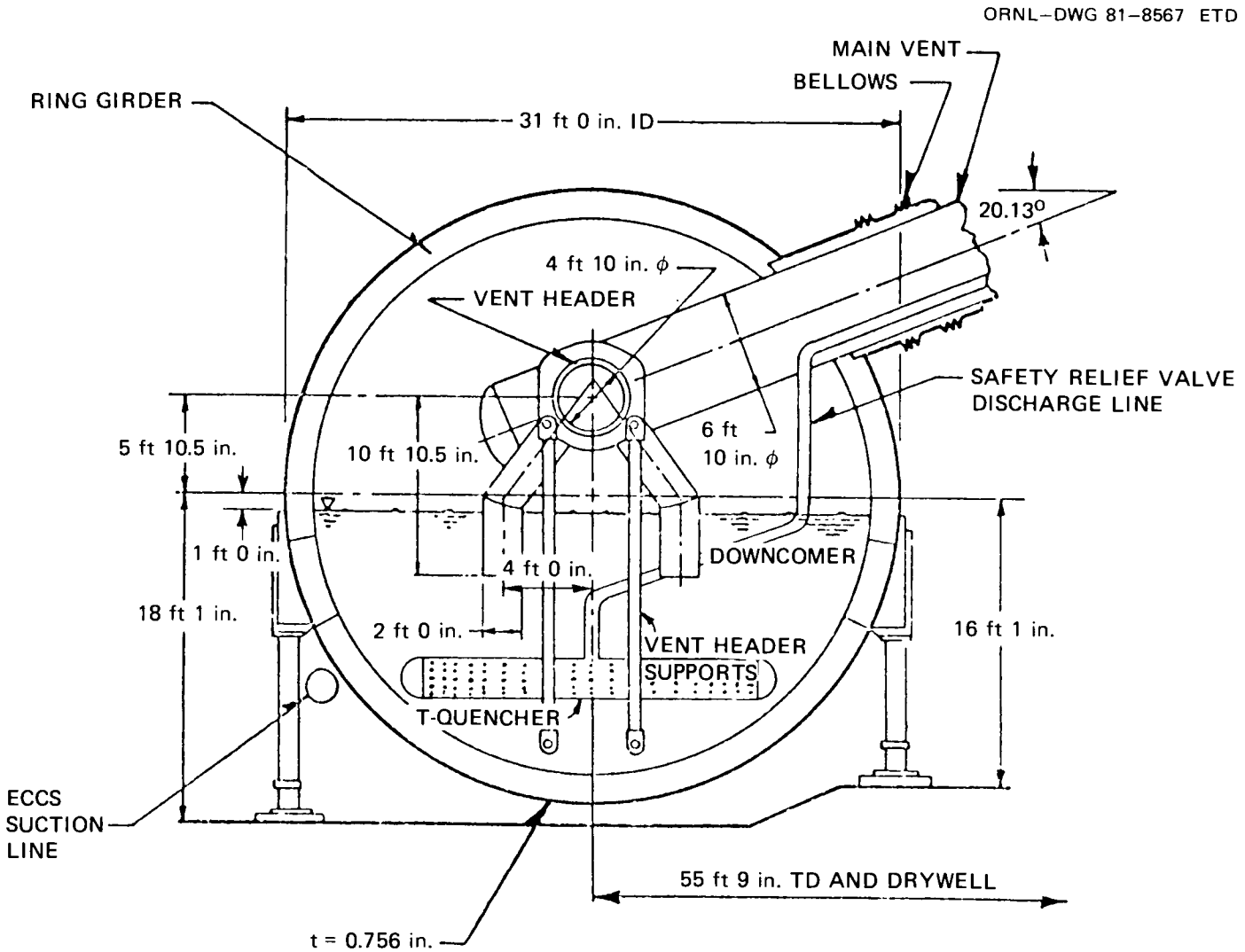

Fig. 4.2. Browns Ferry Mark I containment pressure suppression pool.

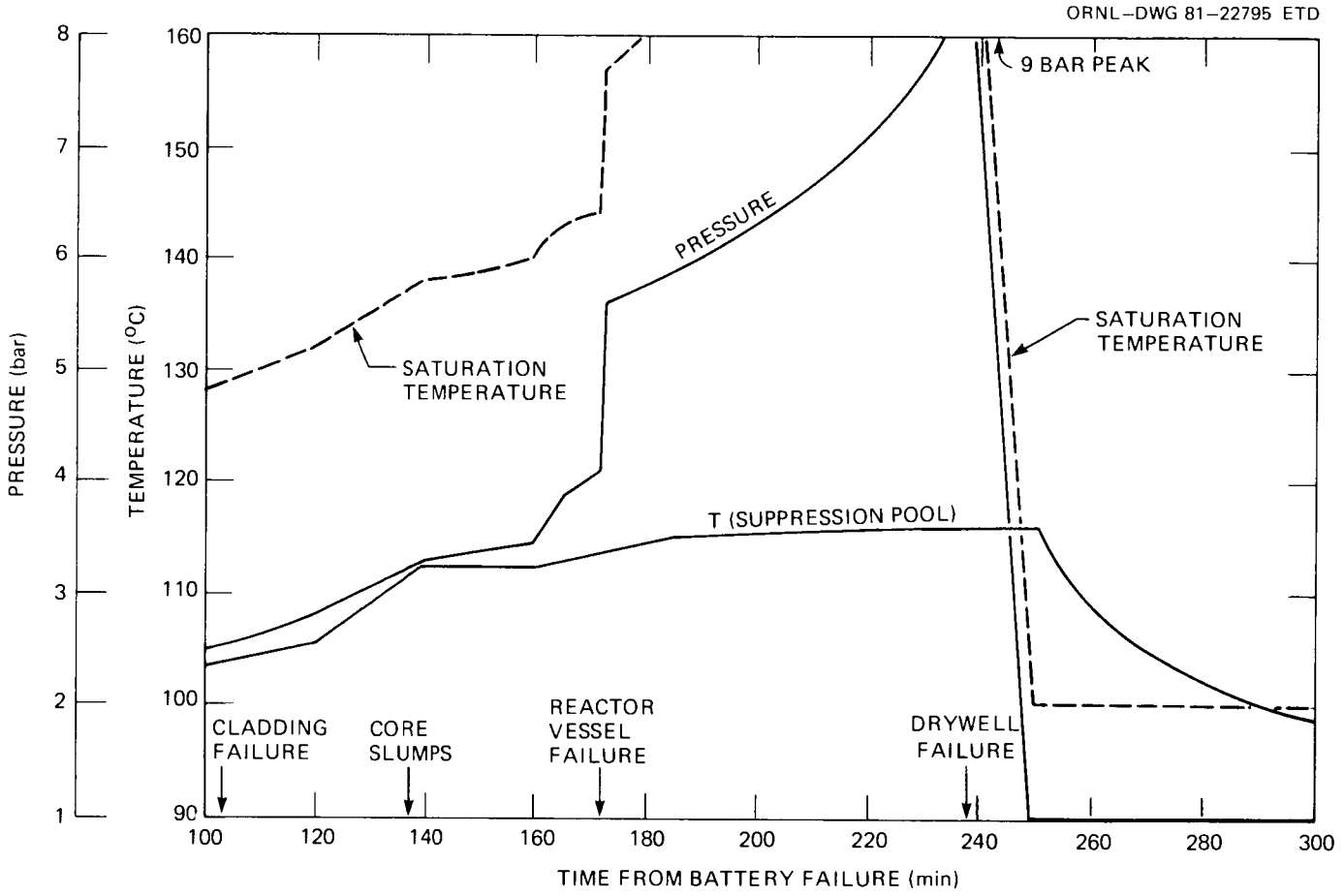

Fig. 4.3. Suppression pool temperature and pressure.

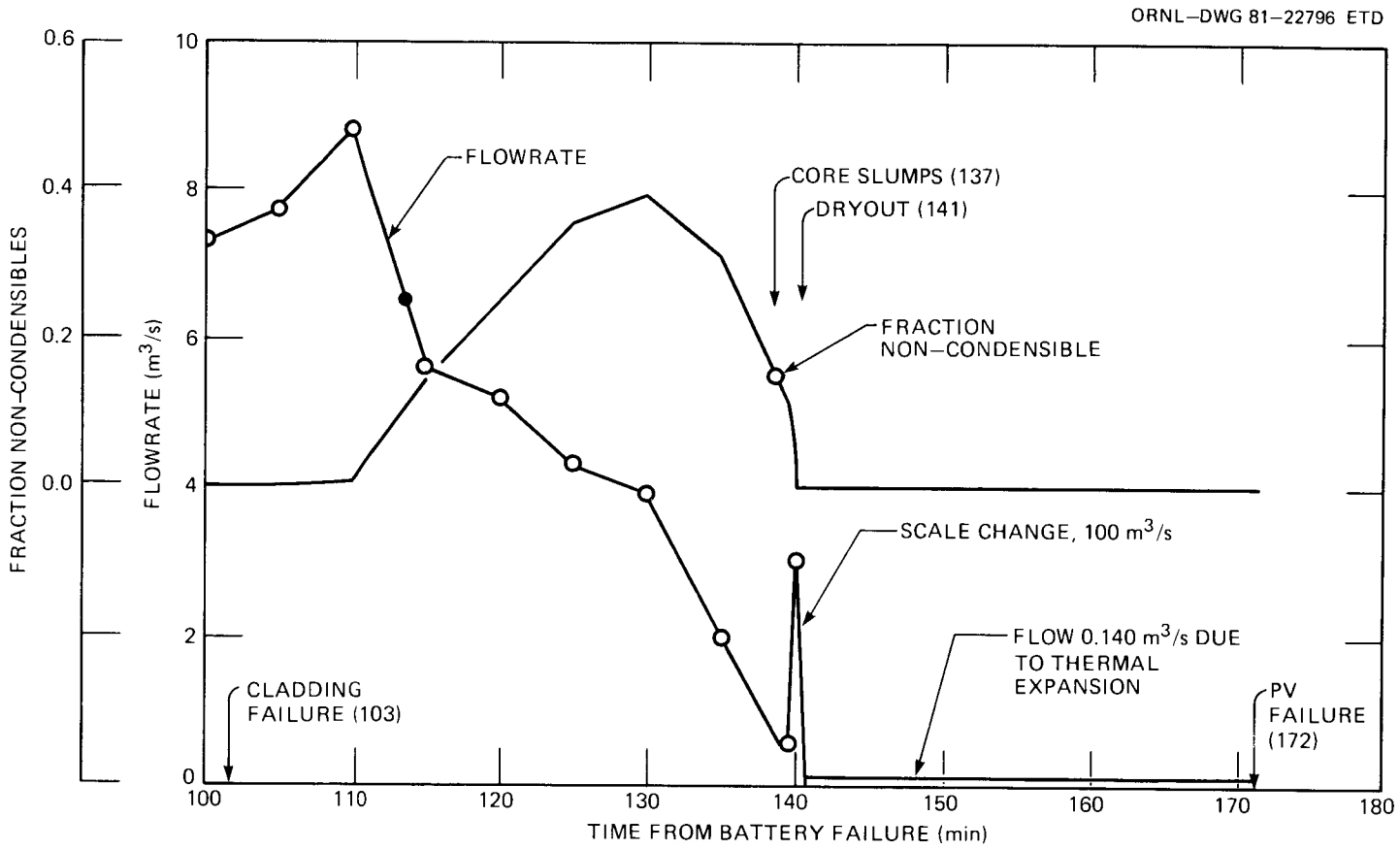

Fig. 4.4. Flow and fraction non-condensibles to suppression pool through T-quenchers.

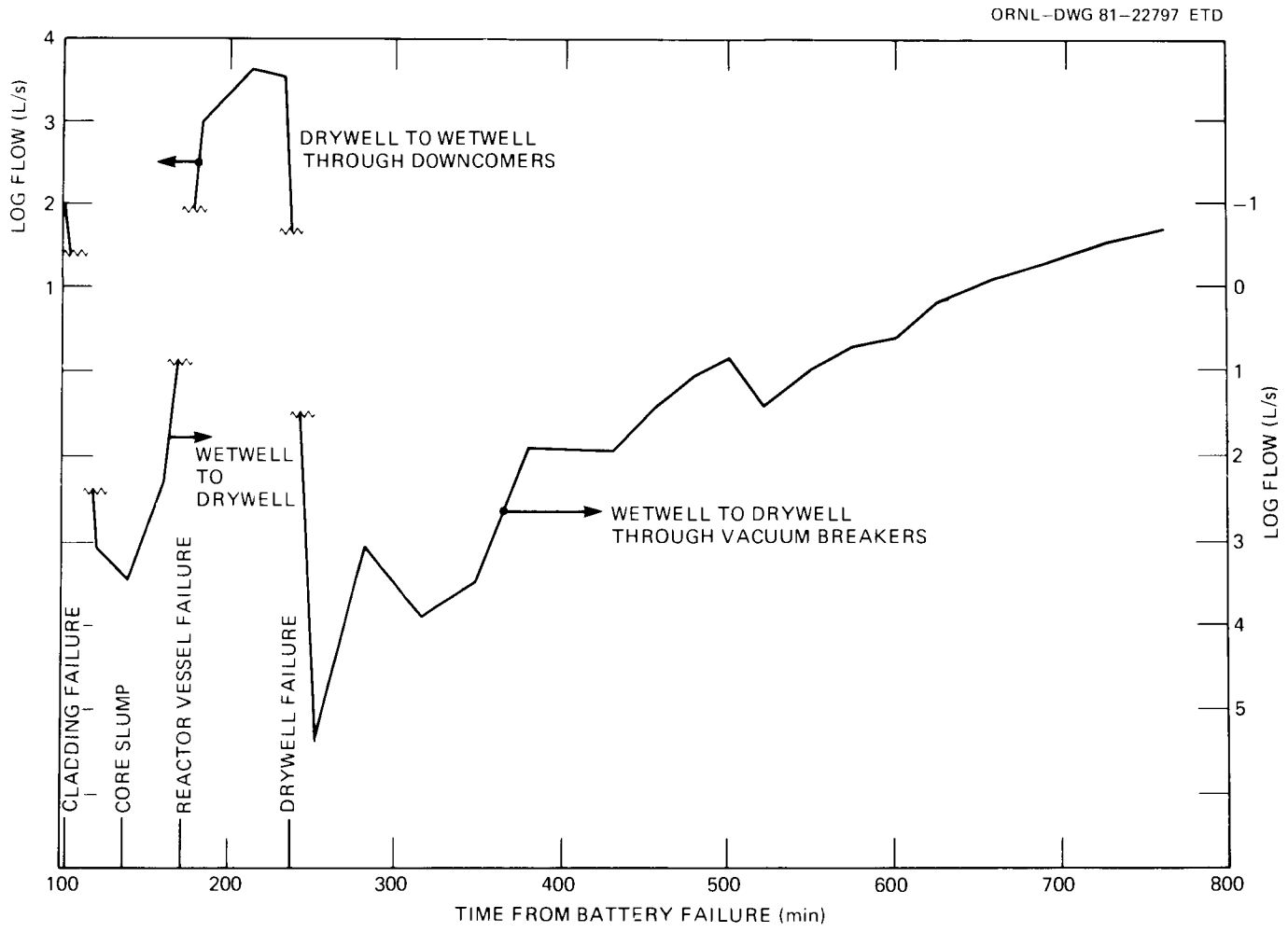

Fig. 4.5. Flow between drywell and wetwell.

Table 4.1. Equilibria of iodine reactions

Reaction		Rate[a]	Equilibrium constants[b] 25°C	100°C	300°C
Volatilities					
$I_2(d) = I_2(g)$		Fast	0.30	3.3	
HOI(d) = HOI(g)		Fast	0.15(?)	1.5(?)	
$CH_3I(d) = CH_3I(g)$		Fast	0.187	1.01	0.063
In water					
Eq. (4.3)	hydrolysis	Fast	4.04×10^{-13}	5×10^{-11}	
Eq. (4.4)	hydrolysis	Slow	$\sim 10^{-13}$		
Eq. (4.5)	redox	Slow			
Eq. (4.6)	redox	Slow			
Eq. (4.7)	redox	Slow	2.6×10^{23}		
Eq. (4.8)	redox	Slow	9.4×10^{16}		

[a] Refers to suppression pool conditions; all reactions probably equilibrate in pressure vessel where T = ~260°C.

[b] Units: for volatilities, K = (bar)/(mol/liter); liquid phase constants are in terms of (mol/liter). Values shown here are for general information and are not used directly in the analysis.

Table 4.2. Summary of iodine deposition expressions and rate constants

	Rate expression	Equations
CsI on PV structure	Mass transfer	(4.19)–(4.22a)
CsI on aerosols	Diffusion controlled	(4.23)
HI and I on PV steel	Deposition velocity	(4.26)
HI and I on aerosols	Assumed negligible	
I_2 on steel	Deposition velocity	(4.27)
I_2 on drywell paint	Deposition velocity	(4.28)
I_2 on wetwell paint	Deposition velocity	(4.29)
I_2 on aerosols	Limited by sorptive capacity	(4.29a)
Org-I on drywell paint	Deposition velocity	(4.30)
Org-I on wetwell paint	Deposition velocity	(4.31)
Org-I on aerosols	Assumed negligible	
Org-I on steel	Assumed negligible	

Table 4.3. Minimum supportable suppression pool decontamination for iodine and particulates, from Rastler[4.17]

Transport pathway and associated events(s)	Minimum supportable DFs	
	Subcooled pool	Saturated pool
Reactor pressure vessel to pool via safety relief valve and quencher (transients)	10^3 CsI, I^-, HI 10^2 particulates 10^2 I_2	10^2 particulates 30 I_2
Reactor pressure vessel to pool via vents (transients following RPV depressurization, or LOCA post blowdown period	10^3 CsI, I^-, HI 10^2 particulates 10^2 I_2	10^2 particulates 30 I_2
Aerosol transport to pool via vents (core-concrete vaporization release)	10^2 particulates 10^2 I_2	10^2 particulates 30 I_2

Table 4.4. Suppression pool decontamination factors assumed in this study

	Flows through the T-quencher from the reactor vessel	Flows through the downcomers from the drywell
HI	10^3	10^2
I_2	10^2	10
Organic I	NA[a]	1
Particulates[b]	10^2	10

[a] No organic iodide production is anticipated in the reactor vessel.

[b] Includes CsI.

Table 4.5. Range of theoretical and measured iodine volatilities

Source	Conditions	Partition coefficient	Effective Henry's Law coefficient (bar/mol)
NUREG 0772,[4.7]	Equilibrium iodate formation, pH=9, T=100°C, [I]=10^{-6} mol/L	5×10^{7}	6×10^{-7}
NUREG 0772,[4.7]	No iodate formation, pH=9, T=100°C, [I]=10^{-6} mol/L (applies to addition as I_2; early time value)	350	9×10^{-2}
Kelley,[4.18]	30<T<70°C 10^{-9}<[I]<10^{-5} mol/L 5<pH<9	2400	1×10^{-2}
Pelletier,[4.19]	T=80°C, [I]=low (?) pH=9	2.5×10^{4}	1×10^{-3}
Pelletier,	T=80°C, [I]=10^{-5} mol/L pH=8.8	2200	1×10^{-2}
Lin,[4.20]	T=25°C, [I]=10^{-6} mol/L	1000	3×10^{-2}

References for Section 4

4.1. T. J. Morrison and N. B. Johnstone, "Solubilities of the Inert Gases in Water," *J. Chem. Soc.* __, 3441 (1954).

4.2. T. J. Morrison, "The Salting-out of Non-electrolytes, Part I. The Effect of Ionic Size, Ionic Change, and Temperature," *J. Chem. Soc.* ___, 3814 (1953).

4.3. T. J. Morrison and F. Billett, "The Salting-out of Non-electrolytes, Part II. The Effect of Various in Non-electrolytes," *J. Chem. Soc.* ___, 3819 (1952).

4.4. R. E. Treybal, *Mass-Transfer Operation*, 2nd ed., McGraw-Hill, New York, 1968.

4.5. C. C. Lin, "Chemical Behavior of Radioiodine in BWR Systems," *J. Inorg. Nucl. Chem.* 42, 1093 (1980).

4.6. R. Sallach and R. Elrick, Chapter 5 in *Technical Bases for Estimating Fission Product Behavior During LWR Accidents*, NUREG-0772 (June 1981).

4.7a. J. T. Bell and L. M. Toth, Chapter 5 in *Technical Bases for Estimating Fission Product Behavior During LWR Accidents*, NUREG-0772 (June 1981).

4.7b. J. T. Bell et al., *Aqueous Iodine Chemistry in LWR Accidents: Review and Assessment*, NUREG/CR-2493, ORNL-5824.

4.8. ____ Devell et al., "Studies on Iodine Trapping by Water Systems at Studsvik," *Nucl. Technol.* 10, 466-71 (1971).

4.9. M. E. Witherspoon and A. K. Postma, *Fission Product Leakage from Artificial Leaks in the CSE*, BNWL-1582 (1971).

4.9a. R. L. Bennet et al., *Reactions of I-Vapor with Paints*, ORNL-TM-2760 (1970).

4.10. A. K. Postma and R. W. Zavodski, *Review of Organic Iodine Formation*, WASH-1233 (1972).

4.10a. R. J. Lemite et al., "Assessment of Iodine Behavior in Reactor Containment Buildings" AECL-6812 (April 1981).

4.11. J. B. Morris and B. Nicholls, *The Deposition of I-Vapour on Surfaces*, AERE-R 4502 (March 1965).

4.12. H. S. Rosenberg et al., *Fission Product Deposition* ... BMI-1865 (May 1969).

4.13. M. F. Osborne et al., *Iodine Sorption on Low Chromium Alloy Steel*, ORNL/TM-7755 (October 1981).

4.14. T. K. Sherwood et al., Chapter 6 in *Mass Transfer*, McGraw-Hill, New York (1975).

4.15. J. M. Genco et al., *Fission Product Deposition* ... BMI-1863 (March 1969).

4.16. Anon., *Technical Bases for Estimating Fission Product Behavior During LWR Accidents*, NUREG-0772, Chapter 5, (June 1981).

4.17. D. M. Rastler, *Suppression Pool Scrubbing Factors for Postulated Boiling Water Reactor Accident Conditions*, NEDO-25420 (June 1981).

4.18. J. L. Kelley et al., "Study of Iodine Partition Coefficients" Rep. No. UVA/532256/NEEP81/101, UVa, (October 1981).

4.19. C. A. Pelletier, "Nuclear Power Plant Related Iodine Partition Coefficients," NP-1271 (December 1979).

4.20. C. C. Lin, private communication.

5. CALCULATION PROCEDURE

5.1 Outline

The calculation of fission product transport consists of the following parts:

1. Specification of the accident sequence and the behavior of the core, pressure vessel, wetwell, drywell, and reactor building. Key parameters such as fuel temperature, coolant temperature, surface temperature of various structures, water level in the core, steam and hydrogen partial pressures, total pressure, and volumetric flowrates, as computed by the MARCH program for the specified accident scenario are employed. These parameters computed by MARCH are called as required from a storage disc.
2. Specification of reactor geometry. The core, pressure vessel, wetwell, drywell and reactor building have been subdivided to represent an idealized, but fairly realistic approximation of the actual geometry. The core is subdivided into 100 control volumes (10 radial, 10 axial) in order to match the control volumes employed in MARCH. These control volumes are described in detail below.
3. Calculation of nuclide inventories. Inventories of all key noble gas and iodine nuclides plus their significant precursors are estimated using the ORIGEN program employing as input core operational and loading data obtained from TVA and the FSAR. Nuclide decays and sources from the decay of daughters are followed as a function of time following reactor shutdown.
4. Release rates from fuel are estimated by methods outlined in Sect. 3.1.
5. Iodine chemical species alterations are followed as described in Sect. 4.2.
6. Transport assumptions. Primarily, convective transport is assumed between communicating control volumes at a rate specified by flows acquired from the MARCH program. Complete mixing is assumed in each control volume. For noble gases, the only holdup is some degree of solubility in the suppression pool.
7. Deposition and revaporization rates of iodine species on various surfaces are estimated by methods described in Sects. 4.3 and 4.4.
8. Aerosol behavior. Estimates of aerosol formation rates from overheated fuel and structure and from the interaction of molten core and concrete materials are described in Sect. 3.2. We could not estimate aerosol behavior under the complex primary system conditions mechanistically,* and have assumed that 80% of the aerosols from the overheated core remain deposited in the reactor vessel. Aerosol behavior in the drywell from the core-concrete reaction is modeled using HAARM-3.

---

*The TRAP-MELT code will be used for this purpose in future fission product transport analyses for other accident sequences.

9. The decontamination affected by the suppression pool is modeled by methods described in Sect. 4.5.
10. Output information includes the inventory of each nuclide in each control volume as a function of time. The type of inventory, e.g., surface deposit or gaseous, is included. The total release and the composition of the release to the atmosphere is totaled as a function of time.

5.2 Fission Product Inventories

The Browns Ferry Unit 1 reactor is currently in its fourth fuel cycle. There are seven different types of fuel in the reactor for Cycle 4. Some of the fuel has been in the reactor since it first reached criticality in 1973, while some of the fuel has been in the reactor only during Cycle 4. The initial fuel composition and the irradiation history of the different types of fuel were used to calculate the fuel inventory for the fission product transport analysis.

5.2.1 Fuel characteristics and loading pattern in cycle 4

The initial characteristics of the various types of fuel assemblies are given in Table 5.1. Type 1 fuel was present in Cycle 1, but was removed from the core before the start of Cycle 4. The remaining seven types of fuel have been in the reactor for differing amounts of time. Types 2 and 3 were in the initial core load, but some of these assemblies were removed after Cycle 2 and reinserted in Cycle 4. Types 4 and 5 were added in Cycle 2, while types 6 and 7 were added in Cycle 3. Type 8 was the only new fuel at the start of Cycle 4.

The initial uranium loading, the uranium enrichment, and the initial gadolinium loading have been varied for the different types of assemblies. The variations are intended to modify the core neutron flux pattern and power distribution. The gadolinium in the fuel is present only in a few rods in each assembly. This should affect the melting point of those rods, but information concerning the exact effect is proprietary to the General Electric Company and was not used in this analysis.

The approximate burnup was calculated from the average power factor of the fuel types and from an approximate irradiation history of the reactor. The power factors (provided by TVA) indicate the relative power output of the assemblies in relation to the average assembly power output of the core. The average power factors are given in Table 5.2. Much more specific power factors are available for the various axial levels and radial zones in the core. The approximate irradiation history was found in *Nuclear Industry* where the capacity factors of the United States' power reactors are given on a monthly basis.

There are a total of 764 assemblies in the core. The assemblies are unevenly mixed by type through the core. The general pattern for Cycle 4 is given in Table 5.3 for the ten radial zones in the fission product transport calculation. Type 3 assemblies are concentrated near the perimeter of the core, while Type 8 assemblies are more evenly mixed in the core.

5.2.2 Calculation of the fission product inventory in cycle 4 core

The information on the initial fuel loading and the power factors for the different types of fuel was used to calculate the fission product inventory in the Browns Ferry core. The ORIGEN2 computer program was used to perform the inventory calculations for the different types of fuel. The axial power factors and the core loading pattern were used to combine the ORIGEN2 calculations into an overall picture of the fission product distribution in the core.

The ORIGEN2 computer program is commonly used to calculate the amounts of the nuclides present in nuclear fuels. During operation of a reactor, the inventories of the various nuclides in the fuel rods change due to three basic processes: fission of the actinide elements, decay of the radioactive fission products, and transmutation of the nuclides. The ORIGEN2 program is specifically designed to follow the results of these processes for the materials present in a reactor.

The equations and calculational procedure used by the program are described elsewhere in much more detail.[5.1] The irradiation of the fuel is handled using zero-dimension geometry and spectrum-averaged neutron cross sections. The decay calculation uses standard techniques with the currently accepted decay chains and half-lives. Transmutation of the nuclides by neutron capture is a portion of the fuel irradiation calculation.

The program is not an exact model of all the effects which are present in an actual reactor and the way in which the program is used further limits its accuracy. After fuel is put into a reactor, the reactor power is cycled up and down, often on a weekly basis. The neutron energy spectrum varies when changes are made in the fuel arrangement. The flux also varies from one location in the reactor to another location due to the proximity of a control rod, and due to the local power density. These factors would have an influence on the ORIGEN2 calculation, but the information required to do a very precise calculation is either very hard to obtain or simply nonexistant. As a consequence, the calculations are performed with approximate power cycles and generically representative neutron energy spectrums (a general spectrum for BWRs was used in this case).

Comparisons have been made between this type of calculation and experimentally measured fission product inventories. Results for some important fission products and actinides were measured by Goode and compared with the results of the ORIGEN program.[5.2] The comparison between the values was generally very close and lends confidence to both the measured and calculated results.

The ORIGEN2 program requires the power output of the fuel being irradiated. The power output is directly linked to the number of fissions occuring and hence, to the inventory of fission products created in the fuel. The power distribution in the Browns Ferry Unit 1 core is very complex, given the spacial distribution of the different types of fuel assemblies in the core. Average power factors were provided by TVA for each type of fuel in the Cycle 4 core. These power factors were given for many axial levels since the power output of the core is not equal over the length of the fuel rods.

The power factors were incorporated into the ORIGEN2 calculation by making two calculations for each different type of fuel (types 4 and 5 and types 6 and 7 were grouped since they only differ in the gadolinium loading). One calculation was at the maximum, and one was at the minimum axial power factor for the fuel type. The resulting fission product inventories were blended to give a radial and axial distribution in the core.

The individual ORIGEN2 calculations were factored into an overall representation of the reactor core by considering the axial power factors and the loading pattern for the fuel. For a particular type of fuel, the power factors were given for every axial level in the core, and were used to interpolate between the ORIGEN2 results for the minimum and maximum power factors. This provided an axial fission product distribution for the average fuel assembly for each type of fuel. The core loading pattern in Table 5.3 indicates how many assemblies are in each of the ten radial zones in the core. The axial fission product distribution for each fuel type was multiplied by the number of assemblies of that type in each radial zone. The final result is a fission product distribution in the core with both an axial and a radial dependence.

This method of obtaining a fission product distribution does not consider several factors which are important variables in determining the actual distribution of fission products in the core. There is a radial power distribution in the core so that assemblies in the perimeter of the core will have a lower power output than those in the center of the core. While this radial power distribution was used to determine the average axial power factors for the fuel types, the method used in this analysis was not specific enough, for example, to indicate the difference between a Type 2 assembly in the center of the core and a Type 2 assembly near the perimeter of the core. A more detailed and more expensive calculation could be made to more accurately represent the radial power distribution, but such a calculation was not included in this analysis.

5.2.3 Core inventory of selected fission products

The total core inventory of the radioactive isotopes of krypton, xenon, iodine, and cesium at the time of reactor scram is given in Table 5.4. The chemical inventories of these elements are given in Table 5.5. The contributions of precursors have not been added into the inventories of their daughters in these tables. However, the inventories used in the fission product transport calculation do reflect the contribution of short-lived precursors.

5.2.4 Selection and handling of species for the noble gas transport analysis

The selection of isotopes and chemical species for this analysis was based on the probable significance of the various quantities on both chemical and radiological grounds. Isotopes were selected with the aid of the ORIGEN2 predictions of isotope inventories. The choice of chemical species for noble gases was predicated on the likely trapping mechanisms for

the noble gases, and the presence of chemically significant amounts of the gases.

Noble gas isotopes of radiological importance. The important noble gas isotopes were selected by considering the number of Becquerels which would be present one day after shutdown. If a very small amount of an isotope remained, the isotope was neglected. If the activity of a given isotope was a significant fraction of the total, the isotope was selected.

There are two general mechanisms which lead to the presence of significant amounts of an isotope for this selection. The isotope can have a reasonably long half-life (>2 hours), as for isotopes such as Kr-85 and Kr-88, or the isotope can have a short half-life if it also has a long-lived precursor, which is the case for isotopes such as Kr-83m and Xe-135. The precursors are halogen isotopes which undergo beta decay to form the noble gas isotopes.

The presence of the long-lived halogen precursors led to the inclusion of a simple decay calculation in this analysis. To have the proper amount of each noble gas isotope at each point in time, the decay of the noble gas as well as its halogen precursor must be considered. The decay calculation used in this analysis is the same as for the general method of the ORIGEN2 program, but in a very abbreviated form. Tests with this matrix method showed good agreement with the original ORIGEN2 calculation for decay.

The noble gases with long half-lives and the long-lived halogen precursors also have precursors. These precursors are generally much shorter-lived than the isotope being studied. As a result, the chemical inventory of the entire decay chain preceeding the chosen isotopes was lumped into the chemical inventory of that isotope as if the entire chain decayed instantly upon shutdown of the reactor. For example, the inventory of Kr-85m includes contributions from Kr-85m, Br-85, Se-85, Se-85m, As-85, and Ge-85. The contribution of these shorter-lived isotopes is generally very small (~1% in this case), but their inclusion does make a noticeable impact on the decay calculation.

The initial screening of noble gas elements is given in Table 5.6. Only the krypton and xenon make significant contributions to the total radioactivity, so all of the other listed elements were neglected. Neon and argon are activation products rather than fission products, and are formed in the cladding and core structures rather than in the fuel. Radon is a daughter isotope from decay of the actinides rather than a fission product. It builds to a low equilibrium level of activity, and is not considered to be very important in reactor accidents.

There are several krypton and xenon isotopes which contribute to the total radioactivity for these elements. The contributions of isotopes which were selected for this analysis are listed individually in Table 5.7. The isotopes which were not selected for this analysis (labeled as "Others" in Table 5.7) have a significant contribution at shutdown, but this activity is very short-lived and would not contribute significantly to the radioactivity released from the reactor building.

The contribution of halogen precursors to the noble gas activity was estimated by a simple decay calculation. The shutdown inventory of each isotope was decayed with the half-life characteristic of that isotope and

neglecting the positive contribution of its precursors. The remaining amount was then compared with the amount predicted by the ORIGEN2 decay calculation which does not neglect the contribution of the precursors. The difference between these two inventories is the amount contributed by the precursors. The results of this comparison are shown in Table 5.8. The importance of the precursors is obvious, especially in the cases of isotopes such as Xe-135 and Xe-135m. The precursors which were explicitly included in the fission product transport analysis are: Br-83, I-131, I-133, and I-135.

Noble gas species of chemical importance. While the major emphasis of this analysis has been the transport of the radioactive species, the presence of the stable species can have an impact on the chemistry and hence on the speed of transport of the radioactive species.

This impact would be an important consideration in certain types of chemical equilibria. Charcoal is used in nuclear plants, in part, to adsorb noble gases and delay their release. If only the radioactive species were considered, the charcoal would probably provide a large degree of retention. However, if both the radioactive species and the stable species are considered, the charcoal might become saturated with the noble gas and give a much smaller retention time. This situation would also occur (primarily for other, more reactive, elements) in other instances of chemical equilibria, and possibly in the eventual uptake of the element in the environment.

An initial screening was made to determine which elements would be present in chemically significant amounts. The chemical quantities of the noble gas elements are shown in Table 5.9. As with the radioactive species, krypton and xenon are the most significant contributors and the other elements can be neglected.

An additional check was made to determine the contribution of the radioactive isotopes to the total chemical inventory of krypton and xenon. The radioactive inventories are given in Table 5.10 and can be compared with the total inventories given in Table 5.9. The contribution of the radioactive isotopes is relatively minor (~6% for krypton and ~0.1% for xenon). Thus, for the example of the charcoal adsorption, the retention time of the charcoal would be almost entirely a function of the amount of the stable species with very little dependence on the amount of the radioactive species. As a consequence, the retention time of the noble gases on the charcoal could be calculated by considering only the stable species and the radioactive species would be assumed to have the same retention time. In other words, the radioactive species can be treated as minor components in the chemical portions of this analysis. This may not be the case with fission product groups other than the noble gases. In cases where the radioactive species do constitute a major fraction of the chemical inventory, the chemical portions of the transport calculation would have to consider the complications caused by the contribution of both the radioactive and stable species.

The contribution of precursors to the chemical inventory of stable noble gas species is insignificant. In this transport calculation, the halogen precursors do make a contribution to the stable isotope inventory through the decay chain but they are not important in the overall analysis of the stable isotopes.

5.2.5 Inventory of iodine nuclides

The criterion for selection of halogen elements and isotopes is similar to the criterion for the noble gases. Isotopes were selected by comparing their contribution to the radioactivity of the element one day after shutdown. Elements were selected if their chemical contribution was thought to be significant to the overall analysis. However, in this case the separation between important and unimportant isotopes is not as clear as it was for the noble gases.

The initial screening of substances is shown in Table 5.11. Bromine and iodine are both important contributors at shutdown, but the bromine activity decays quickly and does not become prominent at a later date. Thus only iodine was considered in this analysis.

The iodine isotopes which contribute to the iodine activity are given in Table 5.12. I-134 is included in the list of considered isotopes even though its contribution is relatively minor after one day. It is clearly significant at shutdown, and remains an important contributor during the first day, becoming negligible thereafter. In contrast, the iodine isotopes listed as 'Others' in Table 5.12 decay within a few minutes of shutdown and were neglected in this analysis.

The important precursors of the iodine isotopes were selected in the same manner as for the noble gases. The contibutions of precursors to the inventories are given in Table 5.13. Precursors make important contributions to both I-132 and I-134, the precursors being Te-132 and Te-134, respectively. The decay chains leading to the iodine isotopes and the tellurium precursors are considered by adding the inventory of the decay chain to the chemical inventory of the daughter.

The chemical behavior of the iodine isotopes will hinge on the assumed chemical compounds being studied and on their interactions with the reactor environment. However, before the chemical forms are chosen, it is important to consider which of the halogens might interfere with the iodine transport. This selection is performed in the same manner as for the noble gases.

The chemical inventory of the halogens is given in Table 5.14. All of the elements are significant contributors except astatine, but only iodine will be considered in this analysis. The fluorine and chlorine would probably be trapped in the cladding material for the duration of the accident because these elements form as activation products in the cladding and core structures, and their chemical reactivity would probably bind them within the metal.

Bromine, like iodine, is formed in the fuel as a fission product and would be expected to leave the fuel in the same manner as iodine. Once out of the fuel, the bromine should be more reactive than the iodine and tend to displace any previously deposited iodine. The transport calculation treats bromine in the same manner as the iodine, and it is considered as a component in the iodine equilibria. This treatment should give a slight increase in the amounts of radioactive iodine released over the amount released if the bromine were ignored, but the increase should be small since the bromine is only marginally important.

For the noble gases, the chemical contribution (in gmol) of the radioisotopes was found to be insignificant when compared to the inventory of the stable isotopes. As a result, the radioactive species were treated as

minor components in the transport calculation, meaning that the transport of the radioactive isotopes is not influenced by the transport of the bulk stable species. This is not the case for iodine. The inventory of the radioactive species is given in Table 5.15 and, as shown, constitutes about 75% of the total iodine inventory. Thus, equilibria involving iodine will be influenced by all of the isotopes which are present. This linkage is considered in this analysis.

5.3 Description of Reactor System Control Volumes

The reactor system is split into four sets of control volumes for the transport calculation. The first unit is the reactor core where the fission products originate and from which they are released. After release from the fuel, the fission products are still contained within the second unit, the reactor vessel. For the Station Blackout accident sequence, it is not necessary to include auxiliary piping such as the recirculation loops in the reactor vessel model. The third and fourth units are the primary and secondary containment structures.

5.3.1 Core control volumes

The core control volumes are grouped into ten radial zones corresponding to the ten radial zones used in the MARCH program calculation. These zones contain equal numbers of fuel assemblies, but the fission products are not produced equally between the zones. The first radial zone is in the center of the core, and the tenth is on the perimeter of the core. The radial zones are treated as parallel paths for the flow of water, steam, and fission products.

Each radial zone is further subdivided into ten axial nodes spaced evenly over the length of the fueled portion of the core. Splitting the core into these radial and axial sections allows for a more comprehensive consideration of the influence of the fission product distribution in the core. This analysis uses a calculated radial and axial distribution of the fission products, but the influence on the transport calculation is relatively minor. The effect is due to the relation between the temperature distribution in the core and the fission product release rate.

The thermal power distribution in the core, shown in Table 5.16, is concentrated in the central region of the core as are the short-lived fission products. This is in contrast to the isotopes indicative of long burnup such as Kr-85. These longer-lived isotopes are concentrated in the older assemblies which are loaded near the perimeter of the core.

The release of fission products from the fuel to the coolant channels is calculated according to the correlations presented in Sect. 3. The fuel rod is assumed to burst in the first axial node that reaches 1300°C. The burst is usually near the top of the core and the fission products are released from the entire radial zone into the coolant channel at that axial level. However, at the onset of melting fission products are also released at the axial level of the melted portion. Once released into the coolant channel, the fission products are free to be carried by the channel flow to other locations in the reactor vessel.

The overall transport calculation is predicated on the flow of fission products from one control volume to the next. During a given increment of time, some of the fluid volume (liquid or vapor) in one node will flow to the next node. The fission product inventory of a node will be carried to the next node in the same fraction as was the bulk fluid. The flow rate and volume of the liquid and vapor phases in the core are used in this calculation to determine the speed of the fission product transport.

The flow of water and steam through the core was calculated with the use of the MARCH computer program[5.4] The MARCH program was modified to output the steam and hydrogen flow rates above the water level in the core. Below the water level, the steam flow is assumed to be proportional to the axial void fraction (computed by MARCH for each axial level). All hydrogen is assumed to be generated above the waterline. The assumed water flow is the rate necessary to support the steam and hydrogen production for the higher nodes in the core.

The volumes of the core nodes were calculated from information provided by the MARCH program and the Browns Ferry FSAR. The coolant volume of an assembly was computed from the total core volume, and the volume occupied by the fuel rods. The split between liquid and vapor volume was made using the axial void fractions calculated by the MARCH program.

5.3.2 Reactor vessel control volumes

A schematic of the Browns Ferry reactor vessel internals is shown in Fig. 5.1 taken from the FSAR. The coolant flow exits from the core sequentially into an upper plenum above the top fuel guide, into a set of parallel standpipes each leading to a water separator, into the downcomer region, into the steam drier assembly, and finally into the upper head volume. The water from the separators flows down by gravity to the outer annular zone in the downcomer region to join the water being recirculated by the jet pumps. The lower plenum volume contains the core support assembly and the control rod guide tubes.

The manner in which the core flow is idealized into seven ex-core control volumes for the purpose of computation is illustrated in Fig. 5.2. The estimated surface areas and free volumes of each ex-core control volume are listed in Table 5.17.

5.3.3 Containment system control volumes

The containment system control volumes are listed in Table 5.18, and Fig. 5.3 illustrates some of the major compartments.

During a Station Blackout, the main condenser control volume is isolated from the outside environment by several closed air-operated valves in the off-gas system, and thus serves as a fission products reservoir except for some leakage into the turbine building through the turbine seals. The flows into the condenser system are leakages from the reactor vessel through the main steam isolation valves and through the steam trap drains on the HPCI and RCIC steam lines. These leakage rates were derived from the results of local leak rate testing as discussed in Appendix A.

The HPCI and RCIC systems provide a leakage-type link between the reactor vessel and the condenser system during the latter stages of a Station Blackout. Normally, the steam supply and turbine exhaust lines of these systems provide a major connection between the reactor vessel and the wetwell water, but in this accident sequence the flow of steam through each system is stopped by a loss of dc power before the core is uncovered. However, the steam supply valves remain open, so steam would flow into the lines and condense in the cool pipes. This condensate is normally removed through steam traps to the condenser system, but downstream drain isolation valves would be closed upon loss of control air during a Station Blackout. As a result, the transport calculation assumes that the pipes leading to the HPCI and RCIC system are partially filled with condensate; the flow to the main condenser is limited to a small leakage through the steam trap drain isolation valves.

The wetwell is divided into two control volumes, one representing the suppression pool and the other representing the wetwell airspace. Wetwell surface areas were estimated from drawings supplied by TVA and include the following structural items: the inner torus surface, the exterior of the ring header, the eight vent headers, the 96 downcomers, the walking platform surface, and the relief valve tailpipes. All wetwell surfaces are assumed to be covered by Placite paint (an epoxy-phenolic).

The drywell control volume is designated number 8 in Table 5.18. The drywell surface area was estimated from drawings supplied by TVA. The following equipment and structural items are included in the surface area estimate: the inner drywell and exterior pressure vessel walls, the floor and pedestal areas, the 185 control rod drive housings, and the steam, feedwater and recirculation flow piping. In addition, an allowance was added for miscellaneous items such as electrical wire conduits.

All drywell surfaces are assumed to be painted with an epoxy-type paint except the reactor vessel exterior and the steam lines which are covered with a reflective stainless steel mirror insulation.

The reactor building is represented by the ninth control volume listed in Table 5.18. Only the estimated refueling zone area above the unit-1 reactor is included in this control volume; areas above units 2 and 3 are excluded.* Although large portions of the reactor building and refueling bay are unpainted (i.e., bare cement), we assume here a completely painted reactor building interior.

The flow pathway through the secondary containment building follows the ventilation zones described in the FSAR. The lower level of the reactor building is connected to the next higher level through open hatches, stairways, and valve operator openings. The upper levels of the reactor building are connected directly to the refueling bay by pressure relief panels to the equipment hatch and to the elevator shaft. Once in the refueling bay, the fission products can pass to the environment either by leakage or via direct flow through the 18 blowout panels located in the refueling bay walls.

---

*The events of the Station Blackout accident sequence are assumed to occur simultaneously at each of the three Browns Ferry Units. Thus the available refueling floor volume has been divided among the units.

According to the plant technical specifications,[5.5] the secondary containment building leaks to the environment at a nominal rate of 100% per day at 62 Pa gauge (0.25 inches of water) overpressure. We, therefore, adopt this leakage rate from the refueling area prior to removal of the blowout panels, and assume that the leakage is not pressure dependent.

Once in the reactor building, the fission products mix with the air in the various levels of the building and subsequently leak to the atmosphere. The pressure relief panels which connect the levels of the reactor building to the refueling floor are considered in this analysis. Until these panels relieve, the flow to the refueling floor and the flow to the atmosphere are dictated by the leakage rates mentioned previously. After the panels relieve, the flow from the lower levels of the reactor building to the refueling floor and on to the atmosphere is assumed to be unobstructed. An assumption is made that the panels relieve when a gas volume addition has been made to the compartment in excess of its capacity to leak. For the blowout panels from the lower levels of the reactor building to the refueling floor, the volume addition used to trigger the blowout is 1.7% of the compartment volume corresponding to the rated pressure for the relief panels of 0.017 bar (36 lbs/ft^2). Similarly, the volume addition for the refueling area is 2.4% of the compartment volume corresponding to 0.024 bar (50 lbs/ft^2) for the pressure relief panels. In this calculation, the volume of the refueling area is taken to be the volume of the refueling floor room plus the volume of the reactor building rooms whose panels have previously relieved.

The air path through the drywell penetrations and through the refueling floor is the only path to the atmosphere considered in this calculation. The presence of the relief panels should preclude any further failure of the building due to pressurization. Thus, direct flow from the primary containment to the atmosphere, or from the lower levels of the reactor building to the atmosphere is not considered. All major flows are directed through the refueling zone. This flash-holdup has an impact on many short-lived nuclides which decay before leaving the building. In addition, reactive and semivolatile compounds deposit to some degree on the building structures which diminishes the calculated release to the atmosphere.

5.4 Iodine Transfer from the Pressure Vessel to the Drywell Following Melt-Through

Following melt-through of the pressure vessel, there soon develops a general pressure equalization throughout the containment system. Hence, the driving force for flow through the suppression pool no longer exists, and the general situation for fission product transport paths is illustrated in Fig. 2.2. Since a significant fraction of the iodine released from fuel is trapped in the pressure vessel (most likely as CsI condensed on fixed surfaces and deposited aerosol particles), it becomes important to estimate the possible rate of leakage from within the failed pressure vessel into the drywell.

The nature of the natural convection currents communicating between the failed pressure vessel and the drywell is highly problematical, depending on the geometry of the failure zone, the distribution of localized heat sources, and the convective effect of the concrete degradation gases. We have estimated the amount of flow from the failed pressure vessel to the drywell using a simple model involving only the gas expansion rate due to temperature increase. Since the MARCH code does not compute pressure vessel temperatures following melt-through, we have assumed MARCH-predicted drywell temperature increases shown in Fig. 1.11, to be typical of the pressure vessel as well.

Figure 1.11 shows the temperature rise of the drywell as predicted by MARCH to be substantial; from ~400 K at the time of vessel melt-through to a maximum of ~1200 K occurring about 6 h later and the highest temperature interval from ~1000 to ~1200 K dominates the degree of release to the drywell in the adopted model.

The model assumptions adopted to estimate the iodine transfer rate from the pressure vessel to the drywell following melt-through of the bottom head are the following:

1. The pressure vessel-to-drywell flow is generated by thermal expansion of the gas within the pressure vessel, with the temperature assumed equal to the drywell inner wall temperature during this interval. (See Fig. 1.11; pressure vessel temperatures are not available.)
2. The pressure vessel gas space is a "mixed pot" with total volume equal to the sum of all internal control volumes.
3. The iodine concentration in the pressure vessel is uniform and given by some fraction of the equilibrium value P_I^*/RT, where P_I^* is the vapor pressure of iodine sorbed on pressure vessel surfaces. We have assumed that 10% of the equilibrium concentration will be attained throughout the pressure vessel.
4. We have assumed that P_I^* is due principally to sorbed CsI: thus P_I^* is determined from Eq. (4.20). These assumption lead to the following expression:

$$q_I(t) = 0.1 \frac{dV_T}{dt} \frac{P_I^*(t)}{RT(t)} \qquad (5.1)$$

where

q_I = iodine transfer rate from the pressure vessel to the drywell, mol/s,

V_T = pressure vessel volume; equal to 4.9×10^8 cm³.

P_I^* = iodine vapor pressure; assumed to be CsI, bar,

T = pressure vessel tempeature; assumed as given in Fig. 1.11, K.

To illustrate the degree of iodine transfer indicated by Eq. (5.1), we integrate from the time of pressure vessel failure out to t = 810 (min) from the time of battery failure, an assumed end-point of the event, for illustration purposes, i.e.,

$$\text{approximate total iodine transfer} = \int_{t_1}^{t_2} 0.1 \frac{dV_T}{dt} \frac{P^*([T(t)]}{RT(t)} dt \quad (5.2)$$

The integral may be evaluated by assuming a function T(t). If we assume a linear temperature increase from 400 K at the time of drywell vent initiation (t_1 = 238 min) to 1200 K at t_2 = 810 min, the assumed end of event, Eq. (5.2) yields a total transfer of 2.3 gmoles of iodine, or ~1.4% of the total inventory.

Estimates for this study indicate that ~ 0.5% of the iodine in the pressure vessel is sorbed atomic iodine, the balance being CsI. This small amount of atomic iodine is significant because of its higher vapor pressure. If it is assumed that all of the sorbed atomic-I is vaporized during the drywell depressurization immediately following drywell failure, the following estimate of pressure vessel-to-drywell leakage results:

Pressure Vessel Temperature Assumption	Pressure Vessel-to-Drywell Leakage (g-moles)		
	CsI	Atomic-I	Total
Linear increase from 450 K at drywell failure to a maximum of 1200 K ~ 400 minutes later	2.3	0.51	2.8
Same as above, except the maximum temperature is assumed to be 1000 K	0.11	0.34	0.45

The fission product transport analysis discussed in this volume has been performed using thermal-hydraulic parameters obtained from the MARCH code results for the Station Blackout Accident sequence. However, it is generally known that the containment temperatures predicted by MARCH after failure of the reactor vessel bottom head are too high due to modeling errors in the subroutine INTER, which calculates the effects of the corium-concrete interaction. As previously noted, most of the iodine transfer from the failed reactor vessel is predicted by the model used in this analysis to occur at temperatures above 1000 K. It is believed that containment temperatures above 1000 K are unrealistic, and we have assumed that the containment temperature does not exceed 1000 K after the corium exits the reactor vessel. As indicated above, this assumption results in an estimated transfer of 0.45 g-moles of iodine from the reactor vessel internal surfaces to the drywell through the failed reactor vessel bottom head. This transfer represents about 0.29% of the initial iodine inventory in the core at the time of battery exhaustion.

ORNL–DWG 81–22798 ETD

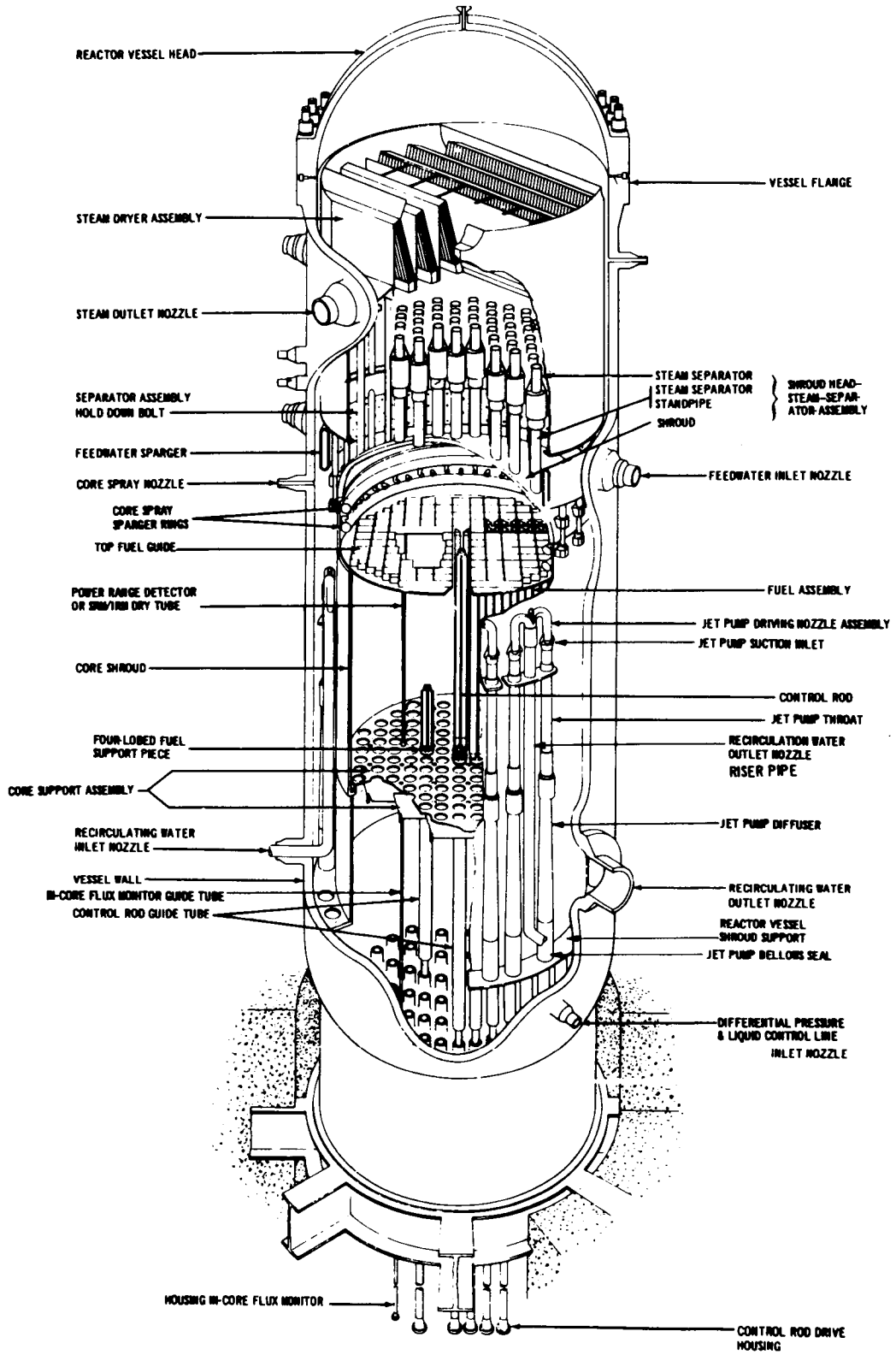

Fig. 5.1. Schematic of the reactor vessel internals (from the Browns Ferry FSAR).

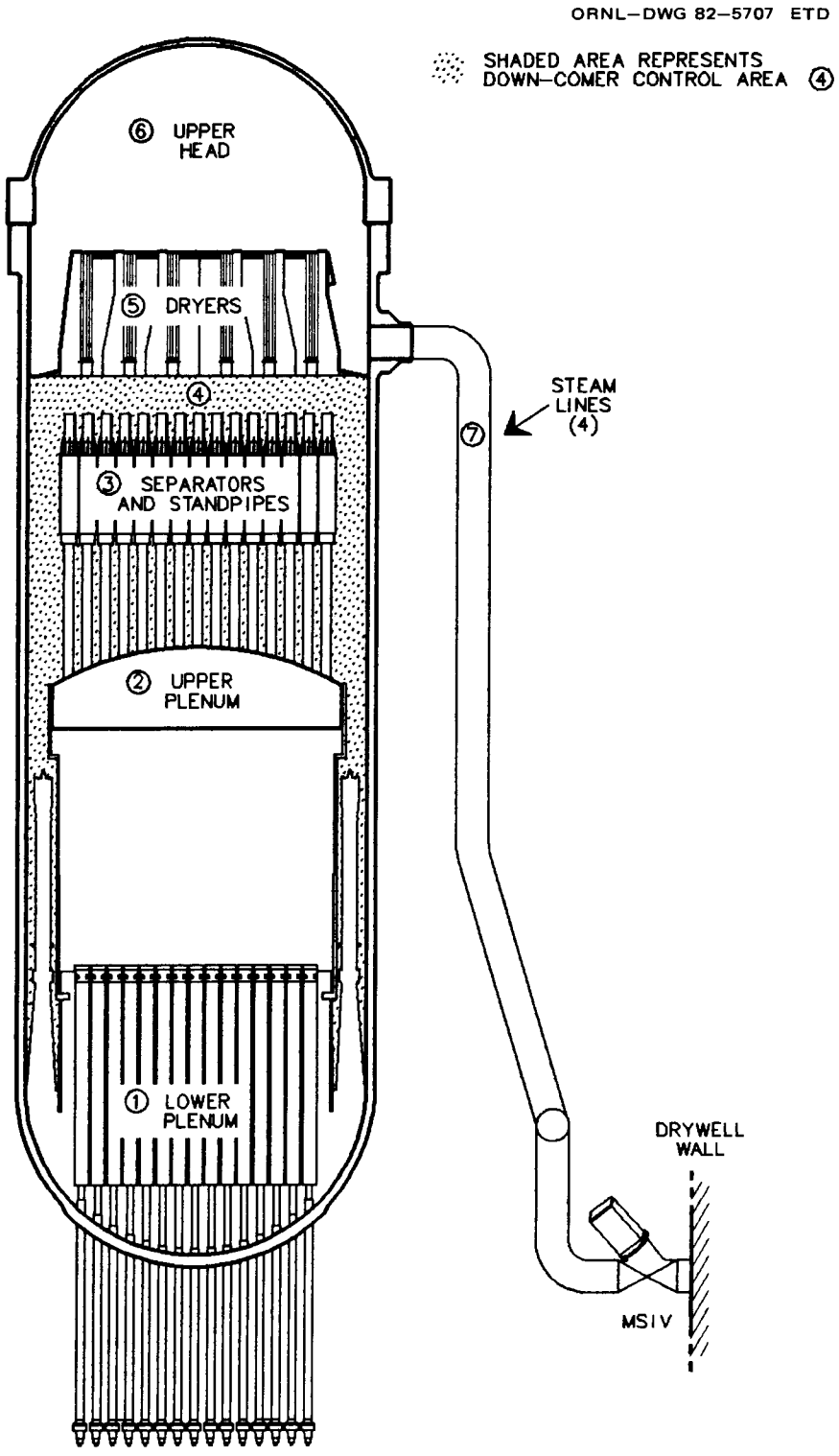

Fig. 5.2. Reactor vessel control volumes (excluding core control volume).

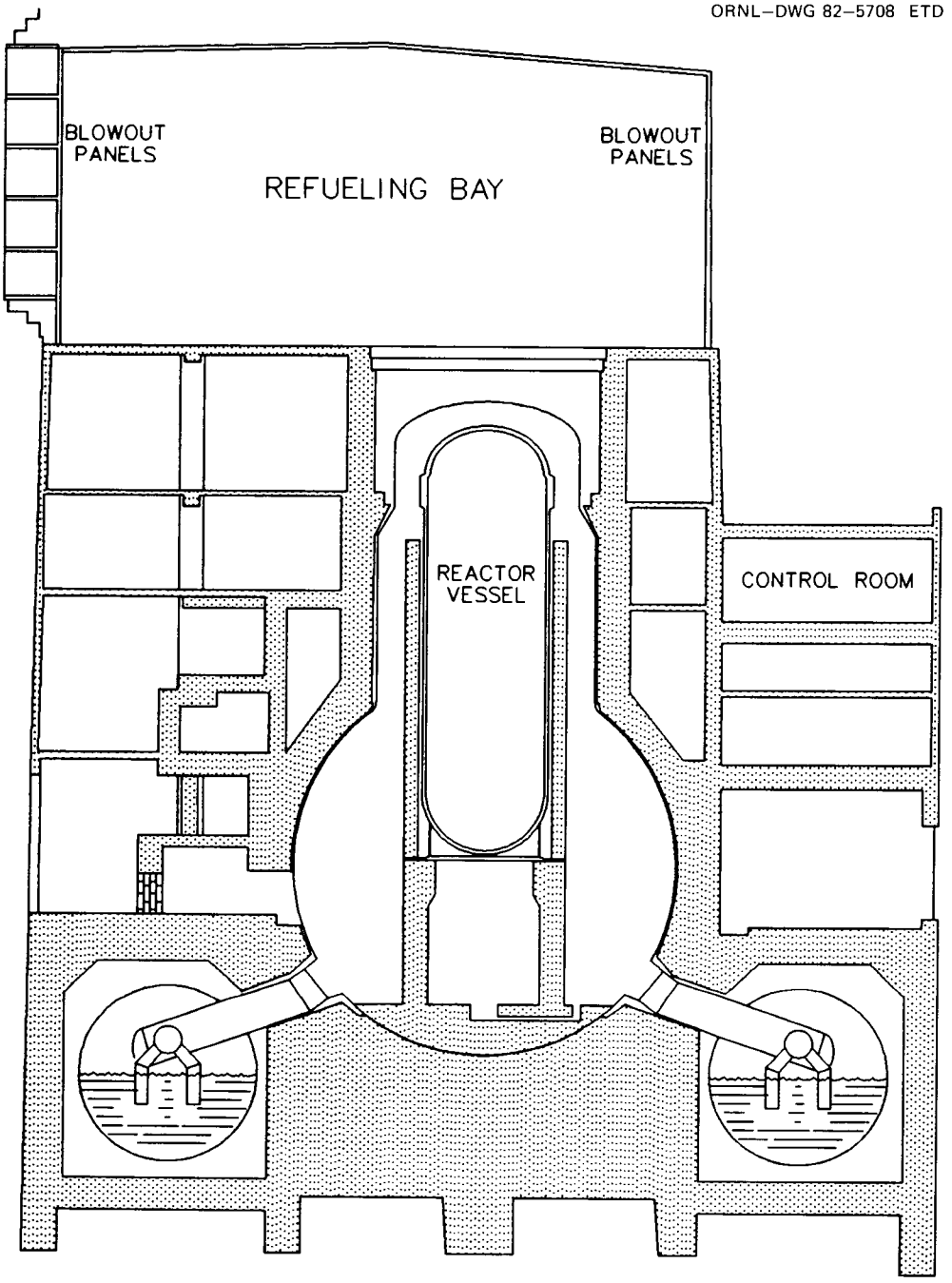

Fig. 5.3. Major compartments in the containment structure.

Table 5.1. Fuel characteristics in Cycle 4 at Browns Ferry Unit 1

Fuel type	Number of assemblies	Cycle inserted	Array size	Initial U loading (kg)	Enrichment (%)	Initial Gd loading (g)	Approximate burnup[a] (MWd/MT)
2	87	1	7 x 7	187.06	2.50	441	30,400
3	127	1	7 x 7	186.93	2.50	547	23,800
4	140	2	8 x 8	183.361	2.74	292	22,900
5	23	2	8 x 8	183.361	2.74	442	24,000
6	87	3	8 x 8	182.52	2.65	355	16,600
7	68	3	8 x 8	182.32	2.65	537	16,900
8	232	4	8 x 8	182.185	2.84	330	8,900

[a]Burnup calculated through 11 months of Cycle 4 operation.

Table 5.2. Average power factors for fuel in Cycle 4

Fuel type	Cycle 1	Cycle 2	Cycle 3	Cycle 4
2	0.991	0.991	1.010	0.972
3	0.922	0.922	0.703	0.532
4		1.188	1.138	1.120
5		1.243	1.218	1.141
6			1.258	0.996
7			1.137	1.143
8				1.140

Table 5.3. Cycle 4 core loading pattern (number of assemblies)

Fuel type	Radial zone: Center									Edge	Core total
	1	2	3	4	5	6	7	8	9	10	
2	12	22	8	7	0	17	4	8	4	5	87
3	0	2	0	9	0	0	1	8	36	71	127
4	17	8	29	17	34	34	0	1	0	0	140
5	12	3	8	0	0	0	0	0	0	0	23
6	0	8	16	0	0	0	19	32	12	0	87
7	14	10	4	16	20	0	0	4	0	0	68
8	21	24	11	28	22	26	52	24	24	0	232

Table 5.4. Core inventory of selected radioisotopes in Browns Ferry Unit 1 at the end of 11 months of Cycle 4 operation

Isotope	Half-life (s)	Total core inventory (PBq)[a]
KR-83m	6.70E 03	4.04E 02
Kr-85	3.40E 08	2.48E 01
Kr-85m	1.58E 04	8.62E 02
Kr-88	1.01E 04	2.34E 03
Xe-131m	1.02E 06	3.56E 01
Xe-133	4.55E 05	6.32E 03
Xe-133m	1.95E 05	2.04E 02
Xe-135	3.31E 04	1.76E 03
Xe-135m	9.36E 02	1.28E 03
I-130	4.43E 04	8.05E 01
I-131	6.97E 05	3.18E 03
I-132	8.28E 03	4.61E 03
I-133	7.52E 04	5.96E 03
I-134	3.12E 03	7.20E 03
I-135	2.41E 04	6.13E 03
Cs-134	6.47E 07	3.07E 02
Cs-134m	1.04E 04	1.12E 02
Cs-136	1.12E 06	1.17E 02
Cs-137	9.54E 08	2.75E 02
Cs-138	1.93E 03	6.01E 03
Cs-139	5.70E 02	5.69E 03

[a] 1.0 Petabecquerel (PBq) = 27,027 Curies.

Table 5.5. Core inventory of Krypton, Xenon, Iodine, and Cesium in Browns Ferry Unit 1 at the end of 11 months of Cycle 4 operation

Element	Total core inventory (gmol)
Krypton	319
Xenon	2810
Iodine	134
Cesium	1500

Table 5.6. Noble gas inventory of example Browns Ferry assembly *(TBq)

	Time (day after shutdown)				
	0	1	3	10	30
Helium	6.07E-5	-	-	-	-
Neon	7.99E-3	-	-	-	-
Argon	2.96E-3	2.90E-3	2.79E-3	2.43E-3	1.63E-3
Krypton	1.71E 4	9.18E 1	5.55E 1	5.55E 1	5.55E 1
Xenon	4.37E 4	1.24E 4	8.14E 3	3.28E 3	2.52E 2
Radon	1.20E-5	1.21E-5	1.21E-5	1.23E-5	1.29E-5

*1 curie = 0.037 terabecqerel (TBq)

Table 5.7. Contributions of isotopes to the krypton and xenon radioactivity in example Browns Ferry assembly (TBq)

	Time (day after shutdown)				
	0	1	3	10	30
Kr-83m	5.29E 2	2.09E 0	2.08E-6	-	-
Kr-85	5.55E 1	5.55E 1	5.55E 1	5.55E 1	5.55E 1
Kr-85m	1.05E 3	2.60E 1	1.55E-2	7.99E-14	-
Kr-88	2.74E 3	7.84E 0	6.36E-5	-	-
Others	1.27E 4	4.14E-3	4.03E-9	4.03E-9	4.03E-9
Total Kr	1.71E 4	9.18E 1	5.55E 1	5.55E 1	5.55E 1
Xe-131m	5.77E 1	5.77E 1	5.66E 1	4.88E 1	2.22E 1
Xe-133	9.77E 3	9.47E 3	7.81E 3	3.21E 3	2.30E 2
Xe-133m	3.22E 2	2.89E 2	1.82E 2	2.18E 1	3.85E-2
Xe-135	2.38E 3	2.42E 3	1.02E 2	3.14E-4	3.96E-20
Xe-135m	2.08E 3	1.23E 2	8.03E-1	1.80E-8	-
Others	2.90E 4	4.59E-2	3.85E-2	2.10E-2	3.74E-3
Total Xe	4.37E 4	1.24E 4	8.14E 3	3.28E 3	2.52E 2

Table 5.8. Precursor contribution to post-shutdown inventories of krypton and xenon (%)

	Time (day after shutdown)			
	1	3	10	30
Kr-83m	97.2	100.0	-	-
Kr-85	-	-	-	-
Kr-85m	-	-	-	-
Kr-88	-	-	-	-
Xe-131m	5.6	14.4	34.1	54.6
Xe-133	9.6	15.8	18.8	19.2
Xe-133m	18.8	31.6	37.6	37.7
Xe-135	84.2	90.4	91.4	91.4
Xe-135m	100.0	100.0	100.0	

Table 5.9. Chemical inventories of noble gases in example Browns Ferry assembly at shutdown

Element	Inventory (gmole)
Helium	1.47E-1
Neon	4.45E-6
Argon	8.44E-6
Krypton	7.59E-1
Xenon	7.50E 0
Radon	1.60E-15

Table 5.10. Chemical inventories of radioactive krypton and xenon in example Browns Ferry assembly (gmole)

	Time (day after shutdown)				
	0	1	3	10	30
Krypton	4.52E-2	4.51E-2	4.51E-2	4.50E-2	4.50E-2
Xenon	1.11E-2	1.07E-2	8.72E-3	3.62E-3	3.04E-4

Table 5.11. Halogen inventory of example Browns Ferry assembly *(TBq)

	Time (day after shutdown)				
	0	1	3	10	30
Fluorine	2.68E-2	-	-	-	-
Chlorine	5.48E-2	9.88E-5	9.88E-5	9.88E-5	9.88E-5
Bromine	9.32E 3	1.99E 1	7.55E 0	2.78E-1	2.25E-5
Iodine	5.96E 4	1.63E 4	8.95E 3	3.13E 3	4.11E 2
Astatine	2.58E-9	2.58E-9	2.56E-9	2.41E-9	1.74E-9

*1 curie = 0.037 terabecqerel (TBq)

Table 5.12. Contributions of isotopes to the iodine radioactivity in example Browns Ferry assembly (TBq)

	Time (day after shutdown)				
	0	1	3	10	30
I-130	2.51E 2	6.59E 1	4.44E 0	3.61E-4	7.36E-16
I-131	5.14E 3	4.77E 3	4.07E 3	2.24E 3	4.00E 2
I-132	7.36E 3	6.03E 3	3.92E 3	8.88E 2	1.26E 1
I-133	1.01E 4	4.66E 3	9.39E 2	3.48E 0	3.92E-7
I-134	1.11E 4	2.37E-4	7.84E-21	-	-
I-135	9.55E 3	7.70E 2	5.03E 0	1.12E-7	-
Others	1.63E 4	2.28E-4	2.28E-4	2.29E-3	2.29E-3
Total I	5.96E 4	1.63E 4	8.95E 3	3.13E 3	4.11E 2

Table 5.13. Precursor contribution to post-shutdown inventories of iodine isotopes (%)

	Time (day after shutdown)			
	1	3	10	30
I-130	0.5	0.5	0.7	1.4
I-131	1.3	2.3	3.0	3.0
I-132	99.9	100.0	100.0	100.0
I-133	2.2	2.2	2.2	2.2
I-134	73.2	73.2	-	-
I-135	-	-	-	-

Table 5.14. Chemical inventories of halogens in example Browns Ferry assembly at shutdown

Element	Inventory (gmole)
Fluorine	1.06E-1
Chlorine	2.80E-3
Bromine	4.82E-2
Iodine	3.71E-1
Astatine	1.99E-22

Table 5.15. Chemical inventories of radioactive iodine in example Browns Ferry assembly (gmole)

	Time (day after shutdown)				
	0	1	3	10	30
Radioiodine	2.80E-1	2.80E-1	2.78E-1	2.75E-1	2.72E-1
Total iodine	3.71E-1	3.69E-1	3.67E-1	3.64E-1	3.62E-1

Table 5.16. Thermal power in core control volumes, 2.4 hours after shutdown (kW)

Axial node		Center	Radial zone								Edge
		1	2	3	4	5	6	7	8	9	10
Top	10	149	136	144	132	146	145	114	112	96	80
	9	277	260	269	253	276	267	241	232	190	141
	8	361	341	351	334	362	352	330	311	256	185
	7	407	387	397	381	412	400	384	358	297	213
	6	431	412	422	407	438	425	417	387	322	230
	5	444	428	436	423	453	440	440	406	339	240
	4	452	436	444	431	462	448	456	418	345	237
	3	452	436	444	433	465	449	467	423	346	226
	2	426	411	417	410	440	423	448	400	322	198
Bottom	1	245	231	241	229	251	246	230	210	172	117

Table 5.17. Reactor vessel control volumes - surface areas and free volumes

Control volume	Surface area (m^2)	volume (m^3)
1. Lower plenum	1004.2	90.7
2. Upper plenum	34.8	27.8
3. Steam separators and standpipes	640.0	38.0
4. Downcomer	1256.9	182.6
5. Steam driers	2945.0	64.4
6. Upper head	197.6	89.0
7. Steam lines	333.9	55.1

Table 5.18. Containment control volumes

Control volumes	Area (m^2)	Water volume (m^3)	Vapor volume (m^3)	Comments
1. Condenser system	[a]	150	[a]	Collects leakage from MSIV's
2. Relief valve 1	[a]	[a]	2.0	Piping to T-quencher
3. Main steam lines	[a]	[a]	165	Path to main condenser
4. HPCI system	[a]	1.5	1.6	Pipe to steam trap
5. RCIC system	[a]	0.21	0.2	Pipe to steam trap
6. Wetwell-1	3,532	3,828		Suppression pool
7. Wetwell-2	5,200		3,660	Wetwell airspace
8. Drywell	24,280		4,502	
9. Building			32,280	Unit 1 reactor building
10. Refueling bay[b]	5,200		27,000	Above 664 ft
11. Release-1[c]				From refueling bay
12. Release-2[c]				Through blowout panels
13. Release-3[c]				Vent through stack
14. Total release[c]				

[a] Not used in this version.

[b] Does not include portion above units 2 and 3.

[c] Dummy control volumes to collect releases to atmosphere.

References for Section 5

5.1. A. G. Croff, *ORIGEN2 – A Revised and Updated Version of the Oak Ridge Isotope Generation and Depletion Code*, ORNL-5621 (July 1980).

5.2. J. H. Goode, R. G. Stacy, and V. C. A. Vaughen, *Comparison Studies of Head-end Reprocessing Using Three LWR Fuels*, ORNL/TM-7103 (June 1980).

5.3. A. G. Croff, *A User's Manual for the ORIGEN2 Computer Code*, ORNL/TM-7175 (July 1980).

5.4. R. O. Wooten and H. I. Avci, *MARCH Code Description and User's Manual*, Battelle Columbus Laboratories/USNRC Report NUREG/CR-1711 (October 1980).

5.5. Browns Ferry Nuclear Plant Technical Specifications.

6. RESULTS

6.1 Introduction

The results presented in this section are based on the fission product transport pathways described in Sect. 2, release rates from fuel described in Sect. 3, and the chemical property and transport rate assumptions described in Sect. 4. Additional calculational bases are given in Sect. 5, particularly Sect. 5.4, which describes the model used for determining the transfer rate from the failed reactor vessel.

6.2 Noble Gas Transport

The predicted inventories of the noble gases krypton and xenon in the various control volumes within the reactor building and the concomitant release to the surrounding atmosphere are plotted as functions of time in Figs. 6.1 through 6.17. These graphs serve to illustrate general time trends, whereas Tables 6.1 and 6.2 provide inventory estimates at several key locations and times in a more quantitative fashion. In each of the figures, the ordinate scale represents the radioactive inventory expressed as a fraction of the radioactive inventory that existed in the core at the time of reactor scram. The abscissa scale refers to times measured from battery failure which also corresponds to the time when the reactor vessel water injection systems (HPCI and RCIC) fail, leading to boiloff of the water in the reactor vessel and core uncovery. As noted in the Preface, the time from the initiating reactor scram and Station Blackout event to battery exhaustion has been assumed to be 4 h.

Figures 6.1 and 6.9 show respectively the inventories of krypton and xenon remaining in the intact portions of the core. After the failure of the water injection systems, the core is uncovered at time 1.0 h* and a relatively rapid decrease in noble gas inventory is predicted following the onset of cladding failures at time 1.7 h and the beginning of core melting at time 2.0 h. About 6% of the total noble gas inventory existing in the fuel at the time of central core collapse into the reactor vessel lower head is predicted to be retained in the outer ring of fuel assemblies which remain standing in place because the decay heat is sufficiently low so that the assumed cladding failure temperature** is never reached.

Figures 6.2 and 6.10 show the fraction of krypton and xenon retained within the slumped fuel in the bottom head of the reactor vessel and after drywell failure, within the fuel debris in the drywell. The abrupt initiation of these curves at 2.3 h (137 min) signifies the time of central

---

*All times in this section are times from battery failure.

**As discussed in Sect. 3.1, the cladding is assumed to fail when the temperature reaches 1300°C.

core collapse. The subsequent inventory decreases are due to the combined effect of radioactive decay plus continued evolution from the fuel debris.

Figures 6.3 and 6.11 show the calculated krypton and xenon inventories in the reactor vessel atmosphere up to the time of vessel failure at 2.9 h (172 min). The sudden decrease at the time of core collapse is due to the large quantity of steam generated when the core falls into the water in the lower head of the reactor vessel; the steam serves to flush the noble gases from the vessel. After the failure of the reactor vessel lower head at time 2.9 h, the concentration of noble gases in the failed reactor vessel would equilibrate with the concentration in the drywell.

The noble gases released from the reactor vessel prior to failure of the lower head are passed into the wetwell pressure suppression pool along with the decay-heat generated steam via a pathway through the primary relief valves and tailpipes to emerge from T-quencher devices* about 14 ft below the pool surface. The steam is condensed and a small fraction of the noble gas effluent is dissolved in the water; most of the noble gas inventory breaks the pool surface and enters the wetwell airspace.

The inventories of krypton and xenon dissolved in the pressure suppression pool are shown as functions of time in Figs. 6.4 and 6.12, respectively. Virtually all of the noble gas release from the fuel into the reactor vessel atmosphere occurs before the central core collapses (Figs. 6.3 and 6.11) and the noble gas inventories in the suppression pool remain approximately constant after this event until the failure of the drywell. There is a slight increase at the time of reactor vessel failure because of the consequent expansion of the drywell atmosphere into the suppression pool through the vent pipes and downcomers. As shown in Figs. 6.4 and 6.12, about 0.4% of the krypton and 4% of the xenon in the core at the time of reactor scram are retained in the suppression pool up to the time of drywell failure.

The primary containment is predicted to fail at 4.1 h after battery failure due to overtemperature-induced degradation of the electrical penetration assembly seals in the drywell. When this occurs, the pressure in the primary containment rapidly drops from 0.90 MPa (130 psia) to atmospheric pressure and about 4% of the water in the pressure suppression pool flashes to steam. As illustrated in Figs. 6.4 and 6.12, the consequent pool boiling drastically decreases the inventory of dissolved noble gases. It should be noted that the xenon inventory in the pool increases somewhat at times after drywell failure because of the source from iodine decay.

The wetwell atmosphere, i.e., the torus airspace above the pressure suppression pool, is the main repository for noble gases between the time of fuel melt initiation and drywell failure. (See Fig. 6.13 for xenon.) These inventories are produced by the predominant fraction of the noble gases released from the T-quenchers that is not dissolved and therefore breaks the pool surface. As shown in Fig. 6.13, there is a significant increase upon reactor vessel lower head failure when the resulting increase in drywell pressure causes the drywell atmosphere to expand into the wetwell through the vent pipes and downcomers. Upon failure of the

---

*The T-quenchers are described in Appendix D of Volume I of this report.

drywell electrical penetration assembly seals, there is a rapid venting of the wetwell airspace through the wetwell-drywell vacuum breakers into the drywell. The steam flashed from the pressure suppression pool sweeps much of the noble gas inventory from the wetwell airspace into the drywell and the resulting decrease in the wetwell inventory of xenon is evident in Fig. 6.13. The inventories of krypton and xenon in the drywell atmosphere are shown in Figs. 6.5 and 6.14, respectively, and the transient increase in these inventories due to influx from the wetwell upon failure of the drywell is indicated. Subsequently, the drywell inventories decrease due to leakage through the failed electrical penetration assembly seals into the Reactor Building.

The buildup of drywell noble gas inventory before failure of the primary containment as shown in Figs. 6.5 and 6.14 is due to the venting of the wetwell airspace back through the vacuum breakers inte the drywell as the pressure suppression pool heats up and the wetwell pressure intermittently exceeds the pressure in the drywell. A maximum occurs after core collapse as a result of the large steam influx into the pressure suppression pool from the reactor vessel at this time. A comparison of Figs. 6.14 and 6.13 confirms that the noble gas inventory in the drywell is significantly less than that in the wetwell atmosphere during this period. After reactor vessel melt-through, Concrete degradation gases from the core-concrete reaction flush the drywell atmosphere into the wetwell through the vent pipes and downcomers until drywell failure.

The inventories of krypton and xenon which have escaped from the primary containment and are maintained in the Reactor Building are shown as functions of time in Figs. 6.6 and 6.15. Before drywell failure, leakage from the primary containment is modeled as discussed in Sect. 2 and Appendix B and there is a relatively slow rate of noble gas escape which begins after the onset of cladding failures. As expected, there is a large and sudden increase in the Reactor Building inventory at the time of gross failure of the drywell; the subsequent decrease is due to the predicted opening of the reactor building to refueling floor to atmosphere blowout panels.

Figures 6.7 and 6.16 illustrate the result of a significant fission product transport pathway to the main condenser system which exists via steam leakage past the shut MSIVs during times prior to reactor vessel failure. The leakage would continued at a reduced rate after the reactor vessel is depressurized into the drywell. As indicated by the results listed in Tables 6.1 and 6.2, approximately 0.08% of the initial krypton and 0.7% of the initial xenon inventory in the core at the time of reactor scram is contained within the main condenser system at the time of drywell failure. From there, these noble gases can leak into the Turbine Building via the seals of the low-pressure turbines.*

The inventories of krypton and xenon contained in the atmosphere surrounding the Reactor Building are shown as functions of time in Figs. 6.8 and 6.17, respectively. The total escape is limited to that provided by the assumed building leakage of 100% of building volume per day until the

---

*Gland sealing steam would not be available under Station Blackout conditions. MSIV leakage is discussed in Sect. A.3.1 and Appendix B.

drywell fails and the blowout panels relieve immediately thereafter; when this occurs, a large quantity of noble gas is passed to the atmosphere. As seen in these figures and in Tables 6.1 and 6.2, about 4% of the initial krypton and 79% of the initial xenon inventory in the core at the time of reactor scram is in the atmosphere at 491 min (about 8 h) after the loss of battery power. The principal attenuation is due to radioactive decay.

6.3 Iodine Transport

The predicted inventories of radioactive iodine in the various control volumes within the Reactor Building and the concomitant release to the surrounding atmosphere are plotted as functions of time in Figs. 6.18 through 6.29. The time scale for each of these figures proceeds from the point of battery failure in the Station Blackout sequence, and the inventories are presented as fractions of the quantity existing in the core at the time of reactor scram. The inventories at key locations at various times during the accident sequence are given in absolute terms in Table 6.3.

The iodine inventory remaining in the intact portions of the core is shown in Fig. 6.18. As indicated in Table 6.3, the total iodine activity in the core at the time of battery failure is 18,900 PBq.* Figure 6.18 shows that the period of rapid iodine loss from the intact core which begins with the onset of cladding failures is terminated with a sudden inventory decrease at the time the central core collapses into the bottom head of the reactor vessel. The results presented in Table 6.3 indicate that the inventory of iodine in fuel immediately after core slump is reduced to 3321 PBq, distributed as 2390 PBq in the molten core debris in the bottom of the reactor vessel and 931 PBq contained in the outer ring of fuel assemblies which does not reach cladding failure or melting temperature and remains standing in place, as discussed previously. After the collapse of the major portion of the core into the reactor vessel bottom head at time 2.3 h, the inventory shown in Fig. 6.18 represents only the iodine inventory in the intact outer ring of fuel assemblies and the subsequent decrease is due to the net effect of tellurium and iodine decay only.

The iodine inventory in the molten core debris is shown in Fig. 6.19. The molten core debris is initiated in the reactor vessel lower head at the time of core collapse (2.3 h) and later transfers to the drywell upon failure of the reactor vessel lower head at time 2.9 h.

---

*It should be recalled that in the Station Blackout accident sequence the batteries are assumed to fail 4 h after the reactor scram and inception of the blackout. Thus, this value reflects the core inventory after 4 h of decay. The iodine inventory in the core at the time of reactor scram was 27,730 PBq.

As shown on Fig. 6.20 and indicated in Table 6.3, the principal iodine repositories are the reactor vessel internal surfaces on which ~80% of the aerosol particles are assumed to have deposited.* These particles possess the major iodine inventory, principally condensed CsI.

The calculated inventory of gaseous iodine in the reactor vessel atmosphere is shown in Fig. 6.21. The inventory builds up rapidly after the inception of cladding failures, then stabilizes as the gaseous iodine is passed to the pressure suppression pool with the steam exhausted through the primary relief valves. The collapse of the central core is reflected as a sudden large decrease in the gaseous iodine inventory caused by the flushing effect of the large amount of steam generated when the slumped core falls into the water in the reactor vessel lower head.

The calculated inventory of iodine sorbed on aerosol particles suspended within the reactor vessel is shown in Fig. 6.22. The calculational model predicts that iodine inventory sorbed on aerosol particles will vary in the same manner as the gas-phase inventory shown in Fig. 6.21. This is reasonable because the gas-phase iodine serves as the source for iodine sorption on the aerosols, and the suspended aersosols would also be flushed from the reactor vessel after core collapse. Comparison of Figs. 6.22 and 6.21 shows that the inventory of aerosol-sorbed iodine is predicted to exceed the gaseous iodine inventory in the reactor vessel throughout the period after cladding failure.

The predicted inventory of radioactive iodine in the pressure suppression pool is shown in Fig. 6.23. Iodine is passed into the pressure suppression pool through the primary relief valves along with the steam and hydrogen gas generated after the core is uncovered and the claddings begin to fail. As discussed in Sect. 4.5, the relief valve discharge enters the pool water through T-quencher devices at a depth of about 4.3 m (14 ft) below the pool surface. Most of the iodine leaving the reactor vessel prior to melt-through is retained in the suppression pool (see Fig. 6.23 and Table 6.3). The inventory in the pool increases rapidly up to the time of core slump (at t = 2.3 h or 137 min) at which time the iodine release rate from the slumped fuel diminishes due to a reduction in the exposed core surface area for evolution and quenching when exposed core surface area for evolution and quenching when the molten core debris rests in the the lower vessel structure.

The gaseous iodine inventory in the drywell is shown in Fig. 6.24. This inventory builds up to a low level before reactor vessel failure because of a small feedback of iodine from the wetwell airspace via the vacuum breakers on the vent pipes, as discussed previously. The inventory decreases upon reactor vessel failure because the pressure in the drywell increases and the drywell atmosphere expands through the vent pipes and downcomers into the pressure suppression pool, emerging from the downcomer exits about 1.2 m (4 ft) below the pool surface. After the initial decrease, and pressure equilibration between the drywell and the wetwell, the iodine inventory in the drywell increases slowly because the small amount of additional iodine release from the corium now enters the drywell atmosphere directly. There is a short period of rapid decrease following

---

*These reactor vessel internal surfaces include the steam separators and the dryer assemblies.

drywell failure as the primary containment pressure is relieved into the Reactor Building. The subsquent gaseous iodine inventory in the drywell is quite low due mainly to the high temperature projected by the MARCH code (see Fig. 1.11). Gas evolution from the corium-concrete reaction also serves to reduce iodine gas phase concentration and thereby reduce the driving force for deposition on drywell surfaces.

Figure 6.25 illustrates the iodine inventory developed in the main condenser system by leakage through the shut MSIVs. Table 6.3 indicates that the iodine activity level in this control volume is 6.4 PBq at the time of drywell failure. Although a great deal of water exists in the main condenser system and there is a large surface area available for deposition, a small portion of this activity would leak into the Turbine Building through the low pressure turbine seals.

Projected levels of inorganic and organic iodine in the reactor building atmosphere are shown in Figs. 6.26 and 6.27, while Figs. 6.28 and 6.29 show respectively the effect of organic iodide and total iodine leakage from the Reactor Building to the surrounding environment.

The predicted total iodine inventory* in the reactor building atmosphere is shown in Fig. 6.26. The buildup before the gross failure of the drywell at time 4.1 h is due to leakage from the drywell penetrations and seals, which is discussed in Sect. 2 and Appendix B. The reactor building inventory increases markedly after the failure of the drywell, then decreases in response to the venting of the building through the blowout panels from the building to the refueling floor, and from the refueling floor to the atmosphere.**

The inventory of organic iodide in the Reactor Building is shown in Fig. 6.27. As can be seen by a comparison of Figs. 6.27 and 6.26, the organic iodide inventory exhibits the same variation with time as the overall iodine inventory, but constitutes an insignificant fraction of the total. The organic iodide inventory is plotted separately because it is much less chemically reactive or soluble in water than gaseous I_2 and therefore behaves differently in the atmosphere.

Figure 6.28 illustrates the inventory of organic iodide in the surrounding atmosphere which results from the release from the Reactor Building and refueling floor through the blowout panels. As seen, organic iodide release forms a negligible fraction of the total release, according to the assumed formation rate model. The principal feature of this model is the assumption that temperatures below 300°C are required for organic iodide production: thence no formation occurs in the drywell and resistance times in the Reactor Building are too short for significant formation on the time scale of ~10 h.

The total iodine inventory in the atmosphere surrounding the Reactor Building resulting from the postulated Station Blackout accident sequence

---

*Mostly gaseous I_2.

**It is important to recall that the refueling floor is common to the three Browns Ferry units and that this study has been conducted under the assumption that the Station Blackout accident sequence occurs simultaneously at each unit. If the accident sequence were to occur on just one or perhaps two units, the pressure buildup on the refueling floor would be less, and the blowout panels might not relieve to the atmosphere.

is shown in Fig. 6.29. The release before the predicted gross failure of the drywell at 4.1 h after battery failure is very small, limited by the assumed leakage rates* from the intact primary and secondary containments. Drywell failure and relief to the atmosphere through the reactor building and refueling floor blowout panels are predicted to occur almost simultaneously and as shown on Fig. 6.29, there is a large, quick release of the iodine inventory built up and stored at pressure within the primary containment prior to this time. Figure 6.29 and Table 6.3 show that about 12 h after battery failure, ~135 PBq, representing about 0.49% of the initial inventory in the core at the time of reactor scram, resides in the atmosphere.

6.4 Aerosol Production in the Pressure Vessel

Table 6.4 lists the projected quantities of aerosols produced in the reactor vessel by overheated core and structure according to the models presented in Sect. 3.2.1. The total quantity produced up to the time of pressure vessel melt-through is estimated as 13.3 kg, representing about 0.008% of the total core plus associated structural mass. This estimate is significantly lower than other estimates, most of which are based on a proportionate scale-up of experimental data. The model adopted here predicts large core masses to produce less aerosols per unit mass than observed in small experiments of the 1-kg scale.

The fraction of aerosols assumed to be deposited on the reactor vessel internal surfaces is 80% (10.7 kg); this is based on information obtained from a series of TRAP-MELT runs using BWR geometry.** The possible range of the fractional aerosol deposition on the extensive surface area internal to the reactor vessel is perhaps 0.6 to 0.99: 0.80 is a reasonable midrange value.

---

*Discussed in Sect. 2 and Appendix B.

**Performed at Battelle Columbus Laboratories; information forwarded by J. A. Gieseke.

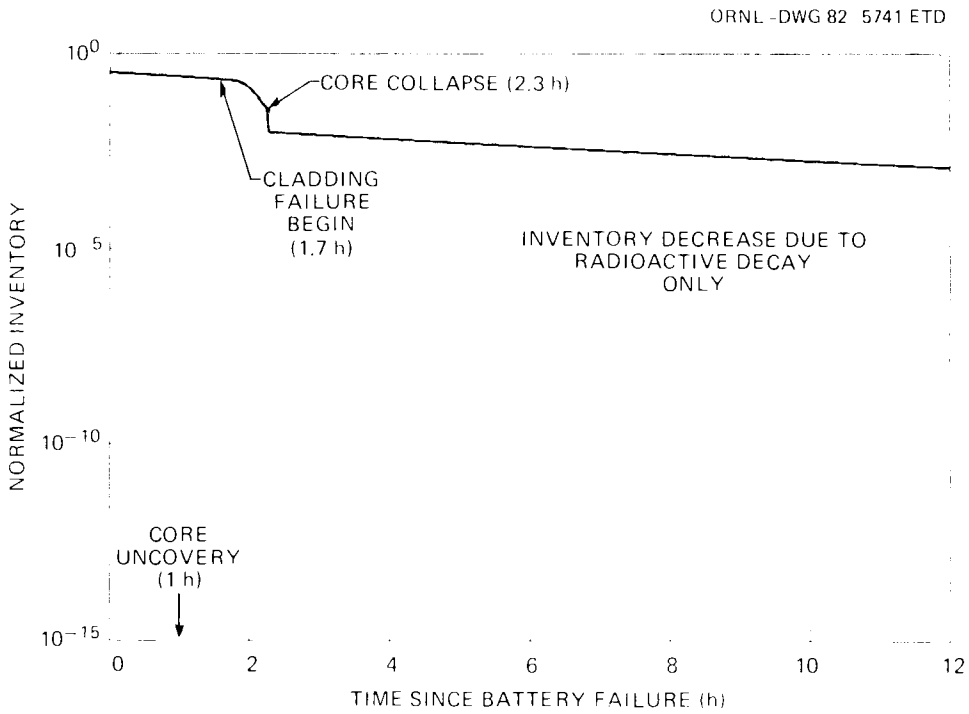

Fig. 6.1. Krypton inventory in intact portions of the core.

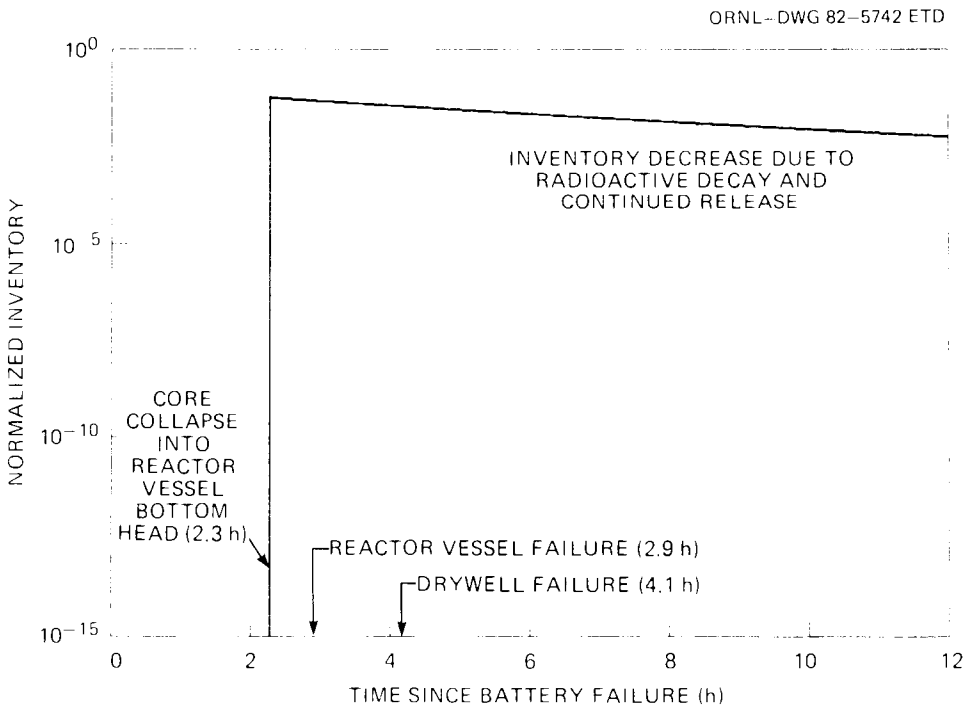

Fig. 6.2. Krypton inventory in molten core debris.

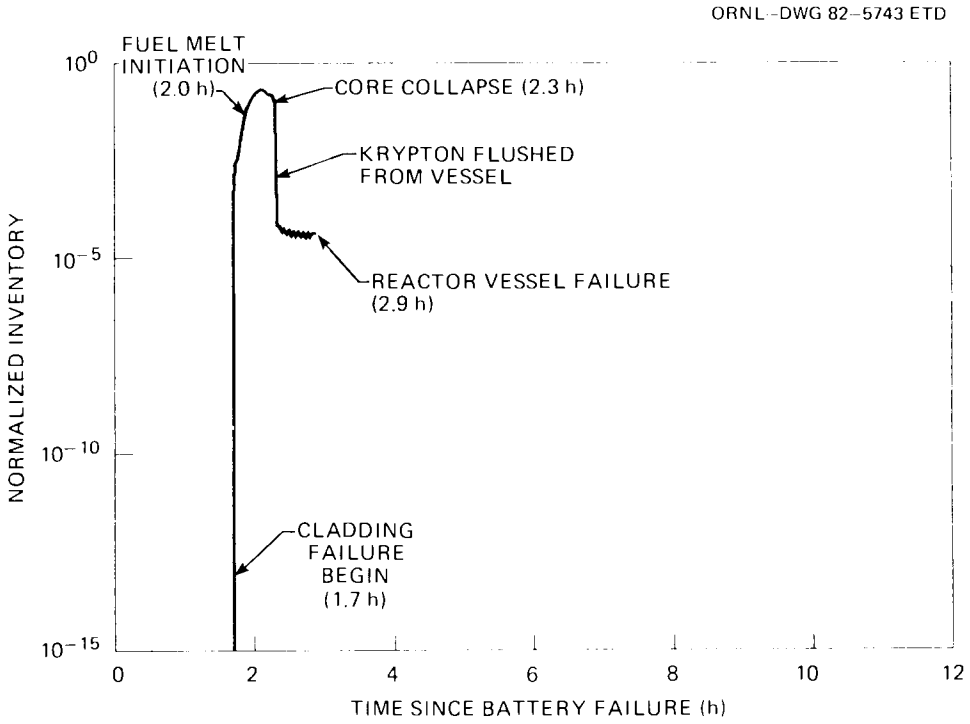

Fig. 6.3. Krypton inventory in reactor vessel atmosphere.

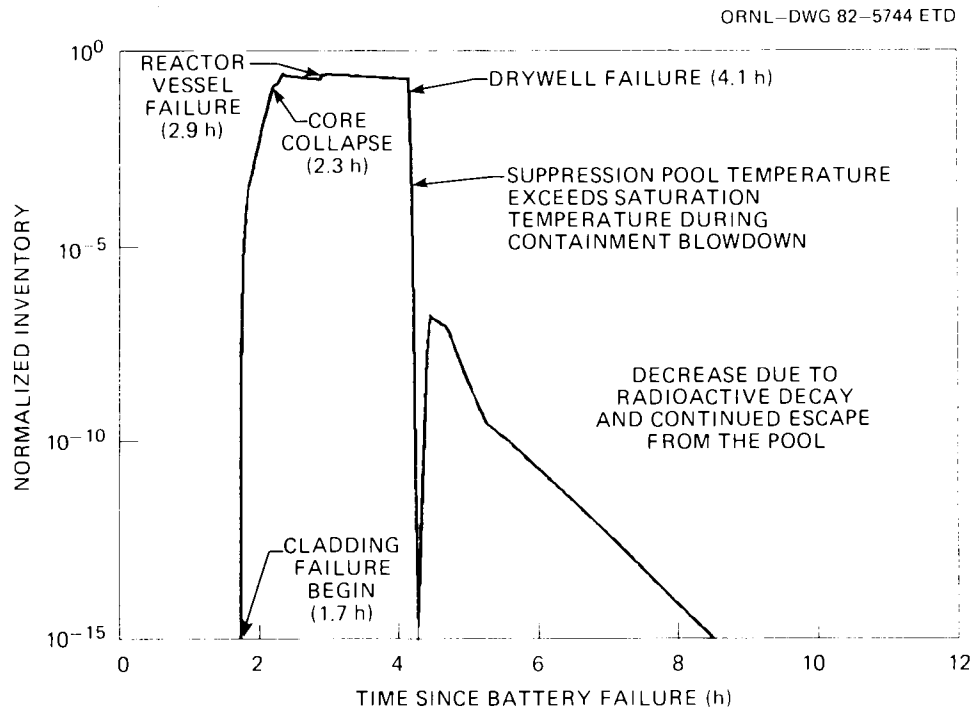

Fig. 6.4. Krypton inventory in the pressure suppression pool.

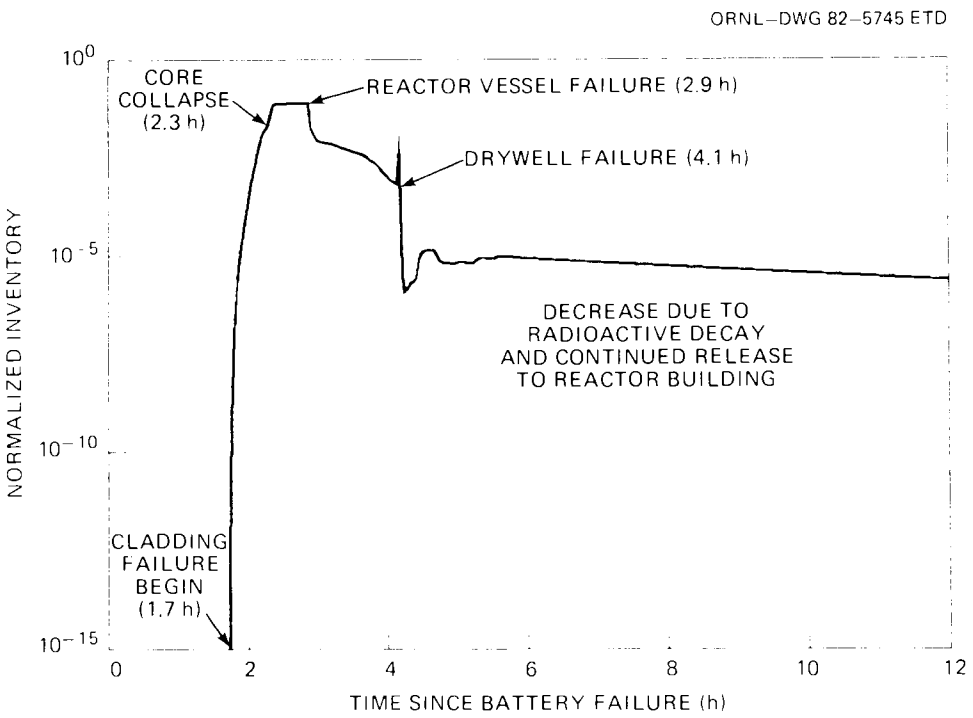

Fig. 6.5. Krypton inventory in the drywell atmosphere.

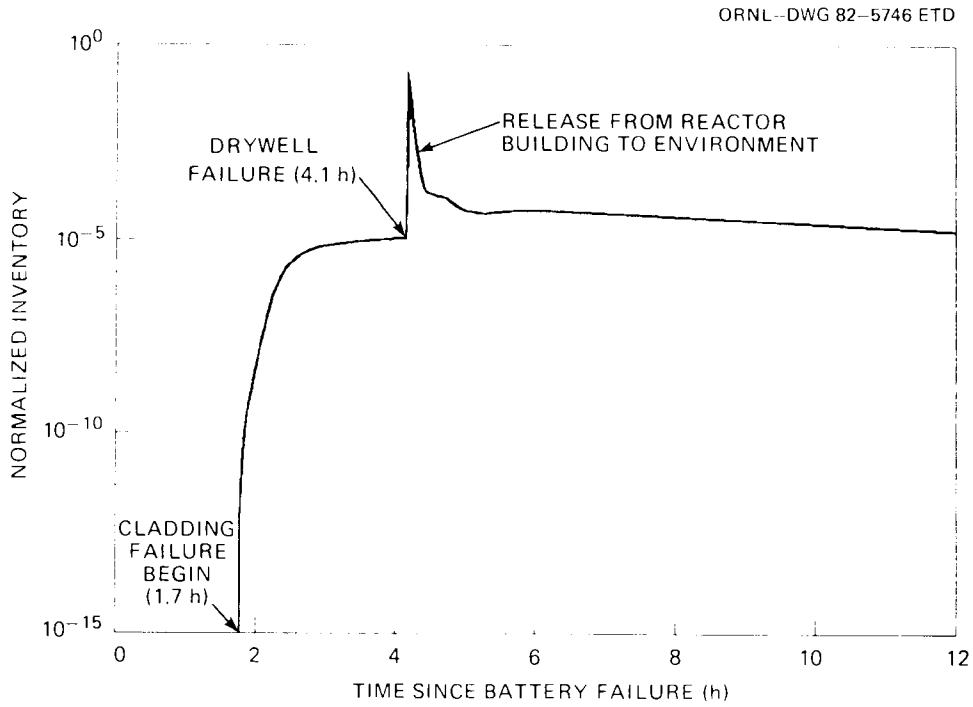

Fig. 6.6. Krypton inventory in the Reactor Building.

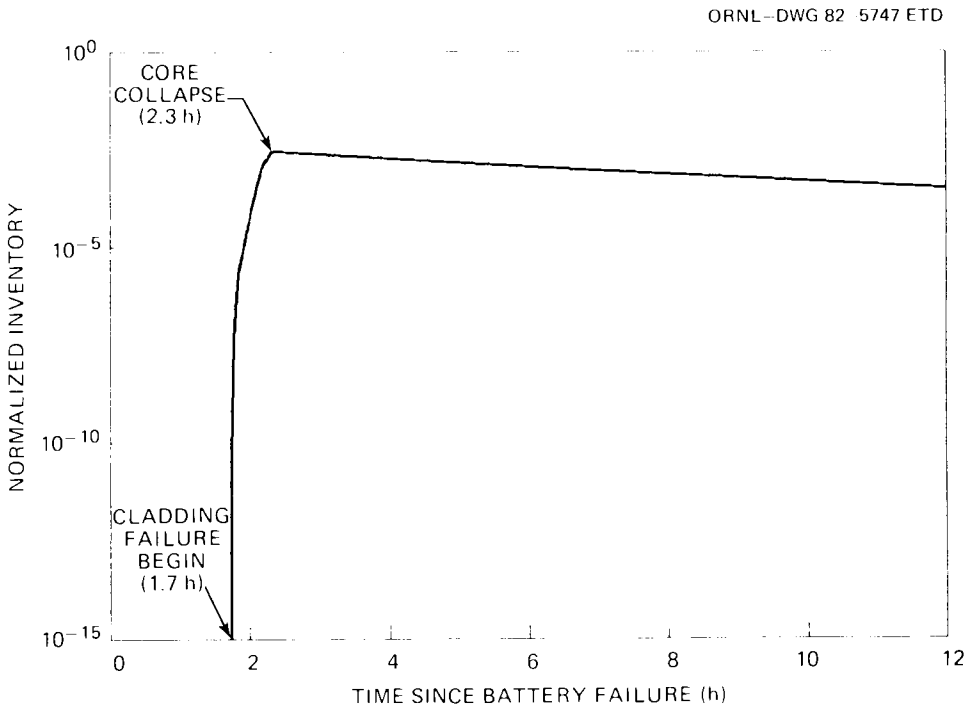

Fig. 6.7. Krypton inventory in the Main Condenser and Turbine Building.

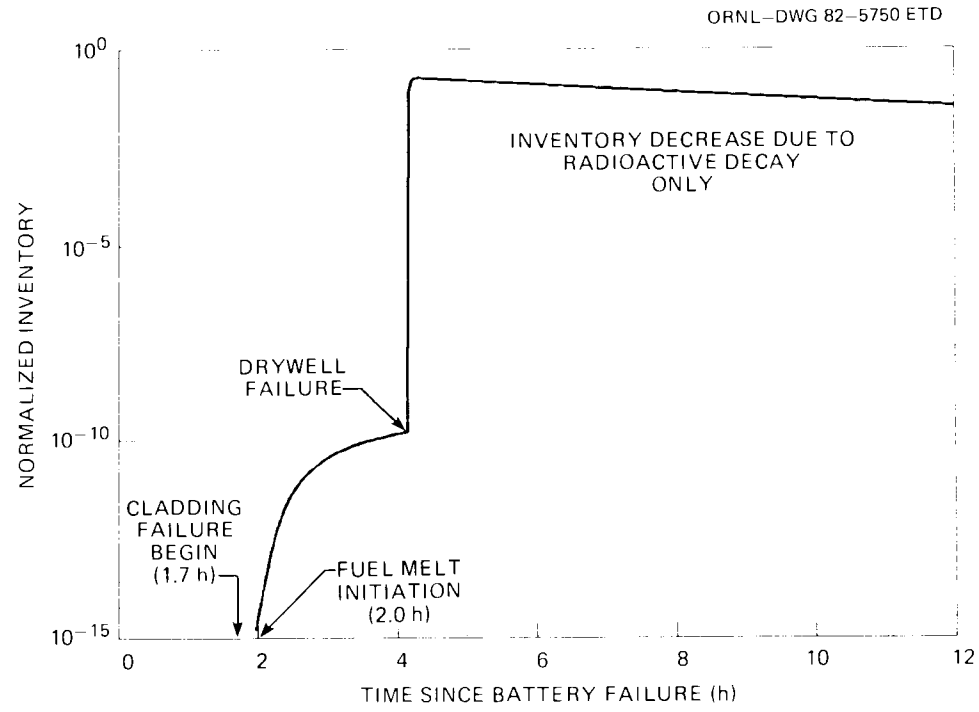

Fig. 6.8. Krypton released form the Reactor Building.

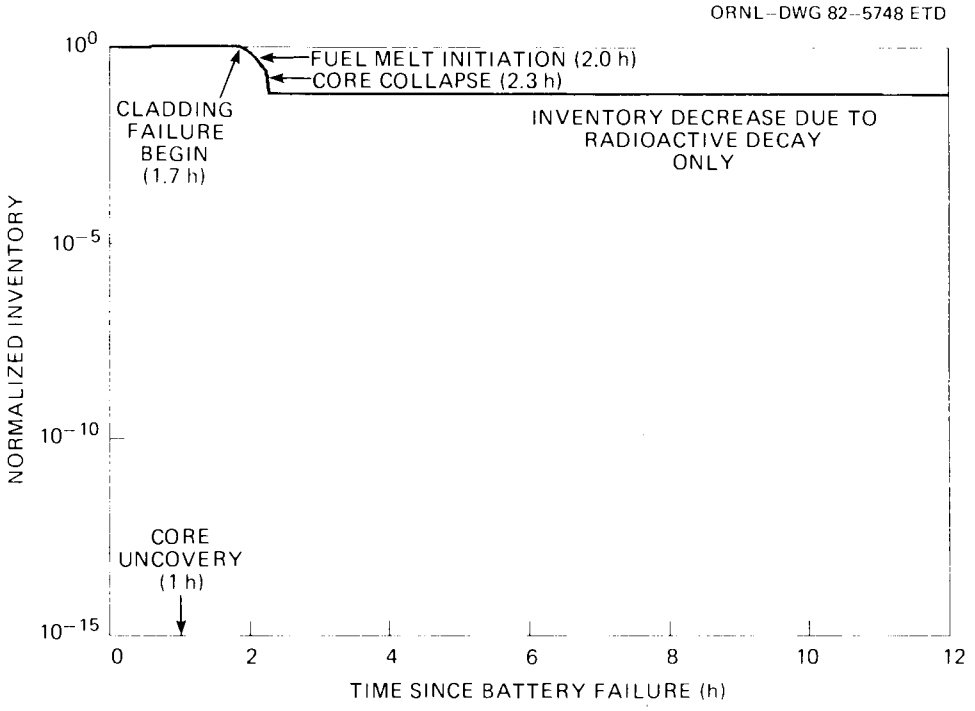

Fig. 6.9. Xenon inventory in intact portions of the core.

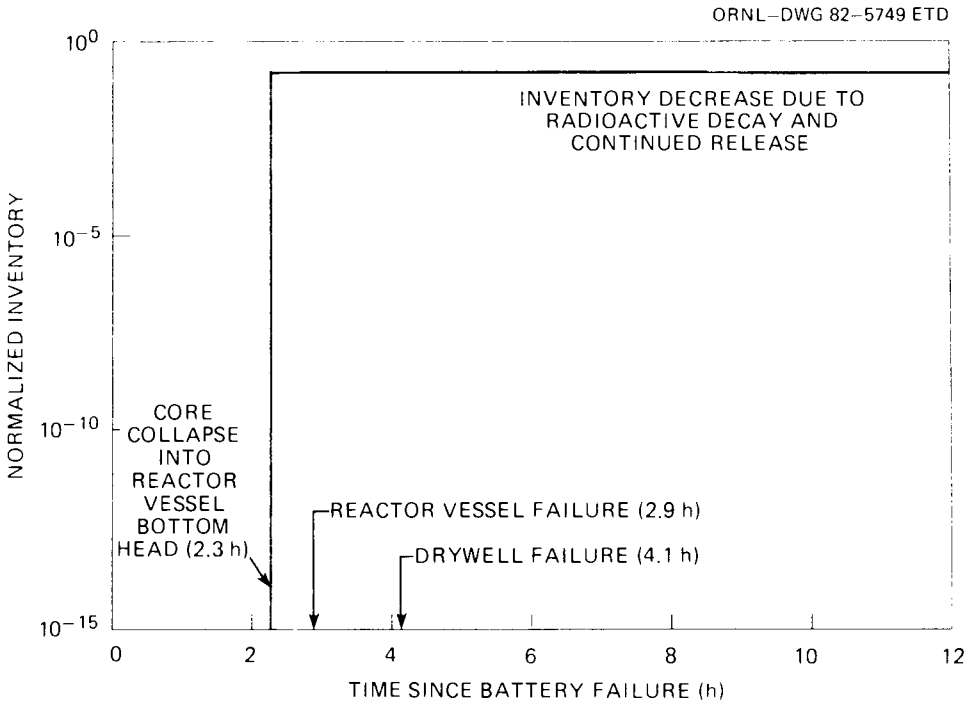

Fig. 6.10. Xenon inventory in molten core debris.

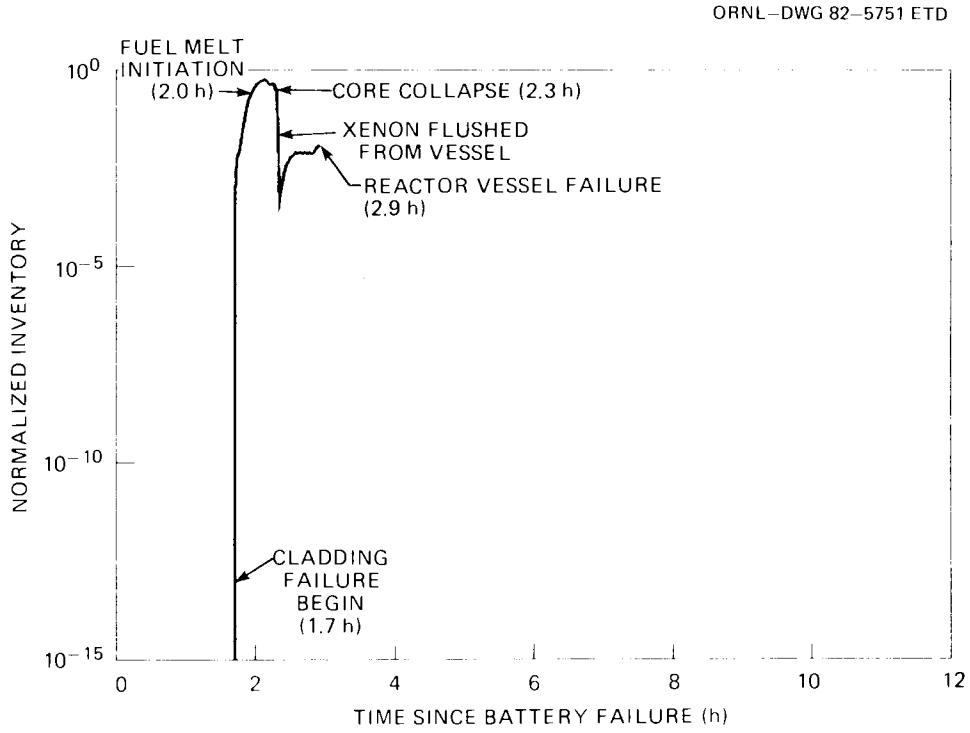

Fig. 6.11. Xenon inventory in reactor vessel atmosphere.

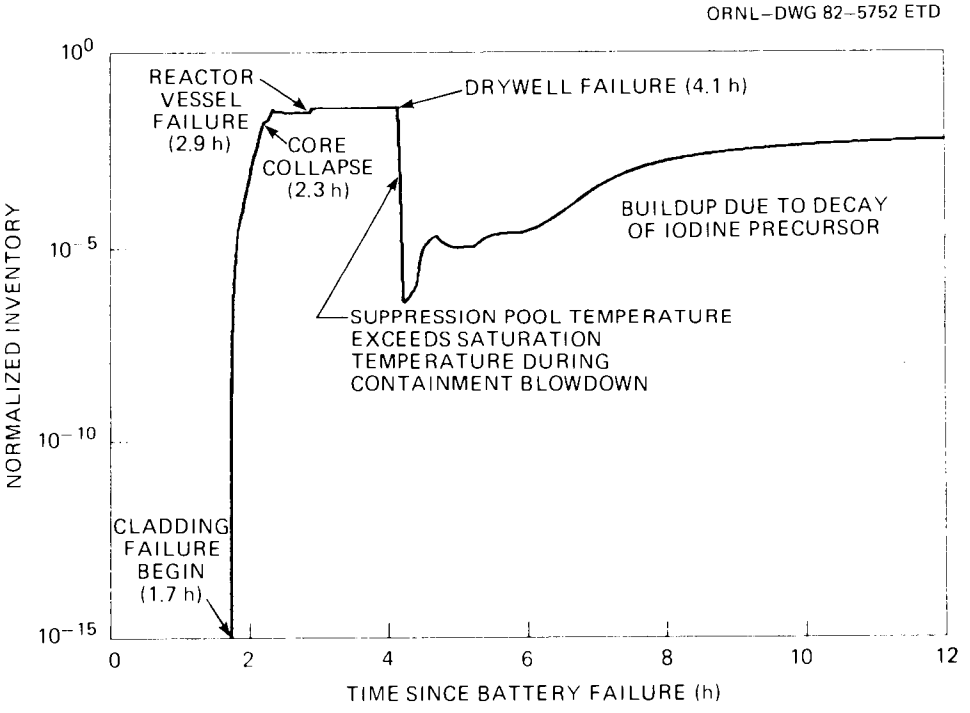

Fig. 6.12. Xenon inventory in the pressure suppression pool.

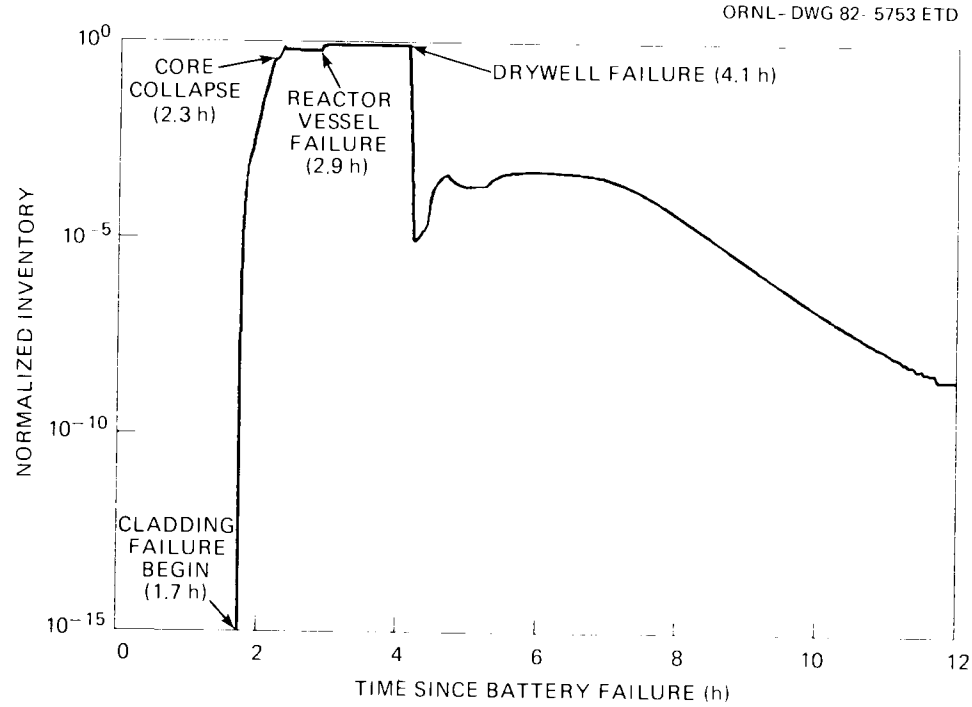

Fig. 6.13. Xenon inventory in the wetwell atmosphere.

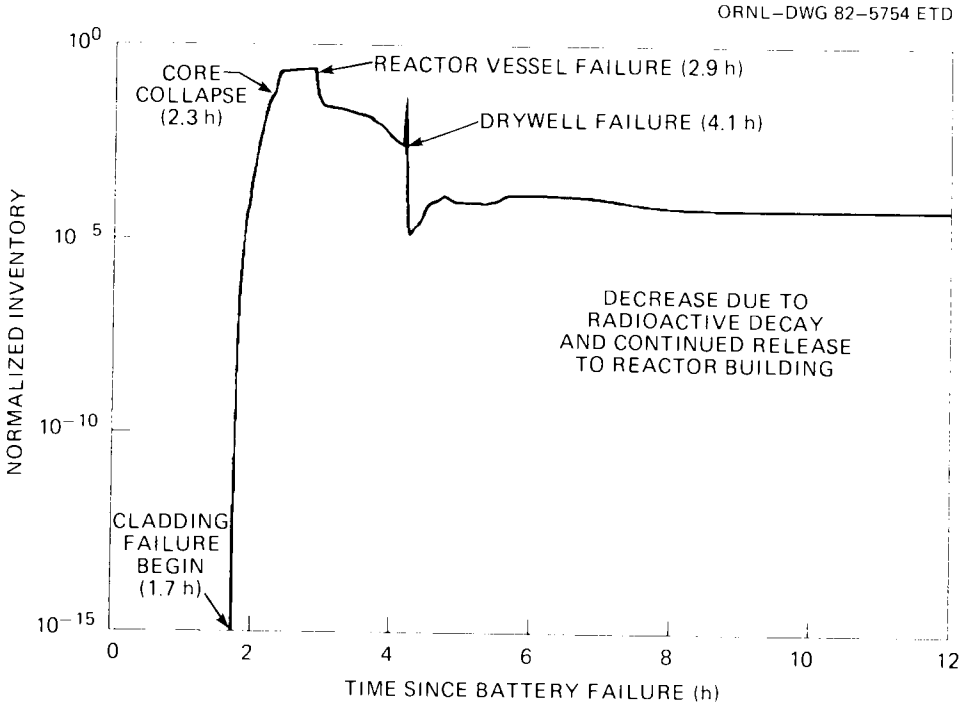

Fig. 6.14. Xenon inventory in the drywell atmosphere.

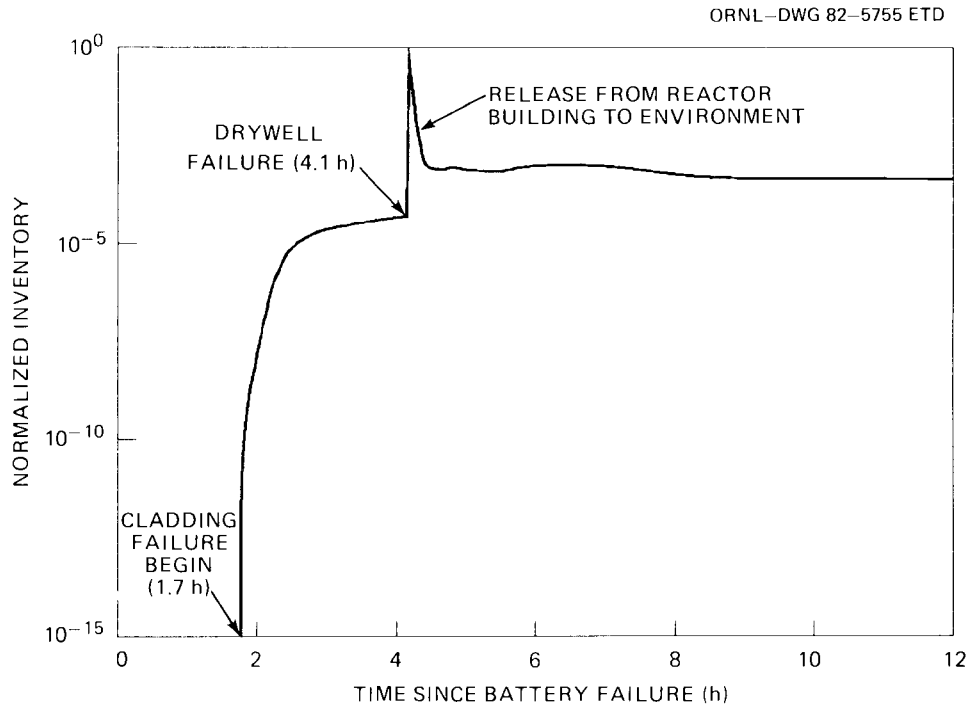

Fig. 6.15. Xenon inventory in the Reactor Building.

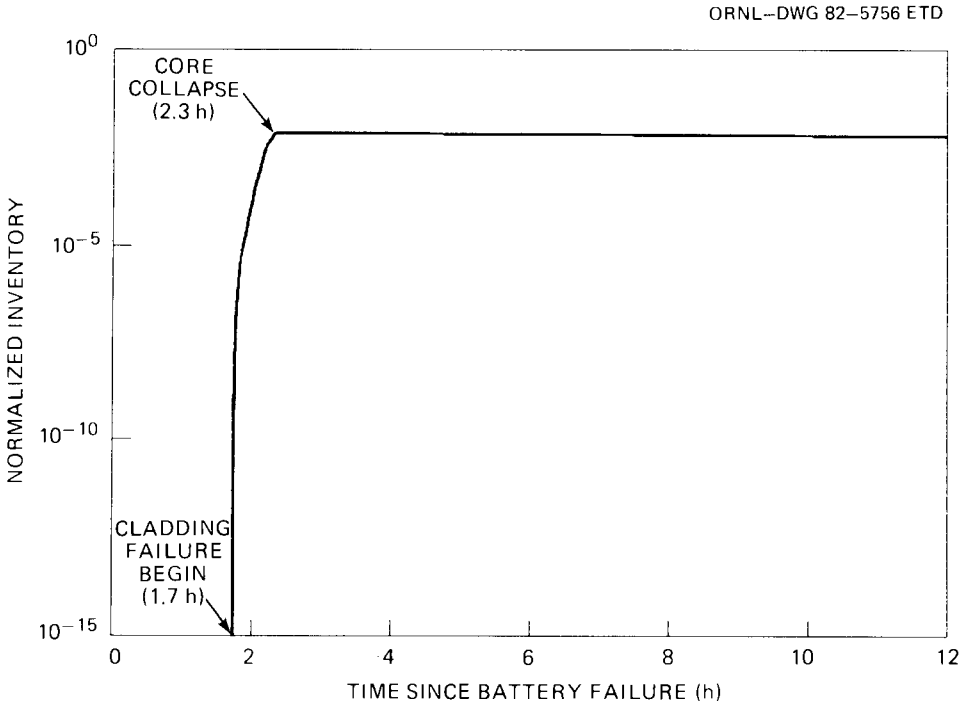

Fig. 6.16. Xenon inventory in the Main Condenser and Turbine Building.

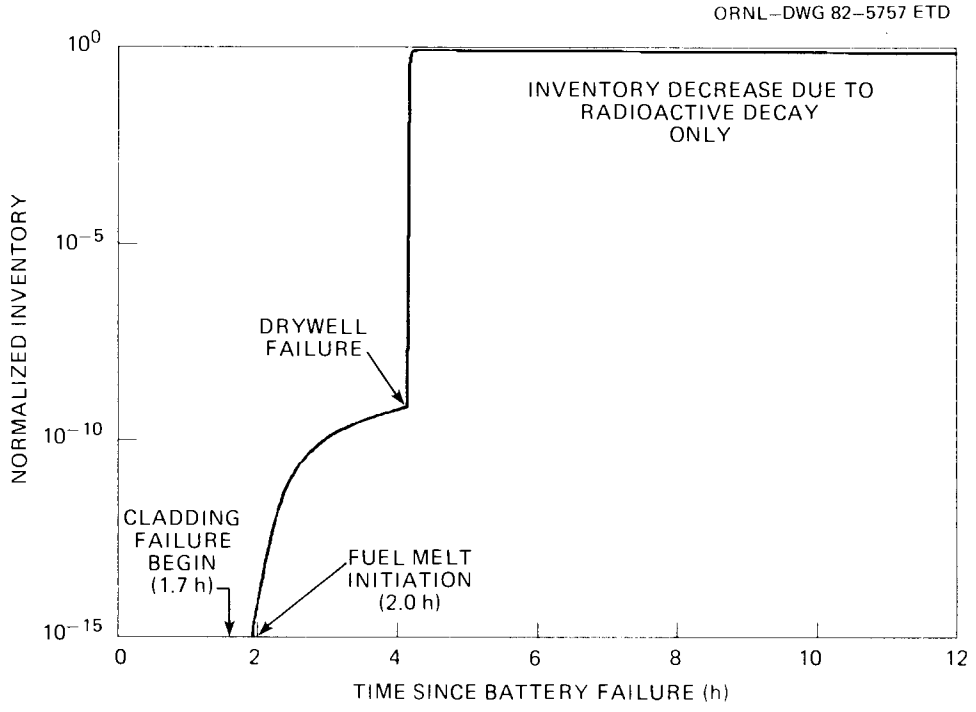

Fig. 6.17. Xenon released from the Reactor Building.

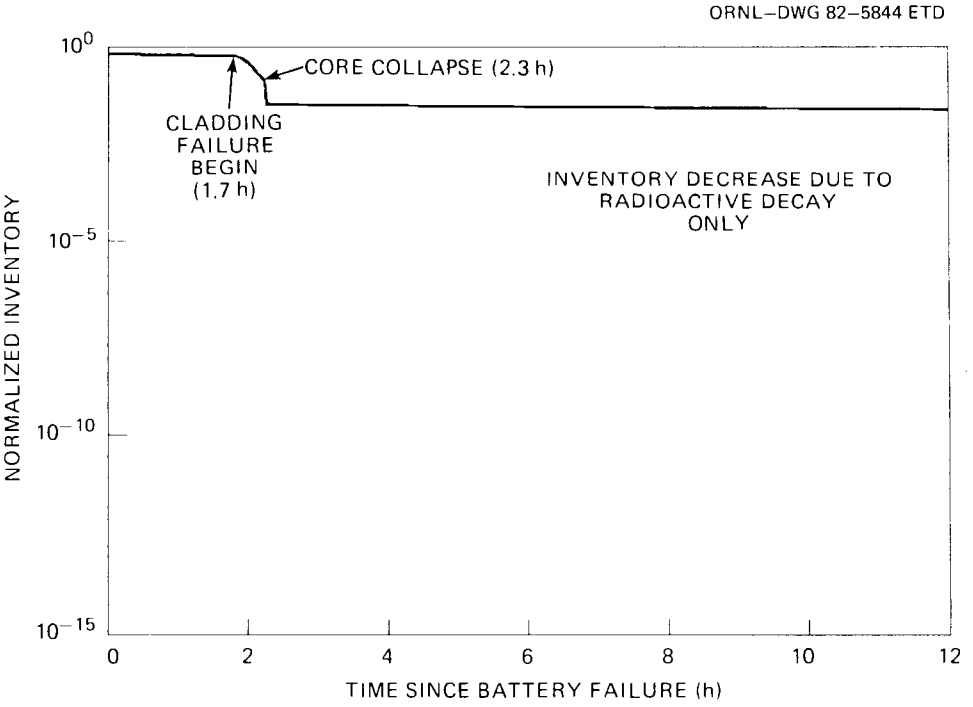

Fig. 6.18. Iodine inventory in intact portions of the core.

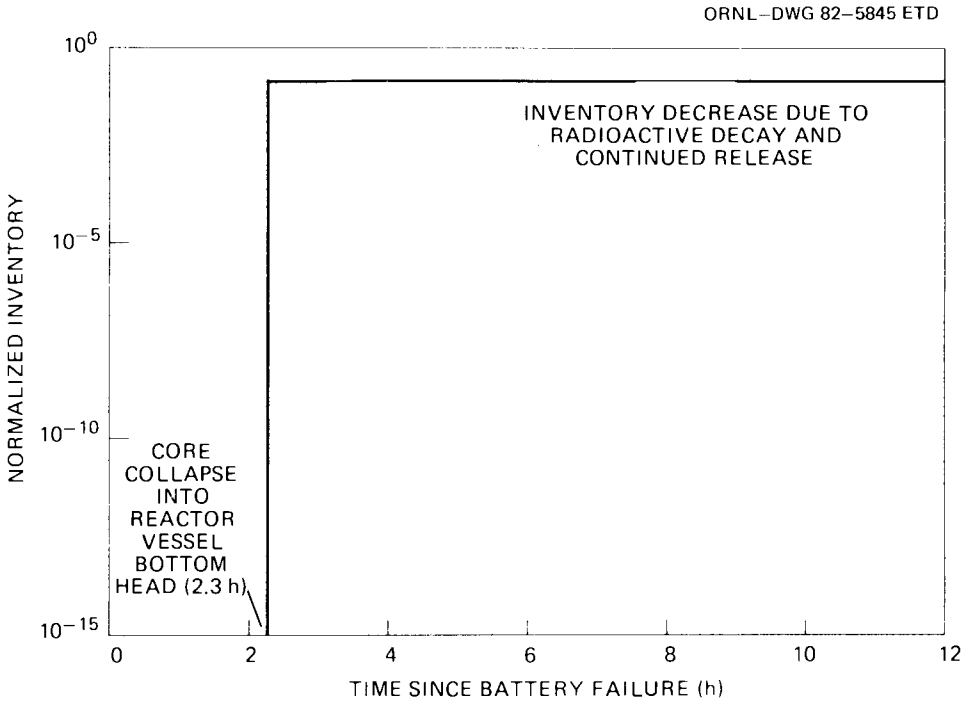

Fig. 6.19. Iodine inventory in molten core debris.

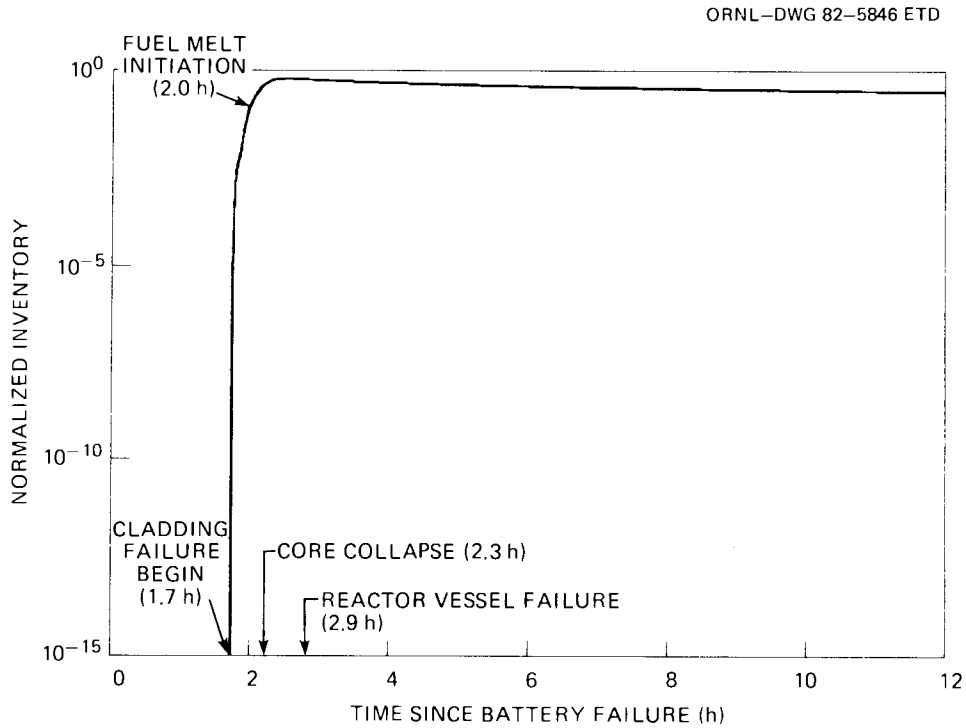

Fig. 6.20. Iodine deposited on reactor vessel internal surfaces.

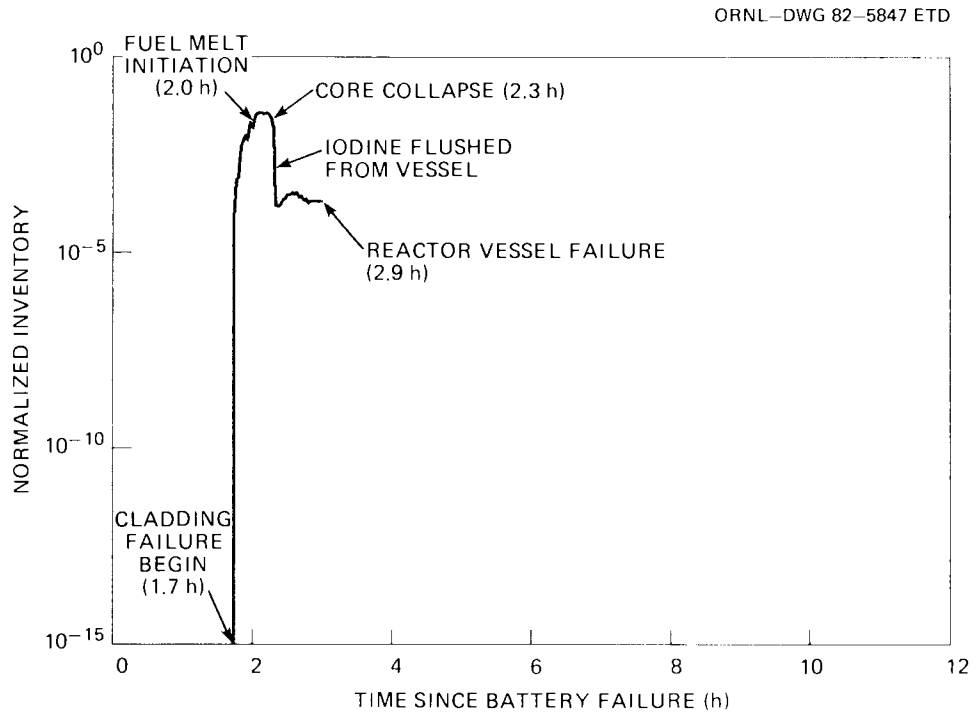

Fig. 6.21. Iodine inventory in reactor vessel atmosphere.

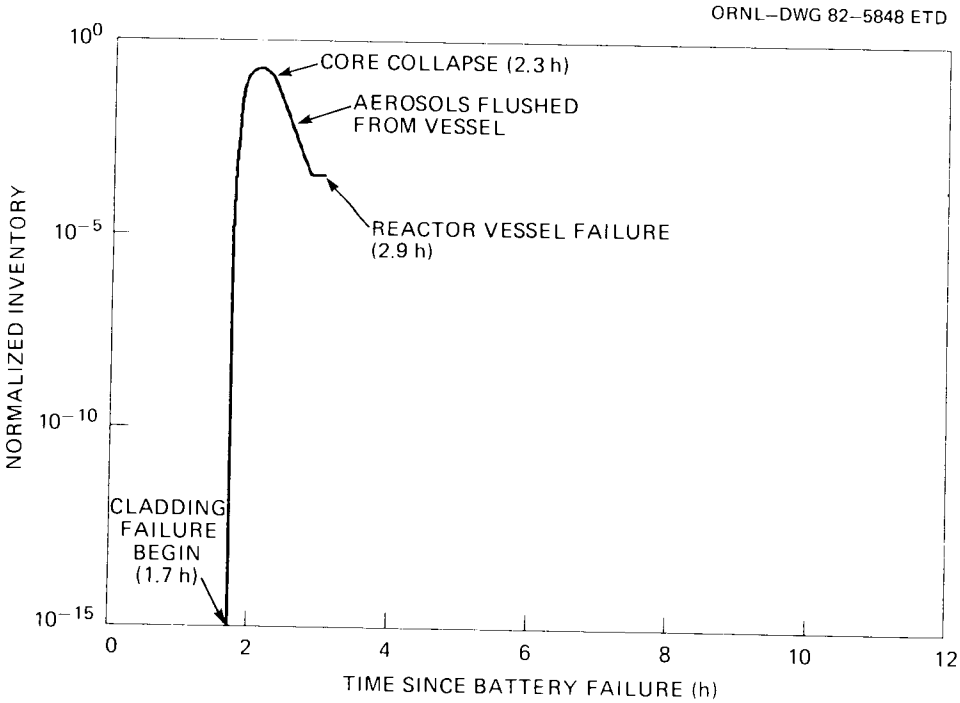

Fig. 6.22. Iodine inventory on aerosols suspended in the reactor vessel.

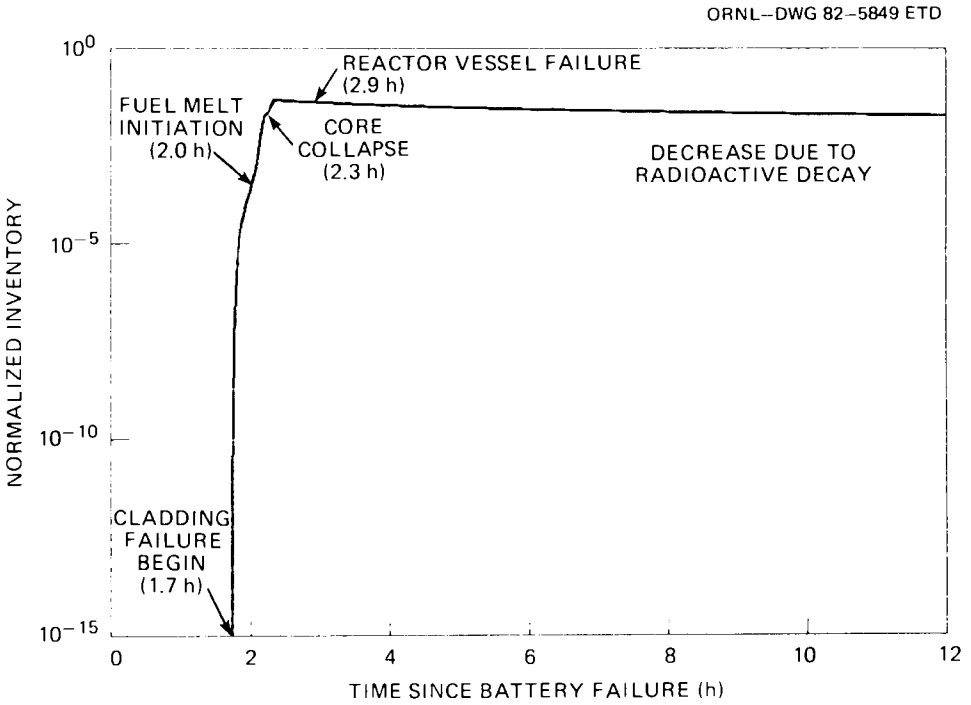

Fig. 6.23. Iodine inventory in the pressure suppression pool.

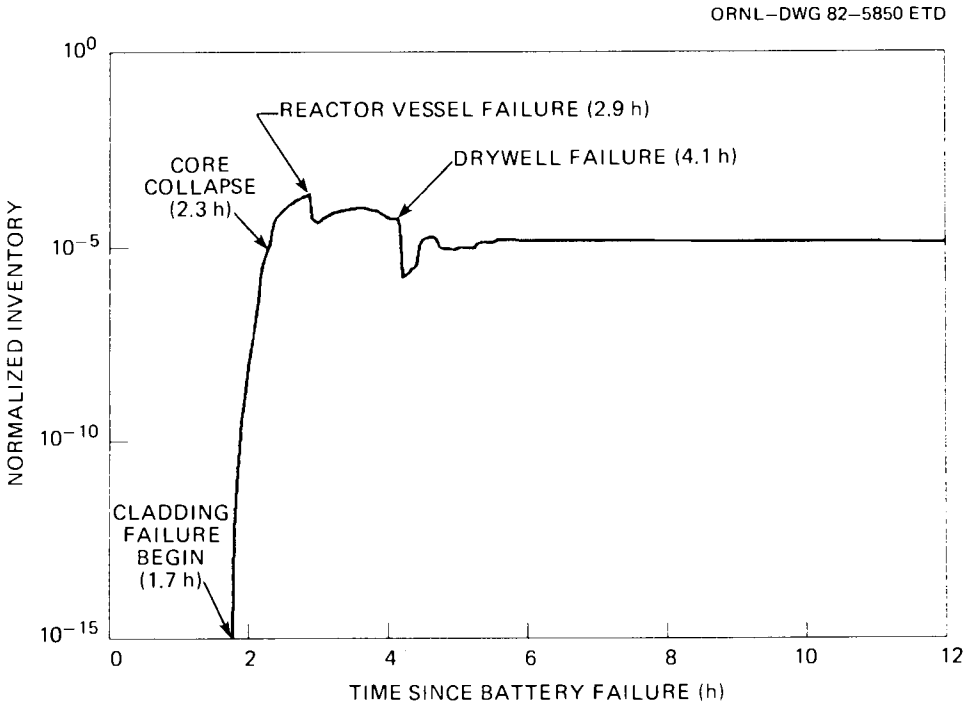

Fig. 6.24. Iodine inventory in the drywell atmosphere.

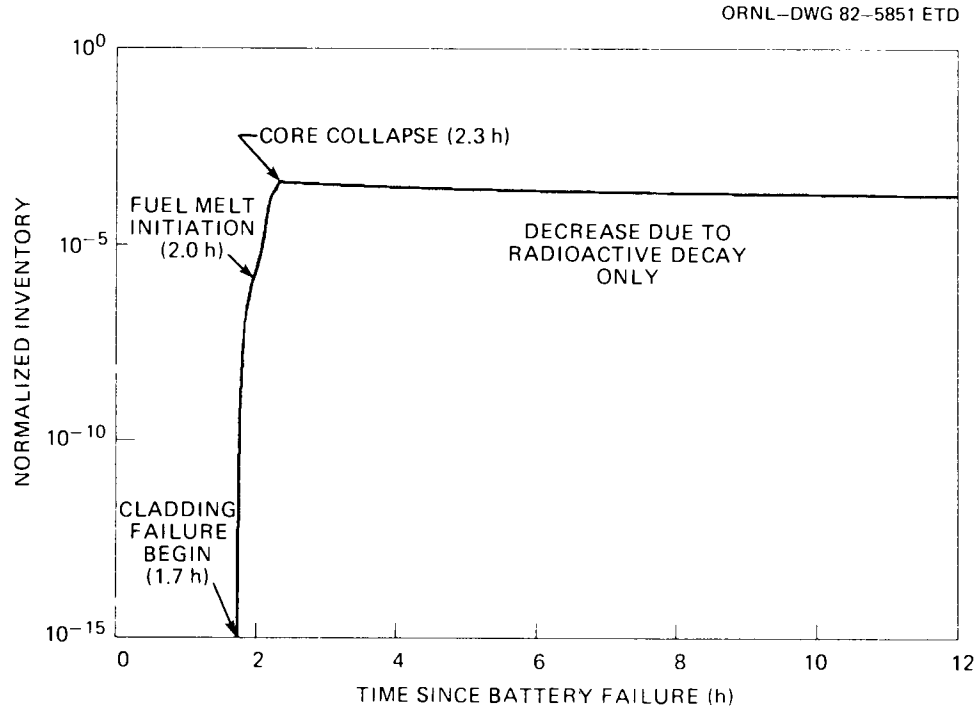

Fig. 6.25. Iodine inventory in the Main Condenser system.

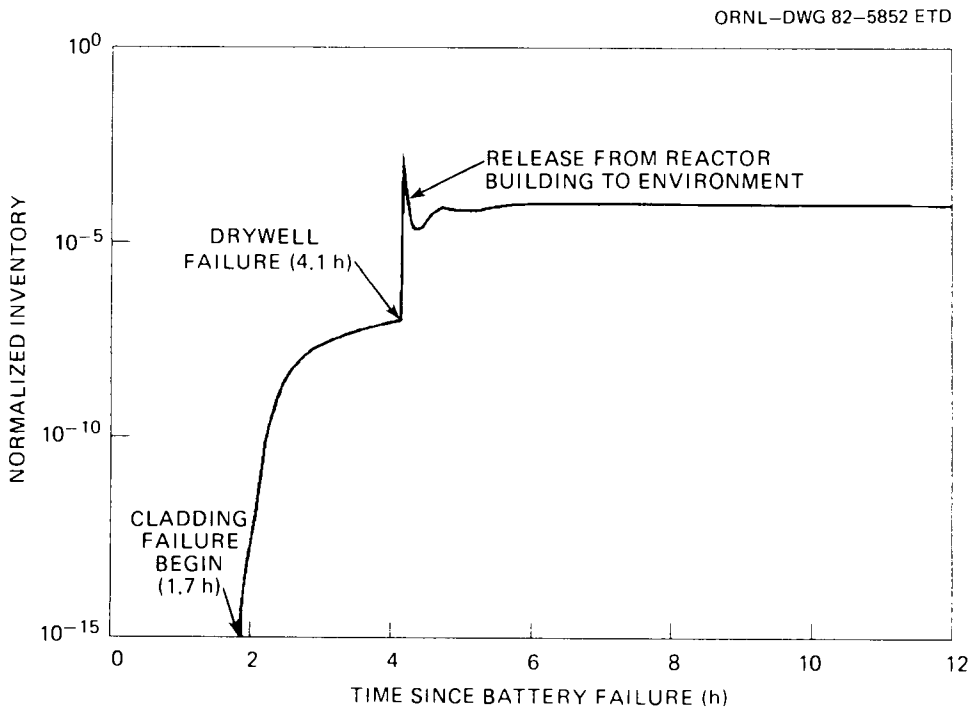

Fig. 6.26. Iodine inventory in the Reactor Building atmosphere.

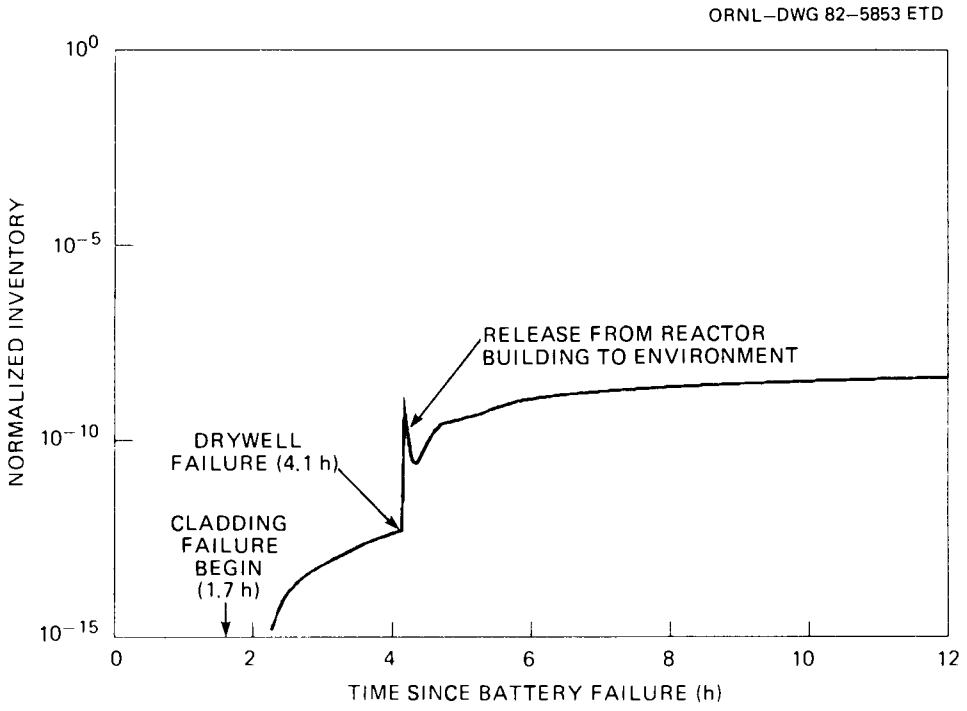

Fig. 6.27. Organic iodide in the Reactor Building atmosphere.

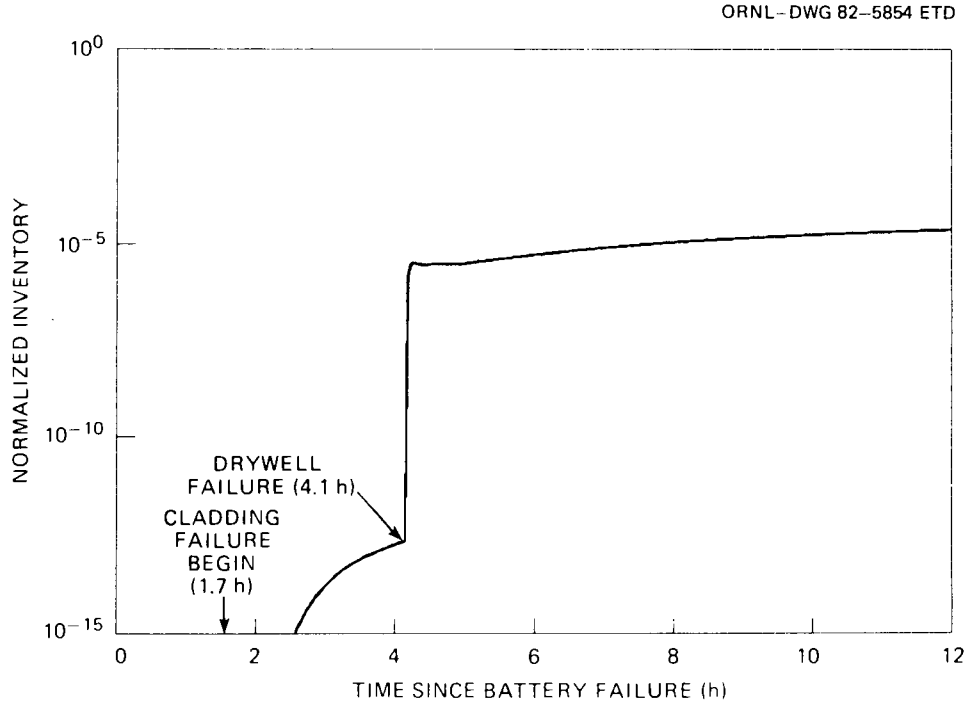

Fig. 6.28. Organic iodide released from the Reactor Building.

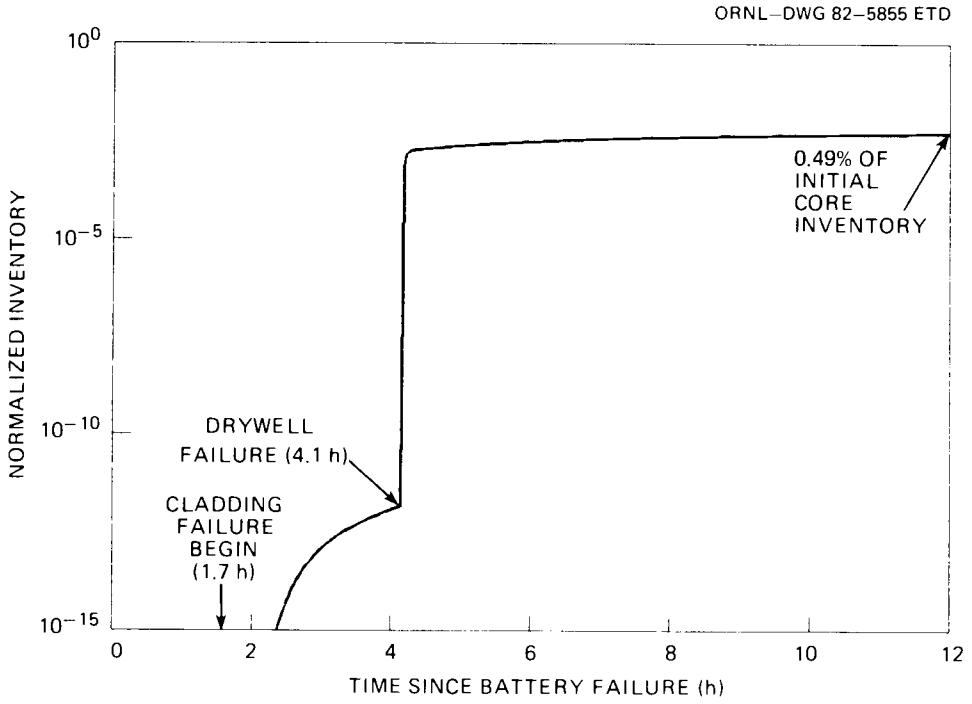

Fig. 6.29. Total iodine release from the Reactor Building.

Table 6.1. Krypton inventories (PBq) at various times and locations

Location	Krypton inventories (PBq)[a]				
	At battery failure (0 m)	After core slump (138 m)	After vessel failure (174 m)	After failure of containment (251 m)	4 hours later (491 m)
Total present	1540	880	771	576	247
Fuel rods	1540	46	40	30	13
Core debris[b]	0	129	112	83	34
Wetwell water	0	16	21	1.8×10^{-5}	-
Wetwell air	0	418	550	4.8×10^{-4}	-
Drywell	0	52	42	7.9×10^{-3}	1.3×10^{-2}
Reactor building	0	1.5×10^{-3}	1.5×10^{-2}	80	9.6×10^{-2}
Main condenser[c]	0	5.6	5.3	4.0	1.7
Atmosphere	0	1.6×10^{-9}	6.3×10^{-8}	379	199

[a] 1.0 petabecquerel = 27,027 curies. Inventory of time of reactor scram = 4,910 PBq.

[b] In bottom of reactor vessel after core slump and in drywell after reactor vessel bottom head fails.

[c] Located in the Turbine building.

Table 6.2. Xenon inventories (PBq) at various times and locations

Location	Xenon inventories (PBq)[a]				
	At battery failure (0 m)	After core slump (138 m)	After vessel failure (174 m)	After failure of containment (251 m)	4 hours later (491 m)
Total present	8980	8880	8990	8996	8810
Fuel rods	8980	540	539	536	518
Core debris[b]	0	1280	1274	1260	1190
Wetwell water	0	200	302	2.5×10^{-3}	10.4
Wetwell air	0	4160	6280	5.2×10^{-2}	0.12
Drywell	0	515	481	0.17	0.48
Reactor building	0	1.5×10^{-2}	0.17	1200	3.7
Main condenser[c]	0	55.9	61.3	59.5	54.8
Atmosphere	0	1.6×10^{-8}	7.2×10^{-7}	5660	6320

[a] 1.0 petabecquerel = 27,027 curies. Inventory at time of reactor scram = 8,020 PBq.

[b] In bottom of reactor vessel after core slump and in drywell after reactor vessel bottom head fails.

[c] Located in the Turbine building.

Table 6.3. Iodine inventories (PBq) at various times and locations

Location	Iodine inventories (PBq)[a]				
	At battery failure (0 min)	After core slump (138 min)	After vessel failure (174 min)	After containment failure (251 min)	6 hours later (711 min)
Total	18,900	16,700	16,300	15,500	12,400
Fuel rods	18,900	931	909	868	699
Slumped fuel[b]	0	2,390	2,330	2,220	1,770
Reactor vessel surfaces	0	10,600	11,800	10,080	7,570
Reactor vessel gas	0	295	-	-	-
Wetwell water	0	571	821	723	452
Wetwell air	0	169	13.7	7.3×10^{-3}	4.6×10^{-3}
Drywell	0	0.24	1.2	4.1×10^{-2}	0.35
Reactor building	0	7×10^{-6}	4.3×10^{-4}	7.7	2.4
Condenser[c]	0	6.6	7.1	6.4	4.5
Atmosphere	0	6.6×10^{-12}	1.8×10^{-9}	36.2	135

[a] 1.0 petabecquerel = 27,027 curies. Inventory at time of reactor scram = 27,730 PBq.

[b] In bottom of reactor vessel after core slump and in drywell after reactor vessel bottom head fails.

[c] Located in the Turbine building.

Table 6.4. Aerosol production in the reactor vessel

Time from battery failure	Mass of aerosols (kg)		
	Total produced	Plated	Suspended in gas
0	0	0	0
60 (core uncovery begins)	0	0	0
103 (first cladding failure)	4.1	2.5	1.5
120 (fuel melt initiation)	8.0	6.3	1.1
137 (core collapse)	11.5	9.3	0.70
172 (failure of bottom head)	13.3	10.7	0.25

7. SUMMARY AND CONCLUSIONS

7.1 Introduction

This report deals with the analysis of noble gas and iodine transport within a specific reactor system (Browns Ferry Unit 1) and for a specified accident sequence (Station Blackout). The postulated accident is a serious one, beginning with a loss of ac power and a failure to initiate the onsite emergency diesel-generators. After battery exhaustion, the accident sequence leads to core uncovery, meltdown, reactor vessel failure and a subsequent failure of the primary containment by overheating of the electrical penetration assembly seals in the drywell. Events during this accident sequence and values of key parameters throughout the reactor vessel, primary containment and Reactor Building (as described in Vol. 1 of this report) are used as input to the calculations for estimation of the degree of fission product movement. Factors which affect the movement through a series of barriers are reviewed. Determination of the transport of the noble gases is relatively simple, but for a reactive material such as iodine, proper assessment of the rate of movement requires determination of the chemical changes along the pathway which alter physical properties, such as vapor pressure and solubility, and thereby affect the transport process.

7.2 Review of Events and Assumptions

The sequence of events in the Station Blackout sequence relative to fission product transport effects is listed in Table 7.1.

The principal fission product pathways for this accident sequence and the secondary pathways are described in Sect. 2. Prior to reactor vessel failure, the principal pathway leads from the failed fuel, through the upper reactor vessel structures, through the primary relief valves and into the suppression pool. Thus all relese from the fuel during this period is subjected to suppression pool scrubbing. Gas flow from the wetwell airspace above the suppression pool back through the vacuum breakers into the drywell begins early in the sequence and leads to a small movement of the fission products which emerge from the pool to the environment via normal leakage from the primary containment and the Reactor Building prior to reactor vessel failure.

The leakage flow paths alter significantly following the failure of the reactor vessel and the accompanying fall of the core onto the concrete floor of the drywell. There is a large gas flow from the pressure vessel into the drywell at the time of pressure vessel bottom head failure and the equalized pressure is estimated to be about 9 bar. The initial increase in drywell pressure forces gas flow into the suppression pool via the vent pipes and downcomers. Following this brief episode, pressures equalize within the drywell-wetwell containment boundary (now including the failed pressure vessel) and thus no further driving force exists to induce flow into the pressure suppression pool. The subsequent (relatively small) release from the core debris is not subjected to pool

scrubbing. The principal leakage pathways during the various phases of the accident are illustrated in Figs. 2.1, 2.2, and 2.3.

The mode and the timing of containment failure are critical factors in the assessment of fission product leakage. As discussed in Volume 1 of this report.[1.1], the postulated mode of containment failure is by degeneration of the electrical penetration assembly seals due to overheating. A slow venting is projected to occur when the drywell temperature reaches ~200°C, followed by gross containment failure and a much larger flow when the temperature reaches 260°C.

Accordingly, the timing of the predicted drywell failure depends on the calculated drywell temperature history which is therefore a critical sequence parameter whose accuracy should be carefully examined. For example, the MARCH code predicts that the drywell temperature increases so rapidly after failure of the reactor vessel lower head that drywell venting at 200°C and gross failure at 260°C occur almost simultaneously.

Flow impediments are negligible within the lower levels of the reactor building, and the installed blowout panels in the path to the refueling bay are projected to fail soon after drywell failure. With the assumption that the accident sequence is occuring simultaneously at all of the three Browns Ferry Units, the blowout panels between the refueling bay and the atmosphere are also projected to fail.

The models for fission product release and aerosol production rates are presented in Sect. 3. Fission product release rates from the fuel are based on the estimated temperature for cladding failure and values for release rate coefficients, depending solely on fuel temperature, which have been determined from examination of the results of release rate experimentation. While the test data show large variation, the release rate coefficients given in Fig. 3.1 indicate approximately equal release rates from fuel for the noble gases, iodine, and cesium above ~1600°C. Release rates from fuel for these volatile fission products at temperatures near melting (~2200°C) are estimated to reach ~50% of current inventory per min.

The rate of release from the molten fuel/structures material collapsed onto the bottom head of the reactor vessel was assumed to be lower than that calculated for an intact core at the same temperature by a factor equal to the ratio of the surface areas in each geometry. Thus, release rates for the molten debris in the reactor vessel bottom head were assumed to be a factor of 250 lower than would be computed for an intact core geometry. Using the same rationale, release rates from the core rubble bed on the drywell floor were assumed to be a factor of 25 less than those for the intact core.

The computed release rates from the largely intact core, from the molten debris in the pressure vessel bottom head, and from the material on the drywell floor depend strongly on the temperatures calculated by the MARCH code. Ten axial and ten radial (100 total) zones are modeled for the intact core at each computational time step. However, after core slump, only one mass-averaged temperature is available for the debris on the reactor vessel bottom head and later in the drywell.

The MARCH-predicted temperature distribution within the intact core leads to some unexpected (and perhaps unrealistic) results. First, the outer radial zone of fuel is predicted to remain relatively cool, not even reaching the cladding failure temperature of 1300°C. We have assumed,

therefore, that this zone, representing about 10% of the core, does not slump but is instead retained at its original location.

MARCH also predicts a very steep axial temperature gradient in the core prior to slump, with an extremely rapid rate of temperature increase in the fuel assemblies just above the lowering water level. This results in low temperatures and the absence of melting at the lowest axial node in each of the radial zones at the time of core slumping. Thus, the MARCH results contain an inherent assumption that the approximately 15% of volatile fission products contained in the lowest axial nodes are transported with the remainder of the slumping core into the base of the reactor vessel at the time of core slump. This is not physically realistic; a coherent core collapse would not be expected to occur in a Boiling Water Reactor.*

The method used for estimating the rate of aerosol formation due to overheating of the fuel and structural material in the reactor vessel prior to failure of the bottom head is described in Section 3.2 and Appendix C. The method is based on a projected effective volatility of aerosol-forming material at the estimated local temperature, determined from melting experiments and an estimate of the mass transfer rate to the bulk gas. The model predicts that about 0.008% of the core and structural mass is aerosolized, which is significantly lower than other estimates for aerosol release from severely damaged cores.

The degree of aerosol formation in the drywell due to core/concrete reaction was determined using an available empirical expression determined from test data. The degree of gas generation in the concrete and the temperature of the rubble are required input parameters, which were determined from the results of the MARCH code.

As a base-case estimate, we have assumed that 80% of the aerosols generated in the pressure vessel are retained on the surface of the steam separators and dryers, and other surfaces internal to the reactor vessel. This estimate is based on a series of TRAP-MELT code runs performed at Battelle Columbus laboratory for the BWR geometry. Estimated aerosol retention in the drywell (Table 3.11) and reactor building (Table 3.19) as predicted by the HAARM-3 code are much lower than for the pressure vessel: only about 5% of the aerosols generated in the drywell are predicted to deposit rather than leak and the degree of aerosol retention in the reactor building is estimated at 10%.

Models for the transport of noble gas and iodine through the reactor vessel, the wetwell, the drywell, and the Reactor Building are described in Section 4. While noble gas transport is simply a matter of acquiring the appropriate convection rates from the MARCH results for the accident sequence analysis, iodine transport rates contain large uncertainties because of chemical interactions between iodine and other fission products, aerosol particles, structural materials, and suppression pool water. Accordingly, a great deal of caution and humility are required armaments for work with this subject matter. It is found that the transport pathway and the sequence flow and temperature parameters are strongly coupled to the

---

*As previously discussed, the MARCH results were adjusted to account for the retention of the outer ring of fuel assemblies in-place following central core collapse.

assumed chemical interactions and transport rates in the determination of the results. Therefore, to focus on just one aspect of the total problem can lead to an erroneous 'common sense' impression regarding the effect on the estimated leakage rate.

The principal iodine transport rate and chemical interaction assumptions described in Section 4 are the following:

1. The mixture of iodine chemical species in the gas phase of the pressure vessel prior to failure of the bottom head was determined using chemical equilibria calculations assuming that a large excess of cesium exists at all locations. Reducing conditions exist, thus the input to this calculation includes the local temperature and the local I/H_2O ratio.

2. The iodine chemical forms in the containment gas volumes are assumed to be molecular iodine and the much smaller quantities of organic iodine produced at rates given by methods discussed in Sect. 4.2.3. The containment iodine sources are (a) vaporization from the pressure suppression pool, (b) evolution from fuel rubble on the drywell floor, and (c) convection from the deposits on the internal surfaces of the failed pressure vessel to the drywell.

3. Mass transfer rates of CsI, HI, I_2, and I onto various contacting surfaces were primarily obtained from published empirical formulae as described in Section 4.3. The rate of mass transport to aerosol particles was calculated using a theoretical expression appropriate to diffusion-limited deposition onto a small spherical particle at a low particle Reynolds number. This expression leads to a high rate of mass transfer to aerosol particles.

4. The net result of the calculational procedures implied in items (1) and (3) is that 99.5% of the iodine retained in the reactor vessel is condensed CsI; the remainder is adsorbed-I.

5. The four principal tellurium isotopes which contribute to the iodine inventory via β-decay (Te-131, Te-132, Te-133, Te-134) were assumed to be transported with iodine along the transport pathway. While these isotopes provide less than 2% of the iodine mass, they are a significant source of iodine radioactivity. Similarly, xenon resulting from iodine decay was added to the local xenon inventory.

6. It was necessary to calculate or assume equilibrium iodine loadings for each iodine species and type of deposition surface. Since CsI deposition occurs via condensation, the potential surface loading is unlimited while sorption processes for other iodine species lead to some maximum level depending upon the nature of the surface, the gas phase partial pressure, and the temperature. Equilibrium loadings were obtained for metal, oxide, and painted surfaces. Aerosol particles were assumed to be oxidic.

7. Iodine volatilites and pressure suppression pool decontamination factors are described in Section 4.5. By far, the most important parameter is the effective iodine volatility during the period of suppression pool boiling as the primary containment is depressurized immediately following drywell failure. Unfortunately, this volatility is highly uncertain as there exist no experimental measurements under comparable conditions of temperature, pH, iodine concentration, redox reactions, and radiation level. Our best estimate is that the iodine volatility under these circumstances is given by a partition coefficient of 10^5; this is a factor of about 500 higher than that projected for these conditions in reference 4.7. The principal reason for the higher estimate used in this study is the considered effect of the radiation in the pressure suppression pool caused primarily by the dissolved cesium, rubidium, and iodine.

8. Several important assumptions relate to the model for estimating the transfer of iodine from the reactor vessel to the drywell after failure of the reactor vessel bottom head. It was judged that this transport step cannot be neglected despite the difficulty of obtaining a good estimate for it. The model used to represent this transport, described in Section 5.4, is based simply on the assumption of uniform mixing within the failed pressure vessel and the gas expansion caused by the temperature increase for the overall drywell as predicted by the MARCH code. The gaseous iodine concentration is assumed to consist of CsI, vaporized to 10% of the saturation concentration, plus all of the absorbed iodine estimated to be in the reactor vessel at the time of failure. As discussed previously, 99.5% of the iodine deposited on internal vessel surfaces is projected to be CsI at the time of vessel failure, with the remainder atomic iodine. Using the estimated vessel temperature increase obtained from MARCH predictions for the drywell leads to an estimated transfer of about 2.8 g-moles of iodine from the pressure vessel to the drywell after pressure vessel failure, or about 1.8% of the initial vessel iodine inventory. This estimate, however, is sensitive to the assumed rate of temperature increase. For example, if the temperature of the internal reactor vessel surfaces were to reach 1000 K instead of 1200 K (see Fig. - 1.11), then the estimated iodine transfer to the drywell would be only 0.45 g-moles or 0.29% of the initial inventory. Since the MARCH code is known to overestimate drywell temperatures, the latter estimate for iodine transfer is considered to be more realistic and has been adopted for this study.

7.3 Review of Results

The net result of the calculations obtained using the previously discussed assumptions concerning the fuel release rates, the chemical interactions, and the transport rates are described in Section 6. Tables 6.1, 6.2, and 6.3 and Figs. 6.1 through 6.29 provide estimates of the inventories of krypton, xenon, and iodine in key control volumes as a function of time. In each case, the last control volume represents the atmosphere

surrounding the reactor building. The more significant aspects of these results are summarized below:

1. Krypton and xenon isotopes move through the reactor vessel/containment/reactor building structures fairly readily. Steaming in the pressure vessel and the wetwell and concrete degradation gas flows provide the necessary convection for flushing the noble gases. However, about 1% of the initial krypton inventory and 7% of the initial xenon inventory is retained in unfailed fuel assemblies at the time the central core collapses into the lower head. Also, hold-up delay allows time for significant decay of krypton isotopes. At about 8 h after battery failure, the atmosphere surrounding the plant is projected to contain 4% of the initial krypton and 79% of the initial xenon activity which existed in the core at the time of reactor scram.

2. Chemical forces create significantly different transport characteristics for iodine relative to the noble gases, despite approximately equal rates of evolution from overheated fuel. In the reactor vessel, high mass transfer rates to aerosol particles allow rapid condensation of CsI onto the aerosol surfaces.

3. An amount equivalent to about 43% of the initial iodine activity is retained in the reactor vessel at the time of failure of the lower head, principally as CsI condensed on aerosol particles that are trapped on internal surfaces. At this time, approximately 3% of the initial iodine activity is contained in the pressure suppression pool, also principally in the form of CsI condensed on aerosol particles. An additional 3% is retained in the unfailed fuel assemblies still standing in place in the outer ring of the original core. The core debris contains an amount equivalent to 8% of the initial inventory.

4. In the 40 minute interval following drywell failure, during which time the mean pressure suppression pool temperature exceeds the saturation temperature, approximately 0.065% of the initial iodine inventory is projected to vaporize from the pool water and flow with the steam from the wetwell airspace through the vacuum breakers to the drywell. This is caused by the vaporization of about 4% of the pressure suppression pool upon the sudden depressurization when the drywell fails, and an estimated iodine volatility given by a partition coefficient of 10^5.

5. It is difficult to estimate the degree of iodine transfer from reactor vessel internal surface deposits to the drywell after reactor vessel failure by melt-through of the bottom head. As previously indicated, a simple gas expansion model predicts that about 0.29% of the initial inventory is transferred to the drywell, based on the best available estimates of the reactor vessel temperature history.

6. Approximately 8% of the initial iodine inventory remains with the molten core/structures debris as it drops to the drywell floor after reactor vessel melt-through. As previously noted, this unexpectedly high iodine retention within the molten fuel mass is due principally

to the steep axial temperature gradients in the core computed by the MARCH code for the period before core slumping.* During the 9-hour period following drywell venting and failure, the average of the calculated debris bed temperatures is about 1350°C for the combined metal plus oxide layers causing a predicted evolution into the drywell of about 0.3% of the iodine in the debris. It is important to recognize that this release would escape suppression pool scrubbing.

7. According to the models used, iodine holdup in the drywell and the Reactor Building is small for the following reasons: (a) low gas phase concentrations are predicted, generally on the order of 10^{-11} moles/cm^3, which create small driving force for sorption. (b) Large predicted gas flows due to core-concrete reaction and concrete degradation are the principal cause of the low gas phase concentrations. (c) The high drywell surface and gas temperatures predicted also serve to diminish sorption on drywell structural and aerosol surfaces.

8. We have assumed that the gaseous iodine species in the drywell and Reactor Building is I_2. If the less volatile species, CsI, persists into these structures, iodine depositions in the drywell and Reactor Building would increase to approximately the predicted degree of aerosol trapping. According to HAARM-3 results and attendant assumptions described in Sects. 3.3 and 3.4, the drywell and the building capture ~5% and 10% of entering aerosol particles, respectively. Therefore, according to present models and sequence parameters, the chemical form of iodine in the drywell and Reactor Building does not significantly affect the release rate to the atmosphere.

9. Organic iodine formation is a negligible factor in this accident sequence according to the production rate models assumed for the time span covered in this analysis. The principal reason is that we assume no production above 300°C and further that organic iodine introduced to an area whose temperature exceeds 300°C is assumed to be converted to I_2. Thus, organic iodide produced in the wetwell gas space is converted to I_2 as it is transported to the drywell (by steam flow through the vacuum reliefs) where the predicted temperature exceeds 300°C from the time of drywell failure. Organic iodide production in the Reactor Building is negligible due to short hold-up times.

10. The estimated iodine in the atmosphere as a function of time is illustrated in Fig. 6.29 and Table 6.3. As noted, approximately 0.5% of the initial iodine activity in the core is projected to be contained in the surrounding atmosphere about 6 h after battery failure (10 h after reactor scram).

11. We note a significant transport pathway from the pressurized reactor vessel through the MSIV's and ultimately to the main condenser system. As shown in Figs. 6.7, 6.16, and 6.25 and Tables 6.1 to 6.3, 0.1% of the Krypton, 0.8% of the Xenon and ~0.03% of the initial

---

*The unmelted lowest nodes of the central core are predicted to fall into the lower head along with the rest of the central core.

iodine inventories are presented in the condenser system. A portion of this activity can be expected to pass into the Turbine Building.

7.4 Summary of Principal Release Pathways and Uncertainties

1. One of the two major iodine release pathways involved in the Station Blackout accident sequence occurs as follows: (a) transport with the molten core/structure in the reactor vessel to the drywell at the time of melt-through of the reactor vessel lower head, (b) evolution from the drywell floor via a 'sparging' release, (c) convection as gaseous iodine and as absorbed iodine on aerosol particles generated by core/concrete interaction through the failed primary containment and the Reactor Building, the convection being provided by concrete degradation gases.

2. The principal uncertainties of the iodine release estimate relate factors involved in this major pathway. These are:

   a. The estimate of the inventory of volatile material in the melt prior to melt-through of the reactor vessel bottom head is of major importance. This estimate in turn depends primarily on the calculated temperature distribution in the core prior to melt-through and on the estimated melt release rates. In particular, improved temperature estimates for the core material both before and after meltdown and core slumping are critical.

   b. The fission product evolution rates under the gas 'sparging' condition when the core debris is on the drywell floor are highly uncertain and directly affect the computed release to the atmosphere.

3. The second major iodine release pathway, of approximately equal importance, consists of the following: (a) release from fuel material prior to reactor vessel failure, (b) capture on reactor vesssel internal surfaces, primarily as CsI condensed on aerosol particles which deposit (mainly by thermophoresis) on the steam dryers, (c) evolution and transport to the drywell after melt-through of the reactor vessel lower head.

4. The major uncertainties relating to this second dominant pathway are:

   a. Verification of the mixture of iodine chemical species which form in the reactor vessel would be desirable in view of the large volatility differences between species.

   b. The estimate of the degree of aerosol deposition on internal reactor vessel surfaces is difficult and subject to large uncertainty due to factors relating both to aerosol formation and deposition mechanisms and the prediction of internal surface temperatures.

   c. The estimate of the leakage rate from the failed reactor vessel to the drywell needs to be improved.

5. The third most significant pathway occurs via the evolution of iodine from the pressure suppression pool during the 40 minute period following drywell failure when the pool temperature exceeds the saturation temperature. The principal uncertainties in this estimate relate to (a) the degree of iodine volatility under these conditions and (b) the nature of the fluid dynamic phenomena accompanying the abrupt depressurization of the large water mass.

Table 7.1. Synopsis of key events

	Time from battery loss (m)
Battery exhaustion	0
Core uncovery begins	60
First cladding failures	103
Fuel melt initiation	120
Central core collapses	137
Reactor vessel failure	172
Drywell vent initiation	238
Drywell seal failure	249

Appendix A

ALTERNATE FISSION PRODUCT RELEASE PATHWAYS

A.1 Introduction

The principal pathway for leakage of fission products to the environment during a postulated major BWR accident is via (1) release into the reactor vessel through the perforated cladding of failed fuel elements, (2) convection with the steam through the primary relief valves into the pressure suppression pool, (3) movement of core material onto the drywell floor after failure of the reactor vessel bottom head, (4) convection throughout the drywell and the wetwell airspace, (5) gross failure of the primary containment structure followed by convection into the Reactor Building, and (6) escape from the Reactor Building, which comprises the secondary containment for a BWR. This six-step pathway is indeed the predominant release mode for the prolonged station blackout severe accident sequence considered here. However, it is important to recognize that other release pathways exist, through which significant contamination can spread to systems outside containment during the early stages of the accident, and that these alternate release pathways would be dominant in accidents that are terminated prior to gross containment failure.

The purpose of this section is to identify the alternate pathways for fission product transport across the boundaries of the drywell and wetwell prior to gross containment failure. This will be done by examination of the major reactor functional systems that penetrate the primary containment boundary. Although all of these systems have some form of provision for valve operation to effect containment isolation under accident conditions, some valve leakage is inevitable, and it is desirable to develop an approximate measure of the leakage magnitude. To this end, the Tennessee Valley Authority (TVA) has provided the results of all local leak rate testing performed at Browns Ferry Unit 1 since August, 1976.

As discussed in Appendix B, the maximum allowable integrated leakage rate La for the Unit 1 primary containment is 2.0% of the containment volume per 24 h at the peak design basis accident containment pressure of 0.443 MPa (49.6 psig); this is equivalent to a leakage of 30.96 m^3/h (STP) (1093.2 scfh). A Containment Integrated Leak Rate Test (CILRT) is required at least once every 3-1/3 years, and the total leakage is reduced to less than 75% of La before return to power operation following each test.

There is an additional requirement for Local Leak Rate Tests (LLRTs) to be conducted at the end of each operating cycle. The allowable summed total of the individually measured containment isolation valve and penetration seal leakages determined during these tests is limited to 60% of La, i.e., a leakage of 18.57 m^3/h (STP) (655.9 scfh). It should be noted that many of the isolation valves tested during the LLRTs are in piping systems which lead directly from the reactor vessel or associated piping to outside containment; the leakage through these valves does not contribute to the overall leakage from the primary containment atmosphere.

Experience has shown that it is invariably necessary to effect repairs to the containment isolation valves and penetration seals in order

to meet the leakage criterion for the LLRTs. However, the measured 'as-found' leakages, i.e., the leakages before any repairs, are recorded as well as the final test results. The as-found leakage rates determined during the LLRTs for the Browns Ferry Unit 1 primary containment conducted at the end of cycle 3 in January, 1980, will be used here as representative* values for leakages through the alternate release pathways. It should be emphasized that the leakages to be discussed in this section are those which were measured before repairs; the total measured LLRT leakage was reduced to 4.07 m^3/h (STP) (143.8 scfh), well below the 60% of La limit, before operation was resumed for cycle 4.

Automatic isolation of the containment under accident conditions is effected by the Primary Containment and Reactor Vessel Isolation Control System (PCIS), which is briefly described in Sect. A.2. It is leakage through the installed check valves and the valves automatically closed by the PCIS which under severe accident conditions would spread contamination outside containment through the alternate release pathways.

The alternate release pathways will be divided into four groups for the purpose of discussion. The first group comprises the pathways for leakage directly from the primary system to outside containment and is discussed in Sect. A.3. The pathways from the drywell atmosphere form the second group, which is discussed in Sect. A.4. The third and fourth groups are concerned with leakage pathways from the wetwell; leakage from the wetwell airspace is discussed in Sect. A.5, and the pathways for water leakage from the pressure suppression pool are discussed in Sect. A.6. A summary of the effects of the alternate pathway leakage is provided in Sect. A.7.

For this examination of alternate release pathways, it is assumed that no independent secondary equipment failures will occur within the reactor functional systems in which the pathways are located. With no independent secondary failures, all valves are assumed to be in their proper positions, and it is assumed that there are no component failures such as heat exchanger tubing ruptures unless the equipment is determined to be overheated or overstressed as a direct result of the conditions imposed by the Station Blackout. It has also been assumed that no additional release pathways are opened through the effects of incorrect operator action. These assumptions reduce the number of possible occurrences and permit concentration on the most probable behavior.

A.2 The Primary Containment and Reactor Vessel Isolation Control System

The Primary Containment and Reactor Vessel Isolation Control System (PCIS) initiates automatic closure of isolation valves in pipelines which penetrate the primary containment whenever certain monitored variables exceed their predetermined setpoints. The system is designed so that once initiated, automatic isolation goes to completion and return to normal

*But conservative, since these as-found leakages were measured at the end of the operating cycle. Nevertheless, these leakages are characteristic of those found at the end of every operating cycle.

operation after isolation requires deliberate operator action. Since these valves protect the primary containment boundary and will function differently in different accident sequences, it is important to understand their operational design.

The isolation valves subject to automatic closure by the PCIS are conveniently divided into eight groups, each characterized by the set of isolation initiation signals which can independently cause automatic closure of the valves included in the group. These eight valve groupings are listed in Tables A.1 through A.8. The general valve classification, the normal position during reactor operation, and the power source needed for opening and closing are provided for each valve in the tables, together with the two-part Browns Ferry Unit 1 valve identification number. The first part of the identification number identifies the system in which the valve is placed, and the key for the valves of each group is provided at the end of each table. The second part of the identification number merely serves to differentiate between the valves within each system. The valve identification numbers are useful for cross-referencing the information in these tables to the figures provided in Sects. A.3 to A.6.

A.3 Alternate Pathways for Direct Leakage from the Primary System to Outside Containment

The pathways for leakage from the reactor vessel and associated piping through the primary containment boundary are discussed in this section. The significant pathways and the associated penetration numbers are listed in Table A.9, together with the as-found leakages for each route as determined during the LLRTs conducted in January, 1980.

A.3.1 Main steam lines pathway

As shown in Table A.9, the majority of the leakage is through the shut main steam isolation valves (MSIVs) in the main steam lines. This portion of the main steam system is shown schematically in Fig. A.1, and the individual leakages for each of the four main steam lines and the bypass line are indicated by the open-headed arrows on this figure. The MSIVs are included in PCIS group I, described in Table A.1.

The MSIVs are 26-in. Atwood-Morrill globe valves with stellite seats. The Technical Specifications limit for leakage is 11.5 scfh per valve, but the as-found results for each set of LLRTs demonstrate that deterioration of the valve seating surfaces due to steam erosion during normal operation leads to leakages which greatly exceed this limit by the end of each operating cycle. The measured as-found leakages at the end of cycles 3 and 4 are compared in Table A.10.

As shown in Fig. A.1, the leakage through each set of main steam line isolation valves is free to pass through orificed drains into the main condenser system. There would be an additional leakage path from downstream of the orificed drains in the main steam piping into the turbine gland sealing steam header since the steam seal valve fails open on loss

of power.* Noncondensables are normally removed from the main condensers through the Offgas System, but this system would be shut down and automatically isolated under blackout conditions. Significant leakage through the MSIVs during the fuel failure stages of a severe accident would cause major contamination of the main condensers, which are located in the Turbine Building. Some of this contamination would leak from the main condenser system into the Turbine Building, primarily through the labyrinth seals of the low-pressure turbines, since effective gland sealing would not exist. The effect of this leakage has been included in the fission product transport analysis by assuming MSIV leakage equivalent to that found during the LLRTs at the end of cycle 3.

Valve repairs are always performed as necessary to bring the MSIV leakages into tolerance before resumption of power operation. The measured as-left leakages at the end of cycles 3 and 4 are listed in Table A.11.

A.3.2 Core spray injection pathways

As shown in Fig. A.2, leakage from the primary system to outside containment is possible through either of the two 360° core spray spargers located within the reactor vessel and the associated Core Spray (CS) system piping. The valves 75-25 and 75-53 shown on this figure are normally shut AC motor-operated valves which are designed to automatically open as the CS pumps start on a low-pressure ECCS injection system initiation signal. These valves would be inoperable during a station blackout when AC power is unavailable.

The leakages indicated by the open-headed arrows in Fig. A.2 are those measured during the LLRTs at the end of cycle 3. The back-leakage through the reactor vessel spargers during the period of fuel failure would contaminate the CS system piping in the Reactor Building. Since the check valves at the discharge of each CS pump would probably also leak, the leakage flow from the reactor vessel should pass back through the CS pumps and into the suppression pool ring header.

A.3.3 Residual heat removal (RHR) system pathways

The pathways for direct release of fission products from the reactor vessel recirculation piping to outside containment via the RHR system are shown in Figs. A.3 and A.4. The indicated leakages are the as-found values during the LLRTs conducted at the end of cycle 3.

Valves 74-53 and 74-67 are normally closed but would automatically open as the RHR pumps start on a low-pressure ECCS initiation signal. Valves 74-47 and 74-48 are manually opened by the operator only when the RHR system is to be placed into the shutdown cooling mode. These valves are all AC motor-operated and would remain shut during a station blackout.

---

*Downstream flow within the main steam lines is blocked by closure of the turbine stop valves and the turbine bypass control valves. Any leakage through these valves would also pass to the main condenser.

The leakages indicated on Figs. A.3 and A.4 would spread significant contamination into the RHR system after fuel failure. Back-leakage through the check valves at the discharge of each pump would pass the leakage into the suppression pool ring header.

A.3.4 HPCI and RCIC steam supply lines pathway

The HPCI and RCIC systems steam supply piping is shown in Fig. A.5. The inboard and outboard primary containment isolation valves for each system are normally open. Valves 73-2 and 73-3 for the HPCI system are in PCIS Group IV (Table A.4) and valves 71-2 and 71-3 for the RCIC system are in PCIS Group V (Table A.5). The inboard valves are AC motor-operated and would remain open during a station blackout. The outboard valves are DC motor-operated but would also remain open during a station blackout unless remote-manually shut by the operator before DC power is lost.

The two valves at the turbine inlet in each system are shut except when the turbine is being operated. The two DC motor-operated isolation valves in the drain line from the steam trap in each system to the main condenser are normally open, but these valves are in PCIS Group VII (Table A.7) and would automatically shut on reactor vessel low water level. For a prolonged station blackout, DC power would be lost before a low reactor vessel water level occurred; however, the drain line isolation valves would either have been spring-closed before this due to loss of control air pressure or would spring-close at the time DC power is lost.

In summary, an open pathway from the reactor vessel through the steam supply piping up to the turbine steam inlet valve would exist in both the HPCI and RCIC systems during a station blackout. This piping would become severely contaminated after the beginning of fuel failure, but the isolation valves in the drain line from this piping would be closed in each system long before fuel failure occurred.

A.3.5 Feedwater line pathways

The pathways for direct leakage of fission products from the reactor vessel to outside containment via the feedwater line penetrations are shown in Fig. A.6. Each pathway is protected by two check valves in series, and the as-found leakage rates through each valve as determined during the LLRTs conducted at the end of cycle 3 are indicated on the figure.

The test results show that significant leakage into the feedwater piping can be expected during the station blackout and that after fuel failure, this piping would be severely contaminated. The valves 71-39 and 73-44 in the discharge piping from the RCIC and HPCI pumps, respectively, are DC motor-operated valves which are shut except when the associated pump is operating. The valve 69-12 in the return line from the reactor water cleanup system is in PCIS Group III (Table A.3) but is AC motor-operated and could not be closed during a station blackout. The CRD hydraulic return line which taps into feedwater line B is not normally used and is isolated by a shut upstream valve 85-50 (not shown).

A.3.6 Pathways from the recirculation system

The pathways for leakage of reactor vessel water through the recirculation system are shown in Fig. A.7. The recirculation water quality sampling valves 43-13 and 43-14 are in PCIS Group I (Table A.1) and are normally shut. If they were open when the blackout occurred, the loss of AC power would cause these air-operated valves to spring-close.

The lines for injection of water into the recirculation pump seals from the Control Rod Drive (CRD) hydraulic system are each protected by two check valves in series. Normally the pressure at the discharge of the CRD hydraulic pump exceeds the pressure in the recirculation loop but during a station blackout the CRD pump would not be running and there would be some leakage into the CRD system as indicated on Fig. A.7.

Water is taken into the Reactor Water Cleanup (RWCU) system both from recirculation loop A and from the bottom of the reactor vessel, as shown in Fig. A.7. Valves 69-1 and 69-2 are in PCIS Group III (Table A.3), but valve 69-1 is AC motor-operated* and could not be closed during a station blackout. Valve 69-2 is DC motor-operated and would close almost immediately following the inception of a station blackout when the reactor vessel level decreased temporarily following MSIV closure; this valve was found to have zero leakage during the cycle 3 testing.

A.3.7 Scram discharge volume pathway

During a station blackout the scram inlet and outlet valves for each of the 185 control rod drive mechanisms would fail open and the vent and drain valves on the scram discharge volume piping would fail shut so that the scram discharge volume would be pressurized to reactor vessel pressure through leakage past the CRD mechanism seals. Any leakage through the scram discharge volume vent and drain valves would provide a path for escape of fission products from the reactor vessel through the CRD mechanism seals and the scram discharge volume piping into the reactor building equipment drain sump. The scram discharge volume vent and drain valves are not included in the LLRTs conducted at the end of each operating cycle.

A.4 Alternate Pathways for Leakage from the Drywell Atmosphere

The pathways for leakage through the primary containment boundary from the drywell atmosphere will be discussed in this section. The significant pathways are listed in Table A.12, together with the as-found leakage rates determined during the LLRTs conducted at the end of cycle 3 in January 1980.

A.4.1 RHR containment spray pathways

The pathways for leakage from the drywell atmosphere into the RHR system through the drywell spray spargers are shown in Figs. A.3 and A.4. Each of the two drywell spray line containment penetrations (X-39A and

---

*In general, inboard primary containment isolation valves are AC motor-operated while the outboard valves are DC motor-operated.

X-39B) is protected by two normally shut AC motor-operated valves outside containment. Late in the station blackout accident sequence after the MARCH-code predicted reactor vessel failure, the vessel pressure and containment pressure would equalize, and leakage through the drywell spray spargers would mix with leakage from the recirculation loop within the RHR system.

A.4.2 Drywell sump pathways

The pathways for leakage from the drywell sumps are shown in Fig. A.5. Each pathway is guarded by two in-series air-operated valves outside containment which are included in PCIS Group II (Table A.2). However, for a station blackout sequence these valves would be spring-closed immediately upon the loss of AC power. The leakage through these valves is passed directly into collection tanks in the radwaste system.

A.4.3 Bellows

Excessive leakage from the drywell atmosphere into the Reactor Building around the outer circumference of large piping that penetrates the drywell boundary is prevented by means of bellows. The bellows for the main steam, feedwater, RCIC and HPCI steam supply, RHR shutdown cooling suction, RHR LPCI injection, core spray injection, RWCU suction, and RHR head spray injection lines are tested as part of the LLRTs conducted at the end of each operating cycle. The test is performed by pressurizing the volume within the bellows and individually measuring both the leakage into the drywell and the leakage into the Reactor Building. Since leakage from the drywell under accident conditions would have to pass through both the inboard and outboard bellows seals, the total bellows leakage of 0.02 scfh given in Table A.12 is the sum of the lower values of the two leakages measured for each bellows during the tests.

A.4.4 Resilient seals

The resilient seals such as those for the drywell head and the personnel air lock are tested by pressurizing the volume between the seals and measuring the total leakage into both the drywell and the reactor building. Since the leakage from the drywell would have to pass through both the inboard and the outboard seals under accident conditions, the resilient seal leakage given in Table A.12 is one-half the total reported in the test results.

It should be noted that 99% of the total measured resilient seal leakage is for the personnel airlock. When the airlock is pressurized, the door into the drywell tends to unseat with test pressure. However, under accident conditions in which the drywell was pressurized, the inner airlock door would tend to seat.

A.4.5 Electrical seals

As with the resilient seals, the reported leakage is the total leakage into both the drywell and the reactor building. To obtain a reasonable estimate of the leakage potential from the drywell to the reactor

building through both seals, the value given in Table 2.12 is one-half of the reported leakage.

The leakage through the bellows, resilient seals, and electrical penetration seals is particularly significant because this leakage is into the reactor building atmosphere. All other leakages discussed previously have been into closed systems outside containment.

A.4.6 Drywell control air suction and discharge pathways

The pathways for leakage from the drywell atmosphere into the drywell control air system are shown in Fig. A.8. The air compressor suction line is protected by two normally open air-operated valves outside containment which are included in PCIS Group II (Table A.2). Both of these valves would immediately fail shut upon the loss of AC power at the inception of the station blackout sequence.

The discharge line from the control air receivers through the primary containment into the control air header within the drywell is protected by two check valves in series. There are no motor- or air-operated valves in this line for improved reliability that the stored air in the receivers will be available to the air-operated equipment within the drywell under accident conditions.

The leakage into the drywell control air system would remain confined within the system.

A.4.7 Containment ventilation and inerting systems leakage

The pathways for leakage from the drywell into the containment ventilation and inerting systems are shown in Fig. A.9. This piping is air-tested at 0.443 MPa (50 psig) in four sections, and the measured leakage for each section is the total through the shut valves on the section boundary.

Proceeding from left to right, the first section shown on Fig. A.9 comprises the piping paralleled by dashed lines between valves 64-29, 64-30, 64-32, 64-33, and 84-19. The total as-found leakage for this section was 30.54 scfh; this leakage is shown associated with valve 84-19, but actually is the total leakage through the five valves on the section perimeter. Normally shut valves 64-29, 64-30, 64-32, and 64-33 are in PCIS Group VI (Table A.4) and if open, would immediately fail shut on loss of AC power in a station blackout.

The second section shown on Fig. A.9 comprises the piping paralleled by dashed lines between valves 64-31, 64-34, and 84-20. The inlet and outlet valves to the compressor were shut for the test, and normally shut valve 64-141 was open. The leakage of 2.76 scfh shown associated with valve 84-20 is actually the total leakage through the three valves on the section boundary. Normally shut valves 64-31 and 64-34 are in PCIS Group VI (Table A.6), and if open, would immediately fail shut on loss of AC power in a station blackout.

The third section comprises the piping between the containment inerting system valves 76-17, 76-18, and 76-19. The measured leakage for this section was zero for the tests at the end of cycle 3. These normally shut valves are also in PCIS Group VI and, if open, would immediately fail shut on loss of AC power in a station blackout.

The fourth section shown on Fig. A.9 comprises the piping between valves 64-17, 64-18, 64-19, and 76-24. The leakage of 28.79 scfh shown associated with valve 76-24 is actually the total measured leakage through the four valves on the section perimeter. Normally shut valves 64-17, 64-18, and 64-19 are in PCIS Group VI and, if open, would immediately fail shut upon loss of AC power in a station blackout.

Leakage into the closed Containment Atmosphere Dilution (CAD) system is considered insignificant and will be neglected here. The leakage from the torus airspace through the vacuum reliefs will be discussed in Sect. A.5.4.

Because of the nature of the testing of the valves in the containment ventilation and inerting systems, it is difficult to obtain a good estimate of the extent of leakage outward from a pressurized drywell under accident conditions. As discussed previously, the normally shut valves in these systems which lie in the pathways from the primary containment to the reactor building ventilation supply fans and ducting are spring-loaded to close and, if open, would fail shut upon loss of AC power; each of these pathways contains at least two of these valves in series. The drywell exhaust pathways to the Standby Gas Treatment System (SBGTS) and reactor building ventilation exhaust are similarly protected. Therefore, although the ducting internal to the containment ventilation and inerting systems would probably become heavily contaminated during the latter stages of a severe accident when a high concentration of fission products existed in the drywell, the spread of contamination into the reactor building supply and exhaust ducting should be small.

A.5 Alternate Pathways for Leakage from the Wetwell Airspace

The pathways for leakage through the torus boundary from the wetwell airspace will be discussed in this section. The significant pathways are listed in Table A.13 with the as-found leakage rates determined during the testing at the end of cycle 3 in January 1980.

A.5.1 RCIC turbine exhaust line pathway

The pathway for leakage from the pressurized torus airspace through the exhaust line vacuum breakers, locked-open valve 71-14, and check valve 71-580 to the RCIC turbine and barometric condenser is shown in Fig. A.10. The exhaust line vacuum breakers function to prevent water from being drawn up into the turbine exhaust line when the exhaust steam in this line condenses after turbine shutdown; their presence also ensures that leakage into the turbine exhaust from a pressurized torus would be from the airspace rather than water from the pool.

As shown on Fig. A.10, most of the leakage would pass into the barometric condenser through either the turbine drains or the (leaking) steam trap. The torus would not become severely contaminated until after the loss of DC power in the Station Blackout sequence, so that the condensate pump would not be operable to pump the contaminated leakage into the RCIC pump suction.

The drain valves 71-7A and 71-7B on the condensate pump discharge are normally open and remain open during RCIC operation, continuously passing

a small flow into the clean radwaste system. These valves are in PCIS Group VII (Table A.7), but the reactor vessel low level which signals closure of this group would not be expected until after loss of DC power in the Station Blackout sequence. Nevertheless, these valves are spring-loaded to shut upon loss of either control air or DC power and therefore would be shut before the torus became severely contaminated.

The contamination entering the turbine exhaust should be mainly confined within the piping associated with the exhaust line, although some may pass through the idle condensate pump up into the RCIC pump suction line. If the leakage were sufficient to pressurize the barometric condenser to 0.170 MPa (10 psig), the relief valve would open to the clean radwaste system.

A.5.2 HPCI turbine exhaust line pathway

The pathway for leakage from the pressurized torus airspace through the vacuum breakers, locked-open valve 73-23, and check valve 73-603 into the HPCI turbine and the gland seal condenser is shown in Fig. A.11. As in the RCIC system, the exhaust line vacuum breakers are provided to prevent suppression pool water from being drawn up into the turbine exhaust line after turbine operation.

As shown on Fig. A.11, most of the leakage would pass into the gland seal condenser through either the turbine drains or the drain pot and (leaking) level control valve (LCV). In the station blackout sequence, the torus would not become severely contaminated until after the loss of DC power so neither the condensate pump nor the gland seal exhauster would be operable.

The drain valves 73-17A and 73-17B on the condensate pump discharge are normally shut. If a high gland seal condenser hotwell level signal is sensed when the HPCI system is not operating, the condensate pump is automatically started, and these valves open to pass the flow to the clean radwaste system. These valves are in PCIS Group VII (Table A.7), and would fail shut upon loss of DC power.

Some of the contaminated leakage entering the gland seal condenser would pass through the idle condensate pump and spread toward the HPCI booster pump suction, but most would pass through the idle gland seal exhauster into the 0.711-m (28-in.) SBGTS ducting. The SBGTS would be inoperable under blackout conditions.

A.5.3 Wetwell containment spray pathways

The pathways for leakage from the wetwell airspace into the RHR system through the wetwell spray spargers are shown in Figs. A.3 and A.4. Each of the two wetwell spray line containment penetrations (X-211A and X-211B) is protected by two normally shut AC motor-operated valves outside containment. This leakage path would not become significant until late in the Station Blackout sequence when the reactor vessel and containment pressure had equalized following the MARCH code-predicted vessel failure. After this, contamination could spread into the RHR system from the recirculation loops, the drywell atmosphere, and the wetwell airspace simultaneously as shown in Figs. A.3 and A.4.

A.5.4 Torus-Reactor Building vacuum breakers

The leakage pathway from the torus airspace into the Reactor Building through the vacuum breakers is shown on the lower right-hand side of Fig. A.9. This pathway is particularly important because during the latter stages of a severe accident, the leakage would spread contamination directly into the reactor building atmosphere.

The torus-reactor building vacuum breakers are provided to prevent the external design pressure for the primary containment from being exceeded. As shown on Fig. A.9, there are actually two vacuum breakers in series on each of two lines to atmosphere. Both of the vacuum breakers on each line are independent of electrical power; one is air-operated and actuated by a differential pressure signal while the other is self-actuating.

A.6 Alternate Pathways for Leakage of Pressure Suppression Pool Water

The pathways for water leakage through the torus boundary from the pressure suppression pool are discussed in this section. The significant pathways are listed in Table A.14 with the as-found leakage rates determined during the LLRTs conducted at the end of operating cycle 3 in January 1980.

A.6.1 RCIC vacuum pump discharge

The pathway for leakage of pressure suppression pool water from the pressurized torus through locked-open valve 71-32 and check valve 71-592 in the barometric condenser vacuum pump discharge line is shown in Fig. A.10. The vacuum pump would be inoperable after the loss of DC power in the Station Blackout sequence, and most of the leakage would pass into the barometric condenser through the vacuum pump although some would pass through the pressure control valve (PCV). This leakage would mix with the leakage from the wetwell airspace discussed in Sect. A.5.1.

A.6.2 HPCI steam trap discharge

The pathway for leakage of pressure suppression pool water from the pressurized torus through locked-open valve 73-24 and check valve 73-609 in the drain line from the steam trap on the HPCI turbine exhaust line is shown in Fig. A.11. This leakage would pass into the gland seal condenser either directly through the (leaking) drain pot level control valve (LCV) or by first passing up through the drain pot and mixing with the leakage from the torus airspace discussed in Sect. A.5.2. The SBGTS would not be operative under Station Blackout conditions, and the most significant effect of both of these leakages into the gland seal condenser would be to spread contamination into the SBGTS ducting shown in Fig. A.11.

A.6.3 Pathway through the head tank line on core spray suction

The pathway for leakage of pressure suppression pool water from the pressurized torus into the keep full system through normally shut valves

75-57 and 75-58 is shown in Fig. A.2. These valves are in PCIS Group II (Table A.2) and are spring-loaded to fail shut upon loss of AC power. If the torus pressure is sufficiently high, this leakage would spread contamination throughout the keep full system.

A.7 Summary of Effects of Alternate Pathway Leakage in the Station Blackout Sequence

In the accident sequence predicted by the MARCH code for a hypothetical prolonged Station Blackout, the reactor vessel pressure and water level are maintained in the normal operating range for as long as DC power remains available. After the unit battery is exhausted, makeup water can no longer be injected into the vessel, and the core becomes uncovered. Fuel failure begins, and the released fission products are convected into the pressure suppression pool with the steam passed through the primary relief valves. Most of the fission products are retained by the pool, but the noble gases and a significant amount of particulate contamination would escape the pool and pass into the wetwell airspace and the drywell.

After some time, the severely degraded core is predicted to slump into the lower plenum of the reactor vessel, burn its way through the vessel bottom head, and fall to the concrete floor of the drywell. The relatively few volatile fission products remaining in the core material at this time are subject to direct release into the drywell atmosphere. The containment pressure increases rapidly after the corium leaves the reactor vessel and gross primary containment failure is predicted to occur when the electrical penetration assemblies fail through temperature-induced degradation of their seals at about 260°C (500°F).

The purpose of this section has been to present a qualitative assessment of the effect of leakage through the alternate release pathways, i.e., the pathways existing before the predicted gross failure of the containment. The alternate pathways which exist for direct leakage from the reactor vessel into several systems outside containment are discussed in Sect. A.3. This leakage bypasses the pressure suppression pool and would cause severe contamination of the main condensers in the Turbine Building and of all emergency cooling systems in the Reactor Building after fuel failure. The attendent radiation levels would discourage attempts at hands-on repair of the affected systems. As shown in Table A.9, the great majority of the leakage from the reactor vessel is through the main steam isolation valves, and the associated leakage has been considered in the fission product transport analysis.

The alternate pathways for direct leakage from the drywell atmosphere are discussed in Sect. A.4. The leakages from the drywell atmosphere into the mechanical systems outside containment are less significant than those from the primary system since there is a much lower level of fission product concentration in the drywell throughout the accident. However, as summarized in Table A.12, there are pathways for direct leakage from the drywell into the reactor building atmosphere through the piping penetration bellows, the resilient seals, and the electrical seals. These pathways would contribute significantly to the levels of radioactivity within the Reactor Building during the period between the onset of fuel failure

and the subsequent gross failure of the primary containment, and the associated leakages have been considered in the fission product transport analysis.

The alternate pathways for leakage from the wetwell airspace are discussed in Sect. A.5. The leakage into the mechanical systems outside containment is again less important than that from the reactor vessel because of the much lower concentration of fission products. However, as summarized in Table A.13, the torus-reactor building vacuum breakers provide a direct path for leakage of the noble gases and the particulate fission products which escape capture by the pool into the reactor building atmosphere. The leakage through this pathway would contribute significantly to the spread of contamination into the reactor building atmosphere during the period before gross containment failure and has been considered in the fission product transport analysis.

The pathways for leakage of water from the pressure suppression pool into the mechanical systems outside containment are discussed in Sect. A.6. Although the pool water would contain a high concentration of dissolved or entrained particulate fission products from the onset of fuel failure, the effect of this leakage would be less severe than that of the leakage into the same systems from the reactor vessel.

As discussed above, the most important alternate release pathways are those which permit a direct transport of fission products into the reactor building atmosphere or into the main condenser system in the Turbine Building. The effect of the leakages through these pathways has been included in the quantitative fission product transport analysis performed in this study.

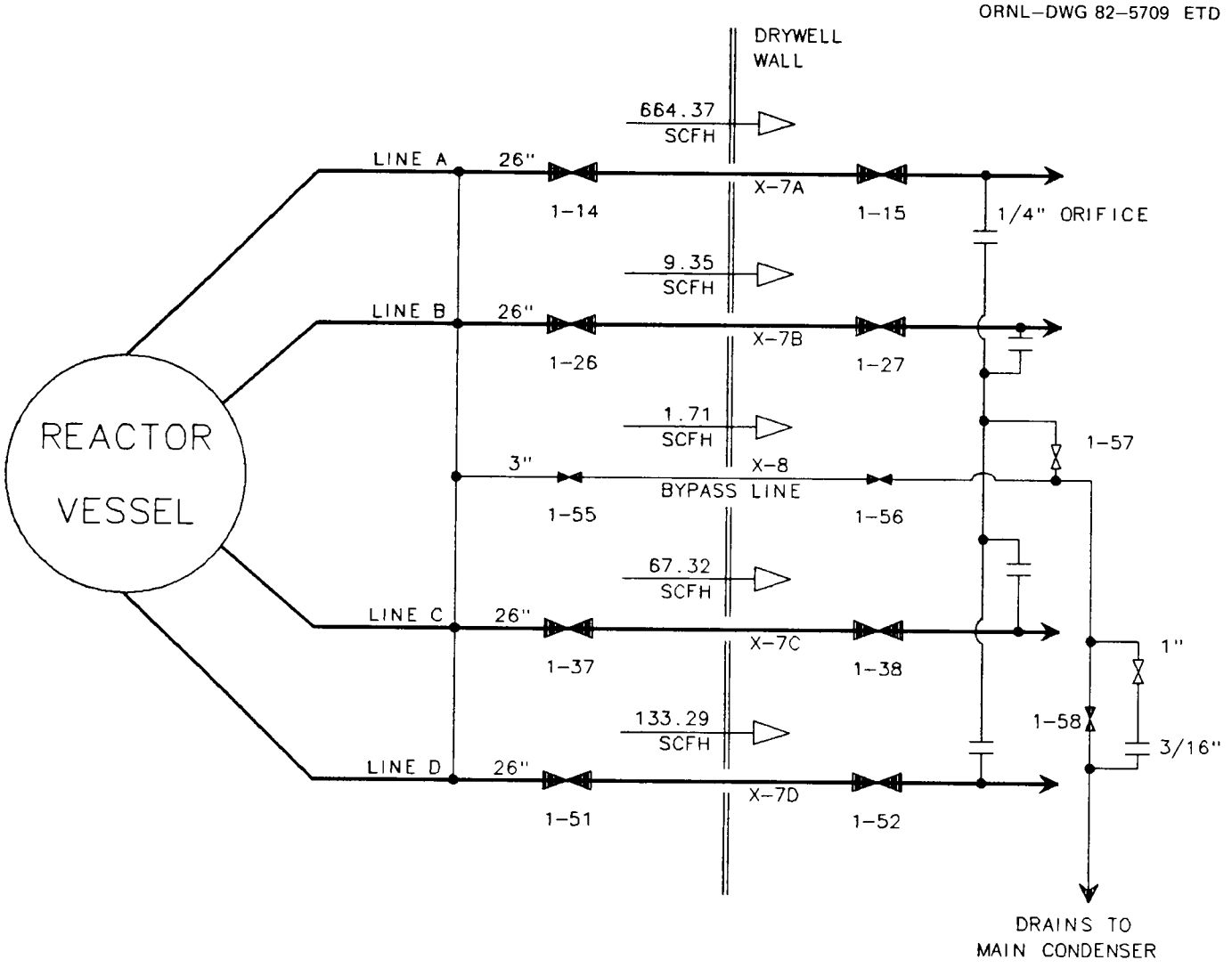

Fig. A.1. Main steam system leakage.

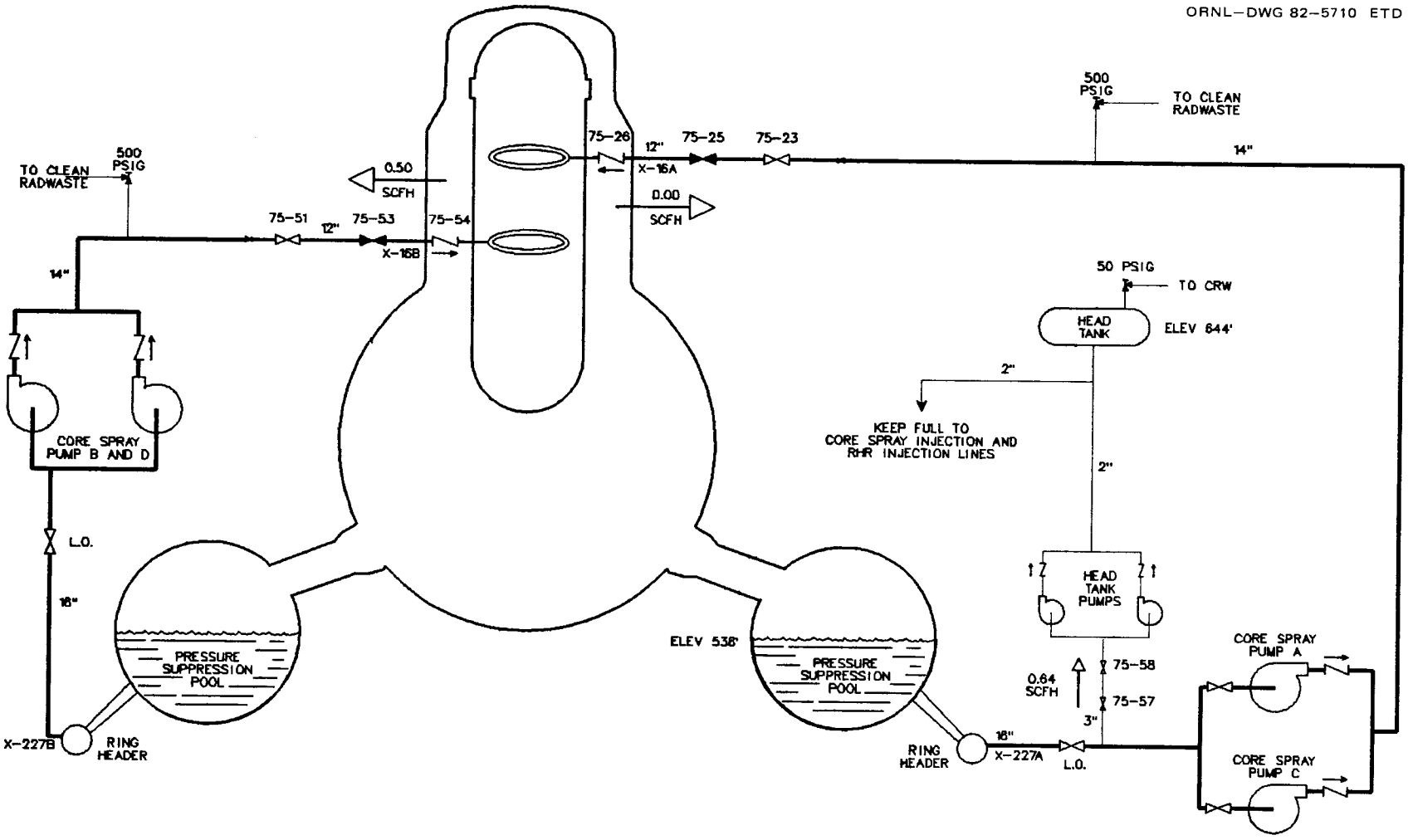

Fig. A.2. Core spray (CS) system leakage.

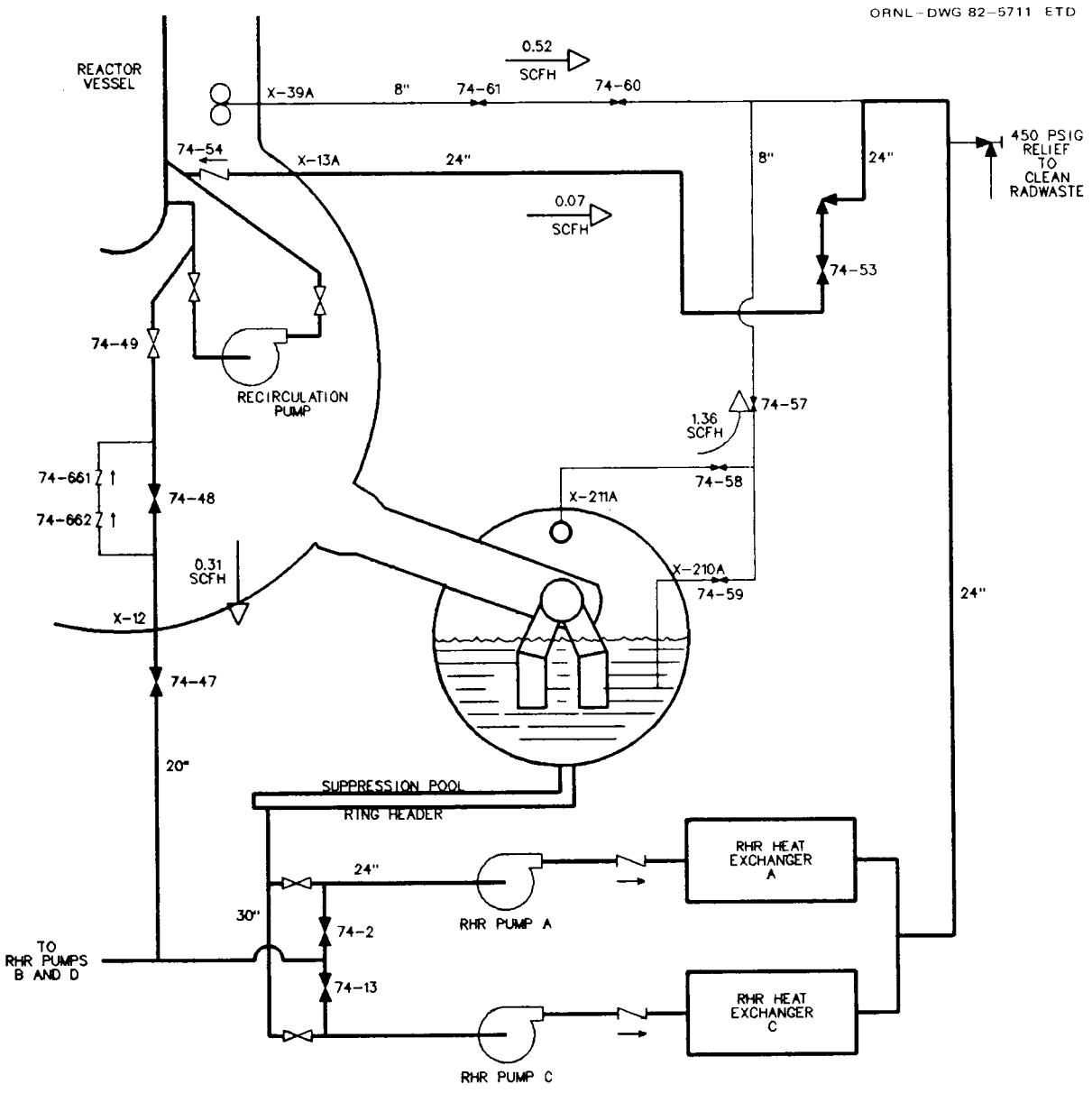

Fig. A.3. RHR system leakage (pumps A and C).

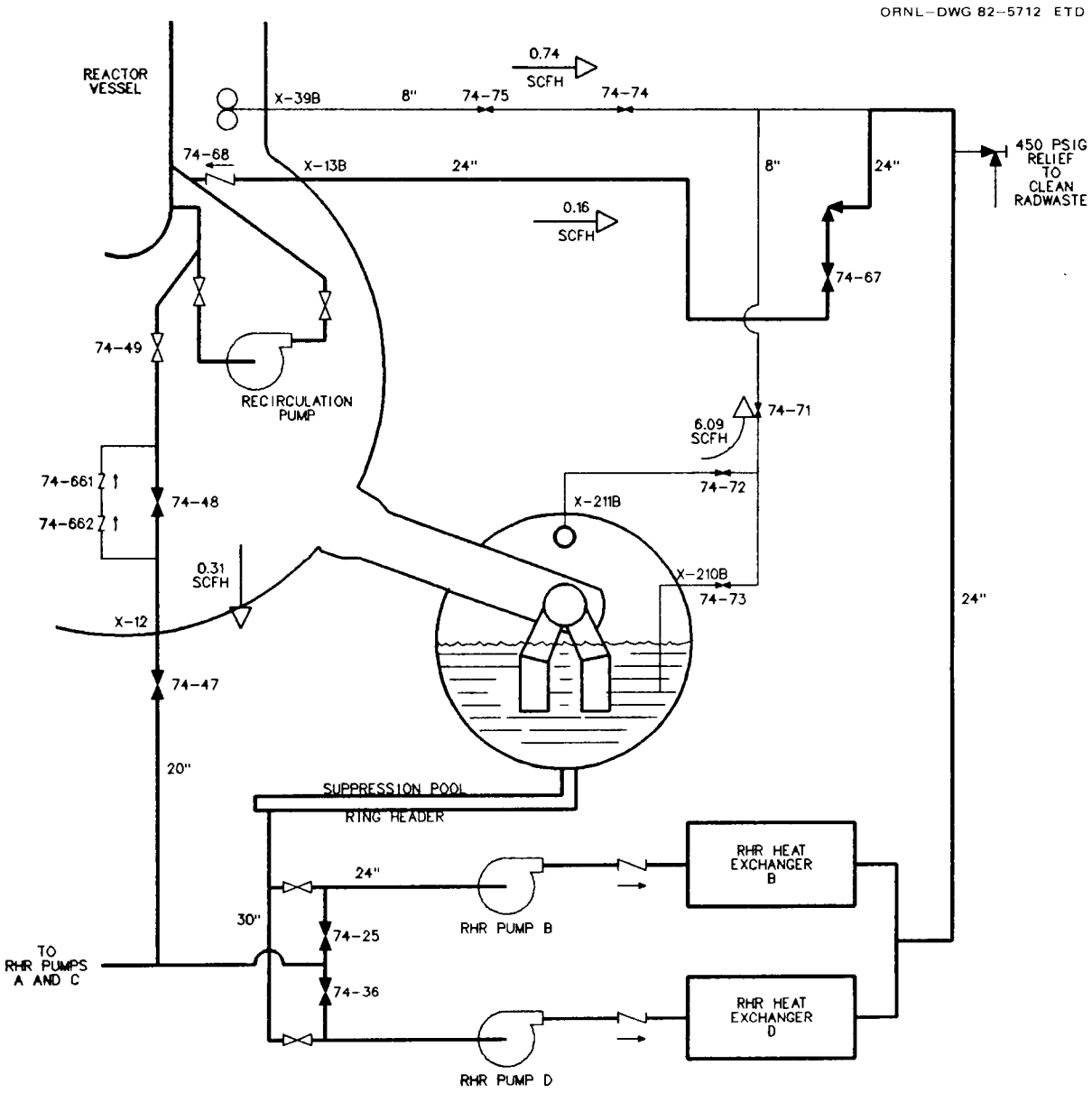

Fig. A.4. RHR system leakage (pumps B and D).

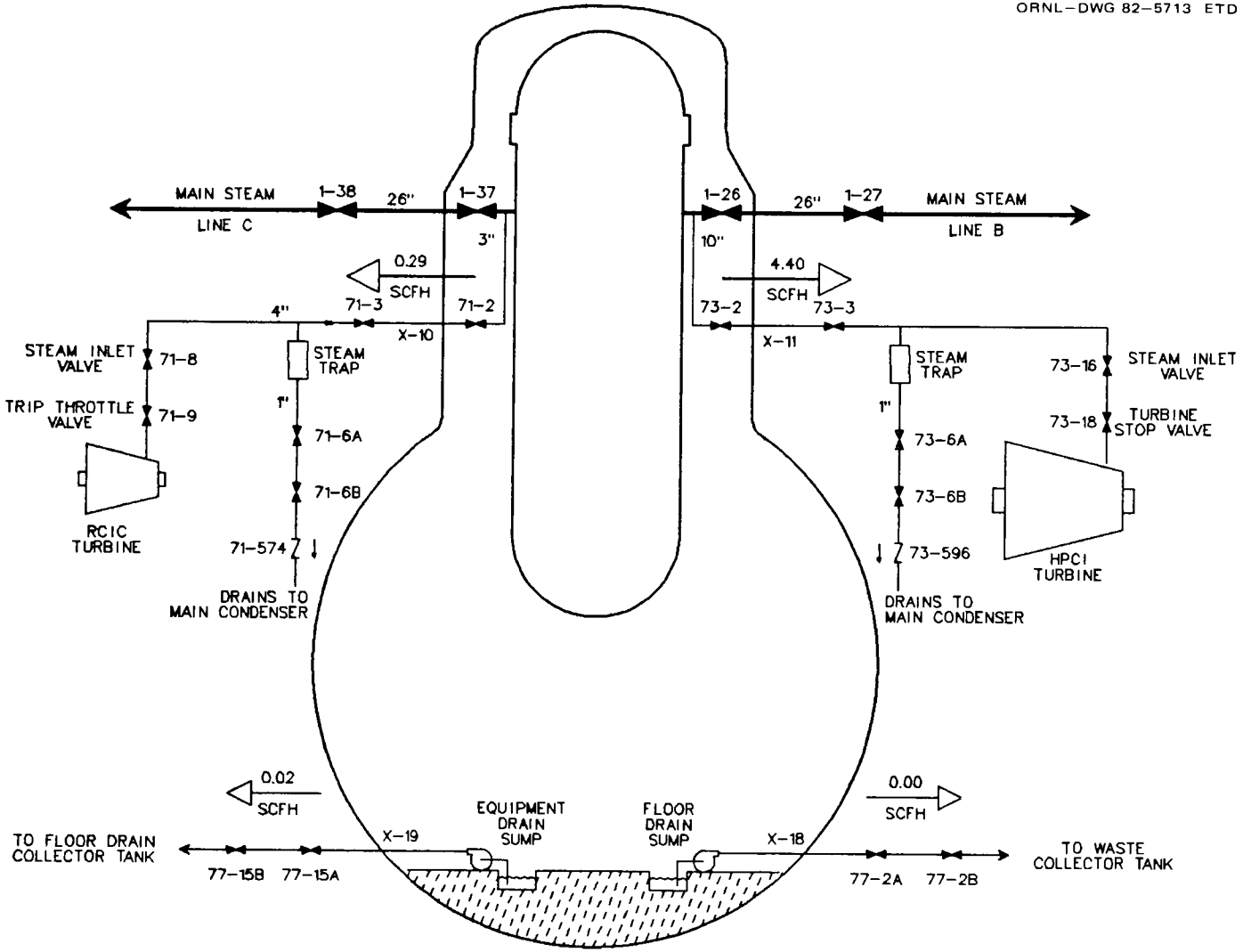

Fig. A.5. HPCI and RCIC systems leakage and drain sumps leakage.

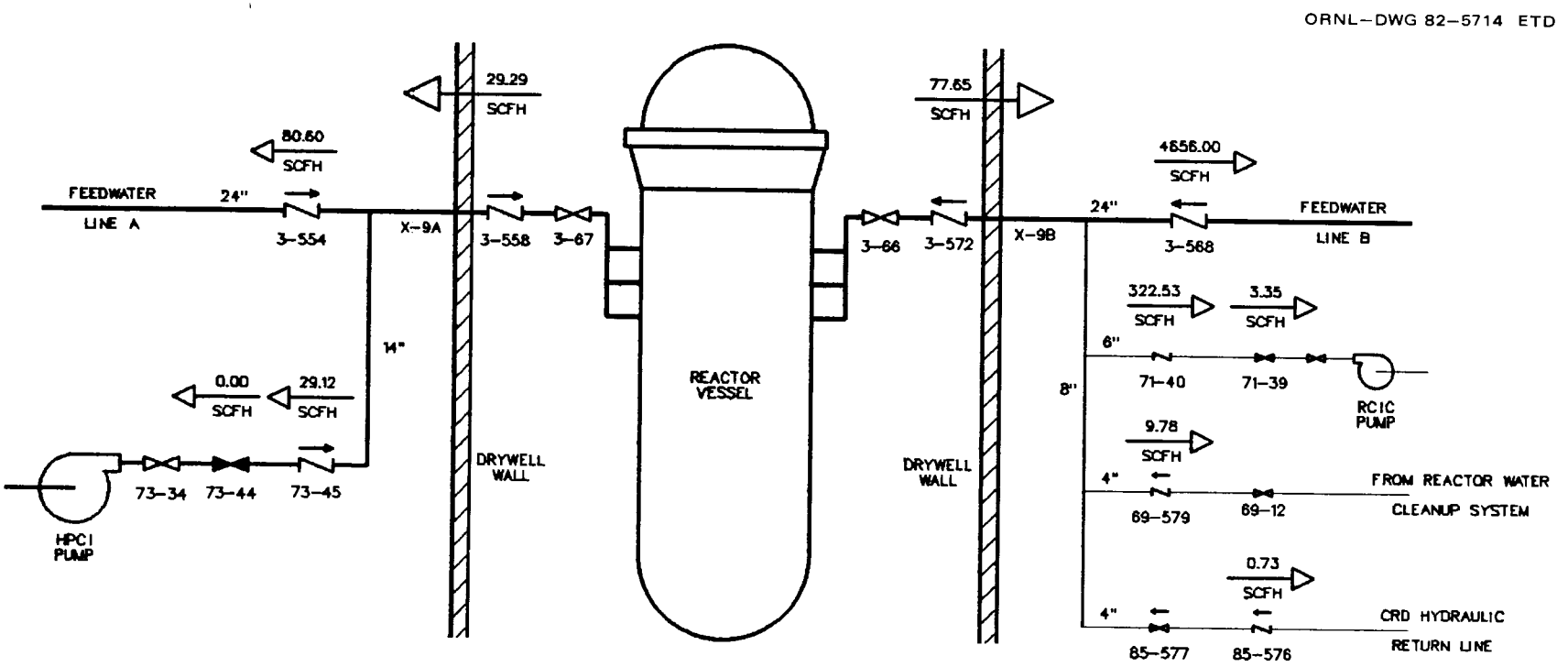

Fig. A.6. Leakage from feedwater penetrations.

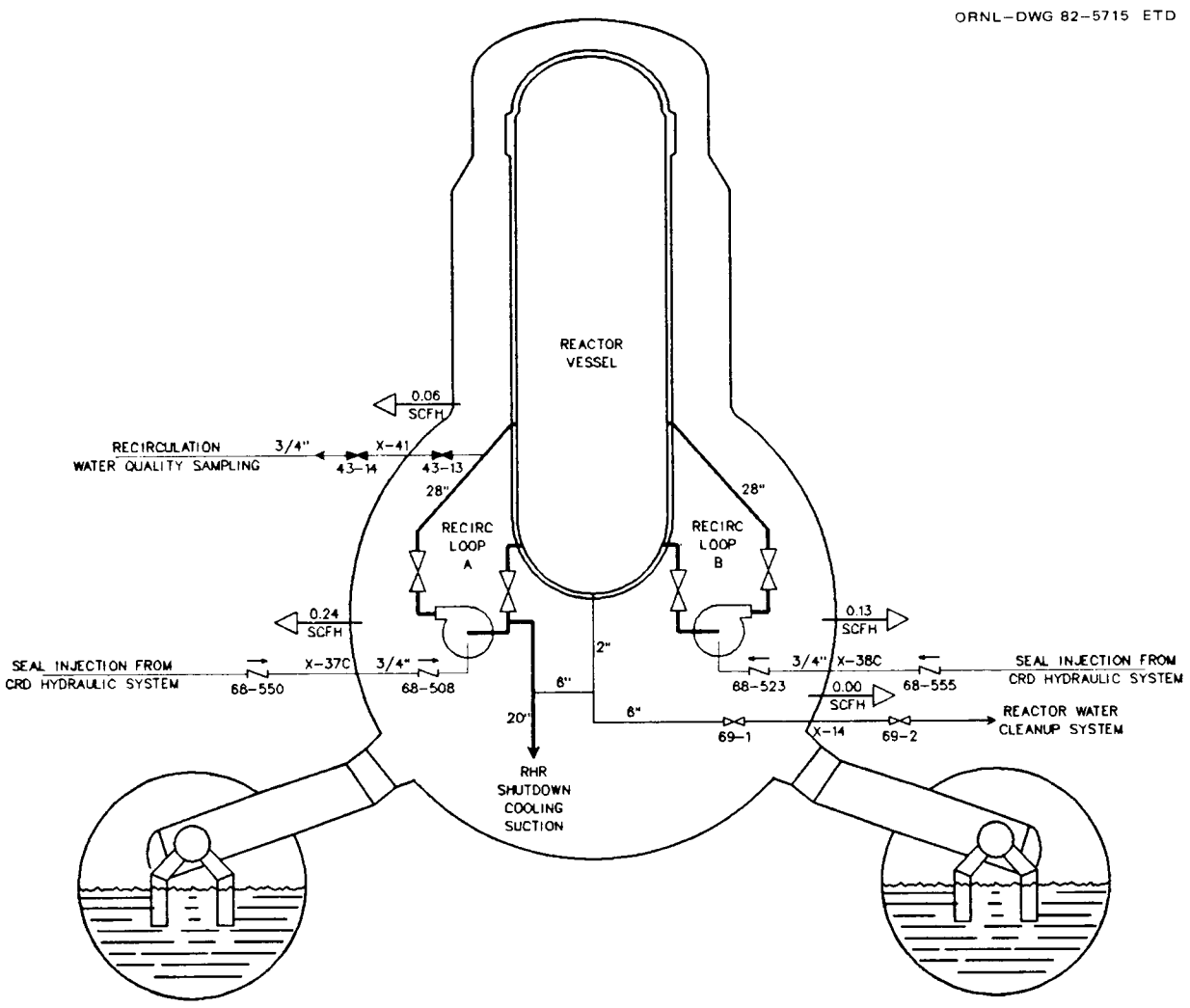

Fig. A.7. Recirculation system leakage.

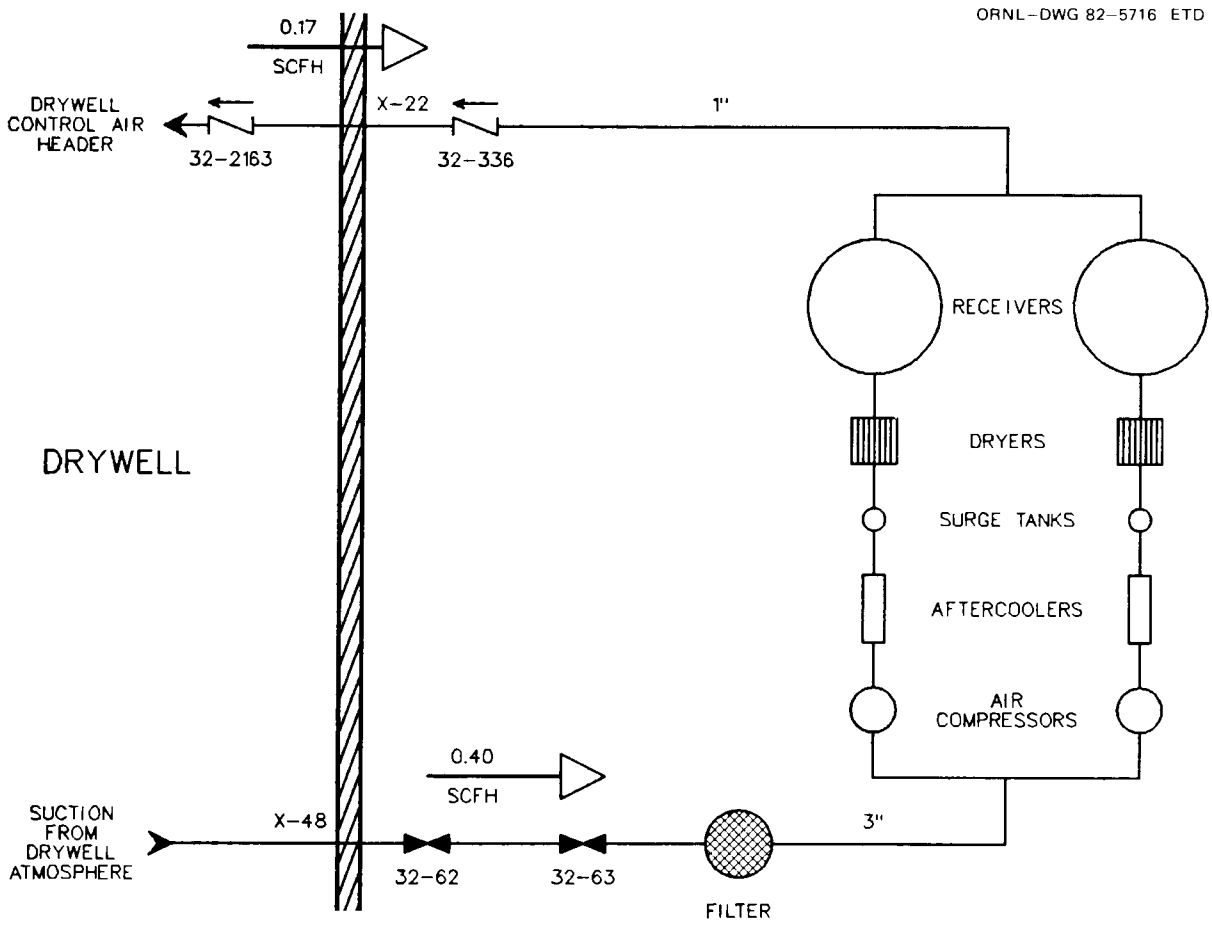

Fig. A.8. Drywell control air system leakage.

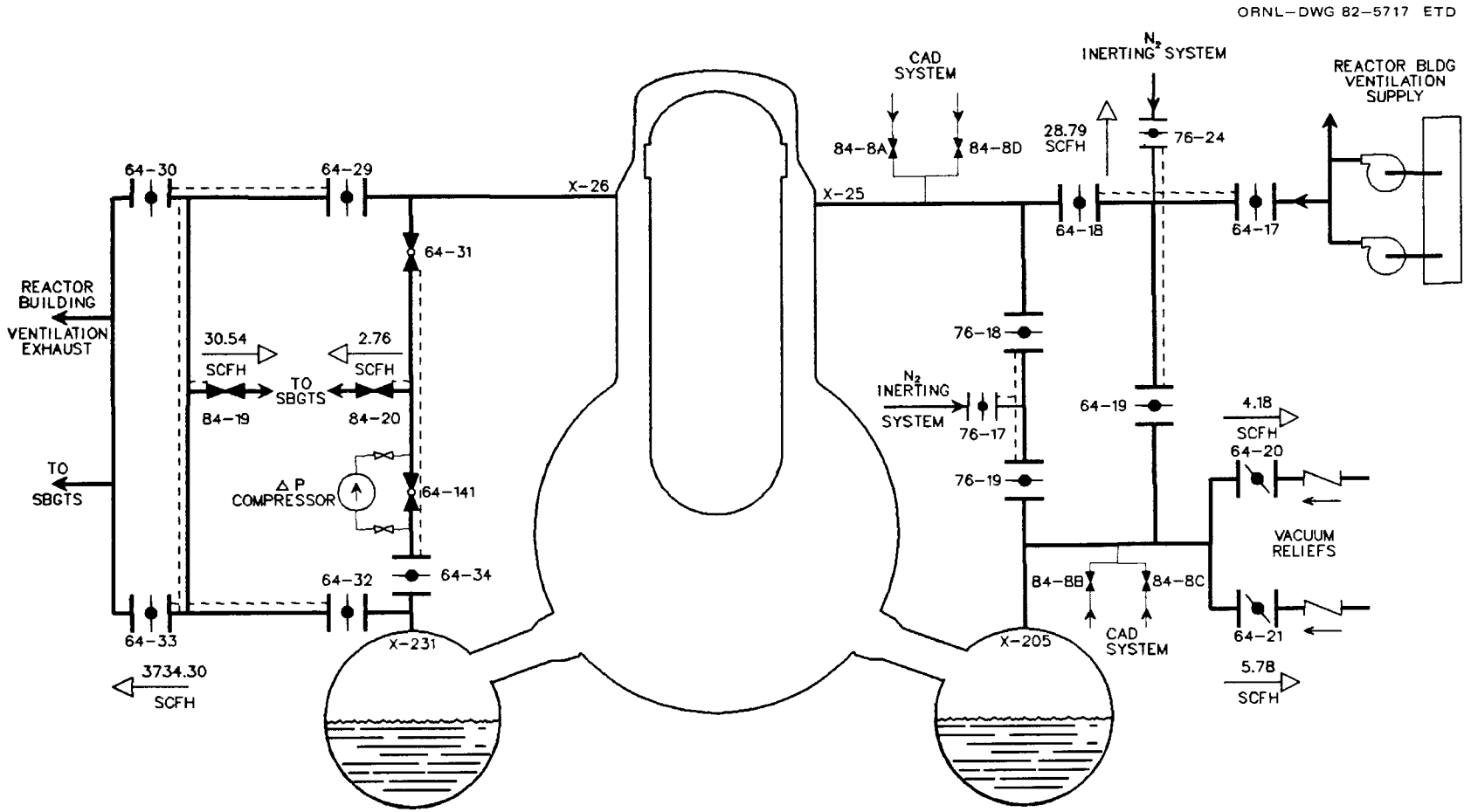

Fig. A.9. Containment ventilation and inerting systems leakage.

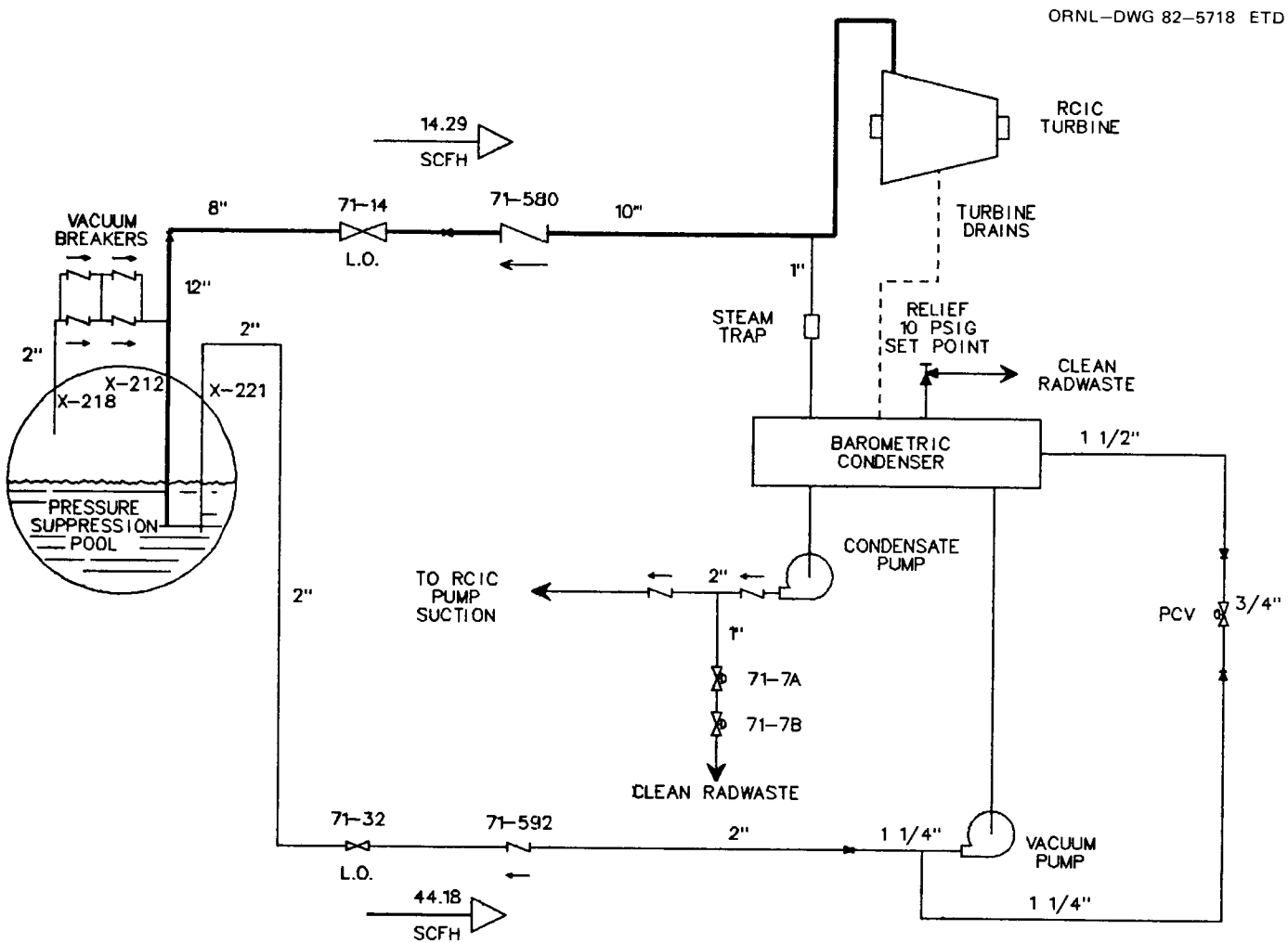

Fig. A.10. Reactor core isolation cooling (RCIC) system leakage.

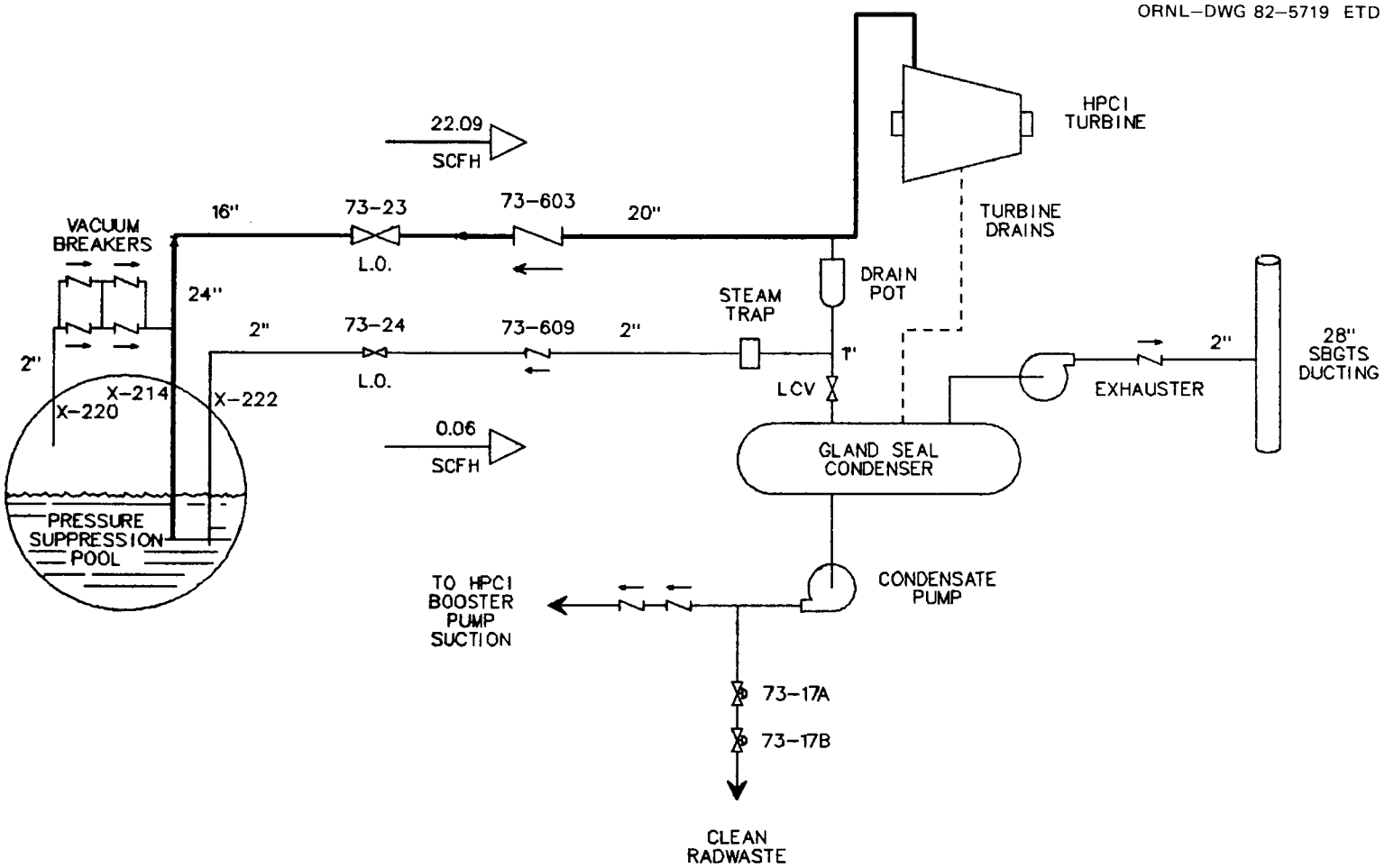

Fig. A.11. High pressure coolant injection (HPCI) system leakage.

Table A.1. PCIS System Group I

Isolation initiation signals

Reactor vessel low low level 12.10 m (476.5 in.)

Main steam line high radiation (3 x normal)

Main steam line high flow (140% of rated flow)

Main steam line space high temperature 90°C (194°F)

Main steam line low pressure 5.79 MPa (825 psig)

Valves and valve numbers	Valve type	Normal position during reactor operation	Power to open	Power to close
Inboard main steam isolation valves 1-14, 1-26, 1-37, 1-51	Air-operated globe	Open	AC and/or DC and air	Air and spring
Outboard main steam isolation valves 1-15, 1-27, 1-38, 1-52	Air-operated globe	Open	AC and/or DC and air	Air and spring
Inboard main steamline bypass 1-55	Motor-operated gate	Shut	AC	AC
Outboard main steamline bypass 1-56	Motor-operated gate	Shut	DC	DC
Inboard reactor water sample 43-13	Air-operated valve	Shut	AC and air	Spring
Outboard reactor water sample 43-14	Air-operated valve	Shut	AC and air	Spring

System number	System
1	Main steam
43	Water quality and sampling system

Table A.2. PCIS Group II

Isolation initiation signals

Reactor vessel low level 13.69 m (539 in.) | High drywell pressure 0.115 MPa (2 psig)

Valves and valve numbers	Valve type	Normal position during reactor operation	Power to open	Power to close
Inboard RHR shutdown cooling supply 74-48	Motor-operated gate	Shut	AC	AC
Outboard RHR shutdown cooling supply 74-47	Motor-operated gate	Shut	DC	DC
Outboard LPCI to reactor[a] 74-53, 74-67	Motor-operated gate	Shut	AC	AC
Inboard RHR reactor head spray 74-78	Motor-operated gate	Shut	AC	AC
Outboard RHR reactor heat spray 74-77	Motor-operated gate	Shut	DC	DC
Outboard RHR flush and drain to torus 74-119, 74-102, 74-120, 74-103	Air-operated gate	Shut	AC and air	Spring
Outboard CS to keep full system 75-57, 75-58	Air-operated gate	Shut	AC and air	Spring
Outboard drywell sumps drain 77-15A, 77-15B, 77-2A, 77-2B	Air-operated gate	Open	AC and air	Spring
Outboard drywell air compressor suction 32-62, 32-63	Air-operated gate	Open	AC and air	Spring

System number	System
32	Drywell control air system
74	Residual heat removal (RHR) system
75	Core spray system
77	Radwaste system

[a] If open, these LPCI valves will shut with a Group II isolation signal only if
- RHR shutdown cooling supply valves 74-47 and 74-48 are both open, and
- Reactor pressure is less than 0.791 MPa (100 psig), and
- There is no LPCI initiation signal

Table A.3. PCIS Group III

Isolation initiation signals

Reactor vessel low level 13.69 m (539 in.)

Reactor water cleanup space high temperature 76.7°C (170°F)

Valves and valve numbers	Valve type	Normal position during reactor operation	Power to open	Power to close
Inboard reactor water cleanup supply 69-1	Motor-operated gate	Open	AC	AC
Outboard reactor water cleanup supply 69-2	Motor-operated gate	Open	DC	DC
Outboard reactor water cleanup return 69-12	Motor-operated globe	Open	AC	AC

System number	System
69	Reactor water cleanup system

Table A.4. PCIS Group IV

Isolation Initiation Signals

HPCI steamline space high temperature 93.3°C (200°F)

HPCI steamline high flow 225%

HPCI steamline low pressure 0.791 MPa (100 psig)

Valves and valve numbers	Valve type	Normal position during reactor operation	Power to open	Power to close
Inboard HPCI steamline isolation[a] 73-2	Motor-operated gate	Open	AC	AC
Outboard HPCI steamline isolation 73-3	Motor-operated gate	Open	DC	DC

System number	System
73	High pressure coolant injection (HPCI)

[a]Inboard isolation valve will also close on a detected pressure of 0.172 MPa (10 psig) between the rupture discs on the turbine exhaust line.

Table A.5. PCIS Group V

Isolation initiation signals

RCIC steamline space high temperature 93.3°C (200°F)

RCIC steamline high flow 300%

RCIC steamline low pressure 0.446 MPa (50 psig)

Valves and valve numbers	Valve type	Normal position during reactor operation	Power to open	Power to close
Inboard RCIC steamline isolation[a] 71-2	Motor-operated gate	Open	AC	AC
Outboard RCIC steamline isolation 71-3	Motor-operated gate	Open	DC	DC

System number	System
71	Reactor core isolation cooling (RCIC)

[a]Inboard isolation valve will also close on a detected pressure of 0.172 MPa (10 psig) between the rupture discs on the turbine exhaust line.

Table A.6. PCIS Group VI

Isolation initiation signals

Reactor vessel low level
13.69 m (539 in.)

High drywell pressure
0.115 MPa (2 psig)

High radiation reactor building ventilation exhaust
100 mr/h

Valves and valve numbers[a]	Valve type	Normal position during reactor operation	Power to open	Power to close
Drywell/torus N_2 purge inlet 76-17, 76-18, 76-19	Air-operated butterfly	Shut	Air and AC	Spring
Drywell/torus air purge inlet 64-17, 64-18, 64-19	Air-operated butterfly	Shut	Air and AC	Spring
Drywell main exhaust isolation 64-29, 64-30	Air-operated butterfly	Shut	Air and AC	Spring
Torus main exhaust isolation 64-32, 64-33	Air-operated butterfly	Shut	Air and AC	Spring
Drywell exhaust valve bypass to SBGTS 64-31	Air-operated globe	Shut	Air and AC	Spring
Torus exhaust valve bypass to SBGTS 64-34	Air-operated butterfly	Shut	Air and AC	Spring

System number	System
64	Containment ventilation system
76	Nitrogen inerting system

[a]All Group VI valves are located outboard of the primary containment.

Table A.7. PCIS Group VII

Valves and valve numbers	Valve type	Normal position during reactor operation	Power to open	Power to close
		Isolation initiation signals: Reactor vessel low level 12.10 m (476.5 in.)		
RCIC steamline drain 71-6A, 71-6B	Air-operated globe	Open	Air and DC	Spring
RCIC condensate pump drain 71-7A, 71-7B	Air-operated globe	Open	Air and DC	Spring
HPCI steamline drain 73-6A, 73-6B	Air-operated globe	Open	Air and DC	Spring
HPCI hotwell pump discharge 73-17A, 73-17B	Air-operated globe	Shut	Air and DC	Spring

System number	System
71	Reactor core isolation cooling (RCIC)
73	High pressure coolant injection (HPCI)

Table A.8. PCIS Group VIII

Valves and valve numbers	Valve type	Isolation initiation signals: High drywell pressure 0.115 MPa (2 psig) — Normal position during reactor operation	Power to open	Power to close
Traveling in-core probe (TIP)[a]	Solenoid-operated ball valves	Shut	AC	AC

[a]The valve closure command is preceded by a TIP withdrawal command.

Table A.9. As-found leakages for pathways from the primary system, end cycle 3

Pathway	Leakage (SCFH)	Test medium and pressure (psig)	Leakage into
Main steam lines (X-7A, X-7B, X-7C, X-7D, X-8)	876.04	Air (25)	Main condensers
Core spray injection (X-16A, X-16B)	0.50	Water (55)[a]	Clean radwaste
RHR injection (X-13A)	0.07	Water (55)[a]	RHR system
RHR Injection (X-13B)	0.16	Water (55)[a]	RHR system
Shutdown cooling suction (X-12)	0.31	Air (50)	RHR system
HPCI steam supply line (X-11)	4.40	Air (50)	HPCI system
RCIC steam supply line (X-10)	0.29	Air (50)	RCIC system
Feedwater line B (X-9B)	77.65	Air (50)	Feed system RWCU system RCIC system CRD hydraulic system
Feedwater line A (X-9A)	29.29	Air (50)	Feed system HPCI system
From recirculation lines (X-14, X-37C, X-38C, X-41)	0.43	Water (55)[a]	CRD system Water quality system RWCU system

[a]The reported leakage is the measured leakage in ft³ of water/h. No conversion factor has been applied.

Table A.10. As-found individual MSIV leakages (SCFH at 25 psig)

Main steam	MSIV	CYCLE 3 (Jan. 1980)		Cycle 4 (May 1981)	
		Individual	Pathway	Individual	Pathway
A	Inboard 1-14	3060.1	664.4	333.8	333.8
	Outboard 1-15	664.4		3368.3	
B	Inboard 1-26	29.4	9.4	18.1[a]	18.1
	Outboard 1-27	9.4			
C	Inboard 1-37	67.3	67.3	45.7[a]	43.6
	Outboard 1-38	3122.1		43.6	
D	Inboard 1-51	3426.9	133.3	2808.1	481.3
	Outboard 1-52	133.3		481.3	
Pathway totals			874.4		876.8

[a]Individual valve leakages were not reported.

Table A.11. As-left individual MSIV leakages (SCFH at 25 psig)

Main steam	MSIV	CYCLE 3 (Jan. 1980)		Cycle 4 (May 1981)	
		Individual	Pathway	Individual	Pathway
A	Inboard 1-14	1.73	0.00	0.70	0.70
	Outboard 1-15	0.00		1.82	
B	Inboard 1-26	6.45	6.45	8.66[a]	8.66
	Outboard 1-27	9.35			
C	Inboard 1-37	6.36	3.71	5.85[a]	5.85
	Outboard 1-38	3.71			
D	Inboard 1-51	3.27	0.00	1.89	1.89
	Outboard 1-52	0.00		9.03	
Pathway totals			10.2		17.10

[a]Individual valve leakages were not reported.

Table A.12. As-found leakages for pathways from the drywell atmosphere, end cycle 3

Pathway	Leakage (SCFH)	Test medium and pressure (psig)	Leakage into
RHR containment spray (X-39A)	0.52	Water (55)[a]	RHR system
RHR containment spray (X-39B)	0.74	Water (55)[a]	RHR system
Drywell sumps (X-18, X-19)	0.02	Water (55)[a]	Radwaste system
Bellows	0.02	Air (50)	Reactor building
Resilient seals	39.13	Air (50)	Reactor building
Electrical seals	0.64	Air (50)	Reactor building
Drywell control air suction (X-48)	0.40	Air (50)	Drywell control air system
Drywell control air discharge (X-22)	0.17	Air (50)	Drywell control air system

[a]The reported leakage is the measured leakage in ft^3 of water/h. No conversion factor has been applied.

Table A.13. As-found leakages for pathways from the wetwell airspace, end cycle 3

Pathway	Leakage (SCFH)	Test medium and pressure (psig)	Leakage into
RCIC turbine exhaust (X-218)	14.29	Water (55)[a]	RCIC system
HPCI turbine exhaust (X-220)	22.09	Water (55)[a]	HPCI system
Wetwell containment spray (X-211A)	1.36	Water (55)[a]	RHR system
Wetwell containment spray (X-211B)	6.09	Water (55)[a]	RHR system
Torus - reactor building vacuum breakers (X-205)	9.96	Air (50)	Reactor building

[a]The reported leakage is the measured leakage in ft^3 of water/h. No conversion factor has been applied.

Table A.14. As-found leakages for pathways from the pressure suppression pool, end cycle 3

Pathway	Leakage (SCFH)	Test medium and pressure (psig)	Leakage into
RCIC vacuum pump discharge (X-221)	44.18	Water (55)[a]	Barometric condenser
HPCI steam trap discharge (X-222)	0.06	Water (55)[a]	Gland seal condenser
Head tank pump suction	0.64	Water (55)[a]	Keep full system

[a]The reported leakage is the measured leakage in ft^3 of water/h. No conversion factor has been applied.

APPENDIX B
PRIMARY CONTAINMENT LEAKAGE

B.1 Integrated Leak Rate Test Requirements

The maximum allowable integrated leakage rate La for the Browns Ferry Unit 1 primary containment is established in the Technical Specifications as 2.0% of the primary containment atmosphere volume per 24 h at a pressure P_p^* of 0.342 MPa [gage] (49.6 psig). With a combined drywell and torus free atmosphere volume of 8492.4 m³ (299,845 ft³), then

$$La = 7.08 \text{ m}^3/\text{h} \ (249.92 \text{ ft}^3/\text{h}) \text{ at } 0.443 \text{ MPa } (49.6 \text{ psig}) \qquad (B\text{-}1)$$

or

$$La = 30.96 \text{ m}^3/\text{h [STP]} \ (1093.2 \text{ scfh}) \ . \qquad (B\text{-}2)$$

The Technical Specifications further provide that a Containment Integrated Leak Rate Test (CILRT) must be performed prior to initial unit operation and must be repeated at 3-1/3 year intervals thereafter although the intervals between tests may be extended up to eight months if necessary to coincide with a refueling outage.

The total containment leakage at the pressure P_p must be reduced to less than 75% of La prior to return to power operation. However, at the Browns Ferry plant the test is conducted at a pressure P_t of 0.172 MPa [gage] (25 psig) and the Technical Specifications limit for allowable leakage during this reduced-pressure test is

$$0.75 \cdot La \ (P_t/P_p)^{1/2} \qquad (B\text{-}3)$$

or 1.065% of the free containment volume per day. It should be noted that equation B-3 conservatively models a leakage which behaves as incompressible flow through a fixed orifice.

The Tennessee Valley Authority (TVA) has made the results[1] of the CILRT conducted on the unit 1 primary containment during the period 20 to 23 February, 1980, available to this study. In this test, the measured containment leakage was 0.685% of containment volume per day at a test pressure of 0.274 MPa (25 psig). This corresponds to 64.3% of the leakage allowed by the Technical Specifications.

B.2 Calculation of Leakage at Other than Test Pressure

From the Darcy equation for compressible flow through valves, pipes, and fittings, the volumetric flow at upstream conditions is proportional

---

*The pressure Pp is the calculated peak containment pressure under accident conditions, as defined in the FSAR.

to

$$\left(\frac{\Delta PT}{P}\right)^{1/2} \tag{B-4}$$

where ΔP = pressure difference across valve, pipe, or fitting, atm

T = upstream temperature, K
P = upstream pressure, atm

Using this relation and recognizing that the pressure differential ΔP can be written as $(P - 1)$ for the primary containment for which the leakage is to atmosphere, then the leakage at pressures other than the test pressure can be expressed as

$$L = L_T \frac{1}{\sqrt{T_t \left(1 - \frac{1}{P_t}\right)}} \cdot \sqrt{T \left(1 - \frac{1}{P}\right)} \tag{B-5}$$

where

L_T = leakage at test pressure
P_T = test pressure in absolute atmospheres
P = containment pressure in absolute atmospheres
T_t = absolute containment temperature during test
T = absolute containment temperature

In this equation, L and L_T represent the leaked volume per unit time as measured at the conditions within the containment, i.e., they are not adjusted to standard pressure and temperature.

With the measured leakage L_T of 0.685% per day at the test pressure P_t of 0.172 MPa [gage] (25 psig) or 2.701 atm, Eqn. (B-5) predicts a leakage of 0.758% per day at a pressure P of 0.342 MPa [gage] (49.6 psig) or 4.375 atm. This can be compared with a predicted leakage of 0.964% per day if the more conservative incompressible flow relation were used, as in Eqn. (B-3). Eqn. (B-5) is believed to provide the more realistic prediction of primary containment leakage and is adopted for use with this study.

B.3 Local Leak Rate Tests

There is an additional requirement in the Technical Specifications for Local Leak Rate Tests (LLRTs) to be performed at the end of each operating cycle. The allowable summed total of the individual isolation valve and penetration seal leakages measured during these local tests is limited to 60% of La which for the unit 1 containment is equivalent to an allowable total leakage of 18.57 m^3/h [STP] (655.9 scfh). It should be noted that much of the local testing is performed on isolation valves located in piping which leads directly from the primary system through the primary

containment boundary; the leakage through these valves does not originate from the primary containment atmosphere.

The TVA has provided the results of the LLRTs conducted just prior to the CILRT discussed in Sect. B.1. Since the 'as-found' measured leakages, i.e., the leakages before any repairs, are recorded as well as the final 'as-left' test results, it is possible to estimate what the overall leakage from the primary containment atmosphere would have been if the CILRT had been conducted before any valve repairs. This is done by adding the difference between the 'as-found' and the 'as-left' local leakages from the primary containment atmosphere to the overall leakage reported in the CILRT.

Some of the LLRTs of the valves and fittings in the pathways from the primary containment atmosphere were conducted with air at a pressure of 0.443 MPa (49.6 psig); the results of these tests were converted to and reported as scfh. Other valves and fittings in the primary containment boundary were tested with water at 0.481 MPa (55 psig) with results recorded as ft^3 of water leaked per hour.* The local leakages from the primary containment atmosphere considered in this study are derived from the reported LLRT results; the leakage into the piping of systems external to the containment is listed in Table B.1, and the leakage directly into the reactor building atmosphere is given in Table B.2. These tables include the source of the leakage, the test medium, and the difference between the as-found and the as-left leakages. The tabulated leakage rates for the water tests have been converted to equivalent scfh of air by multiplying the reported test results by the ratio

$$\frac{55 + 14.7}{14.7} = 4.742 \ . \qquad \text{(B-6)}$$

The LLRT results[1] made available by TVA include values for both the leakage into the drywell and the leakage into the Reactor Building from the volume between the bellows of the bellows-sealed penetrations. The total bellows leakage given in Table B.2 is the sum of the lower values of the two leakages recorded for each bellows. For the resilient seals and electrical seals, only the total leakage into both the reactor building and the drywell is measured. Accordingly, the seal leakages given in Table B.2 are one-half of the values recorded in the test results.

The leakage rates given in Tables B.1 and B.2 should be interpreted as an approximation to the leakage from the primary containment atmosphere through the indicated valves and fittings at a containment pressure of 0.443 MPa (49.6 psig).** It is recognized that there would be differences between the leakage driven by a pressurized containment and the measured leakages which were driven by a locally applied pressure, but the procedure adopted here should provide a reasonable estimate.

---

*Although the measured leakage from the water tests is reported in Ref. 1 as 'scfh,' no conversion factor was applied to the actual leakage.

**The small difference in the water leak rate between 0.481 and 0.443 MPa (55 and 49.6 psig) has been neglected.

B.4 Expressions for Containment Leakage Before Repairs

As discussed in Sect B.2, it is assumed that the measured leakage for the CILRT conducted in February 1980 would have been 0.758% of the free containment volume per day if the test had been conducted at 0.443 MPa (49.6 psig). This is equivalent to a leakage of 414.3 scfh. Tables B.1 and B.2 show that the valve repairs immediately prior to this CILRT reduced the leakage through the primary containment boundary by an estimated total of 399.1 scfh. Thus by addition, the containment leakage before repairs can be estimated to be 813.4 scfh at a containment pressure of 0.443 MPa (49.6 psig). It should be noted that this remains below the maximum allowable value (La) as given in Sect. B.1.

It is worthwhile to carry this procedure one step further and estimate the proportion of the leakage from the primary containment atmosphere that is into the reactor building atmosphere and the proportion that is into piping systems external to the containment. Examination of the information in Tables B.1 and B.2 reveals that 10% of the as-found leakage from the local tests was into the reactor building atmosphere. Based on this observation, it is assumed here that the same proportion would hold for the leakage from the primary containment measured in the CILRT.

With the assumptions stated in this appendix, the predicted containment leakage at 0.443 MPa (49.6 psig) can be summarized as shown in Table B.3, and Eqn. (B-5) can be used to develop expressions for a realistic estimate of the leakage from the primary containment during the period before gross containment failure. The assumed test conditions which would produce the leakages summarized in Table B.3 are

$$P_T = 4.375 \text{ atm}$$

$$T_T = 290.9 \text{ K}^*$$

and with these values, Eqn. (B-5) becomes

$$L = L_T \, (0.06675) \sqrt{T\left(1 - \frac{1}{P}\right)} \qquad \text{(B-7)}$$

where

P = containment pressure in absolute atmospheres
T = containment temperature, K

Finally, substitution of the assumed test leakage into the piping systems outside containment (172.4 ft^3/h) from Table B.3 for L_T yields the leakage into systems

$$L_S = 11.51 \sqrt{T\left(1 - \frac{1}{P}\right)} \text{ ft}^3/\text{h} \qquad \text{(B-8)}$$

---

*The actual average containment temperature during the test at 0.273 MPa (25 psig) varied from 290.2 to 291.6 K.

and similarly, the leakage into the reactor building atmosphere can be expressed as

$$L_{RB} = 0.90\sqrt{T(1 - \frac{1}{P})} \text{ ft}^3/\text{h} \qquad \text{(B-9)}$$

Equations (B-8) and (B-9) were developed for use in the analysis of fission product release from the primary containment during the period prior to gross containment failure. Their derivation is based on the results of leakage tests conducted during January and February 1980 which, although characteristic of the results obtained in similar tests at other times, cannot be considered as permanently accurate values. It is emphasized that Eqns. (B-8) and (B-9) merely provide a means for calculating a reasonable approximation to the volume (evaluated at conditions within the containment) per unit time leaked as a function of containment pressure and temperature.

Table B.1. Assumed leakage from the primary containment into the piping of systems external to the containment, at a pressure of 0.443 MPa (49.6 psig)

Source	Test medium	As-found (SCFH)	As-left (SCFH)	Difference
Drywell containment spray (2 lines)	Water	5.98	3.99	1.99
Drywell sumps	Water	0.09	0.33	-0.24
RCIC turbine exhaust	Water	67.78	1.82	65.96
HPCI turbine exhaust	Water	104.77	0.29	104.48
Wetwell containment spray (2 lines)	Water	35.33	35.33	0.0
RCIC vacuum pump discharge	Water	209.55	0.75	208.80
HPCI steam trap discharge	Water	0.27	0.27	0.0
Head tank pumps suction	Water	3.03	2.65	0.38
Totals		426.80	45.43	381.37

Table B.2. Assumed leakage from the primary containment into the reactor building atmosphere at a pressure of 0.443 MPa (49.6 psig)

Source	Test medium	As-found (SCFH)	As-left (SCFH)	Difference
Bellows	Air	0.02	0.02	0.0
Resilient seals	Air	39.13	21.45	17.68
Electrical seals	Air	0.64	0.64	0.0
Reactor building - torus vacuum breakers	Air	9.96	9.96	0.0
Totals		49.75	32.07	17.68

Table B.3. Correction for valve repairs and apportionment of assumed leakage between piping system and the reactor building atmosphere

	Total (SCFH)	To systems (SCFH)	To reactor building (SCFH)
Measured leakage extrapolated to 0.443 MPa (49.6 psig)	414.3	372.9	41.4
Improvement from valve repairs	399.1	381.4	17.7
Total assumed leakage at 0.443 MPa (49.6 psig) before repairs	813.4	754.3	59.1
Total leakages converted from SCFH to ft^3/h at 49.6 psig	185.9	172.4	13.5

References to Appendix B

1. Reactor Building Containment Integrated Leak Rate Test Browns Ferry Nuclear Plant Unit 1 Conducted February 20-23, 1980. NRC Docket Number 50-259.
2. Browns Ferry FSAR, Sect. 14.7.

Appendix C. THE VOLATILITY OF FISSION PRODUCTS AND STRUCTURAL MATERIALS IN MOLTEN LWR FUEL MIXTURES

Most of the data used to obtain fission product and structural material volatilities came from the SASCHA experiments conducted at Karlsruhe, Germany.[3.17,3.18] In these tests simulated fission products were combined with UO_2 in pellet form, clad with Zircaloy, and melted in thoria crucibles along with stainless steel in argon, air, or steam atmospheres. These are the largest size fuel melting experiments (~100 g UO_2) for which data are available, and the only ones to systematically explore the vaporization of the structural components.

The procedure employed in obtaining volatilities is as follows:

1. Release rates or volatilities in SASCHA tests were compared with similar data from other fuel-melting tests.
2. Best-estimate release rates for SASCHA test geometry were determined and expressed as fraction released per minute.
3. The fractional release rates for each species were converted to vapor pressures assuming that release occurs from the surface of the molten pool with a mass-transfer coefficient equal to 9×10^{-6} mol/$s \cdot cm^2 \cdot atm$.
4. The validity of the mass-transfer/vapor pressure concept was demonstrated by comparing the calculated vapor pressures with those obtained using Raoult's Law (partial pressure = mol fraction x normal vapor pressure).
5. The natural convection mass-transfer coefficient for SASCHA test geometry was calculated and found to be $\sim 6 \times 10^{-6}$ mol/$s \cdot cm^2 \cdot atm$. Extrapolation to full core molten pool size resulted in a slightly lower calculated coefficient, 4×10^{-6} mol/$s \cdot cm^2 \cdot atm$. In consideration of the higher experimental value, we selected 6×10^{-6} as the best estimate value for the fully molten core mass transfer coefficient.

Determination of the relative volatilities of various fission products and structural materials from molten fuel mixtures. Comparison of fission product release rates found in various fuel melting tests is complicated by wide variations in time and temperature. In some tests only the central portion of the fuel melted; in transient tests the actual time molten could only be estimated. In most tests the temperature was at best an estimate, and the actual time molten was probably much less than the full test time. We therefore devised a method of comparing the relative release rates of the various fission products, UO_2, and structural material components for tests conducted in which the fuel was either fully or partially melted.

For each test a release rate coefficient was determined as follows:

$$k_r = \frac{\ln (1 - F)}{t} \quad , \qquad (C.1)$$

where

k_r = release rate coefficient, fraction/min,

F = fraction of species released in time t,

t = time presumed molten, min.

Note that k is the fraction of remaining material released per minute, and t was necessarily estimated for several tests so that the absolute value of k was therefore uncertain.

The volatility comparison was made by plotting the logarithm of k_r as the ordinate for each species as shown in Fig. C.1. The abscissa location for each species was determined by trial-and-error so that the release rate coefficients increased along the abscissa with minimum deviation from a straight line through the plotted points.

The data from SASCHA tests in steam[3,18] are shown in Fig. C.1; SASCHA tests in air[3,17] in Fig. C.2; TREAT transient tests under water or in steam (Refs. C.3, C.4) in Fig. C.3; bare UO_2 melted in tungsten crucibles in helium (Ref. C.5) in Fig. C.3; small fuel samples melted in moist atmospheres in the ORR (Ref. C.6) in Fig. C.3; UO_2 fuel melted in helium by means of centered tungsten resistors (Ref. C.7) in Fig. C.4; fuel melted in air or steam-air mixtures by high frequency induction heating (Ref. C.8) in Fig. C.5; fuel melted in steam atmosphere by high frequency induction heating (Ref. C.9) in Fig. C.6; and unclad fuel melted in the arc-image furnace in impure helium (Ref C.10) in Fig. C.7. The location of each species on the abscissa is the same in Figs. C.1-C.7, and may be referred to as the "relative volatility." The numbers along the abscissa are arbitrary and have no special significance.

The data shown in Figs. C.1 through C.3 demonstrate good consistency. Individual species deviations from the lines drawn in these figures and in the others may result either from an insufficient number of tests from which to obtain a good average or from chemical effects such as reactions with oxygen, zirconium, or stainless steel, when present. One example of a chemical effect is the behavior of tellurium. Two volatility locations are given: Te-1 is the volatility location typical when Zircaloy cladding is present, and Te-2 applies otherwise. The volatility of ruthenium in SASCHA is somewhat lower than in most other tests. Stainless steel has been credited with the capture of ruthenium, (Refs. C.1, C.6) and the presence of oxygen is known to enhance its vaporization (Ref. C.10). Data on the release of molybdenum is sparse and scattered. SASCHA-steam gives low release for molybdenum, SASCHA-air average release, and CDE (Fig. C.6) gives high release. The release of UO_2 in the SASCHA-steam tests appears to be relatively higher than in other tests. The highly reducing conditions provided by Zircaloy-clad fuel melted in helium, Fig. C.4, increased the release of strontium and barium, and decreased the release of tellurium.

Determination of best-estimate release rates. The best estimate volatility line for each type of test is plotted in Fig. C.8. There is a large spread in absolute value of the release rate coefficients. As mentioned before, differences are expected because of known partial melting

and probable errors in time and temperature estimates. The very low CDE release rates suggest that melting probably occured only for a moment rather than for the 30 min test duration.

The differences in slope are striking; our best guess is that test size and geometry are the causes. Since the SASCHA tests are the largest scale and were conducted with good temperature monitoring for measured times in the fully molten condition, we will use the absolute release rates for these tests as our basis for further analysis. The 2400°C line which is identical in both Figs. C.1 and C.2 will be used since a reactor core is expected to increase in melt size at ~2400°C (or melt through the primary vessel) rather than increase further in temperature (Ref. C.2).

Determination of the vapor pressures of structural materials components in molten fuel mixtures at 2400°C. The fractional release rates measured in small SASCHA size tests cannot be correctly applied directly to full size core melts. In order to extrapolate these release rates to larger sizes, we assumed that the controlling mass transfer mechanism was gas phase convection, probably natural convection, for both the SASCHA tests and for large core melts settled into a pool configuration. The rate of mass transport is

$$q = k_G \Delta p = k_G p^* \ , \qquad (C.2)$$

where

q = the mass transport flux, mol/s·cm² surface,

k_G = mass transfer coefficient, mol/s·cm²·atm,

Δp = difference in pressure of transported species from pool surface to exiting gas, atm, and

p^* = vapor pressure at the pool surface in SASCHA tests, atm.

For the case of vaporization from a very hot surface, the partial pressure in the gas far above the surface is very much lower than that at the pool surface, so we will assume that Δp is the same as p^*, the partial pressure at the pool surface. Note that the above equation is similar to the frequently used mass transport equation

$$q = k_c \Delta C \ , \qquad (C.3)$$

where

k_c = mass transport coefficient, cm/s, and

ΔC = difference in concentration, mol/cm³.

We prefer to use the form of Eq. (C.1) for gas-phase controlled mass transport. As explained in the introduction to this section, we will determine the value of k_G for the SASCHA experiments at 2400°C as accurately as possible; then correct it for the full size of the molten pool and its temperature, if needed. The coefficient, k_G, [Eq. (C.2)] should be the

same for every vaporizing component, but the partial pressure will vary with the species.

It is not possible to evaluate both k_G and p* from the SASCHA tests. From our examination of available data, we will assume that $k_G = 9 \times 10^{-6}$ mol/s·cm²·atm, calculate p* for each component of the SASCHA structural materials, and then show that the results are reasonable.

The mass transport flux, q, for each component of the SASCHA tests is obtained from

$$q = \frac{Nk_r}{A} , \qquad (C.4)$$

where

N = amount of the component in the melt, mol,

k_r = release rate coefficient, Eq. (C.2), fraction/s,

A = pool surface area = 19.6 cm² for SASCHA.

The exact amounts of fuel, cladding, and stainless steel were not available for each test, so we assumed that the typical composition was 90 g UO_2, 30 g Zircaloy, and 80 g type 304 stainless steel. The results are shown in Table C.1.

Checking the validity of the vapor pressure natural convection mass transfer model. If the natural convection mass transfer model is valid, the partial pressures of the individual species calculated above should be in reasonable agreement with pressures calculated from published vapor pressures of the pure materials. Some uncertainty is involved in knowing the chemical form of each material at the melt surface. We have made calculations assuming the elemental form to exist (except for UO_2) since only partial oxidation of the SASCHA melts occured. We assumed that Raoult's Law could be used to calculate the partial pressure above the melt. Although significant deviations from Raoult's Law can be expected for the non-ideal solutions typical of the real world, we make use of this ideal relationship only for comparison with the SASCHA-scale experimental results. The experimental results, subjected to our best-estimate averaging will be used in subsequent calculations. Table C.2 summarizes the results of these calculations and demonstrates generally good agreement with experimental values determined from the mass transfer coefficient $k_G = 9 \times 10^{-6}$ mol/s·cm²·atm.

A second test of the validity of the natural convection mass transfer mechanism is to calculate the mass transfer coefficient using published empirical correlations. From a correlation for heat transfer by natural convection above a heated flat surface under laminar flow conditions,[C.11] (Ref. C.11) and the heat transfer-mass transfer analogy, (Ref. C.12) we obtained the following expression for k_G with parameter values given for a

SASCHA test in 2 bar air atmosphere at 2400°C:

$$k_G = \frac{0.14}{M}\left(\frac{\rho^{7/6}\, k_d^{2/3}}{P}\right)\left(\frac{k}{C_p}\right)^{1/12}\left(\frac{g\beta\Delta t}{L\mu}\right)^{1/4}, \qquad (C.5)$$

where

k_G = mass transfer coefficient, mol/s·cm²·atm,

M = molecular weight of the gas, 28.8 g/mol,

ρ = density of gas at average gas film temperature, 4.49×10^{-4} g/cm³ (melt surface temperature = 2400°C, glass container = 200°C, average temperature = (2400 + 200)/2 = 1300°C,

P = system pressure, 2 atm,

k_d = diffusion coefficient of vapor species in gas at average temperature, 1.46 cm²/s,

k = thermal conductivity of gas at average temperature, 2.2×10^{-4} cal/s·cm °C,

C_p = heat capacity of gas at average temperature, 0.28 cal/g·°C,

g = gravitational force, 980 cm/s²,

β = coefficient of volumetric expansion, 1/1573 K,

Δt = temperature difference = (2400 - 200) = 2200°C,

L = length of horizontal surface, 5 cm,

μ = viscosity of gas at average temperature, 5.6×10^{-4} g/cm·s.

From the data given, and Eq. (C.5), $k_G = 5.66 \times 10^{-6}$ mol/s·cm²·atm. This is better agreement with the assumed value of k_G than should be expected considering that SASCHA is not an ideal geometry for calculating natural convection, and the correlation was not verified as applicable to the small size, high temperature conditions of SASCHA.

Extrapolation of the mass transfer coefficient to large size melts. Equation (C.4) applies to laminar flow natural convection. As the size of a molten pool increases, the gas convection becomes turbulent when L reaches ~30 cm; for this size, k_G decreases by a factor of 1.56. For turbulent flow, the natural convection correlations (Ref. C.11) indicate no further change in k_G as the size increases further (L is not a part of the turbulent flow equation). Appling the 1.56 reduction factor to the experimental value of k_G (9×10^{-6}), we obtain in round numbers $k_G = 6 \times 10^{-6}$ mol/s·cm²·atm for large size molten pools where reasonably open space

exists above the pool. The magnitude of k_G is not very sensitive to temperature so we will assume that k_G remains constant for all large molten pools at 6×10^{-6} mol/s·cm²·atm and that the partial pressures shown in Table C.1 are correct at 2400°C.

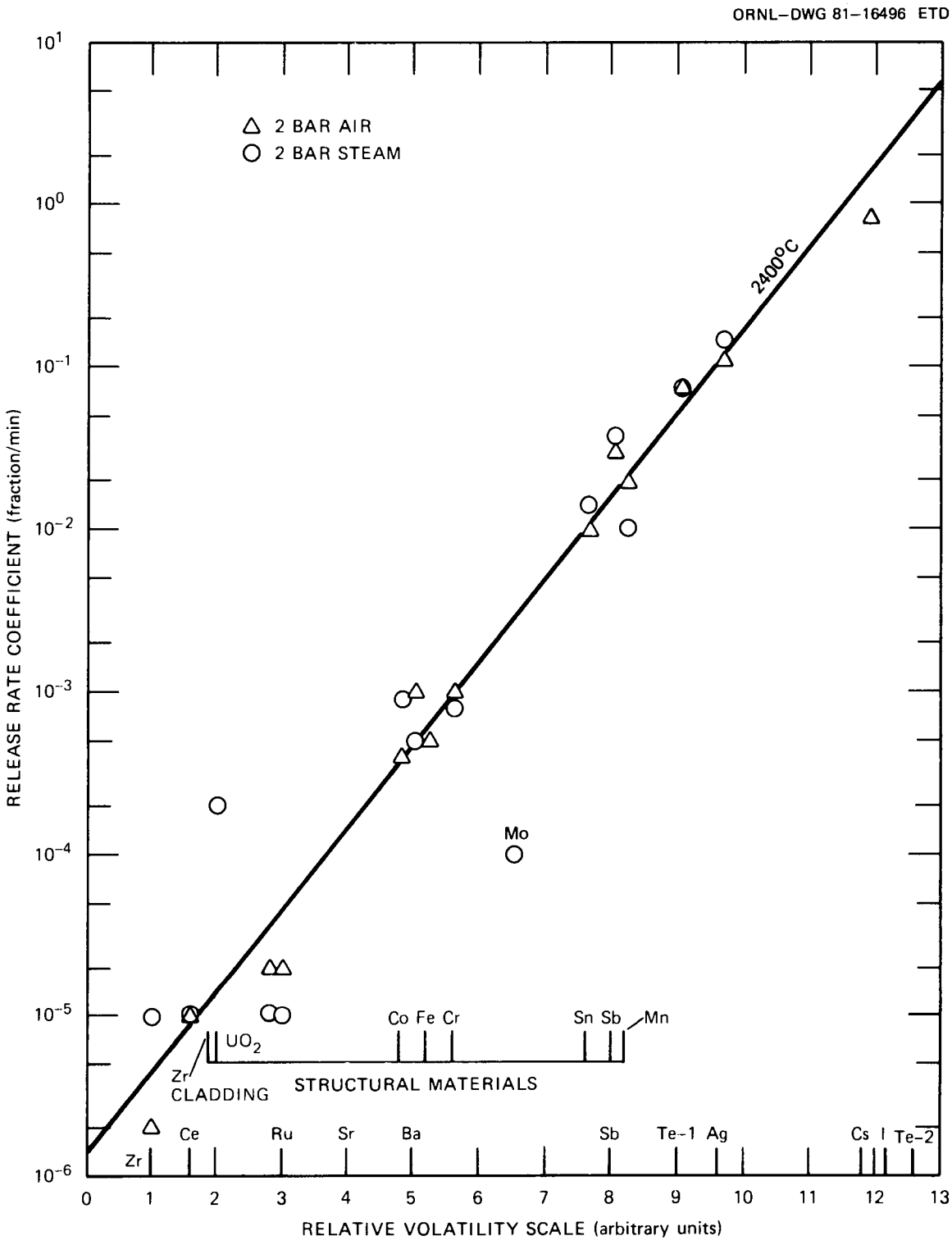

Fig. C.1. Release of material in SASCHA tests.

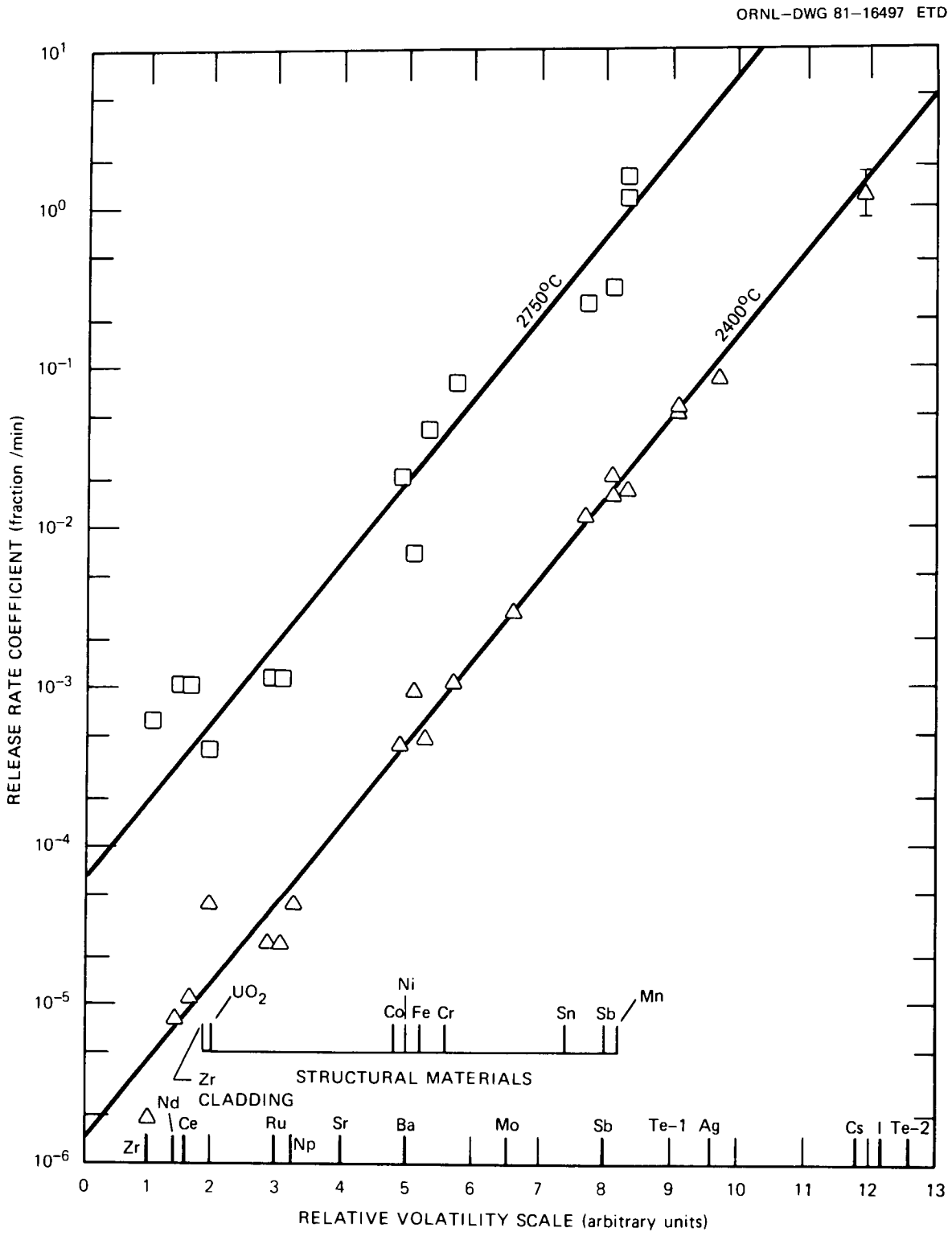

Fig. C.2. Release of material in SASCHA tests, 2 bar air.

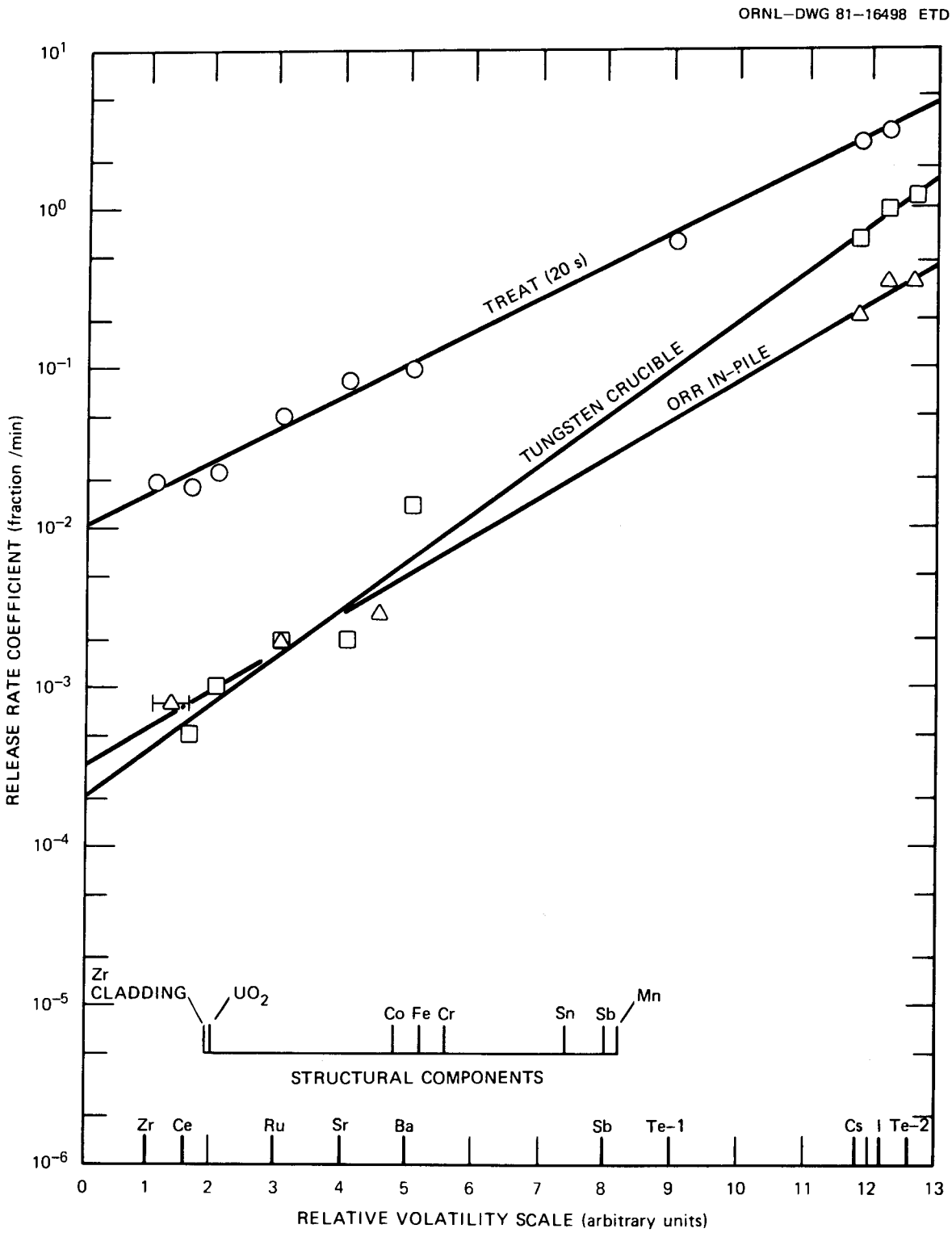

Fig. C.3. Release of fission products from molten UO_2.

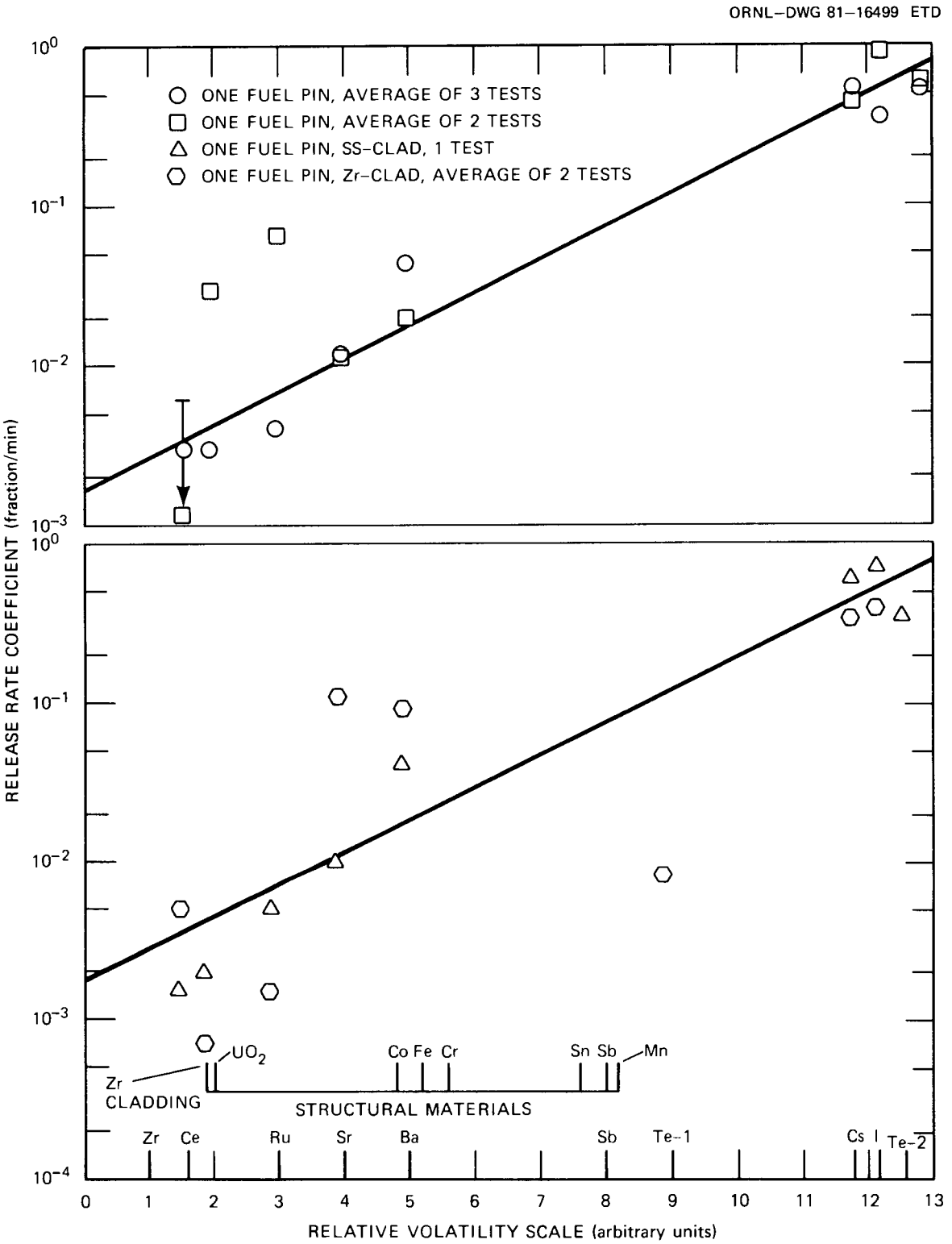

Fig. C.4. Release from fuel melted by centered tungsten resistor.

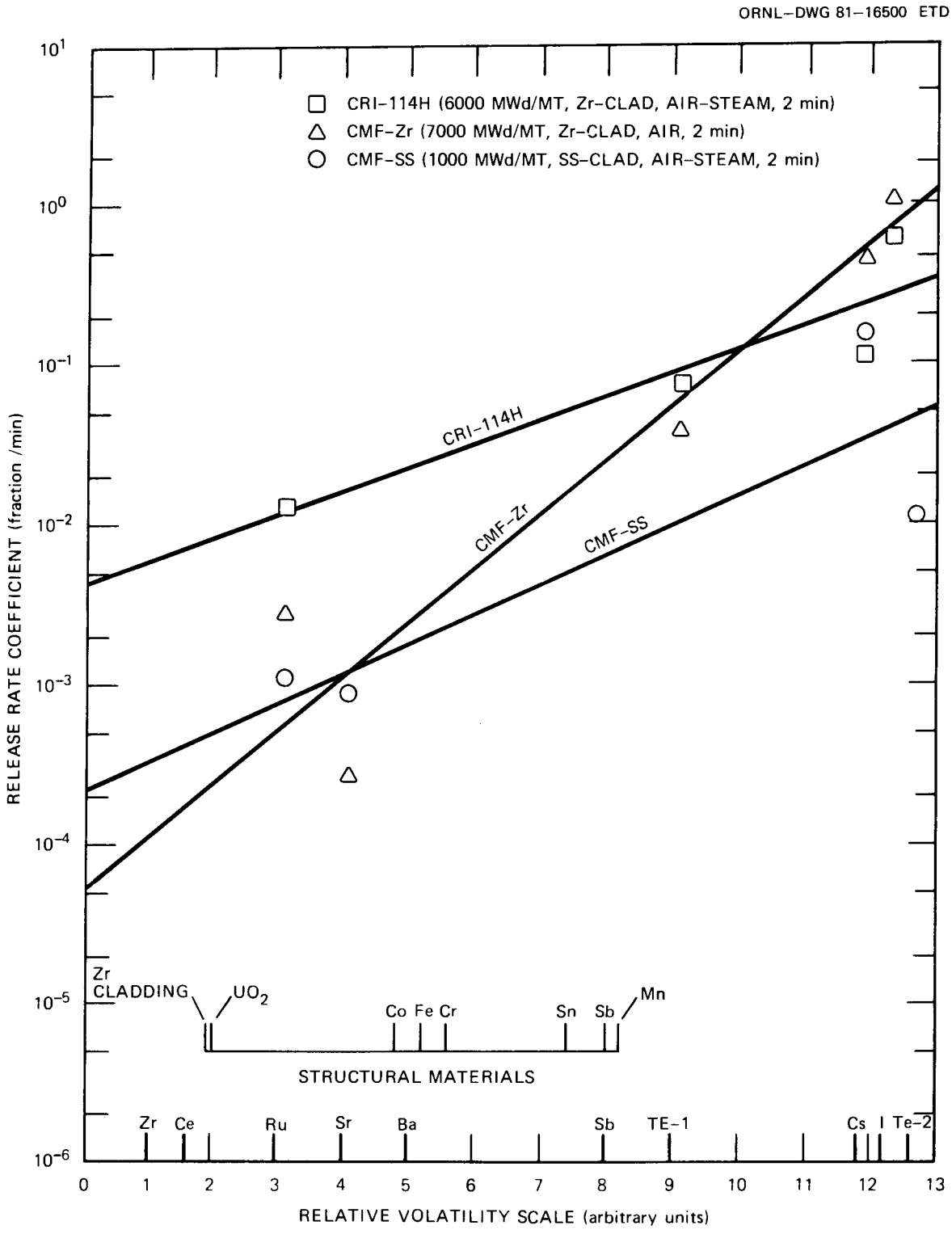

Fig. C.5. Release from fuel melted by high frequency induction.

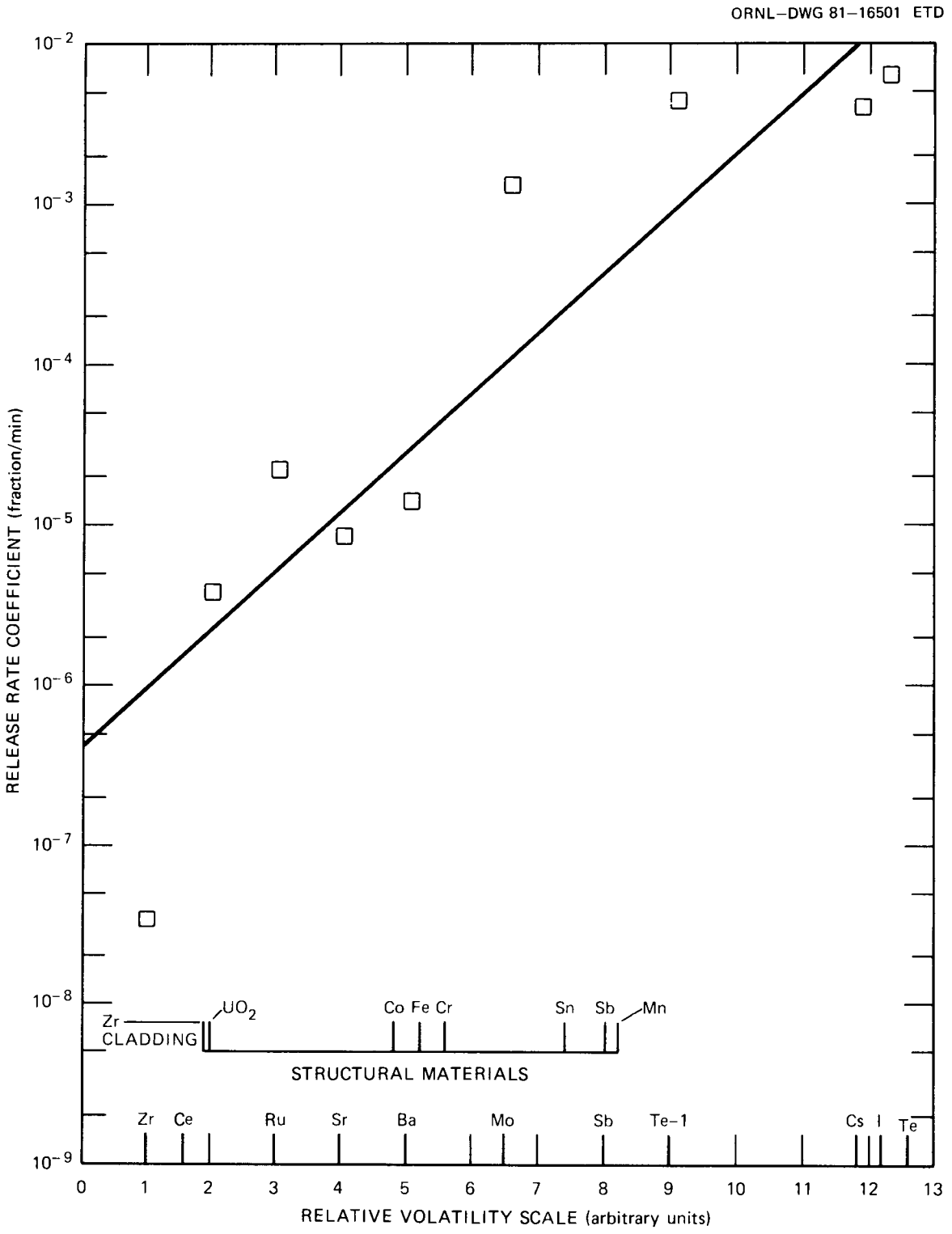

Fig. C.6. Fission product release from CDE (steam, 6 tests, 30 min, Zr–clad).

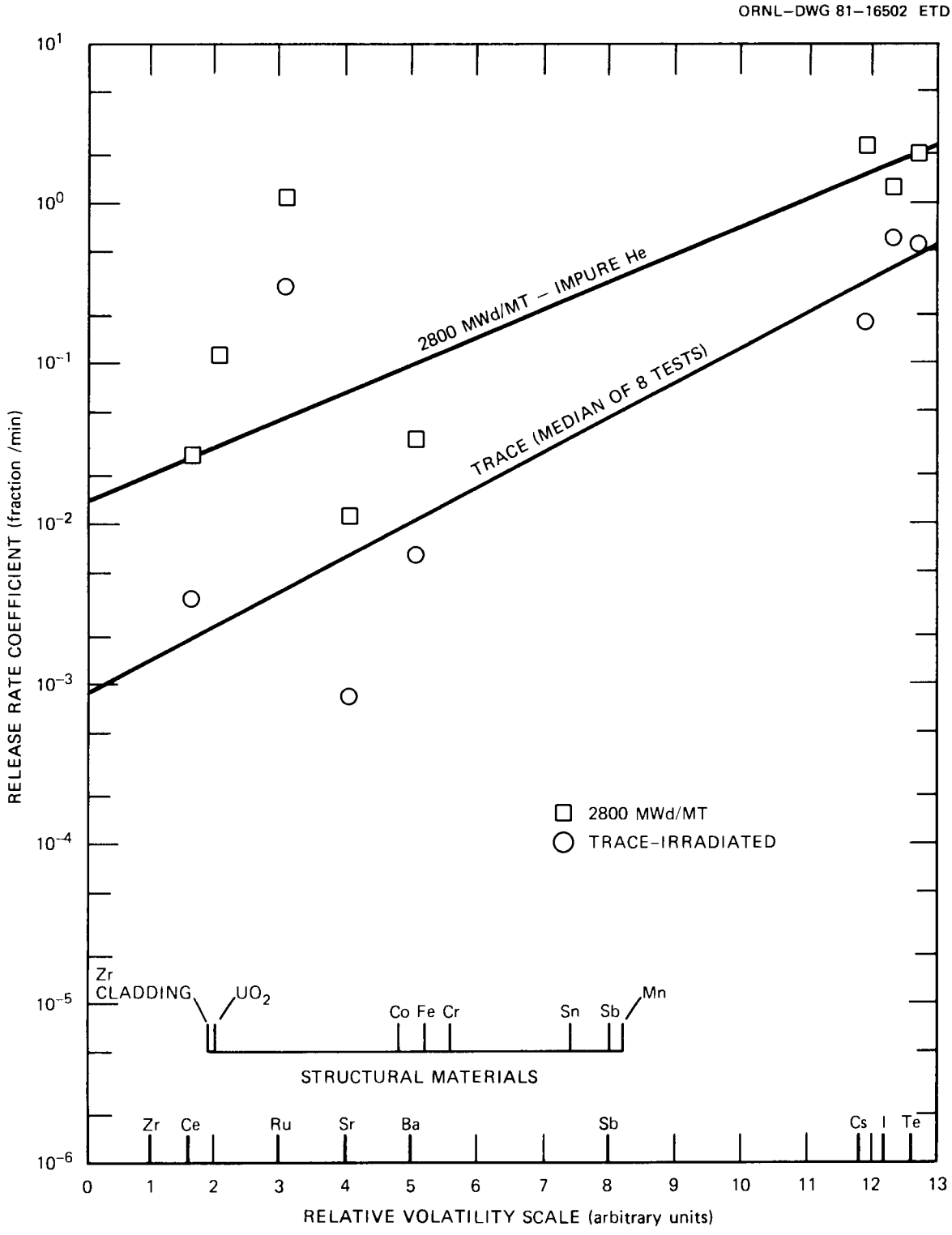

Fig. C.7. Release from fuel melted in He in arc-image furnace with BeO.

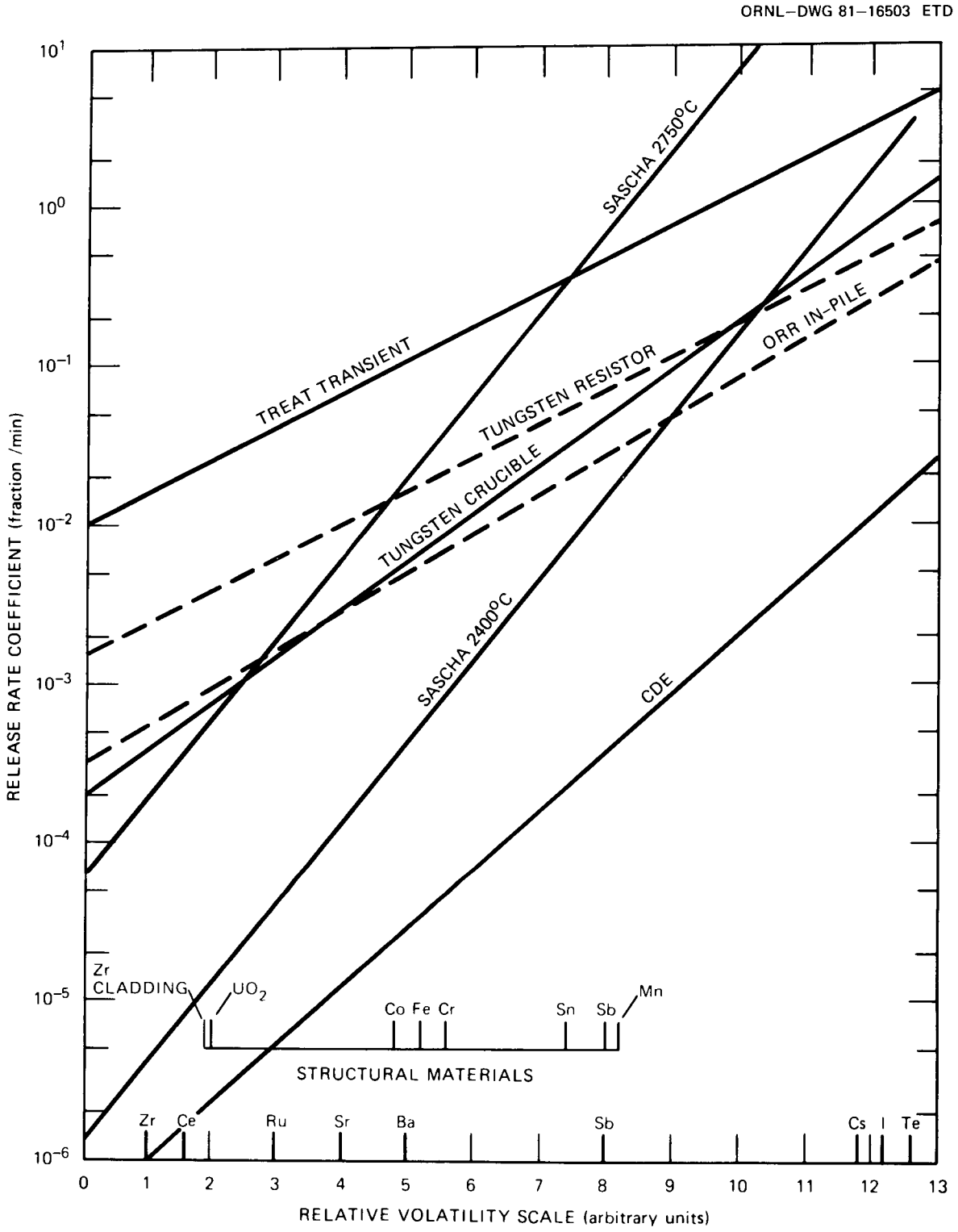

Fig. C.8. Best estimate volatility correlations.

Table C.1. Release of structural materials in typical SASCHA test at 2400°C

Material	Mass in SASCHA (g)	Release rate (fraction/min)	Release rate (g/min)	Release rate (mol/min)	Aerosol composition (mass %)	Effective vapor pressures[a] (atm)
Fe	54.4	6.2×10^{-4}	0.0336	6.05×10^{-4}	36.80	0.0569
Mn	1.6	2.1×10^{-2}	0.0336	6.11×10^{-4}	36.80	0.0576
Cr	15.4	1.0×10^{-3}	0.0150	2.95×10^{-4}	16.43	0.0279
Sn	0.45	1.1×10^{-2}	0.0050	4.20×10^{-5}	5.48	0.0039
UO_2	90.0	1.5×10^{-5}	0.0014	5.00×10^{-6}	1.53	4.0×10^{-4}
Ni	7.4	3.0×10^{-4}[b]	0.0022	3.78×10^{-5}	2.41	0.0036
Zr	29.55	1.3×10^{-5}	3.8×10^{-4}	4.22×10^{-6}	0.42	4.0×10^{-4}
Co	0.6	4.0×10^{-4}	1.3×10^{-4}	4.35×10^{-6}	0.14	3.8×10^{-4}
Si	0.6					
Total	200.0		0.0913	1.60×10^{-3}[c]	100.0	0.151

[a] Calculated assuming $k_G = 9 \times 10^{-6}$ mol/s·cm²·atm.

[b] This release rate was assumed since experimental results were not available.

[c] Average molecular weight = $0.0913/1.60 \times 10^{-3} = 57.1$.

Table C.2. Comparison of calculated and experimental partial pressures in SASCHA at 2400°C

Material	Amount in SASCHA		Vapor pressure of element (atm)	Partial pressure by Rault's Law[a] (atm)	Experimental P if $k_G = 9 \times 10^{-6}$[b] mol/s·cm²·atm
	Moles	Mole fraction in liquid			
Fe	0.974	0.460	0.096	0.044	0.0569
Mn	0.0291	0.0137	5.0	0.0685	0.0576
Cr	0.296	0.140	0.24	0.0336	0.0279
Sn	0.00379	0.00178	0.39	0.0007	0.0039
UO_2	0.333	0.157	0.00117[c]	1.84×10^{-4}	4.7×10^{-4}
Ni	0.126	0.0595	0.066	0.0039	0.0036
Zr	0.324	0.153	1.5×10^{-5}	2.3×10^{-6}	4.0×10^{-4}
Co	0.0102	0.00482	0.06	2.9×10^{-4}	3.8×10^{-4}
Si	0.0214	0.0101			
Total	2.117			0.151	0.151

[a] Partial pressure = vapor pressure of pure substance x mol fraction in liquid.

[b] $P = 94.2 \frac{R \text{ mass}}{MW}$.

[c] Vapor pressure of pure UO_2.

References for Appendix C

C.1. H. Albrecht, V. Matschoss, and H. Wild, "Experimental Investigation of Fission and Activation Product Release from LWR Fuel Rods at Temperatures Ranging from 1500=2800°C," *Proceedings of the Specialists' Meeting on the Behavior of Defected Zirconium Alloy Ceramic Fuel in Water Cooled Reactors*, CONF-790935-3 (September 1979).

C.2. H. Albrecht and H. Wild, "Investigation of Fission Product Release by Annealing and Melting of LWR Fuel Pins in Air and Steam," *Proceedings of the Topical Meeting on Reactor Safety Aspects of Fuel Behavior*, Aug. 2-6, 1981, Sun Valley, Idaho (to be published).

C.3. G. W. Parker, R. A. Lorenz, and J. G. Wilhelm, "Simulated Transient Accidents in TREAT," pp. 8-20 in *Nuclear Safety Program Annual Progress Report for Period Ending December 31, 1966*, ORNL-4071 (March 1967).

C.4. G. W. Parker and R. A. Lorenz, "Simulated Transient Accidents in TREAT," pp. 44-54 in *Nuclear Safety Program Annual Progress Report for Period Ending December 31, 1967*, ORNL-4228 (April 1968).

C.5. G. W. Parker et al., *Out-of-Pile Studies of Fission-Product Release from Overheated Reactor Fuels at ORNL, 1955-1965*, ORNL-3981 (August 1967), p. 98.

C.5a. G. W. Parker, "Effect of Time and Gas Velocity on Distribution of Fission Products from UO_2 Melted in A Tungsten Crucible in Helium," pp. 19-20 in *Nuclear Safety Program Semiannual Progress Report for Period Ending June 30, 1963*, ORNL-3483 (September 1963).

C.6. W. E. Browning et al., "Simulated Loss-of-Coolant Accidents in the ORR," pp. 3-29 in *Nuclear Safety Program Semiannual Progress Report for Period Ending June 30, 1965*, ORNL-3843 (September 1965).

C.7. G. W. Parker et al., *Out-of-Pile Studies of Fission Product Release from Overheated Reactor Fuels at ORNL, 1955-1965*, ORNL-3981 (August 1967), pp. 99-101.

C.8a. G. W. Parker et al., "Fission Product Release from Highly Irradiated UO_2" pp. 6-8 in *Nuclear Safety Program Semiannual Progress Report for Period Ending June 30, 1964*, ORNL-3691 (November 1964).

C.8b. G. W. Parker et al., "Behavior of Fission Products Released from High-Burnup UO_2 in the Containment Mockup Facility," pp. 27-32 in *Nuclear Safety Program Progress Report for Period Ending December 31, 1965*, ORNL-3915 (March 1966).

C.8c. G. W. Parker et al., "Behavior of Fission Products Released from Zircaloy-Clad High-Burnup UO_2 in the Containment Mockup Facility," pp. 73-77 in *Nuclear Safety Program Progress Report for Period Ending December 31, 1966*, ORNL-4071 (March 1967).

C.8d. G. W. Parker et al., "LOFT Support Studies - Fission-Product Release and Transport in Out-of-Pile Tests," pp. 25-30 in *Nuclear Safety Program Progress Report for Period Ending December 31, 1968*, ORNL- (June 1969).

C.9. W. A. Freeby, L. T. Lackey, and D. E. Black, *Fission Product Behavior Under Simualted Loss-of-Coolant Accident Conditions in the Contamination-Decontamination Experiment*, IN-1172 (January 1969).

C.10. G. W. Parker et al., *Out-of-Pile Studies of Fission-Product Release from Overheated Reactor Fuels at ORNL, 1955-1965*, ORNL 3981 (July 1967), pp. 95-97.

C.11. W. H. McAdams, *Heat Transmission*, 3d ed., p. 180, McGraw-Hill, New York, 1954.

C.12. T. H. Chilton and A. P. Colburn, "Mass Transfer (Absorption) Coefficients," *Ind. Eng. Chem.* 26(11), 1183-87 (1934).

Appendix D: ACRONYMS AND SYMBOLS

ANS	American Nuclear Society
ANSI	American National Standards Institute
BCL	Battelle Columbus Laboratories
BFNP	Browns Ferry Nuclear Plant
Br	Bromine
BWR	Boiling Water Reactor
CILRT	Containment Integrated Leak Rate Test
Co	Cobalt
Cr	Chromium
CRD	Control Rod Drive
Cs	Cesium
CS	Core Spray System
DF	Decontamination Factor
DW	Drywell
ECCS	Emergency Core Cooling System
EPA	Electrical Penetration Assembly
EPRI	Electric Poweer Research Institute
Fe	iron
FSAR	Final Safety Analysis Report
HAARM	Heterogeneous Aerosol Agglomeration Revised Model
HOI	Hypoiodous Acid
HPCI	High Pressure Coolant Injection
I	Iodine
$I_2(d)$	Dissolved molecular iodine
ID	Internal Diameter
Kr	Krypton
L	Liter or Leakage
L_T	Leakage at Test Pressure
La	Maximum Allowable Integrated Leak Rate
LACP	Loss of AC Power
LLRT	Local Leak Rate Test
LPCI	Low Pressure Coolant Injection Mode of the RHR System

LOCA	Loss of Coolant Accident
LWR	Light Water Reactor
MARCH	Meltdown Accident Response Characteristics
Mn	Manganese
MPa	Megapascal
MSIV	Main Steam Isolation Valve
Mwd/te	Megawatt Day per Tonne
Ni	Nickel
NRC	Nuclear Regulatory Commission
O	Oxygen
ORNL	Oak Ridge National Laboratory
Pa	Pascal
PC	Partition Coefficient
PCV	Pressure Control Valve
PCIS	Primary Containment and Reactor Vessel Isolation Control System
P_p	Calculated peak Pressure Under Accident Conditions
PSP	Pressure Suppression Pool
P_t	Test Pressure
PV	Pressure Vessel
PWR	Pressurized Water Reactor
RCIC	Reactor Core Isolation Cooling System
RES	Office of Nuclear Regulatory Research
RHR	Residual Heat Removal System
RPV	Reactor Pressure Vessel
RWCU	Reactor Water Cleanup System
SAI	Science Applications Incorporated
SASA	Severe Accident Sequence Analysis
SBGTS	Standby Gas Treatment System
SCFH	Standard Cubic Feet per Hour
Si	Silicon
SI	International System of Units (Systeme International)
Sn	Tin
SNL	Sandia National Laboratories
SRV	Safety Relief Valve

STP	Standard Temperature Pressure
TIP	Traveling Incore Probe
TVA	Tennessee Valley Authority
U	Uranium
WW	Wetwell
Xe	Xenon
Zr	Zirconium

NUREG/CR-2182
Volume 2
ORNL/NUREG/TM-455/V2
Dist. Category RX, 1S

Internal Distribution

1. E. C. Beahm
2. J. T. Bell
3. T. E. Cole
4. D. H. Cook
5. W. Davis, Jr.
6. D. E. Ferguson
7. G. F. Flanagan
8. S. R. Greene
9. R. M. Harrington
10-11. S. A. Hodge
12. T. S. Kress
13. R. A. Lorenz
14. A. P. Malinauskas
15. F. R. Mynatt
16. A. L. Lotts
17. T. W. Robinson, Jr.
18. R. D. Spence
19. I. Spiewak
20. H. E. Trammell
21. C. F. Weber
22-24. R. P. Wichner
25. A. L. Wright
26. R. G. Wymer
27. Patent Office
28. Central Research Library
29. Document Reference Section
30-31. Laboratory Records Department
32. Laboratory Records (RC)

External Distribution

33-34. Director, Division of Accident Evaluation, Nuclear Regulatory Commission, Washington, DC 20555
35-36. Chief, Severe Accident Assessment Branch, Nuclear Regulatory Commission, Washington, DC 20555
37. Chief, Fuel Behavior Branch, Nuclear Regulatory Commission, Washington, DC 20555
38. Office of Assistant Manager for Energy Research and Development, DOE, ORO, Oak Ridge, TN 37830
39. Director, Reactor Safety Research Coordination Office, DOE, Washington, DC 20555
40. R. R. Sherry, Fuel Behavior Branch, Nuclear Regulatory Commission, Washington, DC 20555
41-42. L. D. Proctor, Tennessee Valley Authority, W10D199 C-K, 400 West Summit Hill, Knoxville, TN 37902
43-44. Wang Lau, Tennessee Valley Authority, W10C126 C-K, 400 West Summit Hill, Knoxville, TN 37902
45-46. R. F. Christie, Tennessee Valley Authority, W10C125 C-K, 400 West Summit Hill, Knoxville, TN 37902
47-48. J. A. Raulston, Tennessee Valley Authority, W10C126 C-K, 400 West Summit Hill, Knoxville, TN 37902
49-50. H. L. Jones, Tennessee Valley Authority, W10A17 C-K, 400 West Summit Hill, Knoxville, TN 37902
51-52. Technical Information Center, DOE, Oak Ridge, TN 37830
53-587. Given distribution as shown under categories RX, 1S (NTIS-10)

☆U.S. GOVERNMENT PRINTING OFFICE: 1982-546-067/129